

Università degli Studi di Napoli
“Federico II”

DIPARTIMENTO DI FARMACIA



**DOTTORATO DI RICERCA IN
SCIENZA DEL FARMACO
XXVII ciclo**

*Monoclonal antibodies
as powerful tools in
diagnosis and therapy*

PhD candidate
Dott.ssa ANNALIA FOCA'

Tutors
Prof.ssa T. Iuvone
Dott.ssa A. Sandomenico

Coordinator
Prof.ssa M.V. D'Auria

INDEX

STUDY I

DEVELOPMENT AND STUDY OF ANTI-NODAL MONOCLONAL ANTIBODIES AND THEIR FUNCTIONAL FRAGMENTS AS POTENTIAL ANTI-TUMORAL TOOLS

ABSTRACT

	6
I 1. INTRODUCTION	8
1.1 The superfamily of the Transforming Growth Factor-beta (TGF- β)	8
1.2 Nodal ligands	12
1.3 Human Nodal protein	13
1.3.1 Structure	13
1.3.2 Biological functions	16
1.3.3 Signaling	17
1.3.4 Internalization of Nodal ligand-receptor complexes	17
1.3.5 Inhibitors	18
1.4 Cutaneous melanoma	20
1.4.1 Expression of Nodal in human melanoma	21
1.5 Monoclonal antibodies	23
1.5.1 Antibody structure	23
1.5.2 Monoclonal antibodies in cancer therapy	25
1.5.3 Mechanism of action of therapeutic antibodies	28
1.6 Antibody fragments generated by enzymatic digestion	32
1.7 Aim of the project	34
I 2. MATERIALS AND METHODS	35
2.1 Materials and chemicals	35
2.2 Solid-phase peptide synthesis (SPPS), purification and identification of peptides	36
2.3 Immunogen preparation: conjugation of the immunogen peptide to KLH and BSA	37
2.4 Generation of monoclonal antibodies by Hybridoma technology	38
2.5 Mabs isotypization	39
2.6 Enzyme-Linked Immunosorbent Assays (ELISA)	39
2.7 Monoclonal antibodies purification	42
2.8 Surface Plasmon Resonance (SPR) analyses	43
2.9 Antibody deglycosylation	45
2.10 Enzymatic digestion of 3D1 with a panel of proteases	46
2.11 Purification of Fab/F(ab') ₂ /Fab' fragments	48
2.12 Reduction of the F(ab') ₂ to Fab' and Fab' alkylation	48
2.13 Dot blot analysis	49
2.14 Western blot analysis	49
2.15 Cell culture and antibody treatment	51
2.16 Fluorescence-activated cell sorting (FACS) analyses	52
2.17 Soft agar clonogenic assay	53
2.18 Vasculogenic mimicry assay	53

2.19 Lung colonization in mice induced by C8161 cells	53
2.20 Immunohistochemical analyses	54
I 3. RESULTS	55
3.1 Generation and characterization of anti-Nodal mAbs	55
3.1.1 Antigen design	55
3.1.2 Chemical synthesis, purification and identification of human Nodal and GDF peptides	55
3.1.3 Screening of hybridoma supernatants and epitope identification by ELISA assay	57
3.1.4 Isolation of anti-Nodal mAbs from hybridoma supernatants	58
3.1.5 SPR binding analyses of mAbs to <i>rh</i> Nodal protein	60
3.2 Biochemical characterization of the 3D1 mAb	62
3.2.1 SPR competition assay	62
3.2.2 Production and purification of Fab/F(ab') ₂ /Fab' fragments	62
3.2.3 SPR comparative binding analysis of Fab/F(ab') ₂ /Fab' fragments	70
3.2.4 Epitope mapping assay	70
a. ELISA assay	70
b. SPR analyses	71
3.2.5 Specificity assay	75
3.3 Detection of human Nodal	77
3.3.1 Calibration curve for ELISA detection of <i>rh</i> Nodal protein	77
3.3.2 Preliminary immunoblot analyses	78
3.3.3 Detection of endogenous human Nodal	79
a. Western blot analysis	79
b. FACS analyses	80
3.3.4 Competition assay between 3D1 antigen peptide and endogenous Nodal protein	81
3.4 Functional study of the 3D1 mAb	82
3.4.1 Targeting Nodal in melanoma C8161 cells <i>in vitro</i>	82
a. Effects on Nodal signaling	82
b. Clonogenic assay	84
c. Vasculogenic mimicry inhibition	85
3.4.2 Targeting Nodal in lung colonization induced in mice by C8161 melanoma cells	87
a. Effects on lung colonization	87
b. Effects on the cell cycle	88
c. Immunohistochemical detection of P-Smad2	91
I 4. DISCUSSION	92

STUDY II

GENERATION AND PRODUCTION OF MONOCLONAL ANTIBODIES AGAINST POLYACETYLATED APE/Ref1 PEPTIDES

ABSTRACT	96
II 1. INTRODUCTION	97
1.1 Human Apurinic/Apyrimidinic Endonuclease I	97
1.2 Regulation of the acetylation status	99
1.3 Aim of the project	101
II 2. MATERIALS AND METHODS	102
2.1 Materials and chemicals	102
2.2 Peptide synthesis, purification and identification	102
2.3 Generation of anti-Ac-APE1/Ref1[24-36] mAbs	104
2.4 Enzyme-Linked Immunosorbent Assays (ELISA)	107
2.5 Monoclonal antibodies purification	109
2.6 Acetylation of proteins	109
2.7 Western blot analysis	109
II 3. RESULTS	111
3.1 Antigen preparation and characterization	111
3.2 Screening of hybridoma supernatants on wild-type and acetylated APE1/Ref1[24-39] monoclonal antibodies	113
3.3 Purification of anti-Ac-APE1/Ref1[24-39] monoclonal antibodies	114
3.4 Screening of selected mAbs with library fractions to determine selectivity toward differently acetylated peptides	115
3.5 Dose-response ELISA assays	117
3.6 Selectivity assays	122
a. ELISA assays	122
b. Western blot analysis	124
II 4. DISCUSSION	126
REFERENCES	129
Abbreviations	135
Appendix : original publications	137

STUDY I

DEVELOPMENT AND STUDY OF ANTI-NODAL MONOCLONAL ANTIBODIES AND THEIR FUNCTIONAL FRAGMENTS AS POTENTIAL ANTI-TUMORAL TOOLS

ABSTRACT

Nodal is a potent embryonic morphogen belonging to the TGF-beta superfamily. Typically, it binds to the Alk4/ActRIIB receptor complex in the presence of the co-receptor Cripto-1. Nodal expression is physiologically restricted to embryonic tissues and human embryonic stem cells and is absent in normal cells, including melanocytes. However it re-emerges in a number of human cancers, including melanoma, breast and colon cancer. Recent studies indicate that Nodal expression correlates with melanoma tumor progression toward a metastatic phenotype, indeed inhibition of the Nodal pathway also blocks the tumorigenic capacity and the plasticity of aggressive human melanoma cells. Recently, also Cripto-1 expression has been correlated to the pathogenesis and progression of human melanoma tumor. These findings suggest the hypothesis that inhibition of the Nodal-Cripto-1 signaling, which is supported by a direct binding between the two proteins, is a valid therapeutic approach against melanoma and increases the interest for Nodal as both a diagnostic or prognostic marker and as a potential new target for therapeutic intervention against melanoma. With the aim to produce molecules able to recognize Nodal and to block the signaling by preventing the association with Cripto-1, we have generated and screened a set of monoclonal antibodies targeting a major CBR (Cripto-Binding-Region) site which encompasses residues around Glu49 and Glu50 of human Nodal involved in the interaction with Cripto-1.

With this approach, we have selected one, named 3D1, which strongly associates (K_D about 1.4 nM) with full-length rhNodal. The selected mAb has been successfully tested for its ability to recognize endogenous Nodal protein in a panel of melanoma cell lines by both western blot and FACS analyses. Furthermore, the antibody inhibits the binding of Nodal to Cripto-1, as demonstrated by competitive SPR assays and, most importantly, blocks the Nodal-dependent activation of Smad2/3 in melanoma cancer cells. Notably, the antibody also blocks the Cripto-independent Nodal signalling converging on the MAPKs, as demonstrated by the concomitant effective blocking of MAPK activation. Given the autocrine mechanism of activation of Nodal (Smad2/3 regulate through Smad4 the expression of Nodal itself), the antibody also has the ability to reduce Nodal expression in the supernatants of C8161 cells. In

addition, it is also effective in reducing the C8161 clonogenicity and the typical vasculature-like phenotype induced by Nodal (vasculogenic mimicry). Remarkably, 3D1 *in vivo* strongly reduces lung colonization induced by C8161 metastatic cells, injected in mice. Moreover, immunohistochemical analyses revealed the ability of the 3D1 to affect the progression of the cell cycle by reducing Cyclin B1 and concurrently increasing p27 expression.

The data accumulated on the 3D1 anti-Nodal mAb are all supportive of a huge diagnostic and therapeutic potential of this reagent. Next steps are therefore devoted to antibody affinity maturation to increase binding and selectivity and to humanization, to pave the way to *in vivo* experiments on human cells and tissues.

I 1. INTRODUCTION

1.1 THE SUPERFAMILY OF THE TRANSFORMING GROWTH FACTOR-BETA (TGF- β)

The transforming growth factor- β (TGF- β) superfamily comprises many structurally related ubiquitous cytokines that exerts several regulatory functions in cell processes, including development, cell-cycle progression, cell differentiation, reproductive function, adhesion, motility, bone morphogenesis, neuronal growth, wound healing and immune surveillance ^[1-5]. The ligands of this family are highly conserved across the species, denoting their importance during the evolution, indeed TGF- β orthologs are found from *Caenorhabditis elegans* through humans with equally conserved cell surface receptors and signaling co-receptors.

In mammals, the TGF- β superfamily is composed of more than 30 factors that in turn can be grouped into two sub-families; one family branch includes factors such as Activin, Lefty, Myostatin, Nodal and TGF- β , while bone morphogenetic proteins (BMPs), anti-muellerian hormone (AMH, also known as MIS), and growth and differentiation factors (GDFs) belong to the other branch ^[6-8].

Human Activins, AMH/MIS, AMH/MIS, BMPs, GDFs and Nodals are key regulators of embryonic stem cell differentiation, body axis formation, left-right symmetry and organogenesis. In addition to these functions, in adult organism BMPs are involved in bone growth and repair, Myostatin in inhibition of muscle development and Activins and GDF9 in regulation of gonadal function ^[7].

In normal and premalignant cells, TGF- β promotes homeostasis and suppresses tumor progression directly through cell-autonomous tumor-suppressive effects such as cytostasis, differentiation and apoptosis, or indirectly through effects on the stroma (suppression of inflammation and stroma-derived mitogens). However, when cancer cells lose TGF- β tumor-suppressive responses, they can use TGF- β to initiate immune evasion, growth factor production, differentiation into an invasive phenotype and metastatic dissemination or to establish and expand metastatic colonies ^[9].

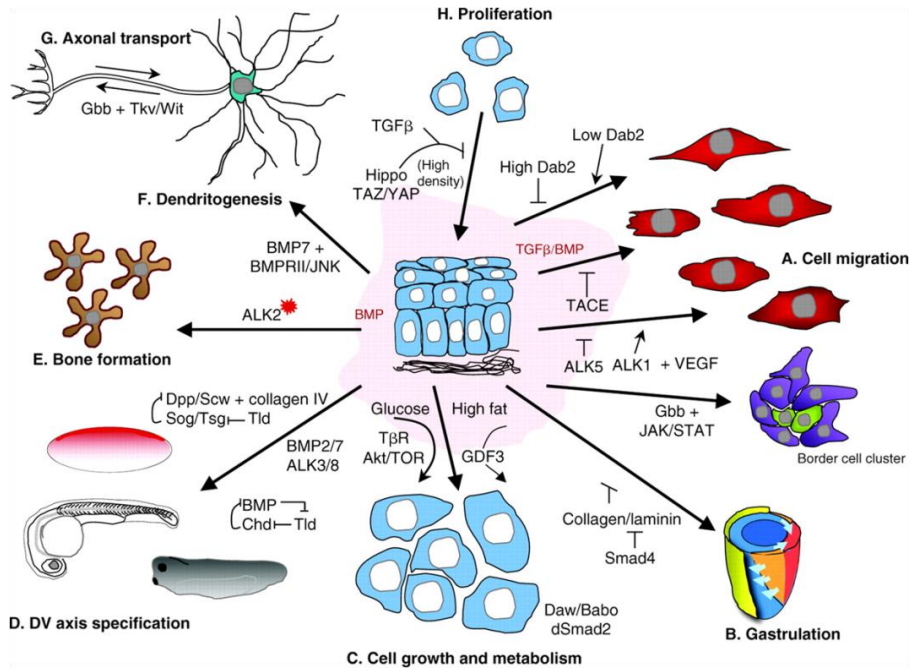


Figure 1.1: A summary of biological responses to TGF β family signalling ^[10].

Members of the TGF- β superfamily consist of both homodimers and heterodimers, characterized by seven cysteine residues, six of these residues form three intrasubunit disulfide bonds crucial for structural integrity, whereas the remaining cysteine residue forms a disulfide bond with the other subunit so as to stabilize the dimer interface ^[11].

The monomeric TGF- β exhibits a general structure that involves two pairs of antiparallel β -strands forming a flattened surface, projecting away from a long α -helix. Of interest, one of the disulfide bonds of the core traverses through a ring formed by two other disulfide bonds generating the “cysteine knot” motif ^[11]. The monomer has been described as a four-digit hand, where each β -strand is linked to a finger. At the N-terminus, fingers 1 and 2 are antiparallel, with finger 2 leading to a general helix ‘wrist’ region, followed by antiparallel fingers 3 and 4 and the C-terminus. The dimeric active form of TGF- β is stabilized by hydrophobic interactions and is usually further strengthened by an intersubunit disulfide bridge ^[11-13].

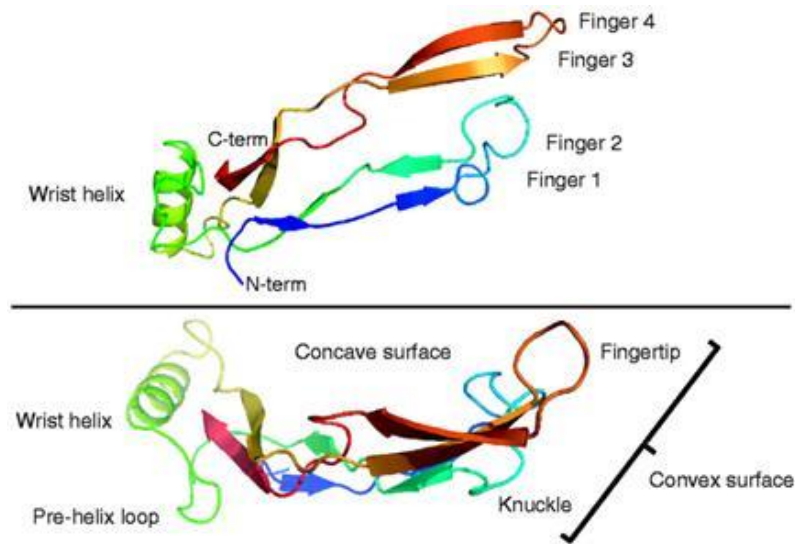


Figure 1.2: The TGF- β fold ^[11].

TGF- β s exert their functions through an endocrine, paracrine and autocrine mechanism ^[11].

Cellular responses to most TGF- β ligands are transduced through interactions with the two single transmembrane-spanning serine–threonine kinase receptors, termed type I and type II receptors ^[14]. Type I and type II receptors are glycoproteins of approximately 55 and 70 kDa respectively, which interact upon ligands binding. All type I receptors possess a highly conserved TTSGSGSG motif in their cytoplasmic region, upstream from the kinase domains, termed the GS (Glycine-Serine) domain, required to regulate their kinase activity. In the absence of ligand, type II and type I receptors exist as homodimers at the cell surface ^[14]. TGF- β signalling is triggered by binding to and bringing together type I and type II receptors on the cell surface to form a ternary holo-complex ^[15,16]. After holo-complex formation, the type II receptor, via its active kinase domain, transphosphorylates the GS domain of type I receptor, which in turn phosphorylates Smads proteins. Smads are intracellular mediators of transcriptional activation, grouped into three functional classes: the receptor-regulated Smad (R-Smad), the co-mediator Smad (co-Smad) and the inhibitory Smad (I-Smad) ^[17].

R-Smads (Smad1, Smad5, and Smad8 for BMP and Smad2 and Smad3 for other TGF- β ligands) are directly phosphorylated and activated by type I receptor kinases. Subsequently they undergo homotrimerization and form hetero-

complexes with the co-Smad, Smad4 (**Fig. 1.3**). The activated Smad complexes translocate into the nucleus where, in association with nuclear cofactors, regulate the transcription of target genes. By contrast, the I-Smads (Smad6 and Smad7) negatively regulate TGF- β signaling through competition with R-Smads for receptor or co-Smad interaction and by targeting the receptors for degradation. On the basis of their downstream signaling, TGF- β ligands act as tumor suppressors in early stages of cancer, while they promote tumor cell proliferation at later stages of carcinogenesis ^[18]. In fact, while TGF- β Smad-2/3 dependent signaling is related to an increased cell proliferation, Smad-7 activation results in decreased cell proliferation ^[19]. In addition, in normal and premalignant tissues TGF- β s act as anti-oncogenic factor, mediating cell cycle arrest in G1 phase; by contrast, TGF- β s secreted from tumours or stroma cells surrounding tumours enhance invasion and metastasis ^[20-22] and they also control tumour development influencing apoptotic pathways. In addition to Smad-mediated transcription, TGF- β s can activate further signalling cascades (**Fig. 1.3**), such as Erk (extracellular signal-regulated kinase), JNK (JUN N-terminal kinase), B-RAF, RAS, PI3K–AKT and p38 MAPK (mitogen-activated protein kinase) pathways. Cellular responses to TGF- β are affected by the balance between cooperativity and counteraction of Smad and MAPK pathways. However, the mechanisms of Erk, JNK or p38 MAPK activation by TGF- β and their biological consequences are still unclear ^[23].

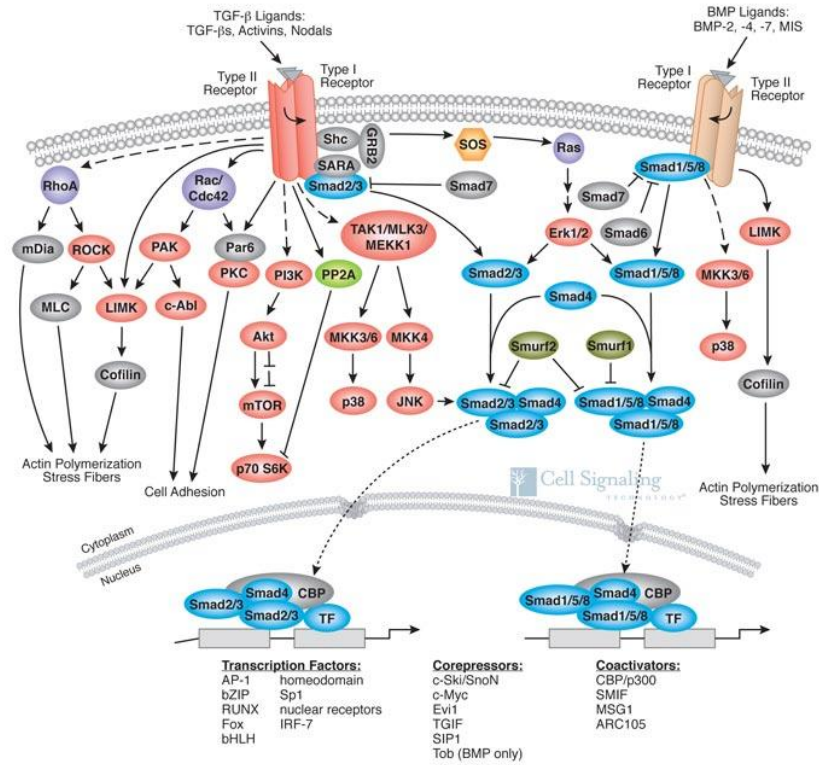


Figure 1.3: Canonical and non-canonical TGF-β signalling [24].

1.2 NODAL LIGANDS

Nodal ligands were initially identified through forward genetic screens in mouse and zebrafish. Whereas there is a single Nodal ligand in mouse, human and chick, multiple Nodal-related ligands are found in frogs (encoded by six *xNr* genes) and zebrafish [*cyclops* (*cyc*; *ndr2* – Zebrafish Information Network), *squint* (*sqt*; *ndr1* – Zebrafish Information Network) and *southpaw* (*spw*)]^[25].

Like most members of the TGF-β superfamily, Nodal proteins are synthesized and secreted as homodimeric precursors with a hydrophobic leader sequence (15-25 aa), an N-terminal pro-domain (50-375 aa) and a mature C-terminal domain of 110-140 aminoacids. Removal of the prodomain through extracellular proteolytic processing, involving subtilisin-like proprotein convertases Spc1/Furin and Spc4/Pace4, is required to produce the mature functional form of the Nodal dimer^[26-28]. Convertases are not simply housekeeping proteases that allow Nodal processing, they also regulate the spatial and temporal distribution of active Nodal ligands. Recent data suggest that the EGF (Epidermal growth factor) - CFC (colony-forming cell) superfamily members are involved in the

maturation process of Nodal by recruiting PACE-4/Furin and Nodal in proximity to the Nodal receptors on the cell membrane, increasing both efficiency of Nodal processing and availability of the its final active form ^[29].

It appears that the cleavage of the prodomain allows Nodal ligands to trigger signal transduction and promotes their turnover through endocytosis^[28]. Moreover the removal of the prodomain reduces Nodal stability and promotes local autocrine signaling, whereas glycosylation stabilizes the mature form of Nodal and increases its ability for paracrine signaling ^[28]. Of interest, although Nodal precursors are more stable than the mature forms ^[28], they exhibit weak induction activity ^[26,27].

1.3 HUMAN NODAL PROTEIN

1.3.1 Structure

Human Nodal is synthesized as pre-pro-Nodal (55 kDa), that is proteolytically processed by the subtilisin-like proprotein convertases PACE-4 and Furin, leading to the active intermediate pro-Nodal (37 kDa) and eventually active Nodal (22 kDa).

The mature form of Nodal is a homodimeric protein of 220 amino acids and each Nodal monomer (110 aa) adopts the canonical, symmetric and elongated TGF- β arrangement (**Fig. 1.4**). The structure involves two antiparallel β -sheets (β 1 and β 2) forming a flattened surface, composed by two and four strands, a short turn linking the first two strands and an amphipathic α -helix (H3) perpendicular to the β -sheets. One of the disulfide bonds of the core crosses a ring formed by the two other disulfide bonds, generating the so called “cysteine knot” motif ^[11]. The overall monomer folding has been described as a hand with the helix mimicking the wrist, the cysteine knot core the palm, and the β -sheets the fingers ^[30]. The convex surface of the fingers corresponds to the “knuckle epitope” while the helix corresponds to the “wrist epitope”; these regions usually bind to the type II and type I receptors, respectively ^[31]. The monomer core with β -sheets and the cysteine knot is conserved across the different members of TGF- β superfamily. The Nodal monomers are covalently linked by a single disulfide bond (Cys76 from both monomers) and intermonomer contacts occur by interactions of the helix H3 with the β -sheets of the neighboring molecule ^[11].

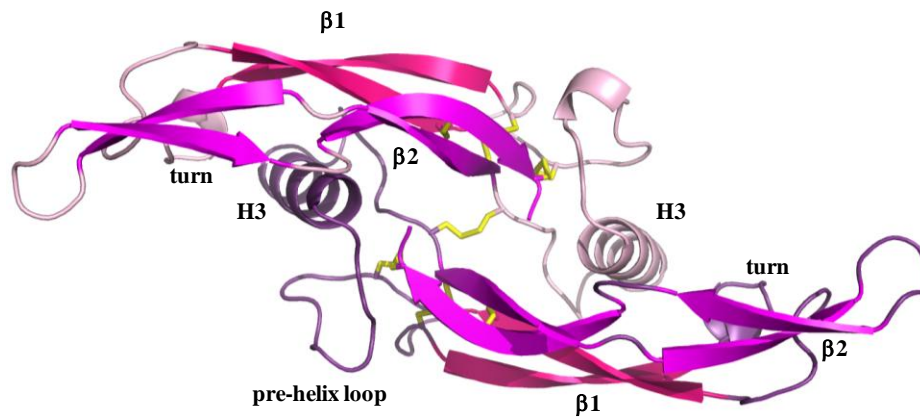


Figure 1.4: Ribbon representation of Nodal dimer model built by Modeller6v2. The color code is based on the sequence of secondary structure elements. The interchain disulfide bridges are shown as yellow sticks, whereas the interchain one as a green stick ^[33].

Docking studies performed to investigate the interaction between Nodal and the EGF-like domain of the co-receptor Cripto ^[32] revealed that, unlike the other TGF- β ^[11], the H3 wrist helix of Nodal doesn't interact with this domain but it exerts only a structural role, contributing to the proper orientation of Nodal regions – the pre-helix loop and the finger tips - directly involved in Cripto binding ^[32].

Residues of human Nodal required for the binding to the EGF-like domain of Cripto-1 are E49, E50, Y58, N79 and T81. In particular, the glutamic acids, E49 and E50, located in the pre-helix loop play a relevant role in the Cripto recognition; in fact, when these residues are mutated to A, affinity for Cripto is remarkably reduced ^[32]. Moreover, the Nodal Y58 can pocket in a polar groove that G87 and T88 residues of the Cripto-1 EGF-like domain form together with the Nodal N79, T81, and G92 residues. The EGF-like domain T88 residue, normally O-fucosylated and well exposed on the surface so that the fucose can be easily accommodated ^[32], is required for Cripto to facilitate Nodal signaling, indeed, when this threonine is replaced by D and/or E residues in Cripto mutants, the affinity for Nodal drastically decreases compared to the wild-type protein ^[33]. Furthermore, T88 is close to Nodal E49 so that its replacement with acidic residues can cause electrostatic repulsions ^[33]. In addition, favorable electrostatic contacts between Nodal E49 and EGF-like R80 are established. Moreover, EGF-like R104, another residue important for Nodal binding, can establish electrostatic interactions at the binding interface with Nodal D97 and

D90 and even cation- π interactions with Nodal Y88 and W27 ^[34]. Finally, favorable aromatic interactions between Nodal W27 and EGF-like F94 occur ^[32]. So far it has been reported that Nodal can bind to ALK4 only in the presence of the co-receptor Cripto, while it binds directly to ALK7 without Cripto ^[35-37]. The amino acids crucial for the interaction are mostly hydrophobic and located in the “wrist epitope” and on the N-terminal region of the ligand and span the entire region that includes loop 23 of the receptor ^[38]. Of interest, very recent biochemical assays have revealed that Nodal is able to bind to ALK4 without the presence of Cripto ^[39] but this results need to be further investigated in biological systems.

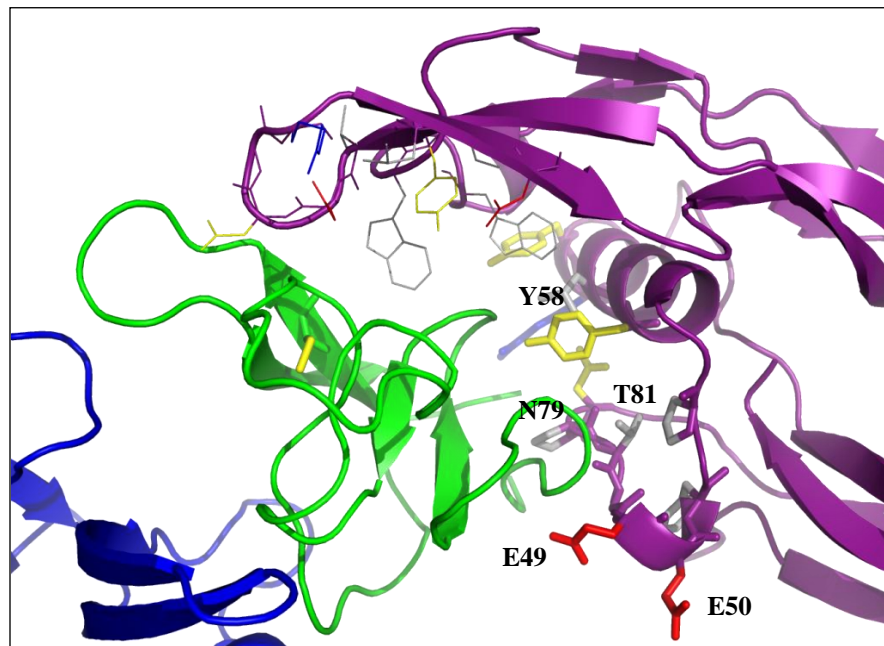


Figure 1.5: Ribbon representation of the proposed model for the interaction between Nodal (purple) and the EGF-like domain of hCripto-1 (green).

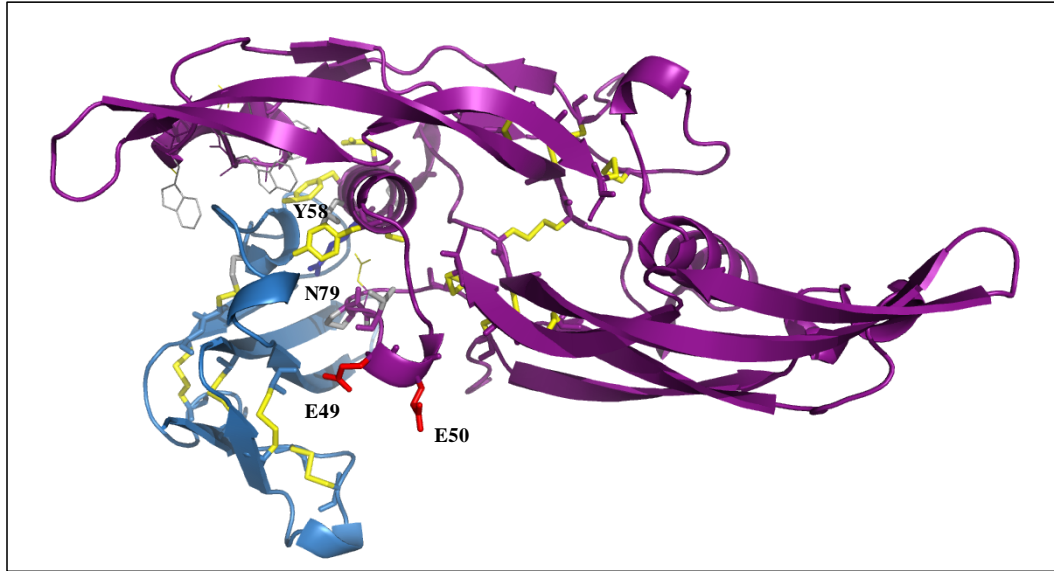


Figure 1.6: Ribbon representation of the proposed model for the interaction between Nodal (purple) and ALK7 (cyan).

1.3.2 Biological functions

Nodal is a potent morphogen and regulator of cell fate in both embryological and adult systems ^[40,25]. Like many other members of the TGF- β superfamily, it is involved in cell differentiation in early embryogenesis playing a key role in signal transfer from the node, in the anterior primitive streak and to lateral plate mesoderm (LPM) ^[41,42].

Furthermore, it was demonstrated that the TGF- β /activin/Nodal signaling is involved in maintaining pluripotency in human embryonic stem (ES) cells since disruption of this signaling pathway results in their differentiation ^[43,44]. In addition, Nodal has been demonstrated to inhibit differentiation of human ES cells along the neuroectodermal differentiation pathway, further supporting a role for Nodal in the maintenance of pluripotency in human ES cells ^[44], whereas in mouse ES cells TGF- β signaling is active but not required for stemness ^[43], suggesting that there are differences in the regulatory pathways involved during the maintenance of pluripotency between human and mouse ES cells.

Nodal signaling plays a dual role in neural development, its inhibition is required to generate the anterior neural tissue while the subsequent maintenance and patterning of neural tissue depends upon axial mesendoderm generated in response to Nodal signaling ^[45].

Nodal can also regulate mesoderm and endoderm formation, establishment of the left–right (LR) axis and subsequent asymmetric development and positioning of visceral organs ^[25,44,46].

Although most genes in the Nodal pathway are rarely expressed during later development and adulthood, it was found that pathway activity is upregulated in many human cancers.

1.3.3 Signaling

Nodal signaling is triggered by its binding to heteromultimeric complexes consisting of the EGF-like domain of the co-receptor Cripto-1 and type I (**ALK 4/7**) and type II (**ActRIIB**) activin-like serine-threonine kinase receptors; this event leads to the phosphorylation and activation of ALK 4/7 by ActRIIB and subsequent ALK 4/7-mediated phosphorylation of Smad-2 and Smad-3 ^[47]. Phosphorylated Smad-2/3 associate with the common mediator (co-Smad) Smad-4 and translocate to the nucleus where, together with transcription factors such as FoxH1, Mixer and p53, regulate expression of target genes, such as Nodal itself and Lefty, its natural inhibitor. Indeed Nodal activates its own transcription via a positive feedback loop. However, it still remains unclear how essential is the role of Cripto-1 for Nodal signaling, since recent studies have demonstrated that the Nodal precursor can bind to ALK 4 in a Cripto-1-independent manner, allowing the expression of Nodal-responsive genes ^[48].

While Nodal is able to bind directly to ALK7 without Cripto-1, the latter is required as co-receptor for Nodal binding to ALK4. However, Cripto-1 is still able to enhance the responsiveness of the ALK7/ActRIIB complex to Nodal, suggesting that both ALK7 and ALK4 cooperate with Cripto-1 in modulating Nodal signaling ^[49,50].

Furthermore, Nodal can activate other important signaling proteins through Smad-independent pathways, such as MAPK (ras/raf/mitogen-activated protein kinase) and PI3K–AKT ^[47].

1.3.4 Internalization of Nodal ligand-receptor complexes

Nodal signal transduction during embryonic development can be regulated by receptor internalization and degradation. The formation of ligand-receptor complexes on the plasma membrane are usually followed by internalization of

the complexes, that can result in switching off receptor-mediated signaling or propagation of the signal ^[51]. TGF- β receptors are internalized through clathrin-coated pits, which facilitate signaling, or through lipid raft-caveolae, which promote proteasomal degradation of the receptors ^[52].

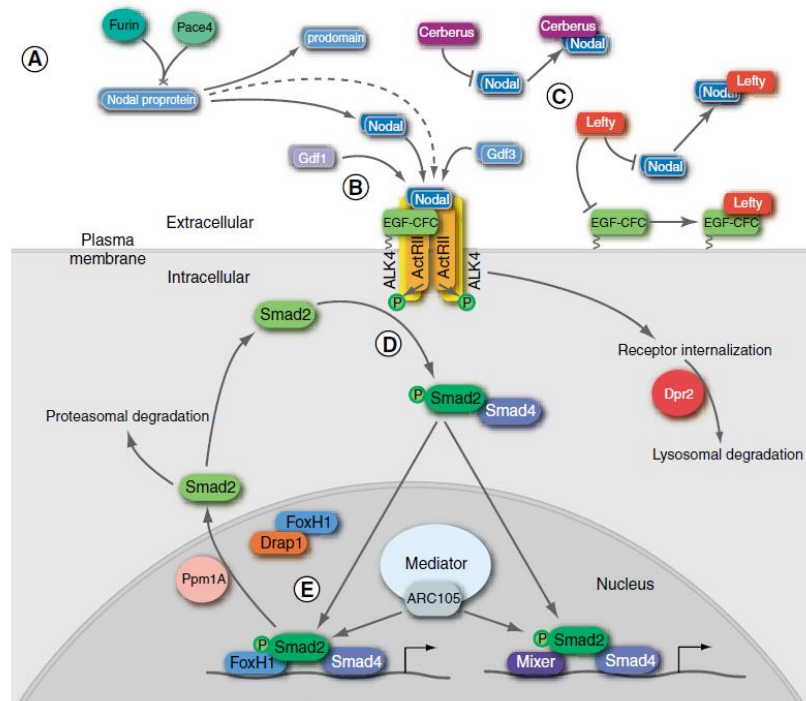


Figure 1.7: Schematic outline of the Nodal signaling pathway ^[53]

1.3.5 Inhibitors

Since Nodal is a key regulator of vertebrate embryological development, its signaling requires a tight spatial and temporal control. However only a few Nodal inhibitors have been identified ^[54] (see **Table 1**).

Table 1. Summary of Nodal antagonists^[54]

Factors	Types	Antagonist mechanisms
Lefty proteins	secreted proteins	inhibit the Nodal signal transduction by binding to the Nodal coreceptors EGF-CFCs as well as the Nodal ligands
Cerberus/ Dan family members	secreted proteins	binds to the Nodal proteins preventing their signal transduction
Tomoregulin-1	transmembrane proteins	binds to egf-cfcs to prevent the Nodal signal transduction
Bmp3/Bmp7	secreted proteins	form heterodimers with Nodal proteins and result in mutual inhibition
Nicalin/Nomo	endoplasmatic reticulum membrane proteins	probably modifies or traps the Nodal signalling components
Dapper 2	endosomal proteins	promotes degradation of Nodal receptors
Drap 1	transcriptional repressor	binds to the DNA binding domain of FoxH1

Lefty-A and -B, two highly divergent members of the TGF- β superfamily, act as specific antagonists of Nodal signaling by directly binding to Nodal or to Cripto-1 preventing the formation of a more active signaling complex between Nodal, the type I and II Activin receptors^[55]. This restriction of Nodal signaling can occur in the extracellular microenvironment where Nodal and Cripto-1 are present, as well as at the cell surface. Notably, the Lefty proteins are not competitive inhibitors of the ALK receptor complex since they fail to bind ALK4 or ActRIIB. Furthermore, in embryological systems, the Lefty genes are often downstream targets of Nodal signaling, which provides a powerful negative-feedback loop for this pathway^[25,56].

Cerberus, a member of the cysteine-knot superfamily, directly binds and blocks Nodal signaling^[57], but it was not expressed as abundantly as the Lefty proteins by human ES cells.

Finally, **Tomoregulin (TMEFF1)**, a transmembrane protein containing two follistatin domains and an EGF motif, indirectly inhibits Nodal signaling in binding to the CFC domain of Cripto-1 and sequestering it from the ALK4 receptor, thus preventing Cripto-1 from functioning as a coreceptor for Nodal^[56].

Deregulation of the expression of key players involved during proper development, such as the morphogen Nodal, results in embryonic lethality or even diseases in adults, such as cancer.

Nodal was identified in several human cancers and it plays a key role during the growth and spread of cancer cells. Therefore, a better understanding of the regulatory processes involved in Nodal expression and function may contribute to develop novel treatment strategies for targeting Nodal in human malignant diseases ^[58].

1.4 CUTANEOUS MELANOMA

The incidence and mortality rates of melanoma have been increasing over the last few decades. American Cancer Society estimated that the incidence of lifetime risk of developing melanoma is approximately 1 in 50 for Caucasians. Overall it is the 6th most common cancer in men and 7th most common in women. While melanoma related deaths also continue to increase, some significant breakthroughs in the understanding of the pathobiology of melanoma have resulted in promising new therapies. Risk factors for developing melanoma comprise prolonged exposure to ultraviolet radiation (UVR), increased number of melanocytic nevi, a family history of melanoma or a history of previous melanoma ^[59].

Melanomas are categorized into subgroups with similar clinical, epidemiologic and molecular features, which may be sensitive to distinct targeted therapy. Several models have been proposed describing melanoma as a linear process evolving from hyperplastic and dysplastic nevi to early and late stage melanoma. Recently, new methods have been proposed for improving the diagnosis of melanoma, as to discriminate benign lesions from melanoma, for instance, multiple tissue marker arrays or fluorescence in situ hybridization DNA.

Current therapies for advanced stage of melanoma employing cytotoxic agents are often associated with serious side effects and with relatively low percentages of response rates ^[59]. Initially, anti-cancer drugs exert their effect, killing of the majority of cancer cells sensitive to the chemotherapeutic agent.

However, many factors lead to chemoresistance such as increased signaling of cell survival pathways, enhanced DNA repair mechanisms or mutations of molecular targets in melanoma cells. Similarly, molecular redundancy and cross-talk between multiple signaling pathways reduce the efficacy in instances of targeted molecular biotherapy. Continuous efforts are dedicated to improving

detection and quantification of chemoresistance, not only to define the molecular mechanisms involved in drug resistance in melanoma, but also to help those patients which present resistance to standard treatments and who may otherwise benefit from a more aggressive or alternative approach. Studies continue to increase the understanding of the biological processes of melanoma and offer the potential for improving current methods for diagnosis and therapy ^[59] .

1.4.1 Expression of Nodal in human melanoma

Several studies in human cancers revealed a key role of Nodal and/or its coreceptors in the growth and spread of malignant cells, however it was demonstrated that Cripto-1 co-receptor also activate a common cancer-related pathway Nodal-independent ^[60], such as the c-Src–MAPK–AKT signaling.

Recent data indicate that Nodal is over-expressed with its co-receptor Cripto and appears to play a predominant role in the growth of several human cancers, including prostate ^[61], testicular ^[62], endometrial ^[63], ovarian ^[64], breast ^[65,66], brain ^[67], pancreatic ^[68,69], colon ^[70], hepatocellular carcinoma ^[71] and melanoma ^[72]. Interestingly, in some of these reports, Nodal expression was detected in the context of veery low Cripto-1 levels, indeed it remains still unclear how Cripto-1 and Nodal can exert their tumorigenic activity independently of each other ^[73]. Notably, it less than 5% of aggressive human melanoma cell lines were found to be Cripto-1 positive; therefore, it seems unlikely that the growth and metastatic potential of melanoma would be entirely dependent on the capability of less than 5% of an entire melanoma population to bind Nodal and induce the protumorigenic activity ^[58]. Studies are in progress to elucidate the role of Cripto-1 and Nodal in human cancer, in particular in melanoma.

Expression studies revealed that the presence of Nodal is restricted to embryonic tissues, hESCs (human embryonic stem cells) and cancer cells, whereas it is absent in normal cells, such as melanocytes ^[74]; indeed, Nodal expression is largely restricted to very early progenitor and reproductive cell types and re-emerges during tumorigenesis ^[58].

In addition, several studies indicate that Nodal expression positively correlates with melanoma tumor progression toward a metastatic phenotype ^[72], thus, metastatic melanoma cell lines (C8161, WM278 and 1205Lu) express high levels of Nodal, while Nodal is weakly expressed or absent in non-metastatic

melanoma cells (C81–61) ^[72]. Furthermore, Nodal expression positively correlates with melanoma progression clinically; indeed Nodal protein is absent in normal skin, is weakly expressed or absent in primary melanomas and it is only rarely observed in poorly invasive RGP melanomas, in contrast to invasive VGP melanomas and melanoma metastases, where Nodal expression is detectable in up to 60% of cases ^[72]. All these studies indicate that Nodal may be considered a useful biomarker of melanoma progression, from a treatable RGP disease to a more aggressive VGP disease, to the presence of metastases.

In addition to serving as a useful biomarker for melanoma progression, Nodal plays a key role in melanoma plasticity, invasiveness and tumorigenicity ^[72]. Several studies have demonstrated that aggressive melanoma cells exhibit a functional plasticity characterized by the expression of genes from different cell types, as well as a reduction in the expression of melanocyte-associated genes. For instance, aggressive melanoma cells express proteins, such as VE-Cadherin, which are characteristically associated with endothelial cells and keratins and vimentins, which are intermediate filaments normally associated with epithelial and mesenchymal cells, respectively ^[75]. Collectively, this gene-expression pattern confers a functional plasticity upon aggressive melanoma cells that enables them to escape normal physiological control and regulation. For example, VE-Cadherin expression by melanoma cells is essential for the formation of tumor-derived vascular networks and provides rapidly growing tumors with a paravascular perfusion pathway, while the expression of keratins is associated with enhanced invasion and metastasis ^[76,77].

Altogether, these findings suggest that Nodal may prove to be not only a diagnostic or prognostic marker but also a potential novel therapeutic target in melanoma.

1.5 MONOCLONAL ANTIBODIES

1.5.1 Antibody structure

Antibodies (immunoglobulin) are roughly Y-shaped glycosylated proteins. Each antibody consists of two identical heavy (H) chains (50 kDa) linked to two identical light (L) chains (25 kDa), giving an antibody molecule two identical antigen-binding sites and thus the ability to bind simultaneously to two identical structures. Each light chain pairs with a heavy chain, and each heavy chain pairs with another heavy chain; the chains are linked by covalent interchain disulfide bonds and noncovalent interactions. Each chain has a tandem series of repeating homology units approximately 110 amino acid residues in length called *Immunoglobulin domains* (Ig-like domain), which fold independently into a compact globular structure. All proteins that exhibit this structural motif belong to the immunoglobulin gene superfamily. An antibody molecule is composed of three major fragments: the two Fabs (Fragment antigen-binding), which are identical and each of which contains the light chain and the first two domains of the heavy chain, and the Fc (Fragment crystallizable), which contains the C-terminal constant domains of the two heavy chains. The Fabs are linked to the Fc by the “hinge region” (located between the CH1 and CH2 domains) which allows them to swing and varies in length and flexibility in the different antibody classes and isotypes. The antigen binding sites (paratopes) are located at the tips of the Fabs ^[78].

A representation of human IgG₁ antibody is shown in **Fig. 1.7**.

Antibody structure consists of two regions: the variable (V) region and the constant (C) region. The variable (V) regions are the sections that constitute the tips of the Y's arms, defining antigen binding properties, vary greatly from one antibody to another, creating a pocket uniquely shaped to enfold a specific antigen epitope. The stem, or constant (C) region, of the Y allow the antibody to bind other components of the immune response; the stem is identical in all antibodies of the same class. The light chain of IgG has two domains called VL and CL while the heavy chain has four domains: one VH and three in the CH region (CH1, CH2, and CH3 or Cg1, Cg2, and Cg3). The heavy-chain V unit is similar to the V part of the light chain, while the three C-region units exhibit strong homology to each other and to the C region of the light chain.

Each V domain contain three regions (CDR1, CDR2 and CDR3) exhibiting high variability of the amino acid sequence, called **hypervariable regions** or **complementarity-determining regions (CDRs)** ^[75], because these segments mark the antibody combining site; the differences in structure are almost entirely confined to these regions. Usually, each CDR is about 10 amino acid residues in length. Intervening sequences between the CDRs have restricted variability and show little difference in amino acid sequence between chains. These invariant segments make up the **framework residues** (FR1, FR2, FR3, and FR4) ^[75], which compose about 85% of the V region. Framework residues define the positioning of the CDRs. When the light and heavy chains are joined, the CDRs of the chains form a cleft that serves as the antigen-binding site of an immunoglobulin. Because the amino acid sequences of the CDRs determine the shape and ionic properties of the antigen-binding site, the CDRs define the specificity of the antibody. ^[78-80]

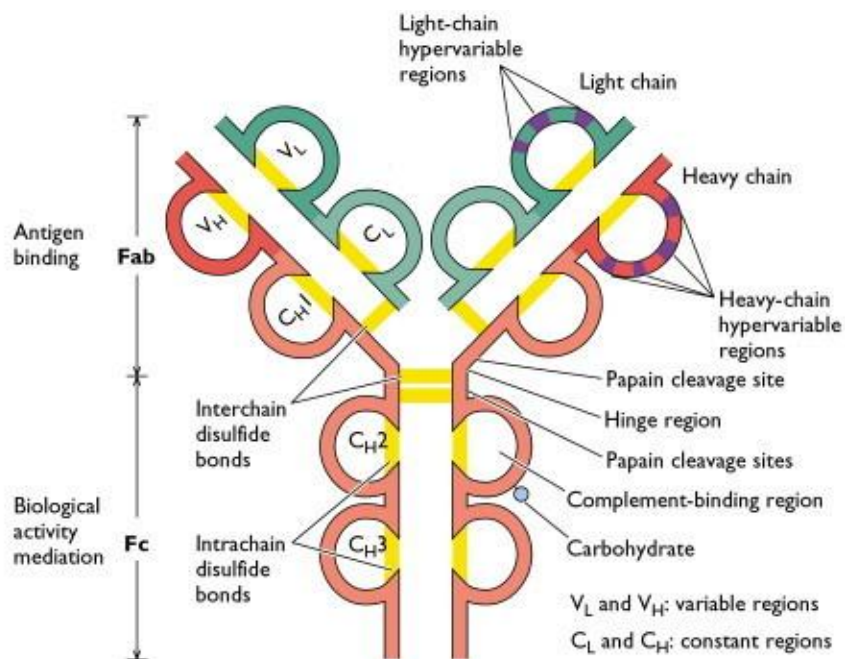


Figure 1.8: Typical structure of an immunoglobulin G₁ (IgG₁) ^[81].

Immunoglobulins can be grouped into five different classes IgA, IgD, IgE, IgM, and IgG on the basis of the kind of heavy chain they bear, respectively designated as α , δ , ϵ , μ and γ . IgGs are further divided into several subclasses (isotypes) — IgG₁, IgG₂, IgG₃, and IgG₄ (in order of relative abundance in

human plasma), with different heavy chains, named γ_1 , γ_2 , γ_3 , and γ_4 , respectively.

All immunoglobulins share the same pool of light chains; there are two types of light chains, *kappa* (κ) and *lambda* (λ). The structural differences among these subtypes are the number and location of interchain disulfide bonds and the length of the hinge region. The two heavy chains are connected in the hinge region by a variable number of disulfide bonds: 2 for IgG₁ and IgG₄, 4 for IgG₂ and 11 for IgG₃. The light chain of the IgG₁ is connected to the heavy chain by a disulfide bond between the last cysteine residue of the light chain and the fifth cysteine residue of the heavy chain. However, for IgG₂, IgG₃ and IgG₄, the light chain is linked to the heavy chain by a disulfide bond between the last cysteine residue of the light chain and the third cysteine residue of the heavy chain.

Cysteine residues that form inter-chain disulfide bonds are located in the hinge region with the exception of the third cysteine residue of the heavy chain in IgG₂, IgG₃ and IgG₄, which is located between the interface of VH and CH1 domains. On the other hand, intra-chain disulfide bonds are buried between the two layers of anti-parallel β -sheet structures within each domain ^[78].

Compared to the other classes of immunoglobulines, IgGs are the most abundant and widely used for therapeutic purposes, thus they are currently the class of choice for the development of therapeutic antibodies, because they show more favourable features, although the IgG₃ are not employed in therapy because of their shorter half-life and their long hinge region, that is easily accessible to proteolysis ^[82].

1.5.2 Monoclonal antibodies in cancer therapy

A century ago, Paul Ehrlich hypothesized that a ‘magic bullet’ could be developed to selectively target disease. This vision became practical with the development of hybridoma technology by Kohler and Milstein, which provided murine mAbs able to recognize with high specificity their antigens ^[83]. The limitations of the first generation of mAbs evaluated in the clinic phase were their immunogenicity and poor ability to recruit immune effector mechanisms, due to their murine nature ^[84]. Indeed, to overcome these issues, new engineered antibodies were generated, by maintaining the human Fc domains and by

grafting either the entire murine variable regions (chimeric antibodies) or the murine complementarity-determining regions (humanized antibodies) into the human IgG framework as to retain targeting specificity ^[84]. Modifications to render mAbs more “human” reducing the foreign nature of these proteins have provided more efficient interaction with the Fc receptors expressed on immune human effector cells. The transition to human IgG backbones has allowed customization of the IgG for desired functions. Most therapeutic mAbs with human backbones are IgG₁ isotype, which effectively mediates Fc domain-based functions, such as antibody-dependent cellular cytotoxicity (ADCC) and complement fixation. Other isotypes, such as human IgG₂, can be also used when the mechanism of action of mAb is to block a soluble target for example the anti-epidermal growth factor receptor (EGFR) antibody, panitumumab (ABX-EGF) ^[83].

Although most of the mAbs approved by the US Food and Drug Administration (FDA) for cancer therapy are still classical humanized or chimeric antibodies, the next generation of mAbs currently under development incorporates additional beneficial modifications, such as alterations in glycosylation and sequence that enhance ADCC or modifications in size and antigen-binding affinity that increase the ability of the mAb to penetrate solid tumors ^[83].

Antibody-based therapeutics have emerged as important components of therapies for an increasing number of human malignancies. Trastuzumab, an unconjugated anti-HER2/*neu* antibody, is broadly used alone and in combination with chemotherapy agents in breast cancer. Antibodies directed against the extracellular domain of the EGFR exhibit activity in advanced cancer, and one (cetuximab) has been approved for for the treatment of the colorectal cancer ^[85,86]. Unconjugated mAbs directed against the B-cell idiotype, against CD20 ^[87,88] and against CD22 ^[89] are useful in treatment of lymphomas as well as an anti-CD20 antibody, rituximab (Rituxan). Radioimmunoconjugates, such as ibritumomab tiuxetan (Zevalin) and tositumomab plus ¹³¹I tositumomab (Bexxar; a mixture of radiolabeled and unconjugated antibody) directed against CD20 show substantial anti-tumor activity ^[90,91] and have entered standard clinical practice for lymphoma therapy. Campath-1H (alemtuzumab), an anti-CD52 antibody that efficiently mediates complement fixation, has been approved for use in chemotherapy-refractory chronic lymphocytic leukemia ^[92].

An immunoconjugate containing an anti-CD33 antibody and calicheamicin has been approved for use in refractory acute-myeloidleukemia ^[93]; indeed, immunotoxins consisting of recombinant antibody fragments conjugated to catalytic toxins exerts anti-tumor activity as well ^[94].

Ipilimumab, an anti-CTLA-4 (cytotoxic T-lymphocyte-associated antigen 4) antibody and anti-PD-1 (programmed cell death protein 1) mAbs, pembrolizumab and the most recently approved nivolumab, are used for the immune-based therapy of metastatic melanoma ^[95,96].

The safety and efficacy of therapeutic mAbs in oncology depend on the nature of the target antigen. Ideally, the target antigen should be abundant and accessible and it should be expressed homogeneously, consistently and exclusively on the surface of cancer cells. Antigen secretion should be minimal, as secreted antigens can bind the antibody in the circulation and could prevent sufficient antibody from binding to the tumour. If the desired mechanism of action is ADCC or CDC, then it is desirable that the antigen–mAb complex should not be rapidly internalized so as to maximize the availability of the Fc region to immune effector cells and complement proteins, respectively. By contrast, good internalization is desirable for antibodies or proteins that deliver toxins into the cancer cell and for antibodies the action of which is primarily based on the downregulation of cell surface receptors ^[97].

Table 2. FDA-approved mAbs for use in oncology ^[98]

Name	Marketed by	Class	Target	First approved indication	Reported mechanisms of action	Approval year
Rituximab (Rituxan™)	Biogen Idec/ Genentech	Chimeric IgG1	CD20	Non-Hodgkin's Lymphoma	ADCC, CDC, Induction of apoptosis	1997
Trastuzumab (Herceptin®)	Genentech	Humanized IgG1	HER2	Breast cancer	Signal inhibition, ADCC	1998
Alemtuzumab (Campath®)	Sanofi-Aventis	Humanized IgG1	CD52	B cell chronic lymphocytic leukemia	CDC, Induction of apoptosis	2001
Ibritumomab tiuxetan (Zevalin®)	Biogen Idec	Murine IgG1	CD20	Non-Hodgkin's Lymphoma	Radioisotope delivery (⁹⁰ Y)	2002
Tositumomab (Bexxar®)	GlaxoSmithkline	Murine IgG2a	CD20	Non-Hodgkin's Lymphoma	Radioisotope delivery (¹³¹ I), ADCC, CDC, Induction of apoptosis	2003
Cetuximab (Erbix™)	Bristol-Myers Squibb/Eli Lilly	Chimeric IgG1	EGFR	Squamous cell carcinoma of the head and neck	Signal inhibition, ADCC	2004
Bevacizumab (Avastin™)	Genentech	Humanized IgG1	VEGF	Colorectal cancer	Signal inhibition	2004
Panitumumab (Vectibix™)	Amgen	Human IgG2	EGFR	Colorectal cancer	Signal inhibition, ADCC	2006
Ofatumumab (Arzerra®)	Genmab/GSK	Human IgG1	CD20	Chronic lymphocytic leukemia	ADCC, CDC	2009
Denosumab (Xgeva®)	Amgen	Human IgG2	RANKL	Bone metastases	Signal inhibition	2010
Ipilimumab (Yervoy®)	Bristol-Myers Squibb	Human IgG1	CTLA-4	Metastatic melanoma	Signal inhibition	2011
Brentuximab vedotin (Adcetris®)	Seattle Genetics	Chimeric IgG1	CD30	Hodgkin Lymphoma	ADC	2011
Pertuzumab (Perjeta®)	Genentech	Humanized IgG1	HER2	Breast cancer	Signal inhibition, ADCC	2012
Trastuzumab emtansine (Kadcyla®)	Genentech	Humanized IgG1	HER2	Breast cancer	ADC, Signal inhibition, ADCC	2013

1.5.3 Mechanism of action of therapeutic antibodies

Available clinically useful mAbs typically use a combination of mechanisms in directing cytotoxic effects on tumor cells. Most interact with components of the immune system through **antibody-dependent cellular cytotoxicity (ADCC)** or **complement dependent cytotoxicity (CDC)** and other alter signal transduction within the tumor cell or act to eliminate a critical cell-surface antigen. Monoclonal antibodies can also be used to delivery payloads (e.g., radioisotopes, drugs or toxins) to directly kill tumor cells or to activate prodrugs specifically within the tumor (antibody-directed enzyme prodrug therapy, ADEPT). Finally, mAbs can be employed in combination with traditional chemotherapeutic agents, attacking tumors through complementary mechanisms of action that may

include anti-tumor immune responses that may have been compromised owing to a chemotherapeutic's cytotoxic side effects on T lymphocytes^[83].

The most important cell-killing mechanisms of mAbs action are described below.

a. Antibody-dependent cellular cytotoxicity

ADCC occurs when antibodies bind to antigens on tumor cells and the antibody Fc domains engage Fc receptors (FcR) on the surface of immune effector cells^[99]. Several families of Fc receptors have been identified and specific cell populations characteristically express defined Fc receptors^[100]. For example, neutrophils commonly express human Fc γ RI (CD64), Fc γ RII (CD32) and the B (lipid-anchored) isoform of Fc γ RIII (CD16). In contrast, human natural killer (NK) cells express only the A (transmembrane) isoform of CD16. This structure facilitates recruitment of adaptor proteins and activation of natural killer cells by antibody engagement of CD16^[101].

b. Complement-dependent cytotoxicity

Although IgM is the most effective isotype for complement activation, it is not widely used in clinical oncology because IgM does not readily extravasate from vascular structures. IgG1 and IgG3 are both very effective for triggering CDC^[102] via the classical complement-activation pathway. In this cascade, the formation of antigen-antibody complexes leads to the unclenching of multiple C1q binding sites in close proximity on the CH2 domains of IgGs (C1q is one of three subcomponents of complement C1). These unclenched C1q binding sites convert the previously low-affinity C1q-IgG interaction to one of high avidity, which triggers a cascade of events involving a series of other complement proteins and leads to the proteolytic release of the effector-cell chemotactic/activating agents C3a and C5a. The complement cascade ultimately leads to the formation of a membrane attack complex, which creates pores in the cell membrane permitting free passage of water and solutes into and out of the cell^[83].

c. Signal transduction changes

Some of the most commonly targeted tumor-associated antigens are growth factor receptors, which are overexpressed in several malignancies. Since their activation under normal conditions induces a mitogenic response and promotes cellular survival, it follows that their overexpression promotes tumor cell growth and resistance to chemotherapeutic agents. By decreasing signaling through these receptors, mAbs can normalize growth rates and resensitize cells to cytotoxic agents ^[83]. Antibodies that target members of the EGFR family are the most potent inhibitors of signal transduction. Some, such as cetuximab and panitumumab, act by physically blocking the interaction between the receptor and its activating ligand ^[103] and by sterically preventing the receptor from assuming the extended conformation required for dimerization ^[104]. Others, such as pertuzumab (2C4), allow ligand binding to occur but sterically inhibit the subsequent receptor heterodimerization required for signal transduction ^[105]. Virtually every clinically effective, unconjugated mAb perturbs the signaling that promotes the proliferation and survival of the targeted cell population. Therapy with mAbs often has the effect of reducing the density of target antigen expression. Examples include the reduction in concentration of a critical growth factor receptor, such as EGFR, from the surface of a tumor cell ^[106] or the clearance of a ligand, such as vascular endothelial growth factor (VEGF), that promotes tumor or vascular growth. However, some mAbs, such as trastuzumab, enter into the cell and are then passively recycled back to the cell surface along with their target antigen ^[107].

d. Tumour antigens as antibody targets

The safety and efficacy of therapeutic mAbs in oncology depend on the nature of the target antigen. The ideal target antigen should be abundant and accessible and should be expressed homogeneously, consistently and exclusively on the surface of cancer cells. Antigen secretion should be minimal, as secreted antigens can bind the antibody in the circulation and could prevent sufficient antibody from binding to the tumour ^[108]. If the desired mechanism of action is ADCC or CDC, then it is desirable that the antigen–mAb complex should not be rapidly internalized so as to maximize the availability of the Fc region to immune effector cells and complement proteins, respectively. By contrast, good

internalization is desirable for antibodies or proteins that are designed to deliver toxins into the cancer cell and for antibodies whose action is primarily based on the downregulation of cell surface receptors [108].

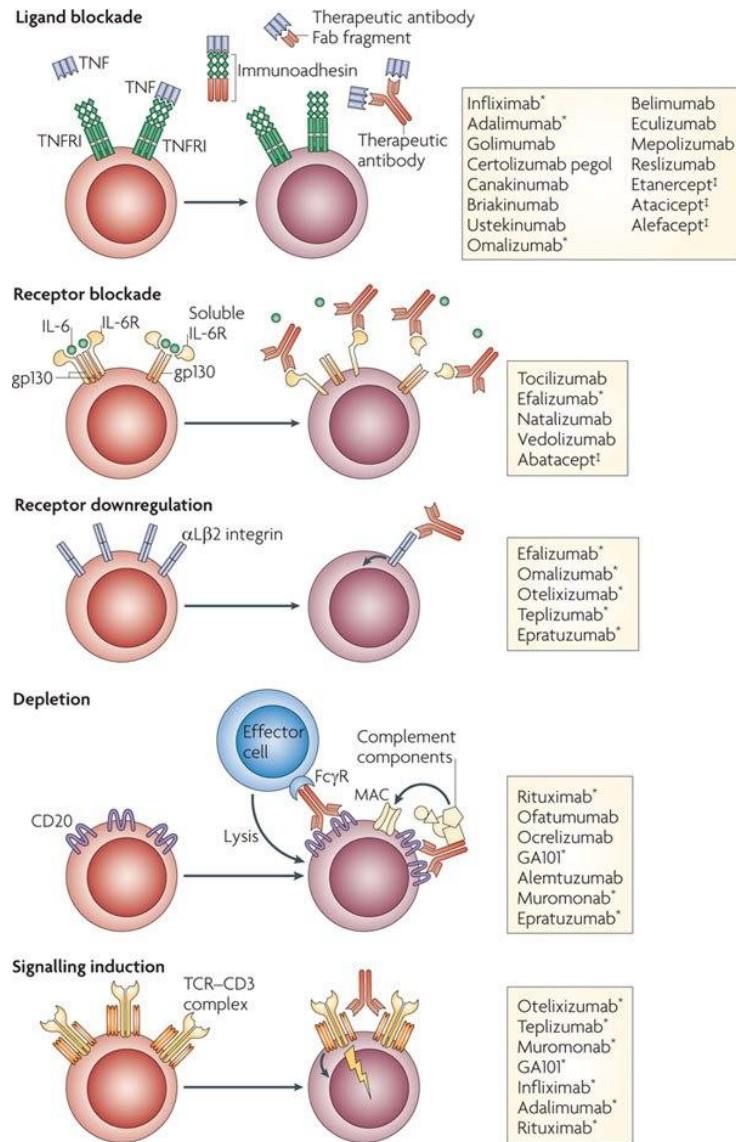


Figure 1.8: Mechanisms of action of therapeutic antibodies [109].

1.6 Antibody fragments generated by enzymatic digestion

Monoclonal antibodies (mAbs) have been widely used for nearly three decades for purposes including imaging and therapy because their selectivity for specific targets.

While intact monoclonal antibody molecules are still most commonly used, they may not necessarily be the most efficient or desired molecular form depending on the application. Because of their relatively large size (approximately 150 kDa), intact mAbs exhibit unfavorable imaging kinetics, relatively poor tumor penetration and present with the potential for eliciting host antibody responses [110]. These limitations were overcome by the reduction of the size of intact antibodies to smaller forms or monovalent and bivalent fragments, achieved either through enzymatic cleavage or by genetic engineering. The latter requires a serious commitment of time and resources while the enzymatic strategy is affordable and easily achievable. Proteolytic fragments of mouse antibodies are widely used as immunochemical, diagnostic and therapeutic tools due to their more advantageous pharmacokinetic properties than those of the intact molecules [110]. Indeed, the smaller size results in clearing faster from the circulation and tumor localization patterns, in better tissue penetration and less steric hindrance leading to more sensitive antigen detection. The removal of the Fc portion avoids the potential of binding with Fc receptors thus reducing non-specific interactions and distribution *in vivo* of the mAb via the Fc receptors found on normal cells and in addition it reduces the immunogenicity *in vivo* [102]. The most widely proteolytic enzyme used to obtain IgG fragments - Fab, F(ab')₂ and/or Fc - of a variety of animal species [111] are papain and pepsin, which split immunoglobulin G (IgG) molecules preferentially in the hinge region.

The typical IgG fragments are summarized below.

F(ab')₂ (110 kDa) fragment consists of two antigen-binding regions joined at the hinge through disulfides. This fragment may contain a small portion of the Fc region [112].

Fab' (55 kDa) can be obtained by the reduction of F(ab')₂ fragments. The Fab' fragment contains a free sulfhydryl group that may be alkylated or utilized for the conjugation with an enzyme, toxin or other protein of interest. Since it is derived from F(ab')₂, it may contain a small portion of Fc [112].

Fab (50 kDa) is a monovalent fragment that is produced from IgG and IgM, consisting of the VH, CH1 and VL, CL regions, linked by an intramolecular disulfide bond.

Fc (50 kDa) fragment contains the CH2 and CH3 region of the heavy chain and part of the hinge region held together by one or more disulfides and noncovalent interactions ^[112]. Fc (Fc-alpha) and Fc μ fragments are produced from proteolytic cleavage of IgG and IgM, respectively. The term Fc is derived from the ability of these antibody fragments to crystallize; these fragments cannot bind antigen, but they are responsible for the effector functions of antibodies, such as complement fixation ^[102].

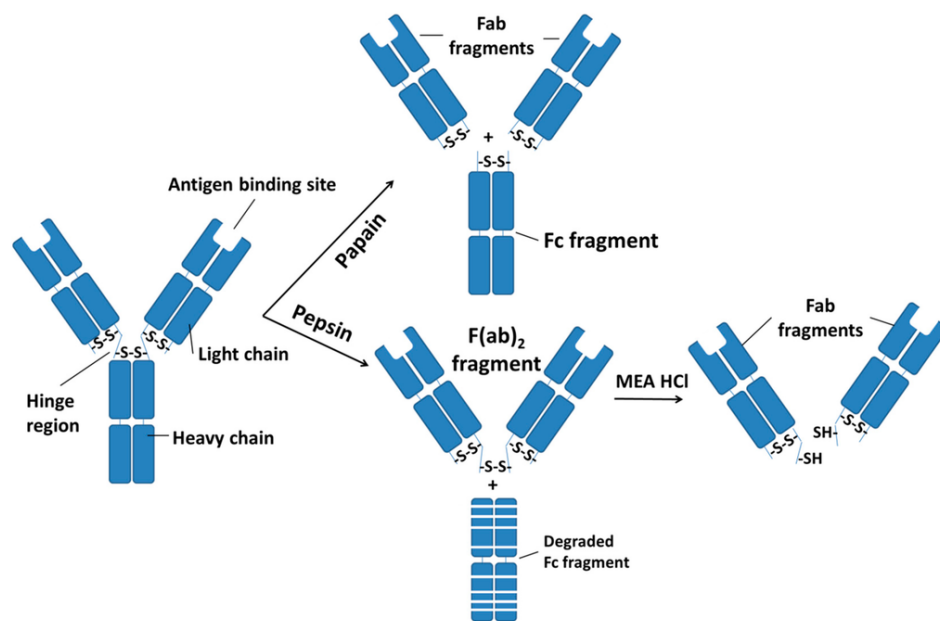


Figure 1.9: Enzymatic digestion of IgG antibodies with papain and pepsin ^[113]

1.7 AIM OF THE PROJECT

The purpose of this project is the development of novel monoclonal antibodies and their functional fragments such as Fab or F(ab')₂ able to bind with high affinity and selectivity the growth factor Nodal and to inhibit its interaction with the co-receptor Cripto-1. Nodal binds Cripto-1 on the EGF-like domain, whereas the site of binding on Nodal comprises the region 43-69, termed CBR (Cripto-Binding Region). Such region encompasses the pre-helix loop and the H3-helix and contains two glutamic acid, E49 and E50, crucial for the recognition and stabilization of the binding of Nodal to the EGF-like domain of Cripto. Within the same region, Y58 has been recently identified as participating to the interaction. Given the relevance of this interaction for several mechanisms associated to tumour growth, Nodal-Cripto-1 inhibitors have the potential to block Nodal-Cripto dependent cellular proliferation. Moreover, since Nodal expression correlates with the progression of melanoma toward a metastatic phenotype, Nodal protein can be considered as a novel diagnostic and prognostic marker in this context, indeed the Nodal binders may be used as diagnostic tools for the specific detection of the protein in tumoral tissues with different degree of aggressiveness and in human biological fluids.

On this bases, we will explore the possibility of developing new monoclonal antibodies specifically targeting the CBR of Nodal with the perspective to inhibit the interaction with Cripto-1 and block the Nodal-associated tumorigenesis. The antibodies can be also potentially used for the selective and sensitive detection of the protein in the biological fluids of individuals overexpressing Nodal to predict the risks of tumour development. The high affinity and selectivity potentially achievable with monoclonal antibodies and the selective expression of the protein in the tumoral compartments, especially in melanoma, provide a robust scientific and technological background for the successful application of this strategy. They will also pave the way for the development of new biotherapeutics that could help to overcome the limitation associated to the currently mAb-based immunotherapy in metastatic melanoma [Ipilimumab anti-CTLA4 antibody) and the most recently approved anti-PD1 Nivolumab and Pembrolizumab].

I 2. MATERIALS AND METHODS

2.1 MATERIALS AND CHEMICALS

Protected amino acids for peptide synthesis were purchased from GL-Biochem (Shanghai, PRC) and IRIS Biotech GmbH (Marktrewitz, DE). The RINK amide resin was from Novabiochem. Coupling agents were from GL-Biochem (Shanghai, PRC). Solvents for peptide synthesis and purification, including acetonitrile (ACN), dimethylformamide (DMF), dichloromethane (DCM), methanol (MeOH) were from Romil (Dublin, Ireland). Other reagents for peptide synthesis, BSA and glutaraldehyde were from Sigma-Aldrich (Milano, Italy). KLH (Keyhole Lympet Hemocyanin) was from Pierce-ThermoFisher (Milano, Italy). Freund's complete and incomplete adjuvant, and all media including Dulbecco's modified Eagle's medium (DMEM), OPTI-MEM and serum were purchased from GIBCO (Life Technologies, Italia) and Sigma-Aldrich (Milan, Italy). HiTrap protein G and Superdex200 10/300 columns, AKTA FPLC, all reagents for SPR analyses and the Biacore3000 system were provided by GE Healthcare. Pierce Rapid mouse antibody isotyping kit was purchased from Thermo Scientific (Rockford, IL, USA). All chemicals used for ELISA assays were provided by Sigma-Aldrich (Milano, Italia). Nunc MaxiSorp 96 multi-well plates were purchased from Thermo Scientific (Denmark). APS and TEMED were purchased from Sigma-Aldrich (Milano, Italia); all the reagents used for electrophoresis analyses, including the ladder proteins and the buffers, were supplied by Biorad. Recombinant proteins were purchased from R&D System (Minnesota, USA).

All the enzymes used to cleave the 3D1 antibody and all the reagents used throughout the digestion were supplied by Sigma-Aldrich (Milano, Italia). Protein purifications were performed on AKTA-FPLC system. For analytical HPLCs an Agilent 1100 system was used. All the reagents used to perform SDS-PAGE and Western blot analyses were purchased from Biorad.

The RPMI 1640 medium, containing 10% Fetal Bovine Serum (FBS) and 1% Penicillin, Streptomycin and Glutamine (PSG) was used for maintaining myeloma cells. The RPMI-GM medium contained RPMI 1640 with added 1% non-essential amino acids (NEAA). For the fusion of splenocytes and myeloma

cells we used an RPMI 1640 medium supplemented with 15% FBS, 2% HAT (Hypoxanthine-Amino-pterine-Thymine), 1% PSG and 10% HES (Hybridoma enhancing supplement). The medium for clone selection was RPMI 1640 supplemented with 15% FBS, 2% HAT, 1% PSG.

2.2 SOLID-PHASE PEPTIDE SYNTHESIS, PURIFICATION AND IDENTIFICATION

2.2.1 Peptide synthesis

The chemical synthesis of each peptide was performed by using an automatic SYRO system (MultiSynTech, Germany).

The wild-type hNodal[43-69] peptide and its variants were prepared as acetylated and amidated derivatives by stepwise solid-phase synthesis following standard fluorenylmethoxycarbonyl (Fmoc) chemistry protocols. A Rink- amide MBHA resin (Sigma-Aldrich, Milano, Italy) with a substitution grade of 0.57 mmol/g and amino acid derivatives with standard protections were used in all syntheses. The syntheses were performed under canonical conditions of peptide synthesis, for each coupling reaction (HATU/DIEA pre-activation, 5-fold excess of Fmoc-protected amino acids). Coupling and deprotection times were kept at 30 and 20 minutes, respectively. Standard side-chain protection groups for Fmoc chemistry were used for all residues. N-terminal acetylation was performed on the resin using acetic anhydride at 0.5 M in DMF with 5% DIEA, 20 minutes at room temperature. The cleavage of peptides from the solid support was performed by treatment with a trifluoroacetic acid (TFA)/tri-isopropylsilane/water (90:5:5, v/v/v) mixture for 90 min at room temperature. Crude peptides were precipitated in cold ether, dissolved in a water/acetonitrile (1:1, v/v) mixture and lyophilized.

2.2.2 Peptide purification

After lyophilisation, peptides were dissolved in a solution of H₂O/CH₃CN 95/5 v/v, containing 0.1% TFA and were purified by reverse-phase HPLC (RP-HPLC) on a Shimadzu LC-8A instrument (Shimadzu Corporation, Milan, Italy) using a semi-preparative 5×1 cm ID C18 monolythic Onyx column (Phenomenex), applying a linear gradient of 0.05% TFA in acetonitrile from 5%

to 70% over 10 min at a flow rate of 15 mL/min, monitoring the absorbance at 214 nm. The collected fractions were lyophilized.

2.2.3 Peptide identification by LC-MS

Peptides purity and identity were confirmed by liquid chromatography–mass spectrometry analysis (LC-MS), analyses were carried out on a LCQ DECA XP ion Trap mass spectrometer (ThermoFisher) equipped with an OPTON ESI source and with a complete Surveyor HPLC system.

2.3 IMMUNOGEN PREPARATION : CONJUGATION OF THE IMMUNOGEN PEPTIDE TO KLH AND BSA

The conjugation reaction of the antigen to carrier proteins was carried out using a w/w ratio of peptide:protein 1:3. 1 mg of *hNodal*[43-69] non acetylated peptide was dissolved in 1 mL of 50 mM phosphate buffer pH 7.0 and 3 mg of carrier protein Keyhole Limpet Hemocyanin (KLH, Pierce & Co., Rockford, Illinois) were dissolved in 1 mL of 50 mM phosphate buffer pH 7.0. The two separate solutions were mixed and glutaraldehyde at final concentration of 0.2% was added. The mixture was incubated at room temperature under stirring; after 2 hours, the reaction was stopped by adding 2 mL of 0.5 M Glycine. Finally, the reaction mixture, placed in a 10 kDa MWCO dialysis membrane, was dialyzed over night at 4° C against 2 liters of PBS buffer, pH 7.4, performing a dialysis buffer-exchanging after 1 hour and after 4 hours. The amount of peptide-protein conjugated was determined by the method of Bradford using the BIORAD kit (Biorad). The same procedure was used to prepare the BSA-peptide conjugated and the glutaraldehyde self-conjugated BSA (BSA₂), omitting the addition of the peptide solution. The KLH-conjugated peptide was used for the effective immunization of Balb/c mice and for the generation of monoclonal antibodies specific for the 43-69 region of *hNodal* protein; the BSA-conjugated peptide was used to screen hybridoma cell culture supernatants.

2.4 GENERATION AND PRODUCTION OF ANTI-NODAL MONOCLONAL ANTIBODIES BY HYBRIDOMA TECHNOLOGY

Murine monoclonal antibodies tested in this research project were generated in the laboratory of Prof. Antonio Leonardi at the University of Naples “Federico II”, Department of Molecular and Cellular Biology and Pathology.

BALB/c mice were housed and handled according to the institutional guidelines. Four-five weeks old Balb/c mice (Jackson Lab) were immunized with 50 μ L of suspension containing about 100 μ g of adjuvant-emulsified KLH-conjugated *hNodal*[43-69] peptide mixture. Two independent injections were carried out sub-cutaneously with 25 μ L of immunogen. Before immunization, 250 μ L blood samples were taken from each mouse from the caudal vein and used as the pre-immune control (T_0 samples). Mice were again immunized with the same amount of immunogen at day 30 after the first immunization ($T = 30$ d), at day 40 ($T = 40$ d) and at day 60 ($T = 60$ d); blood samples were taken from the caudal vein (250 μ L) before every subsequent immunization and tested by ELISA to monitor the increase of antibody titer compared to the pre-immune serum. Mice showing the highest antibody titer were sacrificed and splenectomised.

These immunizations were administered subcutaneously with incomplete Freund's adjuvant (TiterMax Gold Adjuvant, Sigma-Aldrich). A final antigen boost was administered intravenously 20 days before animals were sacrificed and splenectomized. Three days after the boost, spleen cells were collected by surgery from an immunized mouse sacrificed by CO₂ inhalation and for which all efforts were taken to reduce animal suffering; the spleen cells were then fused with myeloma SP2/0 cells in 50% polyethylene glycol (pH 7.4) fusion solution to generate mAb hybridomas. The splenocytes were fused at a ratio of 5:1 with the mouse plasmacytoma cell line SP2/0 (ATCC) using RPMI-GM containing polyethylene glycol 1300-1600 (Hybri-Max, Sigma-Aldrich, Milano) and 7.5% DMSO (Sigma-Aldrich, Milano), following the standard procedure described by Köhler ^[114]. The fused hybridoma cells were re-suspended in 30 mL of selection medium consisting of RPMI-GM medium containing PEG 1300-1600, 10% FBS, 100 U/mL penicillin, 100 μ g/mL streptomycin, 100 μ M hypoxanthine, 16 μ M thymidine and 400 nM aminopterin (RPMI-HAT Sigma-Aldrich, Milano). The cell suspension (100 μ L) was dispensed into 96-well plates and incubated at 37 °C in a 5% CO₂ atmosphere. After 12 hours, an additional

volume of 100 μ L of selection medium was added to each well. After 24 h, half the medium from each well was removed, and fresh selection medium was added. Every 2 or 3 days, medium was replaced with fresh selection medium. After 10 days, aminopterin was omitted from the medium. Between the 12th and 14th day, supernatants from the 96-well plates were collected and screened by ELISA assay. Hybridoma clones with strong reactivity versus the *hNodal*[43-69] peptide were re-cloned twice by limiting dilution, and their reactivity was re-confirmed by ELISA assay. Sub-cloned hybridoma cells were cultured in OPTI-MEM medium containing 10% FBS, adapted gradually to serum-free cell medium and then transferred to the Bioreactor (INTEGRA Biosciences AG, CH-7000 Chur) for large scale production.

2.5 ISOTYPIZATION

Isotype of the anti-Nodal antibodies produced by the selected clones was determined by using the commercial kit specific for murine antibodies, in accordance to the manufacturer's instructions (Pierce Rapid Mouse antibody Isotyping kit, Thermo scientific).

2.6 ENZYME-LINKED IMMUNOSORBENT ASSAYS (ELISA)

2.6.1 Antibody titration in mouse sera

To determine the antibody titer in mouse sera, 96-well ELISA plates were coated with 100 μ L of the BSA-conjugated *hNodal*[43-69] 0.5 μ g/mL in PBS and with BSA₂ as negative control overnight at 4 °C. The plate was then triple-washed three times with PBS containing 0.05% Tween 20 (PBS-T). Non-specific sites of the plate were blocked with 2% BSA and incubated at 37 °C for 60 minutes. Wells were then washed 3 times again and ascitic fluid was added to the wells in three fold serial dilutions starting from 1:100 to 1:100000. The plate was incubated at 37 °C for 1 hour and washed again with PBS-T. Then, 100 μ L of a 1:1000 dilution of HRP-conjugated rabbit anti-mouse Ig (1.0 mg/mL, Biorad, Milano) were added to the wells and incubation was carried out for 1 h at 37 °C. After washing, 100 μ L of 2,2-Azino-bis(3-ethylbenzothiazoline-6-sulfonic acid) (ABTS) substrate solution was added to each well. After 15 min, the reaction was stopped by adding 100 μ L of 1% SDS solution in water to each well. The

Optical Density (OD) was measured at 415 nm by a microplate reader (BioTek, Winooski, VT, USA).

Antibody titers were evaluated sufficiently high when the average absorbance values from triplicate wells incubated with immune sera dilutions at 1:10000 were at least thrice those determined on wells incubated with the pre-immune serum. After generation, hybridomas were screened for their ability to secrete specific mAbs for the *hNodal* antigen. For this purpose, supernatants were tested as described above, by coating plates with both BSA-*hNodal*[43-69] and BSA₂ as control to exclude clones producing antibodies recognizing the BSA-linked glutaraldehyde. Positive clones were stabilized by 3 sequential rounds of cloning performed by the method of limited dilution. At every round, cells were counted and diluted up to about 3 cells/mL; 20 mL of this solution were plated in two 96-well plates, dispensing 100 µL/well, thus reaching about 0.3 cells/well. Cells were incubated for 2 weeks at 37 °C under 5% CO₂, then supernatants from each well were tested again for the presence of antibodies against the antigen peptide. Supernatants showing the highest antibody titer were isolated and again cloned thrice by limited dilution, always testing by ELISA the presence of specific antibodies.

To obtain secreted monoclonal antibodies in absence of serum-derived bovine antibodies, selected clones were adapted to grow in serum-free medium. Thus, medium was first changed to OPTIMEM (Sigma-Aldrich, Milano, Italy) supplemented with 10% FBS, then FBS was progressively reduced and finally removed over a time period of about 4 weeks. Productivity was always monitored by ELISA assays.

2.6.2 Screening of the hybridoma supernatants

hNodal[43-69] peptide and *hNodal*[43-69]E49A-E50A, its mutated variant, in which the glutamic acids 49 and 50 were substituted with two Alanine residues, were coated at 330 nM diluted in PBS on polystyrene conical shaped flat bottom 96-well plates, (Nunc MaxiSorp™, Roskilde, Denmark) at 4°C overnight (100 µL/well). After incubation, the coated wells were washed three times with PBS containing 0.005% Tween-20 (PBS-T) and non-specific binding sites were blocked by incubating with 1% BSA in PBS (300 µL/well) for 1 hour at 37° C. After washing three times with PBS-T, supernatants of hybridomas diluted in

PBS at 33 nM were incubated for 1 hour at 37° C (100 µL/well). After incubation, plates were washed three times with PBS-T and goat anti-mouse HRP-conjugated antibody (1 mg/mL, Blotting Grade Affinity Purified Goat Anti-Mouse IgG (H+L) diluted 1:1000 in PBS was added as secondary antibody (100 µL/well) and incubated for 1 hour at 37° C. After incubation and washes with PBS-T, bound supernatants were detected by adding 100 µL/well of freshly prepared ortho-phenylenediamine (0.4 mg/mL) containing H₂O₂ (0.4 mg/mL) in 0.1 M citrate buffer (pH 5.2) (SIGMAFAST™ OPD tablet Sigma Aldrich). The peroxidase reaction was stopped after 5 minutes with 50 µL/well of 2.5 M H₂SO₄ and the optical density was measured at 490 nm, using a multiwall plate reader (BioTek, Winooski, VT, USA).

2.6.3 Mapping of the 3D1 epitope

The following peptides were used for the epitope mapping : wild type [43-69], [43-69]E49-E50, [43-67], [44-67], [44-67]E49A-E50A, [43-67]P46A-V47A, [44-67]P46A-V47A and the shorter variants [43-56], [52-60] and [56-67]. Peptides were coated at 1 µg/mL; 3D1 mAb, dissolved in PBS, was used as primary antibody at 1 µg/mL.

2.6.4 Specificity of the 3D1 mAb

hNodal[43-56], *hNodal*[1-38], *hNodal*[39-75], *hNodal*[76-100], *hGDF5/6*[43-56] and *hGDF7*[43-56] peptides, stock solution in water, were coated at 1 µg/mL (diluted in PBS) on polystyrene 96-well plates at 4° C overnight (100 µL/well). The ELISA assay was carried out following the procedure already described. 3D1 monoclonal antibody, dissolved in PBS, was used as primary antibody at 1 µg/mL.

2.6.5 Detection of rhNodal

A sandwich ELISA assay was developed to set up the optimal conditions to detect Nodal in biological human samples. 3D1 antibody was coated at 100 ng/mL on black and clear bottom polystyrene 96-well plates, to capture *rhNodal* (recombinant human Nodal) at 4° C overnight. After the incubation, the coated wells were washed three times with PBS containing 0.005% Tween-20 (PBS-T) and non-specific binding sites were blocked by incubating with 1% BSA in PBS (300 µL/well) for 1 hour at 37°C. After washing three times with PBS-T,

rhNodal at scaling concentrations were incubated for 1 hour at 37° C (100 µL/well). After incubation, plates were washed three times with PBS-T and anti-Nodal anti-rabbit monoclonal antibody (EP2058Y, Epitomics) diluted 1:1000 in PBS was added to detect the captured *rhNodal* (100 µL/well) and incubated for 1 hour at 37° C. After incubation and three washes with PBS-T, an HRP-conjugated anti-rabbit antibody diluted 1:5000 in PBS was added (100 µL/well) and incubated for 1 hour at 37° C. After three washes with PBS, the resulting captured *rhNodal*-antibody complex was detected with a QuantaRed™ Enhanced Chemifluorescent HRP substrate (Thermo scientific), mixing 50 volumes QuantaRed Enhancer Solution with 50 volumes QuantaRed Stable Peroxide and 1 volume of the QuantaRed ADHP Concentrate. 100 µL of QuantaRed Working Solution were added to each plate well and incubated for 15 minutes at room temperature. Peroxidase activity was stopped by adding 10 µL of QuantaRed Stop Solution. The enzymatic activity was immediately stopped. The plate was shaken for 10-30 seconds and Relative Fluorescence Units (RFU) of each well were measured using a plate reader. The excitation and emission maxima for QuantaRed Substrate are 570 nm and 585 nm, respectively.

2.7 MONOCLONAL ANTIBODIES PURIFICATION

2.7.1 Protein G affinity chromatography

Antibodies were purified by standard procedures. After centrifugation at 4000 rpm for 20 minutes at 4° C, hybridoma cell-culture supernatants, containing monoclonal IgGs, were filtered on a 0.22 µm filter and loaded onto a HiTrap™ Protein G HP column (GE Healthcare). Purifications were performed on an ÄKTA FPLC™ instrument (GE Healthcare) at a flow rate of 0.6 mL/min, monitoring the absorbance at 280 nm. After washing away the unbound material using PBS (pH 7.4) as loading buffer, the bound antibodies were recovered by changing drastically the pH conditions using 100 mM Glycine pH 2.7 as elution buffer. The eluted antibodies were quickly neutralized by adding 1/10 volume 2 M TRIS pH 9.0. To ensure the stability of purified mAbs, the antibodies were buffer-exchanged into PBS (pH 7.4), using an Amicon® Ultra MWCO 50000 centrifugal filter (Millipore); mAbs were then concentrated, using the same filter. mAbs concentrations were estimated by UV spectrophotometry using the

Bradford assay. Purity of concentrated mAbs was evaluated by 10% SDS-PAGE gel and Coomassie blue staining.

2.7.2 Size-exclusion chromatography

Size-exclusion chromatography purifications were performed on a Superdex™ 200 HR 10/30 (GE Healthcare, Piscataway, NJ) gel filtration column, using PBS pH 7.4 as running buffer, at a constant flow rate of 0.5 ml/min, with a volume of elution of 25 mL and monitoring the absorbance at 280 nm. The final purified product was concentrated using an Amicon® Ultra MWCO 50000 centrifugal filter (Millipore) at 4000 rpm at 4°C.

After concentration, the purified IgGs were quantified by Bradford assay and analyzed by SDS-PAGE on 10% polyacrylamide gel; all the samples were loaded onto the gel under non-reducing conditions. Gel staining was achieved using by Coomassie Brilliant Blue.

2.8 SPR ANALYSES

All real-time binding analyses were performed on a Biacore 3000 instrument from GE Healthcare at 25° C, using certified HBS-EP as running buffer (10 mM HEPES, 150 mM NaCl, 3 mM EDTA, 0.005% Biacore surfactant P20, pH 7.4). Before each immobilization, the optimal immobilization level of the ligand, expressed as RU (Response Unit), was calculated on the basis of the following formula:

$R_{max} = MW \text{ analyte}/MW \text{ ligand} \times \text{Immobilized amount} \times \text{Stoichiometric ratio}$

2.8.1 Binding of purified mAbs to rhNodal protein

For this purpose we used the recombinant human Nodal protein provided by R&D Systems (Minneapolis, Minnesota, USA), *E. coli*-derived, His238-Leu347, with an N-terminal Met. The lyophilized protein was reconstituted at 100 µg/mL in sterile 4 mM HCl, according to the datasheet instructions.

RhNodal protein was covalently immobilized at 5 µg/mL in 10 mM Sodium Acetate buffer pH 4.5 at a flow rate of 5 µL/min by standard amine coupling onto a CM5 sensor, using EDC/NHS chemistry, exposing the primary amine groups or other nucleophilic groups to the reactive succinimide esters and allowing a covalent binding to the dextran matrix. Indeed, before

immobilization, a 50/50 mixture composed by 0.4 M EDC and 0.1 M NHS was used to activate free carboxyl groups on the dextran matrix. The amount of immobilized ligand corresponded to about 4100 response units (RU). Residual reactive groups on the sensor chip surface were deactivated by addition of 1M ethanolamine hydrochloride, pH 8.5. A 10 mM NaOH solution was used as regeneration solution to wash away non-specific linked molecules.

A control channel, prepared by activating with EDC/NHS and deactivating with 1M ethanolamine-HCl, indicated as control blank, was used as reference.

Real-time binding analyses were performed at a flow rate of 20 μ L/min, using HBS-EP as running buffer, injecting a constant volume of 60 μ L.

Stock solutions of purified antibodies in PBS were diluted in HBS-EP and tested at 100 nM; dissociations were monitored for at least 500 s.

After the single-dose screening, dose-dependent binding analyses were carried out with the two antibodies able to bind to *rh*Nodal protein, 3D1 and 5F10. For the 3D1 mAb binding experiments were carried out at concentrations ranging between 6 nM and 100 nM. For 5F10 higher concentrations were used (100, 250, 500 and 750 nM). Dissociations were monitored for at least 500 s.

2.8.2 Competition assay

*Rh*Cripto-1 protein, supplied by R&D System (Minneapolis, Minnesota, USA), was covalently immobilized at 5 μ g/mL in 10 mM Sodium Acetate buffer pH 4.5 at a flow rate of 5 μ L/min onto a CM5 sensor, by standard amine coupling, using EDC/NHS chemistry, reaching an immobilization level of 600 RU. *Rh*Nodal was used at the fixed concentration of 5nM, while the 3D1 was used at increasing concentrations providing a final molar ratio of antigen to antibody 1:0.25, 1:0.5 and 1:1. Each Nodal-3D1 mixture was incubated for 30 min at room temperature, before passing on the sensor chip.

2.8.3 Mapping of the 3D1 epitope

To define the epitope of the anti-Nodal 3D1 mAb, an epitope mapping study was carried out using *h*Nodal [43-67] peptide variants.

The whole antibody was immobilized at 5 μ g/mL in 10 mM NaAc buffer pH 5 at a flow rate of 5 μ L/min by standard amine coupling chemistry on a CM5 sensor chip. The immobilization level reached with the mAb was about 5350 RU. On

another channel of the same sensor chip, the 3D1 Fab' was immobilized at 10 $\mu\text{g/mL}$ in 10 mM NaAc buffer pH 4.5 at a flow rate of 5 $\mu\text{L/min}$, following the standard amine coupling chemistry. The amount of immobilized Fab' was about 2570 RU. Residual reactive groups were deactivated by 1M ethanolamine hydrochloride, pH 8.5. The blank channel was prepared also already described. Real-time binding analyses were performed at a flow rate of 20 $\mu\text{L/min}$, using HBS-EP buffer, injecting a constant volume of 60 μL of sample. 5 mM stock solutions of peptides in water were opportunely diluted in HBS-EP buffer and injected at the following concentrations: 0.5, 1, 2.5, 5, 10 and 20 μM . Dissociations were monitored for at least 500 s; the regeneration solution was 5 mM NaOH.

Experimental sensorgrams from every analysis were aligned, subtracted of blank signal and overlapped. All mathematical manipulations and fitting were performed using the BIAevaluation software, version 4.1 from GE Healthcare.

2.9 ANTIBODY DEGLYCOSYLATION

To improve the splitting of the 3D1 antibody by pepsin to get functional fragments, the antibody was first subjected to a deglycosylation reaction. Peptide-*N*-Glycosidase F, also known as PNGase F, supplied by New England Biolabs (Beverly, MA), was used for this purpose. This enzyme is an amidase that cleaves between the innermost GlcNAc and asparagine residues of high mannose, hybrid and complex oligosaccharides from *N*-linked^[115]. We used the PNGase to remove the single conserved *N*-linked glycan at Asn²⁹⁷ on each CH2 domain of the two heavy chains of the IgG₁. A first preliminary small-scale deglycosylation reaction was performed to set up the optimal conditions. The large-scale deglycosylation reaction was performed incubating 1.5 mg of the mAb, diluted in PBS (pH 7.4), with 11 units of PNGase F at 37° C for 24-48 hours. The time for optimal deglycosylation was fixed at 48 hours.

2.10 ENZYMATIC DIGESTION OF 3D1 WITH A PANEL OF PROTEASES

Small-scale pilot experiments were performed to assess the best reaction conditions to obtain the maximum yield of Fab fragments. To determine the optimal conditions, both the concentration of enzyme (enzyme:mAb ratio) and the reaction time were varied. The reaction was monitored after 2, 4, 6 hours and overnight. After terminating the digestions, fragments were analyzed by SDS-PAGE under reducing and non-reducing conditions. The reduced samples were shortly boiled in a dry block heater for 5 min in the presence of 10% (v/v) β -mercaptoethanol.

2.10.1 Papain digestion

Papain is a cysteine protease of the peptidase C1 family, consisting of a single polypeptide chain with three disulfide bridges and a sulfhydryl group necessary for activity of the enzyme; it exhibits broad specificity, cleaving peptide bonds of basic amino acids (preferably arginine and lysine), leucine, or glycine and it also hydrolyzes esters and amides ^[116].

Papain (Sigma-Aldrich, Saint Louis, Missouri, USA, catalog number P3125) was activated in digestion buffer (phosphate buffer saline, pH 7.4) in the presence of 5 mM L-Cysteine hydrochloride and incubating for 10 min at room temperature. To enhance the enzyme activity, 2 mM EDTA (heavy-metal chelator) was added. 3D1 (3-4 mg/ml), was used at a final w/w ratio of papain to mAb of 1:100. The mAb was mixed with the activated papain at pH 7.4 and the reaction was incubated in a 37° C water bath for 6 hours.

The reaction was stopped by incubating the digestion mixture with 25 mM Iodoacetamide for 20 min in the dark at room temperature to irreversibly inactivate papain.

2.10.2 Ficin digestion

Ficin is a thiol protease, containing a single reactive cysteine at its active site. The amino acid homology of the active site is similar to that of papain. This enzyme hydrolyses the peptide bonds where the carbonyl group is from phenylalanine or tyrosine ^[117].

Ficin (Sigma-Aldrich, Saint Louis, Missouri, USA, catalog number 1987) was activated in digestion buffer (PBS, pH 7.4) containing 10 mM L-Cysteine hydrochloride by incubation for 10 min at room temperature. Enzyme activity was enhanced by adding 2 mM EDTA; the enzyme to mAb 3D1 ratio (w/w) was 1:30. The digestion mixture was incubated for 5 hours in a 37° C water bath. The reaction was stopped by adding 5 mM IAM, mixing carefully and incubating the ficin digest for 20 min in the dark at room temperature.

2.10.3 Pepsinolysis

Pepsin, a member of the Peptidase A1 family, unlike some other endopeptidases, hydrolyzes only peptide bonds; it does not hydrolyze non-peptide amide or ester linkages ^[118].

After the deglycosylation reaction, prior to digestion, the 3D1 antibody was buffer-exchanged into 20 mM sodium acetate buffer (pH 4.0) using an Amicon® Ultra MWCO 50000 centrifugal filter (Millipore). PNGase F was not removed before proceeding to pepsinolysis. Small-scale pilot digestions were conducted on the deglycosylated 3D1 antibody to select the most appropriate conditions for the large-scale production of F(ab')₂. In these experiments the optimum concentration of pepsin (Sigma-Aldrich, Saint Louis, Missouri, USA, catalog number P6887), digestion time and pH were examined. In preliminary experiments 20 mM sodium acetate buffer was used at pH 4.5, but at this pH the pepsin proteolytic activity was greatly reduced. The antibody digestion was completed using an equal volume of a pepsin solution prepared in the same buffer and providing a final w/w ratio of pepsin to antibody 1:25. The resultant enzyme/antibody mixture was incubated for 3 to 6 hours and overnight in a 37° C water bath. At different time intervals, aliquots were removed and the enzyme reaction was stopped by adjusting the reaction pH to neutrality with 2M Tris pH 9. Samples were analyzed on a 12% SDS-PAGE gel under reducing and non-reducing conditions to determine the best digestion conditions, which were then used to produce F(ab')₂ on a large scale. Conditions for large scale production were as follows: 2 mg/mL 3D1 mAb, 20 mM NaAc, pH 4.0, enzyme/antibody ratio 1:25 w/w and incubation in a 37° C water bath for 6 hours.

2.11 PURIFICATION OF Fab/F(ab')₂/Fab' FRAGMENTS

Following the large-scale digestion, to separate the Fab fragments from the Fc portions and other eventual side products of degradation or intact mAb, the digestion mixture containing the deglycosylated Fab/F(ab')₂ fragments were loaded onto a HiTrap™ Protein G HP column (GE Healthcare), equilibrated with PBS, connected to ÄKTA FPLC instrument. Purification was carried out at a flow rate of 0.6 mL/min, monitoring the absorbance at 280 nm. The column was washed with PBS and the Fab fragment was collected in the flow through, using PBS (pH 7.4) as loading buffer; the Fc fragment and intact mAb were eluted from the column with 100 mM glycine, pH 2.7. When the pepsin digest was passed through the column, F(ab')₂ fragments were eluted using 100 mM glycine pH 2.7 and then neutralized using 2 M TRIS, pH 9. The relevant eluted fractions were collected, buffer-exchanged into PBS and concentrated using an Amicon® Ultra MWCO 10000 centrifugal filter (Millipore). The purity of Fab and F(ab')₂ fractions was detected by SDS-PAGE which was performed on a 12% gel under reducing and non-reducing conditions according to the method of Laemmli. Samples were treated with loading buffer in the absence and presence of β-mercaptoethanol (boiled at 100° C for 2 min) and stained with Coomassie Brilliant Blue. After digestion samples were stored at -20°C.

Fab and F(ab')₂ fragments were further purified by size-exclusion chromatography to check for high molecular weight aggregates. SEC was performed on a Superdex™ 200 10/300 GL column (GE Healthcare), connected to ÄKTA FPLC system. The column was eluted at a flow rate of 0.5 mL/min, using PBS as running buffer and the column effluent was monitored at 280 nm. The eluted final products were concentrated, using an Amicon® Ultra MWCO 10000 centrifugal filter (Millipore) and analyzed by 12% SDS-PAGE gel under reducing and non-reducing conditions.

2.12 REDUCTION OF THE F(ab')₂ TO Fab' AND Fab' ALKYLATION

Fab' fragments were produced by reducing selectively the hinge-region disulfide bonds of F(ab')₂ using 5 mM 2-Mercaptoethylamine (Thermo Scientific Pierce), that is a mild reductant. To promote the activity of the 2-MEA, 20 mM sodium acetate buffer pH 4.0 was added to the F(ab')₂ fragments dissolved in PBS pH 7.4 to adjust the pH at 6.0. 2 mM EDTA was also added. The mixture was

incubated for 1 hour at 37° C. After the incubation, PBS was added to the mixture to adjust the pH to neutrality. Reduction of F(ab')₂ to Fab' fragments was checked and confirmed by 12% SDS-PAGE gel under reducing and non-reducing conditions.

After reduction, Fab' fragments were incubated with 25 mM IAM for 30 min at room temperature in the dark to alkylate the free cysteine residues of the interchain disulfide bonds in the hinge region to block their reformation.

2.13 DOT BLOT ANALYSIS

Increasing amounts of *rhNodal* (50, 100, 150 and 200 ng) were spotted through circular templates directly onto a polyvinylidene difluoride (PVDF) membrane (Millipore). PVDF membranes was previously soaked in methanol 100% for 5 min. The blot was blocked with 5% milk (NFDM) in Tris-buffered saline containing 0.1% Tween-20 (TBS-T) for 1 h at room temperature under shaking; next, the membrane was probed overnight at 4° C with 3D1 mAb as primary antibody at 2 µg/mL in 2.5% NFDM in TBS-T under shaking. The membrane was then triple-washed with TBS-T and incubated with GAM-HRP as secondary antibody diluted 1:1000 in TBS-T for 1 h at room temperature under agitation. The target protein was detected using the enhanced Chemi-luminescent Substrate method with the SuperSignal West Pico kit provided by Pierce Chemical Co. (Rockford, IL USA), following the manufacturer's instructions. Signals were acquired with the ChemiDoc™ XRS video densitometer (Bio-Rad, Hercules, CA), using the Quantity One® software (Bio-Rad), that was used to performed the densitometer analysis as well.

2.14 WESTERN BLOT ANALYSES

Protein lysates of the cell lines were collected, quantified and subjected to SDS-PAGE gel electrophoresis and Western blot using standard protocols.

2.14.1 Detection of recombinant human Nodal

Increasing amounts of *rhNodal* (50, 100 and 200 ng) were loaded under reducing and denaturing conditions onto a 15% SDS-PAGE gel; after electrophoresis, proteins were transferred onto a PVDF) membrane, previously soaked in methanol 100% for 5 min, then equilibrated in transfer buffer (10 mM Tris base, 100 mM Glycine, 10% Methanol and 0.5% SDS) for at least 3 minutes. The

semi-dry electrophoretic transfer was performed at 18 eV for 40 min, using a Trans-Blot® SD (Bio-Rad) instrument. The western blot analysis was performed following the protocol previously described in the section **2.13**.

2.14.2 Detection of endogenous Nodal protein in human melanoma cell lines

Western blot analyses for the detection of endogenous Nodal protein were performed using the following human skin malignant melanoma cell lines: PES, A-375, SK-MEL, WM 266 and LCM. HEK-293 cells and 100 ng of *rhNodal* protein were used as positive controls. Cells were lysed using a lysis buffer (50 mM Tris-HCl pH 7.5, 500 mM NaCl, 1% NP, 10 mM EDTA, 1 mM MgCl₂, 1 mM CaCl₂, 10% Glycerol), with added a cocktail of protease inhibitors (Roche, Switzerland) and PMSF (Phenyl-MethaneSulfonylFluoride), a serine protease inhibitor, performing three freeze/thaw cycles. Samples were quickly frozen using a dry ice/ethanol bath and subsequently thawed at room temperature. Cycles of freezing and thawing caused cells to swell and break. Cell lysates were cleared by centrifugation at 12,000 for 20 min at 4° C and the supernatants containing all protein whole lysates were quantified by Bradford assay.

50 µg of cell lysate from each sample were applied to a 15% SDS-PAGE gel under reducing conditions and electrophoresed for 3 h at 80 V. Separated proteins were transferred onto a PVDF membrane. The western blot analysis was performed following the protocol previously described.

2.14.3 Competition between 3D1 antigen peptide and endogenous Nodal protein

Thirty micrograms of H9 and H14 human embryonic stem cell total protein lysates, obtained as previously described, were separated on a 15% SDS-PAGE gel under reducing conditions and the resolved proteins were transferred onto a PVDF membrane. 50 ng of *rhNodal* protein were used as positive control. The western blotting procedure was as previously described. The membranes were blocked, then probed with the 3D1 alone at 4 µg/mL in 2.5% NFDM in TBS-T and with the 3D1 mAb at 4 µg/mL pre-incubated with its antigen, the CH[43-56] peptide at 10 µg/mL. The blots were probed with GAM-HRP as secondary antibody and detected as already described.

2.14.4 Effects on Nodal expression

Twenty-five micrograms of total C8161 cell lysates were loaded per lane. Western blot analyses were performed following the protocol previously described. The blot was probed for detection of Nodal protein using anti-Nodal anti-rabbit monoclonal antibody (EP2058Y, Epitomics). The blot was then stripped and probed for β -Actin to determine equal loading using a mouse anti- β -Actin antibody (β -Actin (C4): sc-47778 Santa Cruz). Densitometric values for Pro-Nodal [39 kDa] were corrected by values determined for β -Actin.

2.14.5 Detection of Phospho-Smad, Phospho-MAPK, Cyclin B1 and p27

Thirty micrograms of total protein lysates (C8161) were loaded per lane on a 15% SDS-PAGE gel under reducing conditions. Western blot analyses were carried out using the procedure previously described. The membranes were probed with a rabbit polyclonal anti-Cyclin B1 (cyclin B1 antibody (H-20) sc-594, Santa Cruz Biotechnology), anti-p27 (p27 antibody (C-19) sc-528, Santa Cruz Biotechnology), anti Phospho-Smad (MBS617171, My Biosource) and anti-Phospho-MAPK antibody (MBS835580, My Biosource).

2.15 CELL CULTURE AND ANTIBODY TREATMENT

All human cell lines were purchased from ATCC (American Type Culture Collection) and cultured in T175 flasks at 37° C, in a humidified (90 %) and CO₂ (5 %) containing atmosphere.

HEK293 cells (immortalized human embryonic kidney cells, adherent), the following human aggressive melanoma cell lines, PES, A-375, SK-MEL, WM 266, LCM and LCP and the human embryonic stem cells, H9 and H14, were cultured and maintained in complete DMEM-F12 medium (Dulbecco's modified Eagle's medium-F12) supplemented with 10% FCS, and 1% penicillin/streptomycin. The human cutaneous amelanotic melanoma C8161 cells, characterized as highly aggressive, invasive and metastatic ^[119], were cultured and maintained in RPMI 1640 (Invitrogen, Carlsbad, CA) supplemented with 10% fetal calf serum (FCS, Gemini Bio-Products, Woodland, CA). Medium was changed routinely twice per week and cells were splitted into a new flask containing fresh medium, when they reached 80-90% confluence.

All cells were passaged every second or third day in proportion of 1:4 or 1:6, respectively. For passaging the cell culture, medium was removed and PBS (room temperature) was used to wash the cells. PBS was removed as well and cells were detached with about 2 mL of 0.05% trypsin/EDTA solution (Invitrogen). The flasks were placed in the incubator (37°C) for around 5 minutes. With a Zeiss model 25 inverted microscope (Carl Zeiss, Inc.) cells were monitored for detachment and for assuming a round shape. Fresh medium was added to neutralize trypsin.

The cell lines were genotyped by short tandem repeat (STR) PCR amplification and authentication confirmed. C8161 cells were treated with the 3D1 anti-Nodal antibody at 4 µg/mL, whereas an IgG was used as control (Santa Cruz anti-Nodal antibody).

For most *in vitro* experiments, antibodies were diluted in complete RPMI and added to cells daily for a period of 72 hours.

2.16 FLUORESCENCE-ACTIVATED CELL-SORTING (FACS) ANALYSES

LCP, A375 and WM266 cells were collected by centrifugation. After aspiration of supernatant, the cells were resuspended in 500 µL of PBS and formaldehyde was added to obtain a final concentration of 4%. Cells were fixed for 10 min at room temperature. After fixation, cells were permeabilized by adding 500 µL of PBS-Tween 20.

1×10^6 cells were aliquoted into each vial; 1 ml of PBS (incubation buffer) was added to each vial and cells were washed by centrifugation at 4000 rpm for 5 min at 4°C. Cells were resuspended in 100 µL of solution of 3D1 anti-Nodal antibody (primary antibody), diluted in PBS at the following concentrations: 0.1, 0.5, 1 and 2 µg/mL. A standard IgG1 isotype was used as negative control. Cells were incubated with the primary antibody for 1 hour at 4°C under shaking. After incubation, cells were washed by centrifugation in 1 mL of PBS, resuspended and incubated with a FITC-conjugated anti-mouse antibody (secondary antibody), diluted 1:1000 (1µg/mL) in PBS, for 40 min at 4° C in the dark under stirring. Cells were washed by centrifugation with 1 mL of incubation buffer, re-suspended in 500 µL of PBS and analyzed on flow cytometer. Fluorescence was evaluated using the BD FACScalibur™ System.

2.17 SOFT AGAR CLONOGENIC ASSAY

Colony forming assays were prepared in triplicate wells with C8161 melanoma cells. Briefly, for each well, 5,000 cells were suspended in 0.35% agarose in complete RPMI or in complete RPMI containing 3D1 anti-Nodal antibody at 4 $\mu\text{g}/\text{mL}$ or an IgG used as negative control. Suspensions were pipetted onto a solidified layer of 0.5% agarose in complete RPMI in six-well dishes. Cells were cultured for three weeks, then clusters of > 50 cells were scored and photographed using a Zeiss model 25 inverted microscope (Carl Zeiss, Inc.) and Hitachi HV-C20 CCD camera (Hitachi Denshi Ltd., Woodbury, NY, USA).

2.18 VASCULOGENIC MIMICRY ASSAY

An aliquot of growth factor-reduced Matrigel (14 mg/ml; BD Biosciences) was warmed up at room temperature. Before completely thawed, it was transferred onto ice and its liquid was kept on ice for at least 10 min. Then 50 μL of Matrigel was plated to 96-well plates at a horizontal level that allows the Matrigel to distribute evenly and incubated for 30 min at 37° C.

C8161 cell pellets ($1-2 \times 10^4$) were re-suspended with serum-free RPMI and loaded on the top of the Matrigel. The 3D1 mAb, the blocking anti-Nodal antibody (Santa Cruz) that was used as positive control and an IgG1 used as negative control were added at 3 $\mu\text{g}/\text{mL}$ and at 4 $\mu\text{g}/\text{mL}$ to the serum-free medium. Each conditional group contained 4-6 wells. Following incubation at 37° C overnight, each well was analyzed directly under a microscope. 100 μL of 10% formalin saline-based solution was gently added for the tubules fixation. Under a microscope with 10x phase contrast, tubules in each field were imaged and an average of tubules from 3-5 random fields in each well was counted.

2.19 LUNG COLONIZATION IN MICE INDUCED BY C8161 CELLS

250,000 C8161 metastatic human melanoma cells were injected retro-orbitally in 16 nude mice and characteristically colonized first to the lung; lung colonization was established after 4 days. Following colonization, animals received by intraperitoneal delivery alternate injections of 100 μg of either of 3D1 monoclonal antibody (N=8) or control IgG (N=8) over the next 10 days, every

other day (5 total injections). The mice were sacrificed on days 12 and their lungs were examined macroscopically and immunohistochemically.

2.20 IMMUNOHISTOCHEMICAL ANALYSES

Four-micron thick, formalin-fixed, paraffin-embedded lung mice tissue sections were prepared and immunohistochemistry was carried out on a Microm HMS 710i autostainer (Thermo Scientific Lab Vision, Waltham, MA, USA). Briefly, following antigen retrieval and blocking steps, sections were incubated in Cyclin B1, p27 and P-Smad antibody at 5 µg/mL for 60 minutes, followed by biotinylated anti-mouse secondary antibody (Biocare Medical, LLC, Concord, CA, USA), and then streptavidin-horseradish peroxidase (Thermo Scientific Lab Vision). Colour was developed with 3,3'-diaminobenzidine substrate (Thermo Scientific Lab Vision) and sections were counterstained with hematoxylin (Biocare Medical, LLC). As a negative control, adjacent serial sections were incubated with ChromPure mouse Ig (Jackson Immunoresearch Labs, West Grove, PA, USA) at the same concentration. Cyclin B1, p27 and P-Smad staining was scored on a scale of 0 to 3 at 10 × and 63 × magnification to determine, respectively, percentage and intensity of Cyclin B1, p27 and P-Smad staining within the area of interest (0, no staining; 1 = < 10% or weak; 2 = 10 to 50% or moderate; 3 = > 50% or strong). The two scores were then multiplied to obtain a Cyclin B1, p27 and P-Smad Scoring Index (SI).

I 3. RESULTS

3.1 GENERATION AND CHARACTERIZATION OF ANTI-NODAL MONOCLONAL ANTIBODIES

3.1.1 ANTIGEN DESIGN

On the basis of previous docking and binding studies^[32], the region of human Nodal (Uniprot Q96S42) including the H3-wrist helix along with the pre-helix loop was chosen as *hNodal*-like antigen.

As reported by Calvanese et al.^[32], the *hNodal*[43-69] peptide, referred to the 1-110 residues numbering and corresponding to the mature form of the endogenous protein (238-347 aa), is involved in the binding with the co-receptor Cripto and it contains two glutamic residues, E49 and E50, which are crucial to stabilize the interaction. With the aim to select anti-Nodal antibodies able to recognize these two hot-spots residues, we devised a simple and new strategy of screening. After immunization and hybridoma generation, cell supernatants were screened using a mutated form, named *hNodal*[43-69]E49A-E50A peptide, in which E49 and E50 were replaced with two alanines.

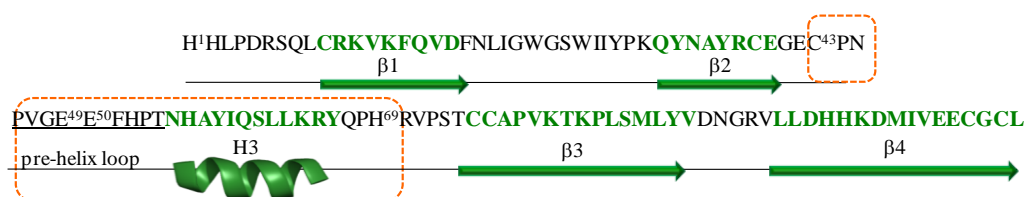


Figure 3.1: Aminoacid sequence and secondary structure of the Nodal monomer.

3.1.2 CHEMICAL SYNTHESIS, PURIFICATION AND IDENTIFICATION OF HUMAN NODAL AND GDF PEPTIDES

hNodal[43-69] peptide and mutated variants were synthesized with either a free amino group at the N-terminus (used for conjugation with KLH and immunogen preparation), or acetylated and amidated to better mimic the peptide within the protein structure.

A set of mutated variants of *hNodal*[43-69] peptide, reported in **Table 1**, were designed to define the epitope and to investigate the contribution of specific residues to the recognition with antibodies. Peptides 1 to 7 (**Table 1**) included

variants of *hNodal*[43-69] bearing doubly mutated residues, at the N-terminus; shorter peptides (entries from 8 to 10, **Table 1**) were used to confirm the epitope at N-terminus region.

To confirm the specificity of recognition in the full-length protein, three peptides (entries from 11 to 13, **Table 1**) mimicking the N-terminal portion [1-38], the central region [39-75] and the C-terminal region [76-100] of the mature form of human Nodal^[120] were tested. Peptides 14 and 15 in **Table 2**, reproducing the human GDF 5 and GDF6/7 region (GDF : Growth Differentiation Factors; GDFs are close structural homologs of Nodal^[33]) were tested to explore the selectivity of antibody among TGF- β family ligands. The sequence were chosen on the basis of multiple alignment of *hNodal*[43-69] peptide versus all TGF- β ligands performed by using the BLAST server (<http://www.expasy.org/proteomics>); alignments are reported in **Fig. 3.2**.

All peptides were synthesized, purified and identified as described in the Methods section **2.1**; they were obtained with an average yield of 50% and with a purity level above 95%, as determined by LC-MS analysis. (**Table 1**).

Table 1. Nomenclature, aminoacidic sequence and MW of *hNodal* peptides

	<i>hNodal</i> peptides	Sequence	MW Theor.	MW Exp.
1	[43-69]	CPNPVGEEFHPTNHAYIQSLLKRYQPH	3217.592 amu	3216.6 amu
2	[43-69]E49A-E50A	CPNPVGAAFHPTNHAYIQSLLKRYQPH	3100.56 amu	3100.6 amu
3	[43-67]	CPNPVGEEFHPTNHAYIQSLLKRYQ	2983.335 amu	2982.3 amu
4	[44-67]	PNPVGEEFHPTNHAYIQSLLKRYQ	2880.192 amu	2879.3 amu
5	[44-67]E49A-E50A	PNPVGAAFHPTNHAYIQSLLKRYQ	2764.119 amu	2763.5 amu
6	[43-67]P46A-V47A	CPNAAEETFHPTNHAYIQSLLKRYQ	2929.244 amu	2928.6 amu
7	[44-67]P46A-V47A	PNAAEETFHPTNHAYIQSLLKRYQ	2826.101 amu	2825.5 amu
8	[43-56]	CPNPVGEEFHPTNH	1618.728 amu	1617.8 amu
9	[52-60]	HPTNHAYIQ	1121.202 amu	1121.2 amu
10	[56-69]	AYIQSLLKRYQPH	1657.916 amu	1658.0 amu
11	[1-38]	HHLPDRSQLCRKVKFQVDFNLIGWGSWIIYPKQYNR	4719.428 amu	4718.4 amu
12	[39-75]	CEGECNPVGEEFHPTNHAYIQSLLKRYQPHRVPSTC	4279.778 amu	4278.7 amu
13	[76-100]	CAPVKTPLSMLYVDNGRLLDHHKDMIVEECGCL	3969.720 amu	3968.6 amu

Table 2. Nomenclature, aminoacidic sequence and MW of *hGDF* peptides

	<i>hGDF</i> peptides	Sequence	MW Theor.	MW Exp.
14	GDF5	CEFPLRSHLEPTNH	1720.908 amu	1719.8 amu
15	GDF 6/7	CDFPLRSHLEPTNH	1706.881 amu	1705.7 amu

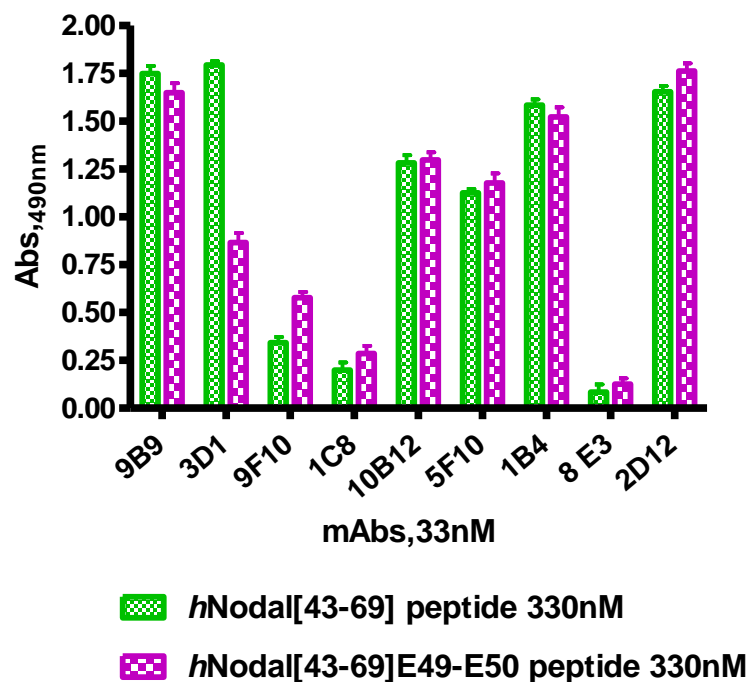


Figure 3.3: ELISA-based screening assay of hybridoma supernatants. *hNodal*[43-69] and *hNodal*[43-69]E49A-E50A peptides were coated at 1 µg/mL (330 nM). Hybridoma supernatants were tested at a concentration of 5 µg/mL total protein (33 nM assuming the occurrence of purified antibodies).

3.1.4 ISOLATION OF ANTI-NODAL mAbs FROM HYBRIDOMA SUPERNATANTS

Supernatants from the six monoclonal antibodies (mAbs, 9B9, 3D1, 10B12, 5F10, 1B4 and 2D12) showing the strongest signal for binding to Nodal peptides, were purified by Protein G affinity chromatography (**Fig. 3.4A**) and concentrated as described in the section of Methods. High yield and high purity were achieved for all the antibodies and, as expected, a band of 150 kDa was detected by 10% SDS-PAGE under non-reducing conditions (**Fig. 3.4C**).

MAbs isolated from hybridoma supernatants were further purified by size-exclusion chromatography to evaluate the presence and even to remove possible aggregates (**Fig. 3.4B**). All mAbs showed a similar gel filtration profile, with a retention volume of 11-12 ml, according to a protein molecular weight of 150 kDa. As can be seen, no aggregates were detectable, as well as confirmed by 10% SDS-PAGE under non-reducing conditions. All purified mAbs were identified as IgG₁ isotype with kappa light chains.

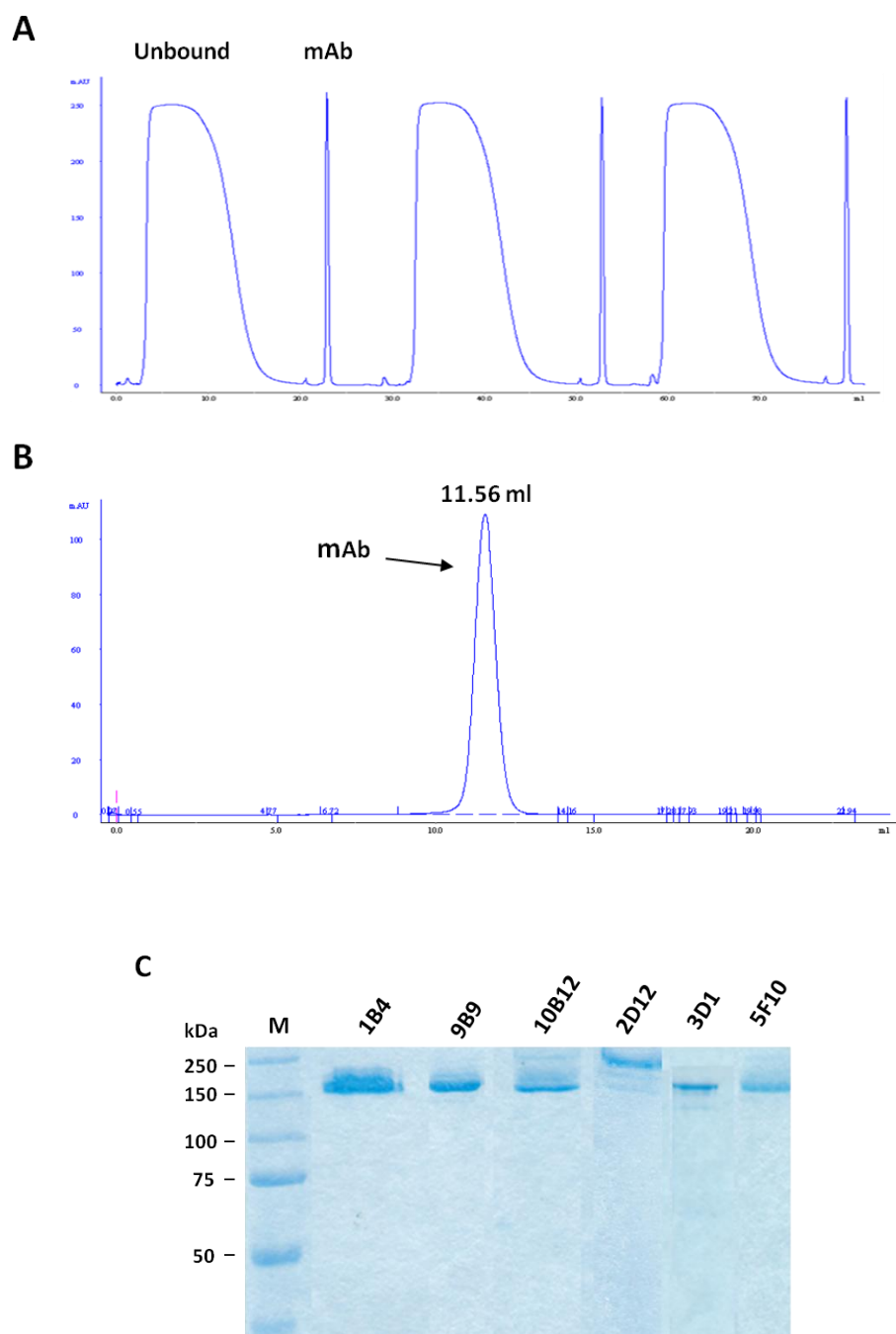


Figure 3.4: (A) Representative chromatogram of Protein G affinity purification of a mAb from hybridoma supernatant, sharp peaks are due to the elution of the bound mAb with 100mM Glycine pH 2.7; (B) Representative SE chromatographic profile of an anti-Nodal mAb; (C) 10% SDS-PAGE analysis of two steps purified anti-Nodal mAbs.

3.1.5 SPR BINDING ANALYSES OF mAbs TO *rh*NODAL PROTEIN

After selection, the ability of the purified monoclonal antibodies to bind to the full-length recombinant human Nodal protein was evaluated and considered a pre-requisite for their use as diagnostic tool. This screening was carried out by SPR direct binding. MAbS were initially tested at 100 nM; at this concentration only two antibodies, 3D1 and 5F10, were able to bind to the full-length *rh*Nodal protein. To determine their affinity constant, dose-dependent binding assays were next carried out. Analyses were performed injecting increasing concentrations of antibodies; association and dissociation rate constants were determined from each run. A global fitting of the data allowed the estimation of a K_D value of 1.42 nM for the interaction between the 3D1 and the protein. A K_D of 83 nM was instead measured for the interaction of the 5F10 antibody. The 3D1 displayed rapid association (k_a $6.95 \cdot 10^5 \text{ M}^{-1} \text{ s}^{-1}$) and slow dissociation rate (k_d $6.55 \cdot 10^{-4} \text{ s}^{-1}$) constants, resulting in a high binding affinity to the protein. The 5F10 mAb, compared to the 3D1, exhibited lower affinity, as result of slower association (k_a $1.91 \cdot 10^4 \text{ M}^{-1} \text{ s}^{-1}$) and quicker dissociation (k_d $1.08 \cdot 10^{-3} \text{ s}^{-1}$) rates; moreover, it recognized the protein at higher concentrations, revealing a weak binding.

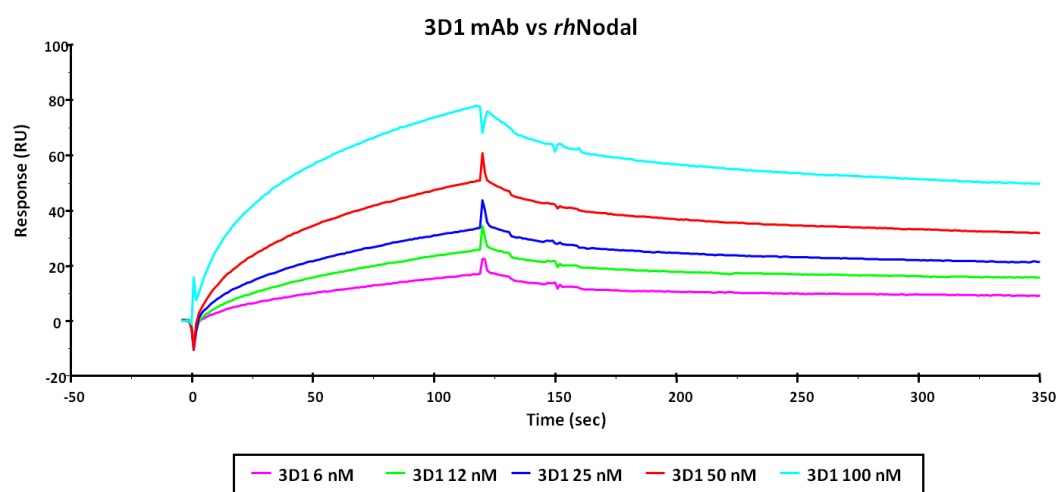


Figure 3.5A: Overlay plot of SPR sensorgrams showing the interaction between 3D1 mAb and *rh*Nodal immobilized on a CM5 sensor chip. The interaction was monitored at concentrations of mAb ranging between 6 and 100 nM, obtaining dose-dependent binding curves.

Table 3. Association and dissociation rate constants and K_D values determined for the binding of the 3D1 mAb to *rhNodal* functionalized sensor chip

3D1 mAb	k_a (1/Ms)	k_d (1/s)	K_D (M)	SD
6 nM	1.28×10^6	6.29×10^{-4}	4.91×10^{-10}	0.0129
12 nM	9.79×10^5	6.30×10^{-4}	6.98×10^{-10}	0.0504
25 nM	6.42×10^5	6.20×10^{-4}	9.68×10^{-10}	0.165
50 nM	3.61×10^5	6.97×10^{-4}	1.93×10^{-9}	0.331
100 nM	2.12×10^5	6.44×10^{-4}	3.03×10^{-9}	1.07
average	6.95×10^5	6.55×10^{-4}	1.42×10^{-9}	0.326

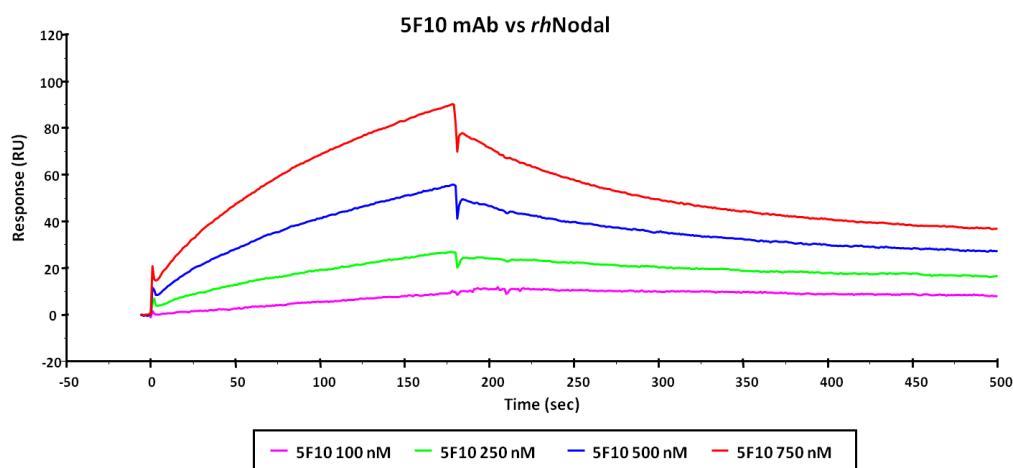


Figure 3.5B: Overlay plot of SPR sensorgrams showing the interaction between 5F10 mAb and *rhNodal* immobilized on a CM5 sensor chip. The interaction was monitored at concentrations of mAb ranging between 100 and 750 nM, obtaining dose-dependent binding curves.

Table 4. Association and dissociation rate constants and K_D values determined for the binding of the 5F10 mAb to *rhNodal* functionalized sensor chip

5F10 mAb	k_a (1/Ms)	k_d (1/s)	K_D (M)	SD
100 nM	2.60×10^4	8.16×10^{-4}	3.14×10^{-8}	0.0246
250 nM	1.81×10^4	1.08×10^{-3}	5.97×10^{-8}	0.0818
500 nM	1.31×10^4	1.33×10^{-3}	1.02×10^{-7}	0.148
750 nM	9.40×10^3	1.30×10^{-3}	1.38×10^{-7}	0.0286
average	1.91×10^4	1.08×10^{-3}	8.28×10^{-8}	0.0708

In light of these results, 3D1 was chosen for subsequent studies.

3.2 BIOCHEMICAL CHARACTERIZATION OF THE 3D1

3.2.1 SPR COMPETITION ASSAY

By SPR assay, after achieved dose-dependent binding between *rhNodal* and its co-receptor *rhCripto-1*, a dose-dependent competition experiment using 3D1 monoclonal antibody was carried out to evaluate the ability of the mAb to interfere in the binding of Nodal to Cripto. Data shown in **Fig. 3.6** revealed that the antibody at 1:1 molar ratio was able to inhibit the binding of Nodal to Cripto-1 by approximately 70%. This is a preliminary evidence that the 3D1 is able to block the formation of Nodal/Cripto-1 complex and this result supports the hypothesis that the 3D1 can be a neutralizing antibody for the upstream Nodal signaling.

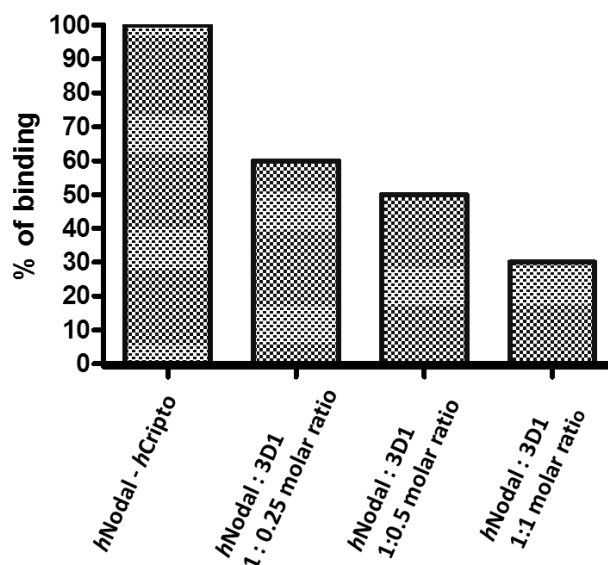


Figure 3.6: Inhibition of *rhNodal/rhCripto-1* complex by SPR concentration-dependent competition assay. A plot of % of binding versus increasing antibody concentrations is reported. *RhNodal* was used at the fixed concentration of 5 nM.

3.2.2 PRODUCTION AND PURIFICATION OF Fab/F(ab')₂/Fab' FRAGMENTS

In the attempt to produce smaller antibody fragments useful for crystallization studies, we tried to obtain 3D1-derived Fab fragments by enzymatic digestion. After unfruitful attempts to obtain the Fab under canonical conditions using several enzymes (not shown), we ended up with a protocol foreseeing deglycosylation of the antibody prior digestion^[121]. For this purpose 3D1 mAb was deglycosylated with the Peptide-*N*-glycosidase F (PNGase F) to remove a

single *N*-linked glycan at Asn²⁹⁷ on each CH2 domain of the two heavy chains. This was expected to render the IgG₁ molecule more sensitive to proteases activity, because the glycan pattern reportedly affects antibody's resistance to proteases digestion, especially by pepsin. After the deglycosylation reaction, the whole antibody was digested by using three different proteases: papain, ficin and pepsin.

Papain and ficin were used to prepare the monovalent Fab fragment by splitting the antibody above the hinge region; instead, pepsin was used to produce the bivalent F(ab')₂ fragment by cleaving the antibody on the carboxyl side of cysteine residues within the hinge region, below the disulfide bond.

All digestions were completed after 6 hours of incubation. SDS-PAGE analyses showed the disappearance of the 150 kDa band corresponding to the whole antibody under non reducing conditions and the disappearance of the 50 kDa band representing the intact heavy chain under reducing conditions. The reaction with papain led to the formation of a Fab with an apparent MW of about 40 kDa (non reducing conditions) or 25 kDa (reducing conditions), **Fig. 3.7A**. The treatment with ficin led to fragments with the same array of molecular weights (**Fig. 3.7B**). Remarkably, pepsin (**Fig. 3.7C**) converted 3D1 into F(ab')₂, MW about 100 kDa, without formation of other fragments.

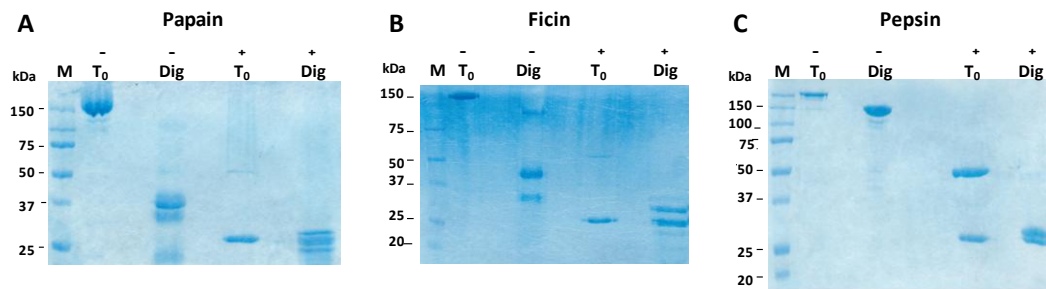


Figure 3.7: 12% SDS-PAGE analysis under non reducing (-) and reducing (+) conditions of products obtained following digestion of the 3D1 mAb with three different proteases – (A) Papain, (B) Ficin and (C) Pepsin- T₀ : 3D1 antibody ; Dig : proteolytic digest of 3D1 after 6 hours.

Fab and F(ab')₂ fragments were isolated from the digestion mixture by a two-step purification procedure, that included Protein G affinity chromatography to remove the Fc portions and possible intact antibody (uncut) and size-exclusion chromatography to both evaluate the presence and remove aggregates and to remove residual proteases. Integrity and purity of the products were confirmed

after each step by SDS-PAGE analysis under reducing and non-reducing conditions.

In the chromatograms of the Protein G affinity purification reported below, the first peak corresponded to the Fab from papain (**A**), the Fab from ficin (**B**) and the Fc portion (**C**) degraded by pepsin into small sub-fragments, eluted in the flow through. By contrast, the second peak corresponded to the Fc portion from papain and ficin digestion, [(**A**) (**B**) respectively] and the F(ab')₂ (**C**) obtained from pepsin digestion. F(ab')₂, instead of Fab, was eluted with Glycine because it contained a small portion of Fc.

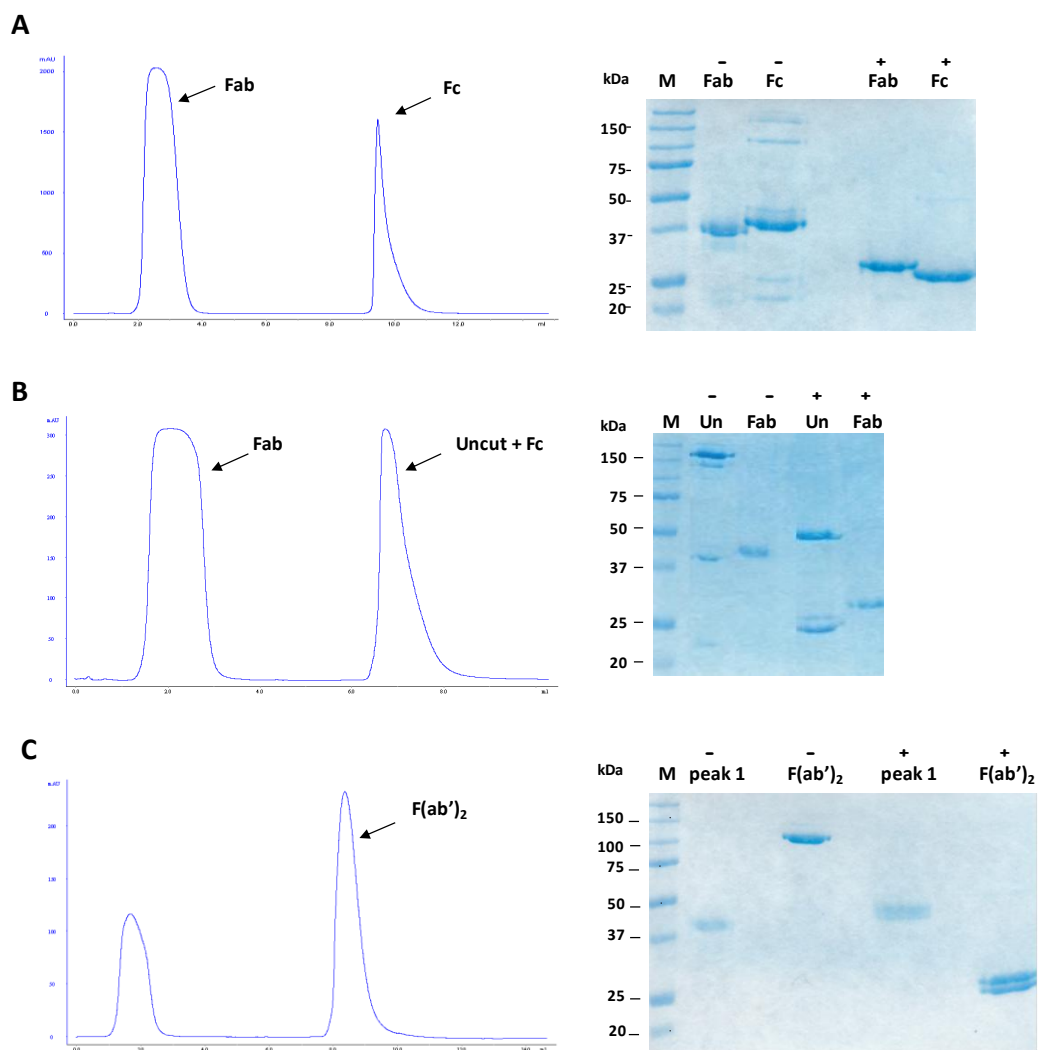


Figure 3.8: Chromatograms of Protein G affinity purification and SDS-PAGE analysis of products obtained from papain (**A**), from ficin (**B**) and from pepsin digestion (**C**).

Fab and F(ab')₂ fragments partially purified by the affinity chromatography step were purified to homogeneity by size-exclusion chromatography.

SE-chromatographic profiles showed absence of aggregates and presence of highly homogenous products; moreover, the elution volume of each single product was in agreement with the expected molecular weight: ~ 45 kDa for the Fab obtained with papain and ficin digestion, ~ 110 kDa for the F(ab')₂ obtained with pepsin. Purity estimated on 12% non-reducing and reducing SDS-PAGE was also higher than 99%. By SDS-PAGE analysis the identity of final products was confirmed as well; as expected, the F(ab')₂ fragment exhibited, under non reducing conditions, an homogenous band at approximately 110 kDa, while under reducing conditions, two separated bands with different mobility at around 25 kDa, the slower one corresponded to the heavy chain, higher than the other one due to the presence of a small Fc portion, while the faster one corresponded to the light chain.

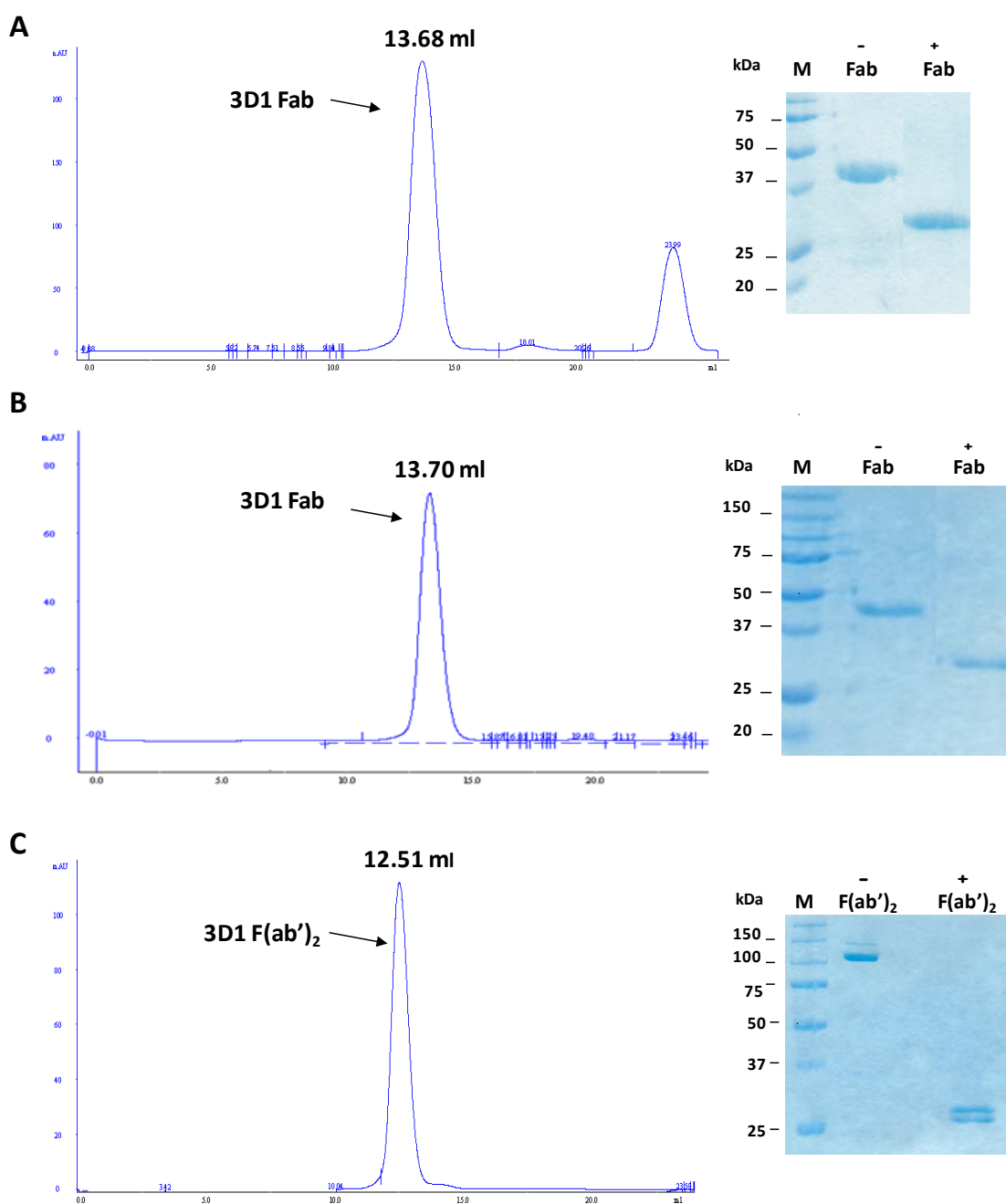


Figure 3.9: SEC profiles with the retention volume and SDS-PAGE analysis of Fab obtained by papain digestion (A), Fab obtained by ficin digestion (B) and $F(ab')_2$ obtained by pepsin digestion (C).

Next, Fab' fragment was obtained by reducing selectively the hinge-region disulfide bonds of $F(ab')_2$ using Mercaptoethylamine. The reaction was successfully achieved after 3 hours as shown by SDS-PAGE analysis under non reducing conditions (Fig. 3.10A) by the absence of the $F(ab')_2$ band at 110 kDa and the presence of the ~45 kDa band corresponding to the Fab' fragment. Additional smaller bands approximately at 25 and 20 kDa were other

unimportant products of the reduction reaction. To carry out further analyses, the Fab' was alkylated with 25 mM IAM to block the reformation of the hinge region disulfide bonds. Subsequently, Fab' was purified by size-exclusion chromatography to confirm its identity and to evaluate the presence of eventual aggregates. As indicated by the presence of a single peak eluted at 13.65 ml (Fig. 3.10B), no aggregates were detected.

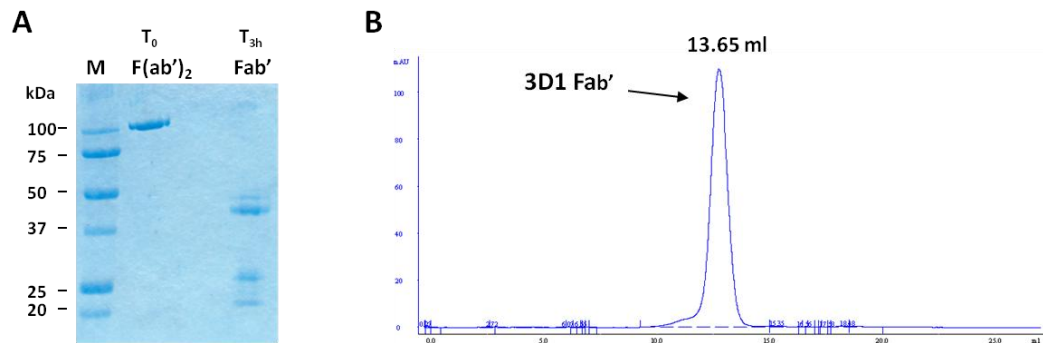


Figure 3.10: (A) 12% SDS-PAGE analysis under non-reducing conditions of the F(ab')₂ reduced to Fab'; (B) SE-chromatographic profile of the Fab'.

3.2.3 SPR COMPARATIVE BINDING ANALYSES OF Fab/F(ab')₂/Fab' FRAGMENTS

The ability of the different purified antibodies fragments, obtained by proteolytic cleavage, to bind to *rhNodal* protein was assessed by a comparative binding assay carried out by SPR technique. Fragments were tested at a concentration up to 100 nM. Unfortunately, Fab fragments obtained by digestion with papain and ficin were unable to bind to the immobilized protein; a plausible explanation was that also the CDRs were multiply cleaved by the proteases leading to antibody inactivation.

Table 5. Fab fragments tested by SPR

Sample	Binding vs <i>rhNodal</i>
Fab from Papain	-
Fab from Ficin	-
F(ab') ₂ from Pepsin	+
Fab' from F(ab') ₂	+

The 3D1 F(ab')₂ and Fab' fragments bound to the immobilized *rhNodal*, displaying similar association and dissociation rate constants and consequently the same affinity for *rhNodal* ($K_D=15$ nM, See **Fig. 3.11** and **Fig. 3.12**). This K_D is 10-fold lower compared to that exhibited by the whole antibody ($K_D=1.4$ nM); this effect was probably due to partial local unfolding resulting from the low pH treatment required for the pepsin digestion^[122].

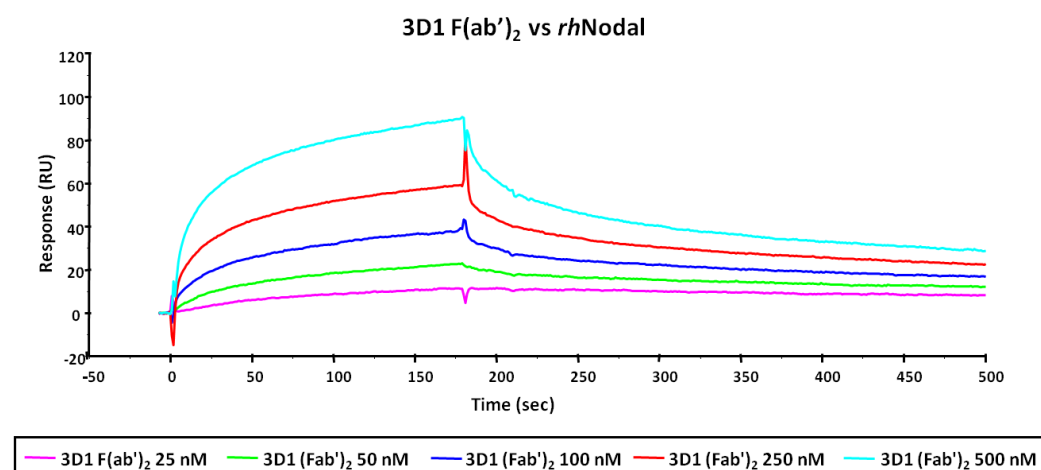


Figure 3.11: Overlay plot of SPR sensorgrams showing the binding of the 3D1 F(ab')₂ to *rhNodal* immobilized on a CM5 sensor chip. The interaction was monitored at concentrations of F(ab')₂ ranging between 25 and 500 nM, obtaining dose-dependent binding curves.

Table 6. Association and dissociation rate constants and K_D values determined for the binding of the $F(ab')_2$ to *rhNodal* functionalized sensor chip

$F(ab')_2$	k_a (1/Ms)	k_d (1/s)	K_D (M)	SD
25 nM	$4.40 \cdot 10^5$	$1.13 \cdot 10^{-3}$	$2.57 \cdot 10^{-9}$	0.0214
50 nM	$2.77 \cdot 10^5$	$1.35 \cdot 10^{-3}$	$4.87 \cdot 10^{-9}$	0.0578
100 nM	$1.87 \cdot 10^5$	$1.63 \cdot 10^{-3}$	$8.71 \cdot 10^{-9}$	0.323
250 nM	$8.21 \cdot 10^4$	$1.67 \cdot 10^{-3}$	$2.03 \cdot 10^{-9}$	0.446
500 nM	$4.58 \cdot 10^4$	$1.84 \cdot 10^{-3}$	$4.02 \cdot 10^{-8}$	1.63
average	$2.06 \cdot 10^5$	$1.52 \cdot 10^{-3}$	$1.53 \cdot 10^{-8}$	0.496

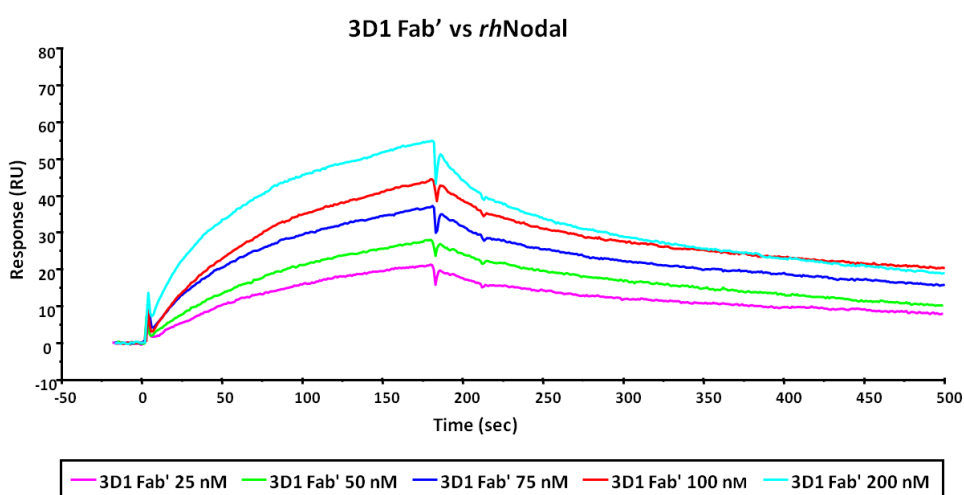


Figure 3.12: Overlay plot of SPR sensorgrams showing the binding of the 3D1 Fab' to *rhNodal* immobilized on a CM5 sensor chip. The interaction was monitored at concentrations of Fab' ranging between 25 and 200 nM, obtaining dose-dependent binding curves

Table 7. Association and dissociation rate constants and K_D values determined for the binding of the Fab' to *rhNodal* functionalized sensor chip

Fab'	k_a (1/Ms)	k_d (1/s)	K_D (M)	SD
25 nM	$3.42 \cdot 10^5$	$2.02 \cdot 10^{-3}$	$5.91 \cdot 10^{-9}$	0.0347
50 nM	$1.59 \cdot 10^5$	$2.62 \cdot 10^{-3}$	$1.65 \cdot 10^{-8}$	0.0245
75 nM	$1.50 \cdot 10^5$	$1.92 \cdot 10^{-3}$	$1.28 \cdot 10^{-8}$	0.0949
100 nM	$1.18 \cdot 10^5$	$1.56 \cdot 10^{-3}$	$1.32 \cdot 10^{-8}$	0.0909
200 nM	$7.59 \cdot 10^4$	$2.31 \cdot 10^{-3}$	$3.04 \cdot 10^{-8}$	0.145
average	$1.69 \cdot 10^5$	$2.09 \cdot 10^{-3}$	$1.58 \cdot 10^{-8}$	0.078

3.2.4 EPITOPE MAPPING STUDY

To finely delineate the epitope of the 3D1 antibody, a mapping of the original antigen was carried out. For this purpose, the antigen peptide and its mutated variants (see **Table 1**) were assayed by ELISA and by SPR.

a. ELISA assay

ELISA assays were carried out to by coating the different peptides, probing the binding with 3D1 and detecting with a secondary anti-mouse antibody. As shown in **Fig. 3.13**, the highest signal was detected with the short [43-56] peptide, whereas weaker signals were detected with variants bearing the mutated E49 and E50. No binding was observed with the variants in which P46 and V47 were mutated to alanines, as well as with other shorter peptides.

These data confirmed the high specificity of the 3D1 for N-terminal residues, specifically C43, P46, V47, E49 and E50.

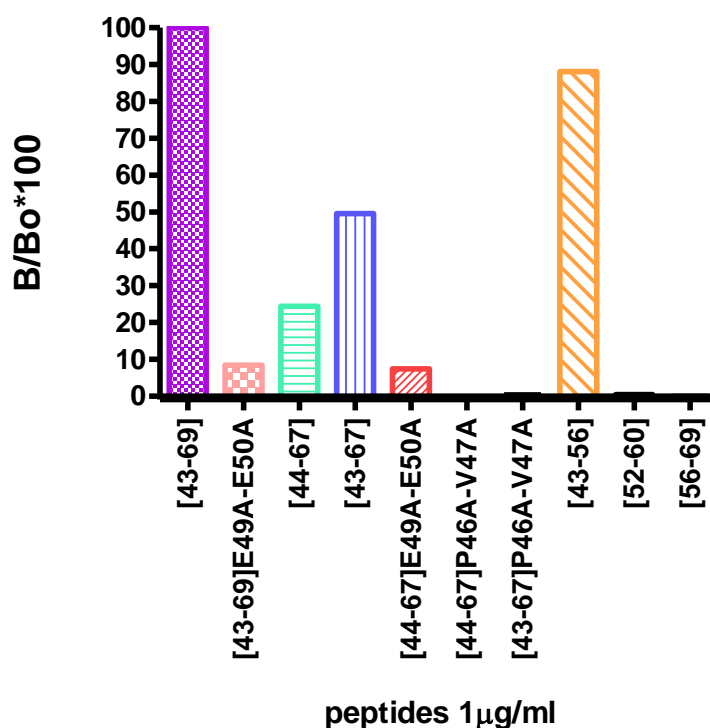


Figure 3.13: Mapping of 3D1mAb epitope; peptides were coated at 1 µg/mL; absorbance values of each peptide was normalized to the [43-69] peptide, considered as 100% of signal.

b. SPR analyses

SPR dose-response binding assays were performed with peptides [43-67], [44-67] and [43-56] to extrapolate K_D values. Sensorgrams are reported in **Fig. 3.14**. In **Table 8** are reported the relevant data obtained by the analyses. These data suggest that region [43-56] is the epitope of the 3D1 mAb and that residues from 46 to about 50 are the most crucial for the recognition. The region falls within the pre-helix loop, encompassing the two glutamic acid residues crucial for the binding of Nodal to Cripto. The 3D1 is not a conformational antibody because it mostly recognizes a linear epitope; in addition, this finding was confirmed by SPR analysis by the absence of binding with the other two smaller variants, [52-60] and [56-69], even tested at very high concentrations (data not shown). Furthermore, C43, which seems to have a role in the binding to the antibody, likely only plays a conformational role, helping the peptide to adopt a structure more prone to antibody recognition.

Table 8. *hNodal* peptides screened in the epitope mapping study and K_D values determined for the binding of the positive peptides to 3D1 mAb/Fab' functionalized sensor chip. No fitting means that fitting of binding and association curves did not converge to any value.

<i>hNodal</i> peptides 0.5-20 μM	Sequence	K_D vs 3D1 mAb	K_D vs 3D1 Fab'
[43-67]	CPNPVGEEFHPTNHAYIQSLLKRYQ	613 nM	590 nM
[44-67]	PNPVGEEFHPTNHAYIQSLLKRYQ	NO FITTING	NO FITTING
[44-67]E49A-E50A	PNPVGAFHPTNHAYIQSLLKRYQ	NO BINDING	NO BINDING
[43-67]P46A-V47A	CPNAAEETFHPTNHAYIQSLLKRYQ	NO BINDING	NO BINDING
[43-56]	CPNPVGEEFHPTNH	405 nM	371 nM
[52-60]	HPTNHAYIQ	NO BINDING	NO BINDING
[56-69]	AYIQSLLKRYQPH	NO BINDING	NO BINDING

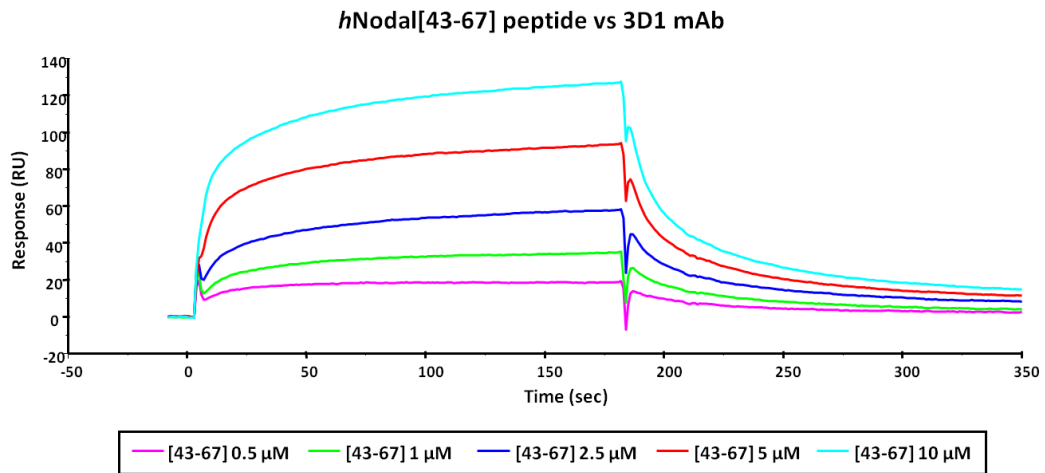


Figure 3.14A: Overlay plot of SPR sensorgrams showing the interaction between peptide [43-67] and 3D1 mAb immobilized on a CM5 sensor chip. The interaction was monitored at concentrations of peptide ranging between 0.5 and 10 μM , obtaining dose-dependent binding curves.

Table 9. Association and dissociation rate constants and K_D values determined for the binding of *hNodal*[43-67] peptide to 3D1 mAb functionalized sensor chip

[43-67] vs mAb	k_a (1/Ms)	k_d (1/s)	K_D (M)	SD
0.5 μM	$8.43 \cdot 10^4$	$3.95 \cdot 10^{-3}$	$4.69 \cdot 10^{-8}$	0.0167
1 μM	$2.01 \cdot 10^4$	$3.37 \cdot 10^{-3}$	$1.68 \cdot 10^{-7}$	0.0277
2.5 μM	$5.56 \cdot 10^3$	$2.91 \cdot 10^{-3}$	$5.23 \cdot 10^{-7}$	0.0564
5 μM	$3.03 \cdot 10^3$	$2.48 \cdot 10^{-3}$	$8.17 \cdot 10^{-7}$	0.0731
10 μM	$1.45 \cdot 10^3$	$2.32 \cdot 10^{-3}$	$1.60 \cdot 10^{-6}$	0.0999
average	$2.29 \cdot 10^4$	$3.01 \cdot 10^{-3}$	$6.31 \cdot 10^{-7}$	0.0548

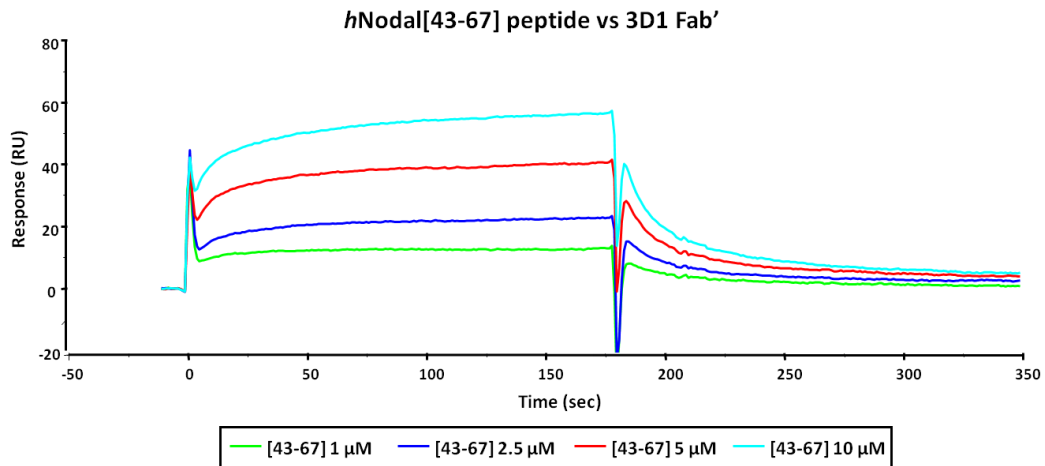


Figure 3.14B: Overlay plot of SPR sensorgrams showing the interaction between *hNodal*[43-67] peptide and 3D1 Fab' immobilized on a CM5 sensor chip. The interaction was monitored at peptide concentrations ranging between 1 and 10 μM , obtaining dose-dependent binding curves.

Table 10. Association and dissociation rate constants and K_D values determined for the binding of hNodal[43-67] peptide to 3D1 Fab' functionalized sensorchip

[43-67] vs Fab'	k_a (1/Ms)	k_d (1/s)	K_D (M)	SD
1 μ M	$5.62 \cdot 10^4$	$2.65 \cdot 10^{-3}$	$4.71 \cdot 10^{-8}$	0.018
2.5 μ M	$1.05 \cdot 10^4$	$2.67 \cdot 10^{-3}$	$2.55 \cdot 10^{-7}$	0.0449
5 μ M	$4.27 \cdot 10^3$	$2.26 \cdot 10^{-3}$	$5.29 \cdot 10^{-7}$	0.0727
10 μ M	$1.70 \cdot 10^3$	$2.60 \cdot 10^{-3}$	$1.53 \cdot 10^{-6}$	0.0338
average	$1.82 \cdot 10^4$	$2.55 \cdot 10^{-3}$	$5.90 \cdot 10^{-7}$	0.0424

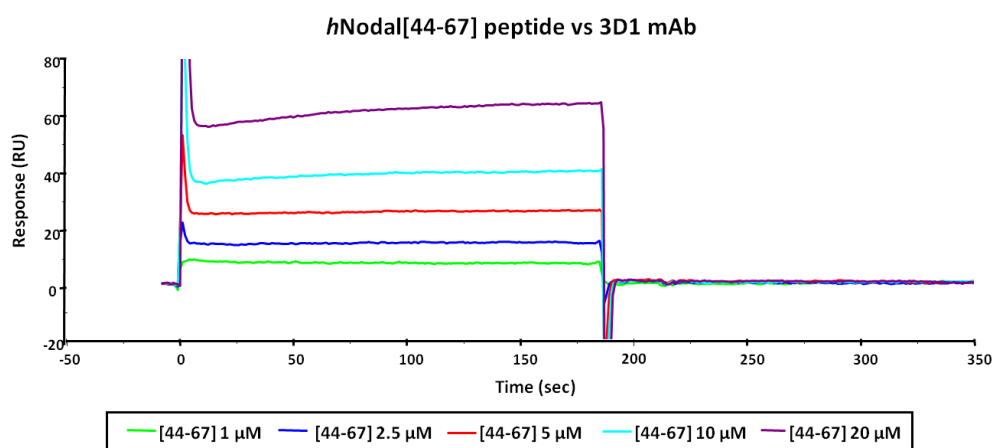


Figure 3.15A: Overlay plot of SPR sensorgrams showing the interaction between hNodal[44-67] peptide and 3D1 mAb immobilized on a CM5 sensor chip. The interaction was monitored at peptide concentrations ranging between 1 and 20 μ M, obtaining dose-dependent binding curves.

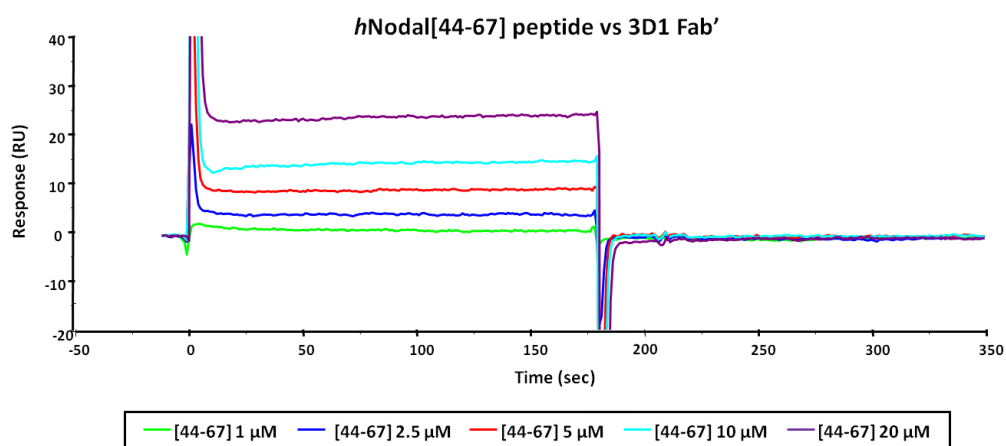


Figure 3.15B: Overlay plot of SPR sensorgrams showing the interaction between hNodal[44-67] peptide and 3D1 Fab' immobilized on a CM5 sensor chip. The interaction was monitored at peptide concentrations ranging between 1 and 20 μ M, obtaining dose-dependent binding curves.

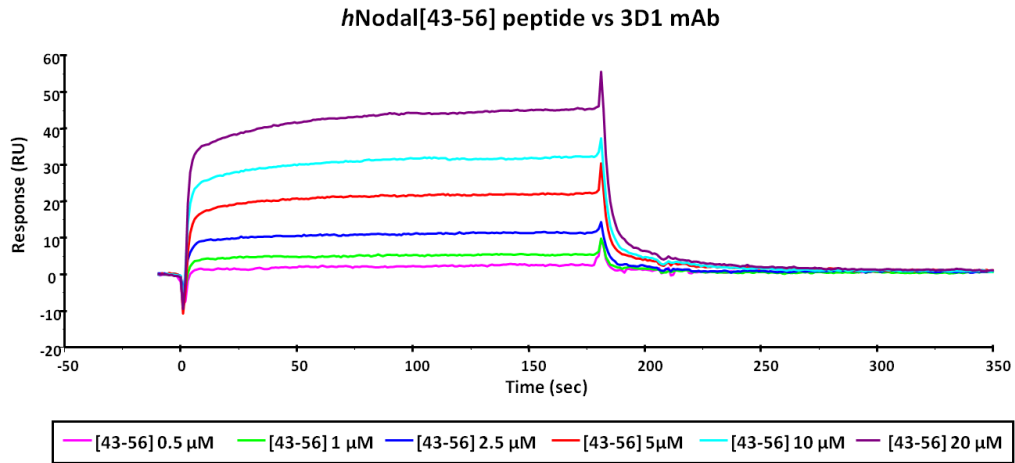


Figure 3.16A: Overlay plot of SPR sensorgrams showing the interaction between *h*Nodal[43-56] peptide and 3D1 mAb immobilized on a CM5 sensor chip. The interaction was monitored at peptide concentrations ranging from 0.5 to 20 μM, obtaining dose-dependent binding curves.

Table 11. Association and dissociation rate constants and K_D values determined for the binding of *h*Nodal[43-56] peptide to 3D1 mAb functionalized sensor chip

[43-56] vs mAb	k_a (1/Ms)	k_d (1/s)	K_D (M)	SD
0.5 μM	$2.42 \cdot 10^4$	$1.61 \cdot 10^{-3}$	$6.66 \cdot 10^{-8}$	0.0316
1 μM	$1.17 \cdot 10^5$	$1.83 \cdot 10^{-3}$	$1.57 \cdot 10^{-8}$	0.0867
2.5 μM	$2.90 \cdot 10^4$	$1.97 \cdot 10^{-3}$	$6.79 \cdot 10^{-8}$	0.152
5 μM	$6.51 \cdot 10^3$	$1.58 \cdot 10^{-3}$	$2.43 \cdot 10^{-7}$	0.0325
10 μM	$3.22 \cdot 10^3$	$1.62 \cdot 10^{-3}$	$5.04 \cdot 10^{-7}$	0.0826
20 μM	$1.21 \cdot 10^3$	$1.86 \cdot 10^{-3}$	$1.53 \cdot 10^{-6}$	0.0348
average	$3.02 \cdot 10^4$	$1.75 \cdot 10^{-3}$	$4.05 \cdot 10^{-7}$	0.07

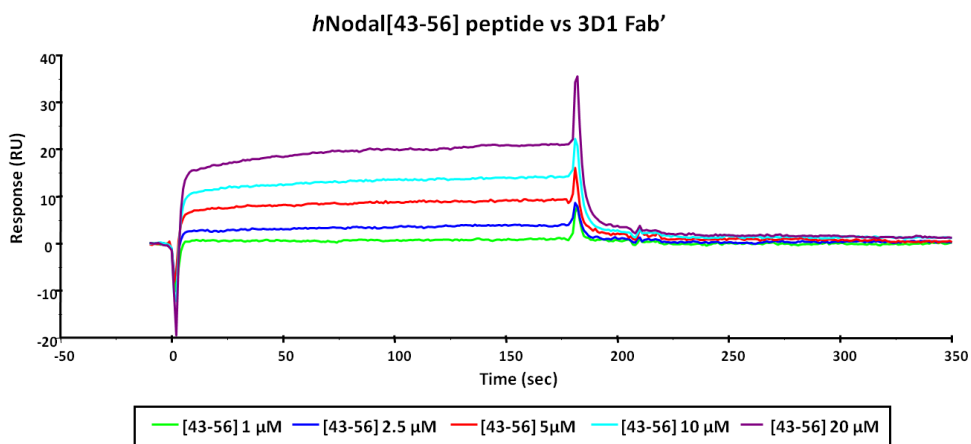


Figure 3.16B: Overlay plot of SPR sensorgrams showing the interaction between *h*Nodal[43-56] peptide and 3D1 Fab' immobilized on a CM5 sensor chip. The interaction was monitored at peptide concentrations ranging from 1 to 20 μM, obtaining dose-dependent binding curves.

Table 12. Association and dissociation rate constants and K_D values determined for the binding of *hNodal*[43-56] peptide to 3D1 Fab' functionalized sensor chip.

[43-56] vs Fab'	k_a (1/MS)	k_d (1/s)	K_D (M)	SD
5 μ M	$2.88 \cdot 10^3$	$5.36 \cdot 10^{-4}$	$1.86 \cdot 10^{-7}$	0.0325
10 μ M	$1.72 \cdot 10^3$	$5.29 \cdot 10^{-4}$	$3.08 \cdot 10^{-7}$	0.0826
20 μ M	$9.43 \cdot 10^2$	$5.85 \cdot 10^{-4}$	$6.20 \cdot 10^{-7}$	0.0348
average	$1.85 \cdot 10^3$	$5.50 \cdot 10^{-4}$	$3.71 \cdot 10^{-7}$	0.05

3.2.5 SPECIFICITY ASSAY

ELISA assays were performed to further assess the specificity of the 3D1 mAb for the region of Nodal [43-56], involved in the binding with the co-receptor Cripto. New Nodal peptides were therefore screened for binding to 3D1. These peptides came from a previous study (Saporito et al., PhD Thesis, 2009) and were: *hNodal*[1-38], mimicking the N-terminal portion, *hNodal*[39-75], mimicking the central region and *hNodal*[76-110] mimicking the C-terminal portion of the mature form of human Nodal. Other peptides mimicking the region of the TGF- β ligand GDF and matching the 43-69 region of Nodal [GDF5 and GDF6/7, see **Table 1** and **Fig. 3.2** (Multiple alignment)] were also used for this purpose. The specificity of 3D1 for Nodal was especially required given the presence of GDF ligands ^[123] in plasma and serum, and the proposed use of the antibody as diagnostic tool for detecting Nodal in human biological samples. Testing by SPR of these reagents was prevented by their poor solubility in HBS-EP buffer.

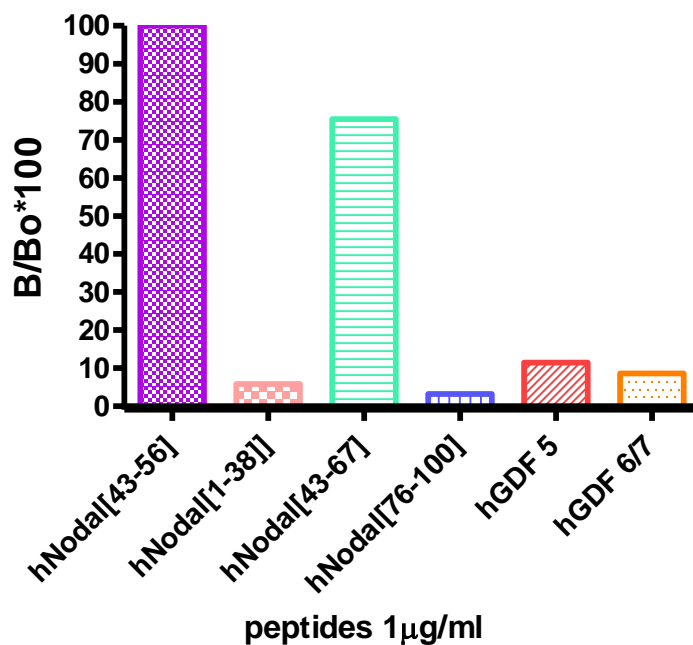


Figure 3.17: Bar graph representing the specificity of the 3D1 for the central region of human Nodal; peptides were coated at 1 µg/mL. *hNodal*[43-56] peptide was considered as 100% of signal. The signal was expressed as % of relative absorbance measured at 490nm and calculated as $B/B_0 \times 100$.

As shown in **Fig. 3.17**, only fragment [39-75] of Nodal, containing the region 43-69 used to generate the antibody, did bind with similar efficiency 3D1, whereas the other peptides were essentially unreactive. This result confirmed the selectivity of the monoclonal antibody for the Nodal epitope and the poor or no recognition with proteins sharing similar sequences.

3.3 DETECTION OF HUMAN NODAL

3.3.1 CALIBRATION CURVE FOR ELISA DETECTION OF *rh*NODAL PROTEIN

To prove the principle that 3D1 can be used as a diagnostic tool, a fluorescence ELISA assay was set up to define the lowest amount of protein detectable in human biological samples, such as serum/plasma and urine. To enhance the sensitivity, we set up a capture assay that made use the 3D1 antibody in coating and a rabbit monoclonal antibody (EP2058Y, Epitomics) for the detection. By this assay, the lowest detected quantity of *rh*Nodal, with a significative S/N ratio, was 50 pg (See **Fig.3.18**), as shown in the graph below, in which on x axis the ng of protein are reported as function of fluorescence intensity.

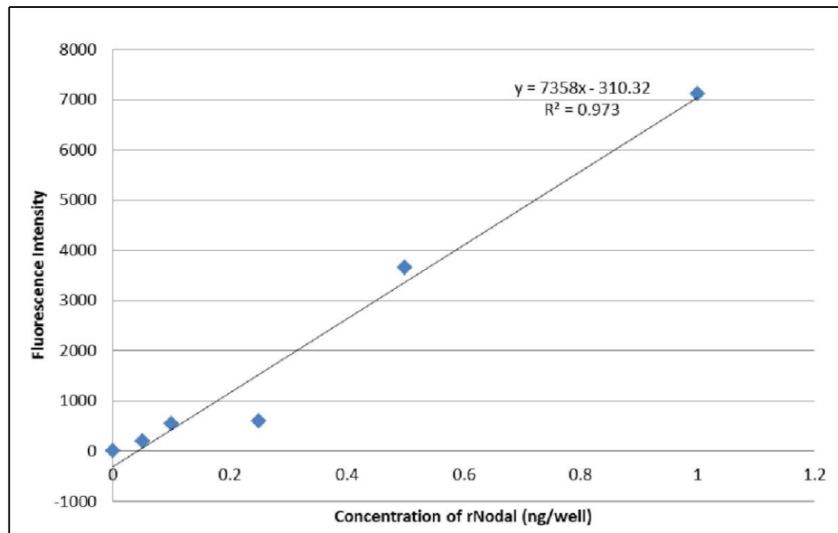


Figure 3.18: ELISA calibration curve of the detection of *rh*Nodal.

3.3.2 PRELIMINARY IMMUNOBLOT ANALYSES

A dose-response dot-blot analysis was performed to evaluate the ability of 3D1 to recognize different amounts of native *rhNodal* spotted on a PVDF membrane. This analysis was carried out to preliminarily evaluate the minimum amount of *hNodal* detectable under these conditions.

As shown in **Fig.3.19**, 3D1 could stain as less as 50 ng of protein.

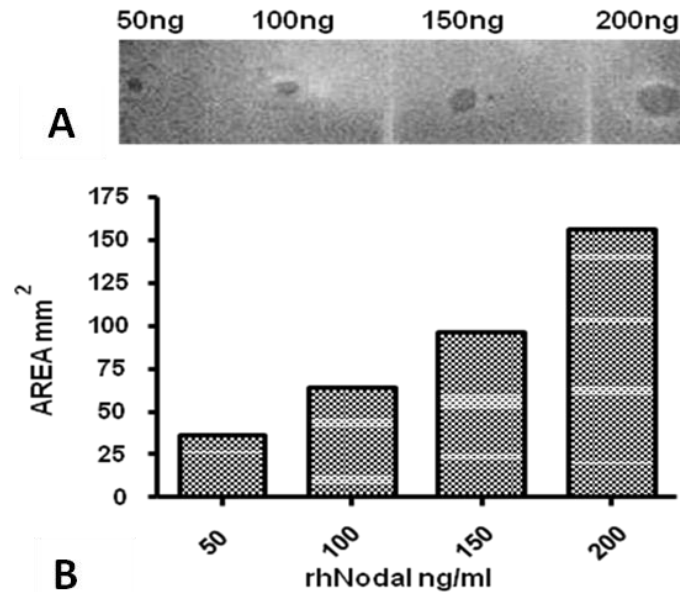


Figure 3.19: (A) Dot blot analysis on Nodal protein. Nitrocellulose membrane was spotted with Nodal at 50, 100, 150 and 200 ng, and then probed with 3D1 at 2 µg/mL. (B) Dot blot densitometric analysis.

Before performing western blot analyses to detect endogenous Nodal in cell lysates, preliminary dose-response western blot analysis was carried out to check the ability of the 3D1 to recognize the human Nodal protein under reducing and denaturing conditions. As shown in **Fig. 3.20**, 3D1 was able to detect as low as 50 ng of Nodal under these conditions.

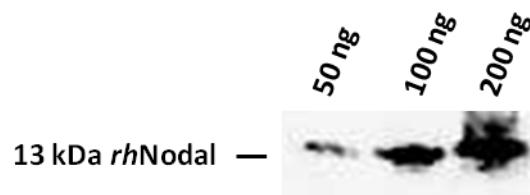


Figure 3.20: Dose-response western blot analysis probed using the 3D1 mAb; *rhNodal* was loaded at increasing concentrations 50-200 ng under reducing conditions on 15% SDS-PAGE.

3.3.3 DETECTION OF ENDOGENOUS NODAL PROTEIN

a. Western blot analysis

To evaluate the use of the 3D1 as diagnostic tool, western blotting analyses were carried out to explore the ability of the mAb to recognize the endogenous forms of Nodal protein in human melanoma cells. As shown in **Fig.3.21**, 3D1 was able to detect the immature endogenous form pro-Nodal (approximately 37 kDa) in a panel of melanoma cell lines and in non-melanoma HEK-293 cells, used as positive control. The smaller mature form of Nodal, approximately 13 kDa, is only barely detected, suggesting it is likely highly unstable and/or cleaved predominantly outside the cell.

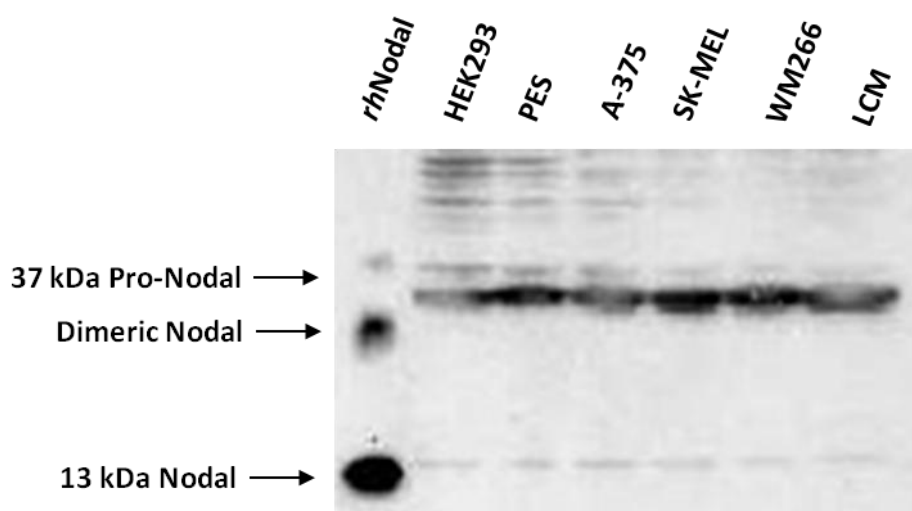


Figure 3.21: Western blot analysis of melanoma cell lysates separated by 15% SDS-PAGE under reducing conditions. As positive control HEK-293 cells and 100 ng of *rhNodal* were loaded. 3D1 antibody was used at 2 $\mu\text{g}/\text{mL}$. Detection was achieved using GAM-HRP antibody and ECL as substrate.

b. FACS analyses

The capability of the 3D1 to recognize the endogenous Nodal protein expressed in melanoma cell lines was also confirmed by cytometric analyses.

FACS analyses (**Fig. 3.22**) showed that 3D1 was able to bind to native Nodal protein (non-reducing and non denaturing conditions) also in intact cells at very low concentrations (0.1 $\mu\text{g/mL}$) and in a dose-dependent manner, as demonstrated by the increase of the signal intensity with increasing antibody concentration, indicated by the shift in fluorescence intensity to the right. However it was not possible to determine which form of Nodal protein was detected in melanoma cancer cell lines by FACS analyses, since both species were detected by the 3D1 in western blot analysis.

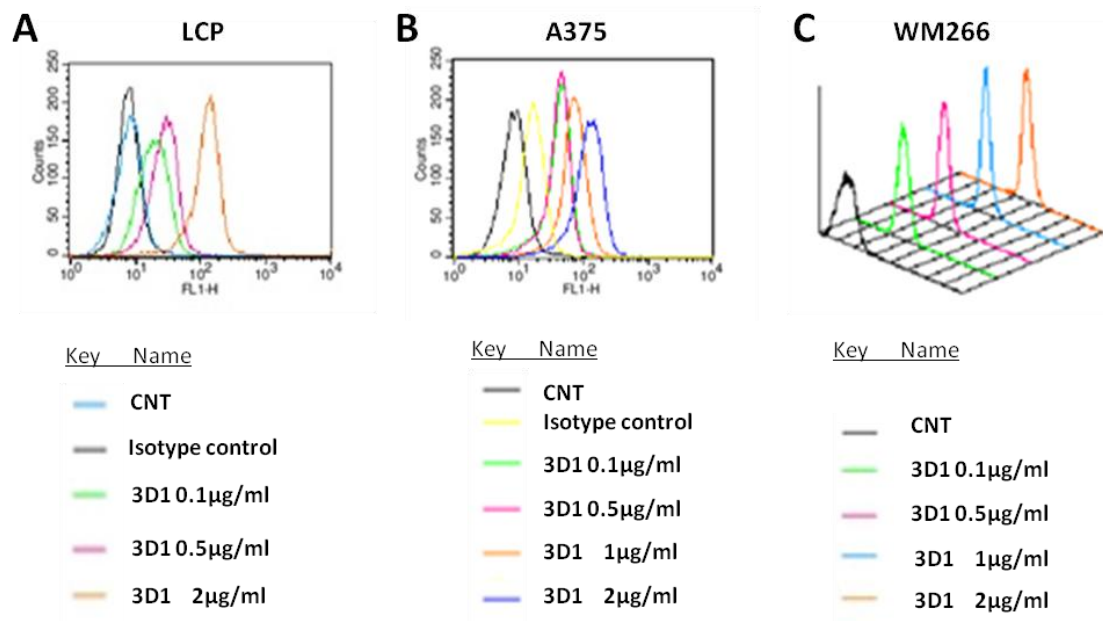


Fig. 3.22: (A, B and C) Cytofluorimetric analyses of human melanoma cell lines (LCP, A375 and WM266), after fixation and permeabilization; an isotype IgG1 antibody was used as negative control.

3.3.4 COMPETITION ASSAY BETWEEN 3D1 ANTIGEN PEPTIDE AND ENDOGENOUS NODAL PROTEIN

To confirm the specificity of the binding of the 3D1 mAb to its antigen, a competition assay between the synthetic antigen peptide and endogenous Nodal protein expressed in human embryonic stem cells was performed probing the blots either with the 3D1 alone or following pre-incubation with the *hNodal*[43-56] peptide, named here CH. As reported in **Fig.3.23**, both forms of endogenous Nodal were no longer detectable when the mAb was pre-incubated with the peptide, suggesting that 3D1 binds to the same region also on the native endogenous protein.

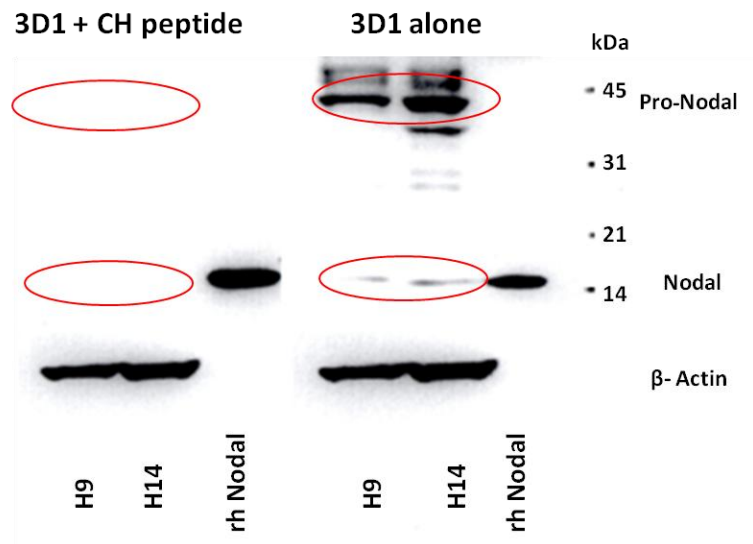


Figure 3.23: Competition assay between the CH peptide and endogenous human Nodal in human embryonic stem cells lysates. 3D1 was used at 4 μ g/mL and the CH peptide at 10 μ g/mL.

3.4 FUNCTIONAL STUDY OF THE 3D1 mAb

Functional study of the 3D1 mAb was carried out in collaboration with the group of Dr. Mary Hendrix of the Ann and Robert H Lurie's Children Hospital of Chicago.

For this study C8161 human metastatic cutaneous melanoma cells were selected as highly aggressive melanoma cell model to investigate the effects of the 3D1 antibody *in vitro* and *in vivo* on Nodal protein.

3.4.1 TARGETING NODAL IN C8161 MELANOMA CELLS *in vitro*

In order to evaluate the ability of the 3D1 anti-Nodal to act as a blocking antibody, the following functional *in vitro* assays were performed:

- a. Effects on Nodal signaling
- b. Clonogenic assay
- c. Vasculogenic mimicry assay

a. Effects on Nodal signaling

The effects of 3D1 mAb on the C8161 cells were firstly tested on the Nodal downstream signalling pathway. Cells were thus treated with the antibody at 4 µg/mL and the Smad-dependent and independent pathways (MAPKs activation) were monitored by determining the reduction of Smad and MAPK phosphorylation over time. As shown below in **Fig.3.24**, 3D1 was able to strongly and very rapidly inhibit protein phosphorylation in a very short time period (4 hours) and the effect was detectable also after three days.

These results showed that 3D1 was able to potently inhibit both Smad-dependent and Smad-independent Nodal signalling.

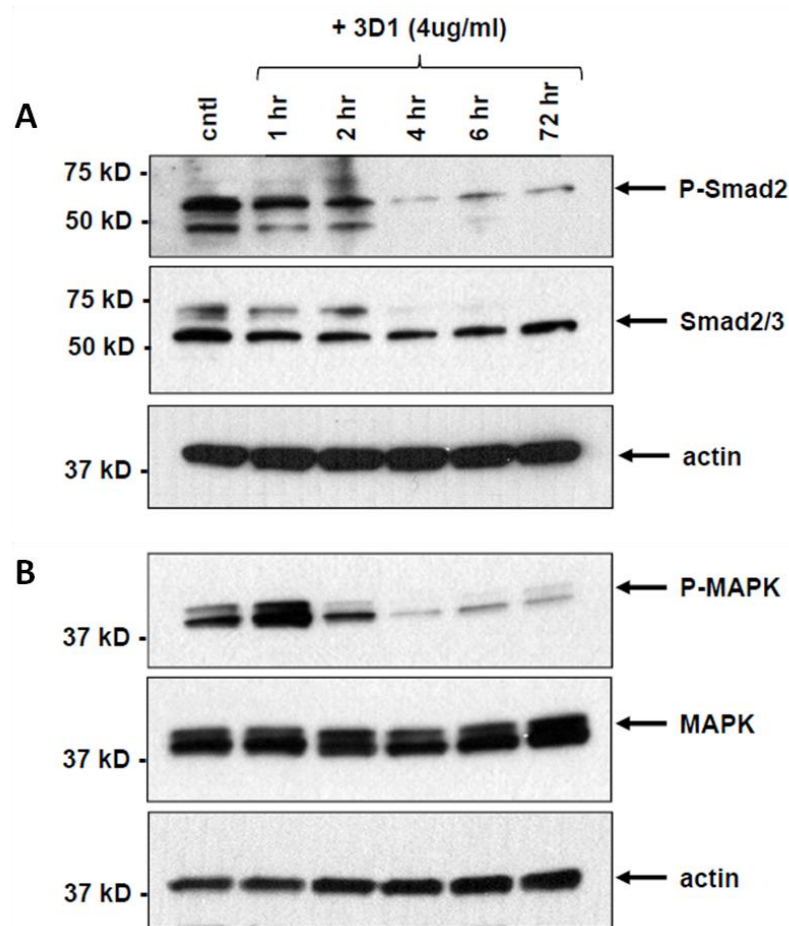


Figure 3.24: Western blot analysis of the total and activated forms of (A) Smad and (B) MAPK in C8161 cells following treatment with 3D1 mAb at 4 µg/mL.

A further relevant effect was observed on the expression of Nodal itself. C8161 cells were treated with 3D1 at 4 µg/mL and the reduction of pro-Nodal expression was monitored by western blotting. As shown in **Fig. 3.25**, 3D1 was able to reduce Nodal expression by approximately 50% at the concentration used and the reduction was similar to that achieved with a commercially available Santa Cruz anti-Nodal blocking antibody (<http://www.scbt.com/>).

Data clearly showed that 3D1 mAb was able to bind soluble Nodal protein and to inhibit its autoregulated expression and the binding to the co-receptor Cripto or to other interactors sharing the same interacting surface. This in turn inhibits the activation of Smad-dependent and Smad-independent (MAPK) Nodal pathways.

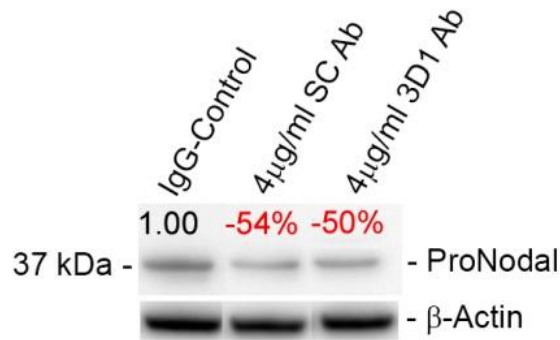


Figure 3.25: Treatment of human melanoma cell line C8161 with 3D1 anti-Nodal antibody causes a reduction of Nodal expression.

b. Clonogenic assay

Colony formation assay or clonogenic assay is an *in vitro* cell survival assay based on the ability of a single cell to grow into a colony. This assay essentially tests the ability of every cell in the population to undergo unlimited division, thus it is the method of choice to determine cell reproductive death after treatment with cytotoxic agents and can also be used to assess their effectiveness [124].

Clonogenic soft agar assay was performed to evaluate and measure the effect of 3D1 antibody treatment on the ability of the C8161 aggressive human melanoma cells to form colonies. As can be appreciate by macroscopical observation and in the bar graph of **Fig. 3.26**, C8161 showed a decrease in their ability to form non-adherent spheroidal clusters. Indeed, the 3D1, compared to an IgG used as negative control, was able to reduce the C8161 clonogenicity by approximately 60%.

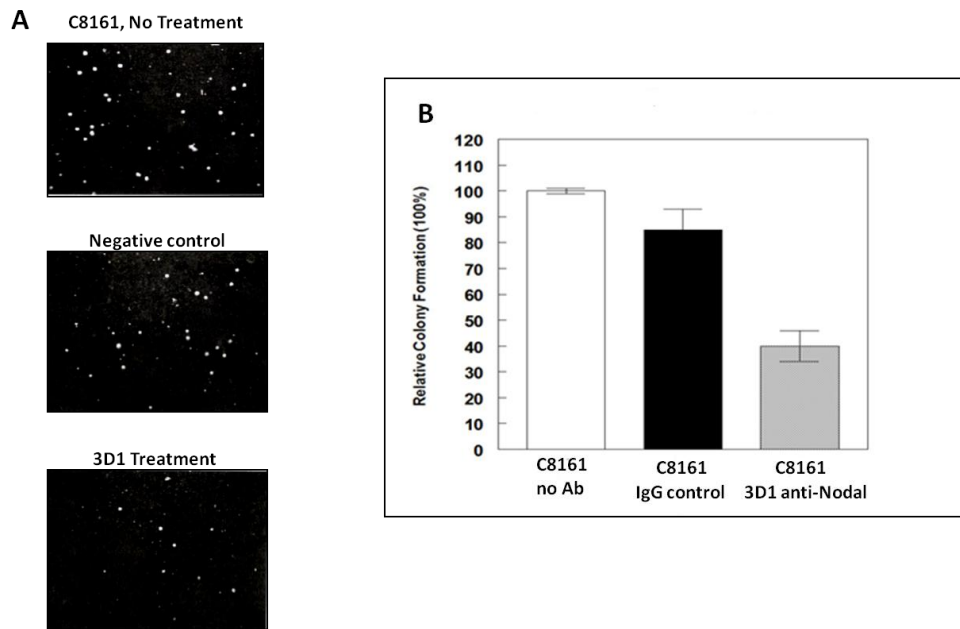


Figure 3.26: 3D1 anti-Nodal antibody affects colony formation of human melanoma cells. **(A)** A representative image of the colony forming assay for C8161 is shown ($25 \times$ final magnification). **(B)** A significant reduction in the ability of C8161 cells to form colonies in soft agar was observed using 3D1 anti-Nodal antibody $4 \mu\text{g/mL}$, compared with no antibody treatment or IgG control ($*P < 0.05$).

c. Vasculogenic mimicry inhibition

“Vasculogenic mimicry” (VM) describes the functional plasticity of aggressive cancer cells able to form *de novo* matrix-rich vascular networks in three-dimensional matrices *in vitro*, mimicking the model of the endothelial vascular networks. In this model a perfusion pathway for rapidly growing tumors and transporting fluid from leaky vessels and/or connecting with endothelial-lined vasculature was proven ^[125]. The initial morphological and molecular characterization of VM was made in human melanoma where it was found that the tumor cells co-expressed endothelial and tumor markers, and formed channels, networks and tubular structures rich in laminin, collagens IV and VI, and heparin sulfate proteoglycans, containing plasma and red blood cells - indicating a perfusion pathway for rapidly growing tumors, as well as an escape route for metastasis ^[125].

A vasculogenic mimicry assay was performed to evaluate the ability of 3D1 to inhibit or reduce the capability of the C8161 to form *de novo* matrix-rich vascular networks. As shown below, C8161 cells, treated with the 3D1 for 24

hours, did not complete the formation of networks characteristic of the vasculogenic mimicry seen in the control cells (see **Fig. 3.27**). Indeed 3D1 remarkably reduced the ability of the C8161 to engage in vasculogenic mimicry *in vitro* compared with no antibody or a non-function-blocking IgG control antibody. The effect of 3D1 was similar to that induced by a commercial polyclonal anti-Nodal antibody (Nodal Antibody (H-110) : sc-28913, Santa Cruz). Thus, 3D1 is able to reduce plasticity and invasiveness of the C8161, features that are related to the expression of Nodal protein.

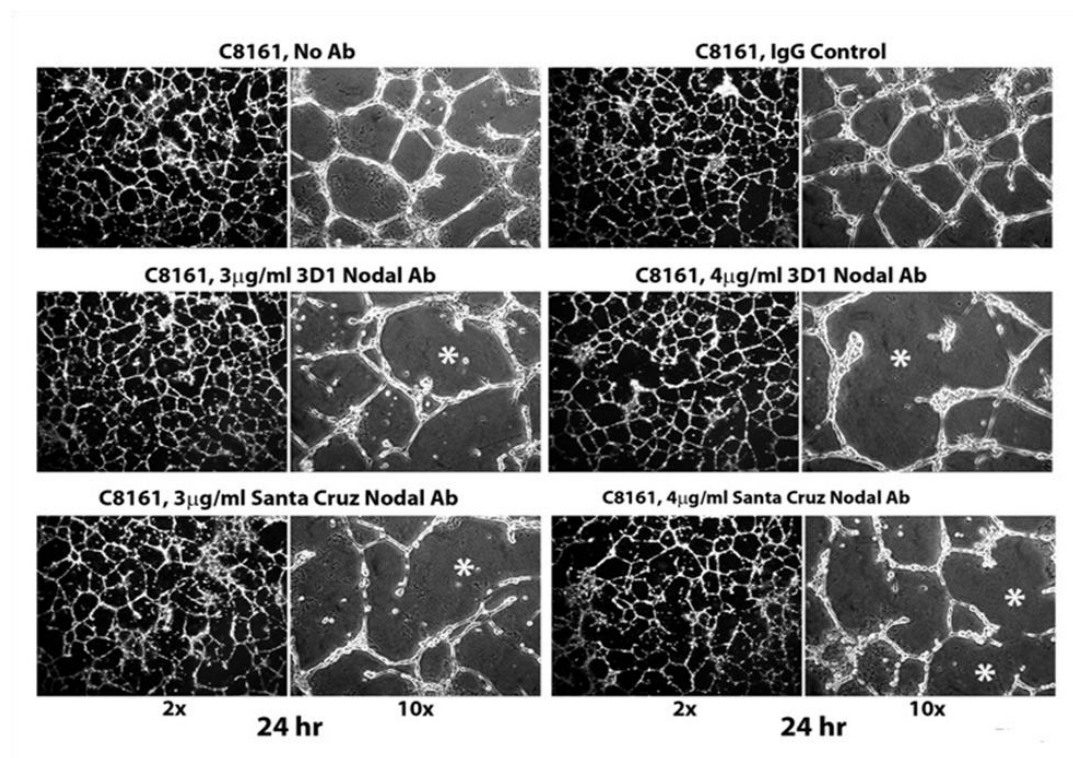


Figure 3.27: Effect of 3D1 mAb on the formation of vascular-like structures by C8161 cells. (2 x and 10 x final magnification).

3.4.2 TARGETING NODAL IN LUNG COLONIZATION INDUCED IN MICE BY C8161 MELANOMA CELLS

After evaluating the *in vitro* effectiveness of the 3D1 monoclonal antibody on C8161 cells, *in vivo* experiments were performed to assess the effects of 3D1 treatment on lung colonization induced in nude mice by injecting C8161 metastatic melanoma cells. Experiments were performed monitoring lung colonization by immunohistochemical analyses.

a. Effects on lung colonization

Histological examination of the lung tissue revealed a significant reduction in the number and size of the colonies induced by metastatic C8161 cells in the lungs of mice treated with the 3D1 anti-Nodal antibody compared to the mice treated with the control IgG antibody (See **Fig. 3.28A**). As shown in **Fig. 3.28A**, most of the lung surface area (~80) was occupied by tumor burden. By contrast, in the **Fig. 3.28B**, the presence of healthy tissue was predominant, indeed the lung tumor burden was approximately only ~10%.

This evidence showed the remarkable ability of the 3D1 to reduce lung colonization induced by metastatic cells.

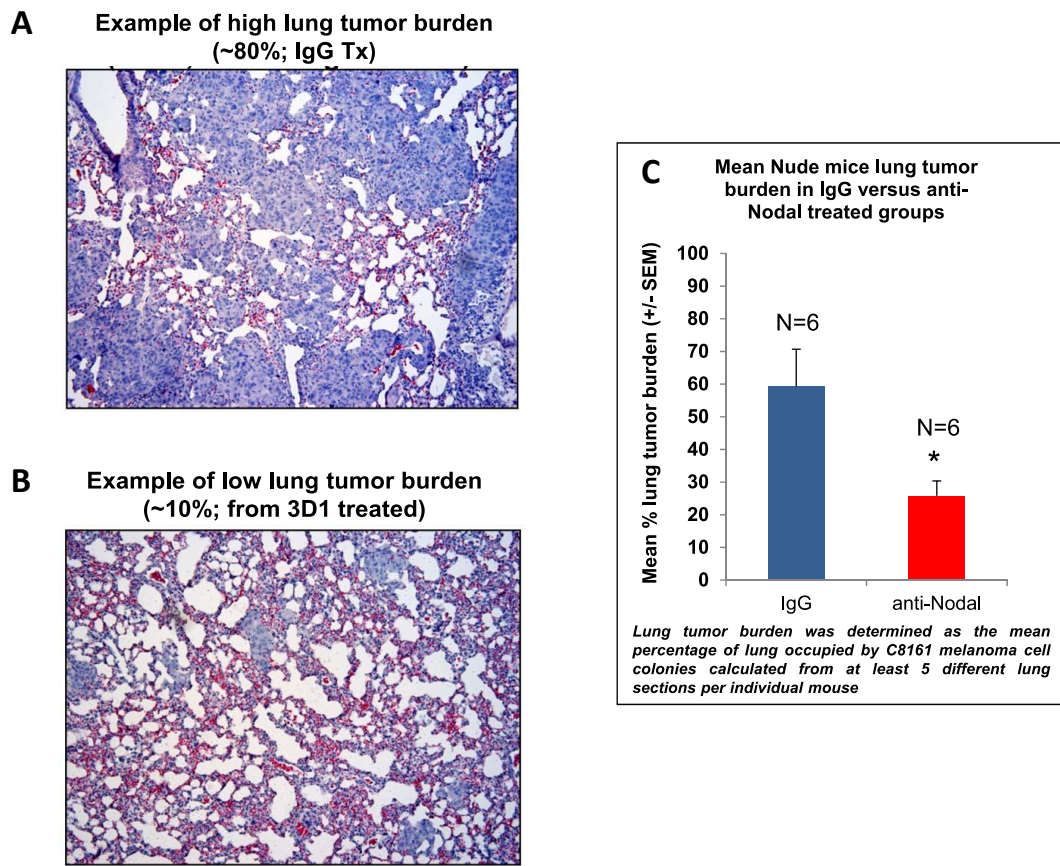


Figure 3.28: Histological examination of a lung section of Nude mice treated with (A) control IgG and (B) the 3D1 anti-Nodal mAb. (C)*Lung tumor burden was determined as the mean percentage of lung occupied by C8161 melanoma cell colonies calculated from at least 5 different lung sections per individual mouse. The effects of 3D1 treatment are expressed as Mean% tumour burden (\pm SEM).

b. Effects on the cell cycle

Immunohistochemical analysis were performed to detect Cyclin B1 and p27 expression in C8161 lung colonies in Nude mice treated with the 3D1 to evaluate the effects of the mAb on the cell cycle. Cyclin B1 is over-expressed in several cancers compared to normal cells and tissues; in most tumors the expression of cyclin B1 is unrestricted to particular phases of the cycle, whereas in normal lymphocytes, the expression of cyclin B1 is restricted to very late S and G2 + M phases of the cell cycle. The cyclin-dependent kinase (Cdk) inhibitor p27 regulates cell proliferation, cell motility and apoptosis; it blocks the entrance of the cell in S phase, binding to the cyclins. Immunohistochemical analysis of lung sections of nude mice treated with the 3D1 revealed the ability of this mAb to reduce remarkably the progression of cell cycle of cells from

mice lungs, as indicated by the reduction in Cyclin B1 staining and on the other side the increase in p27 staining (See **Fig. 3.29**).

The effects of the 3D1 mAb on Cyclin B1 and p27 expression were confirmed by *in vitro* detection of these markers of the cell cycle, carried out by western blot analysis on C8161 treated for three days with either 3D1 or control IgG (See **Fig. 3.30**).

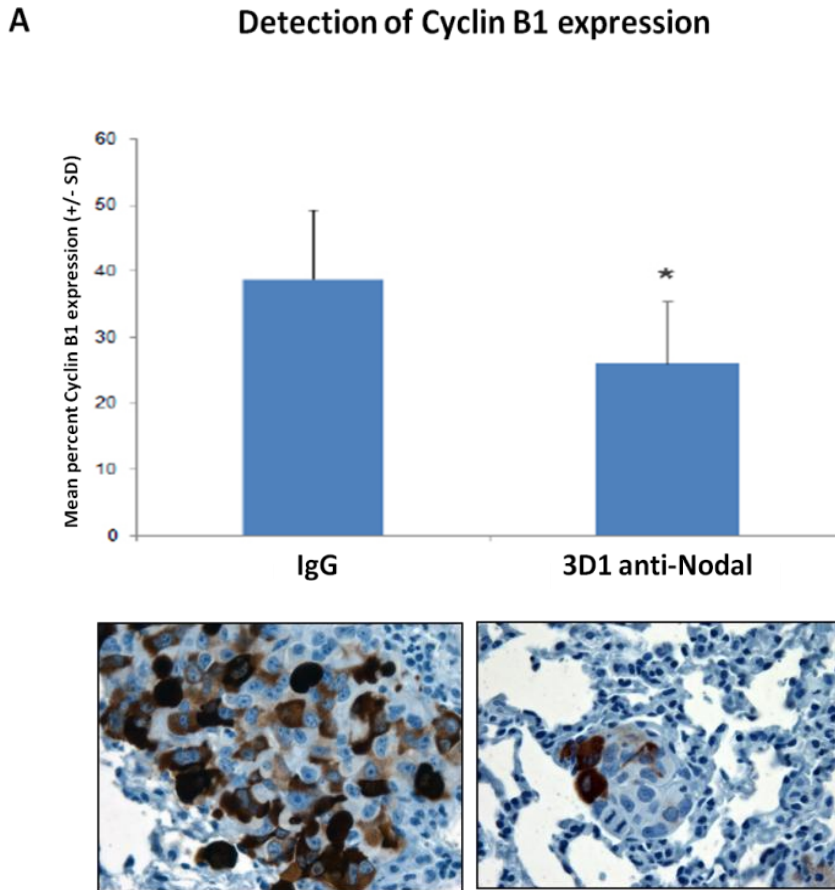


Figure 3.29A: Detection of Cyclin B1 expression by IHC in C8161 lung colonies formed in Nude mice treated with control IgG or 3D1 anti-Nodal. N = 3 mice. Cyclin B1 positive cells (brown stain) detected at high power (63X objective). Mean percent Cyclin B1 positive cells representative of 5 different C8161 lung colonies/mouse. (*P = 0.0215; t-test)

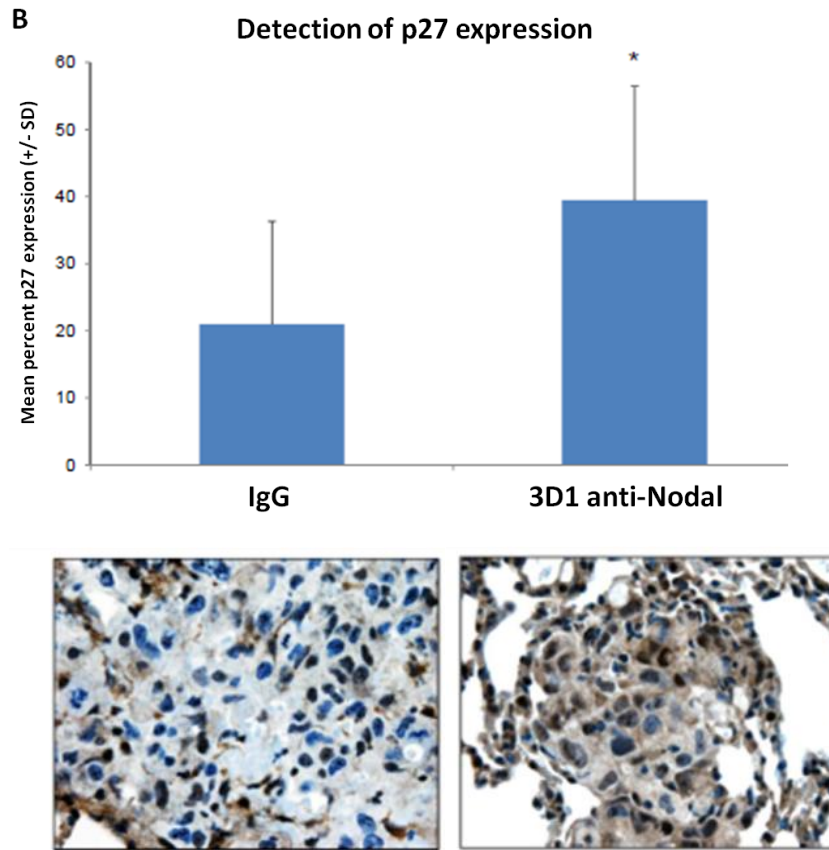


Figure 3.29B: Detection of p27 expression by IHC in C8161 lung colonies formed in Nude mice treated with control IgG or 3D1 anti-Nodal. N = 3 mice. p27 positive cells (brown stain) detected at high power (63X objective). Mean percent p27 positive cells representative of 5 different C8161 lung colonies/mouse. (*P = 0.0215; t-test)

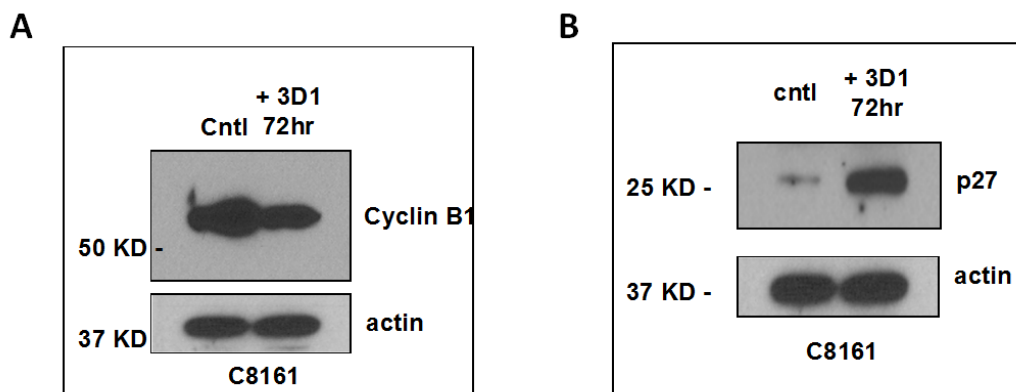


Figure 3.30: Detection of (A) Cyclin B1 and (B) p27 in C8161 melanoma cells treated for 72 hours with the 3D1 anti-Nodal antibody versus a control IgG antibody (cntl) by western blot analysis.

c. Immunohistochemical detection of P-Smad2 expression

Immunohistochemical analyses were performed on lung sections also to detect P-Smad2 expression.

As shown by the nuclear staining, a decrease in P-Smad2 expression was revealed in the sections of lungs of mice treated with the 3D1 (See **Fig.3.31**). This evidence confirmed the result obtained *in vitro* by western blot analysis performed on the C8161 cells.

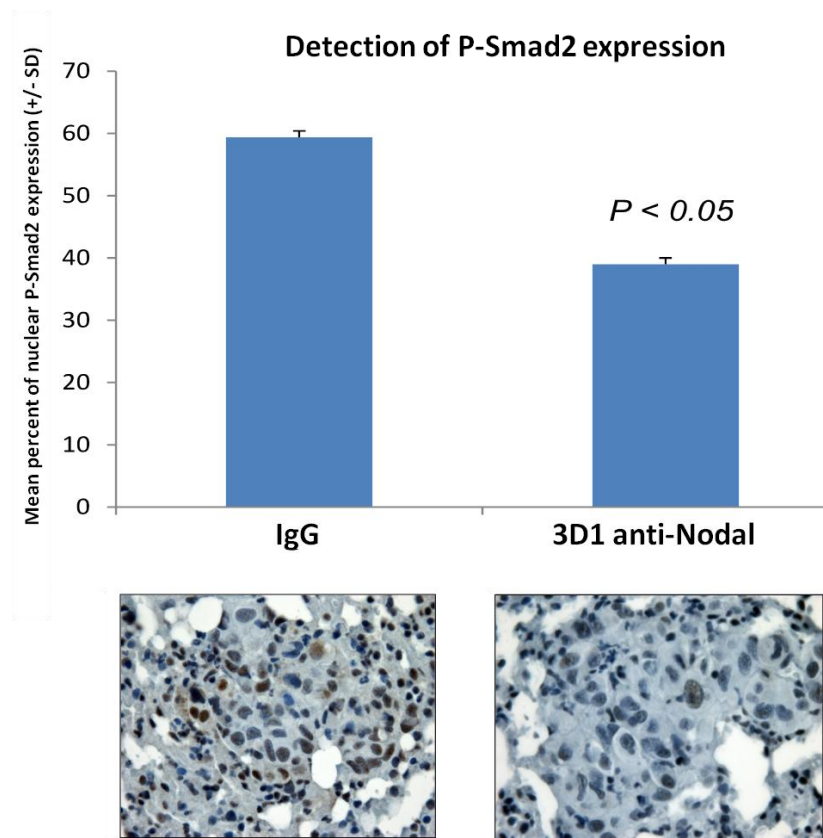


Figure 3.31: P-Smad2 staining in C8161 lung colonies formed in Nude mice treated with control IgG or 3D1 anti-Nodal. N=3 mice/group. Mean percentage of P-Smad2 nuclear staining calculated from counts obtained in 8 different fields/lung/mouse.

I 4. DISCUSSION

Nodal, a member of the TGF- β superfamily, is a potent morphogen and regulator of cell fate in both embryological and adult systems. Nodal expression is largely restricted to very early progenitor and reproductive cell types whereas it is almost absent in adult tissues and normal cells, including melanocytes. Its re-expression in the adults is strongly associated with tumorigenesis and protein levels are much higher in tumor cells and tissues where it supports uncontrolled cell growth, proliferation and differentiation. Several studies reported that Nodal expression positively correlates with melanoma tumor progression toward a metastatic phenotype; moreover, its over-expression is paralleled by that of the co-receptor Cripto-1, suggesting the occurrence of tumor growth mechanisms supported by the concomitant presence of both proteins and by their interaction with the activin receptor complex. In light of this evidence, Nodal is considered a novel diagnostic and prognostic marker other than a very important and interesting new therapeutic target. So far, no Nodal inhibitors contrasting its anti-apoptotic and tumorigenic activity have been reported. Nodal down-regulation, which blocks both Cripto-dependent and independent signalling, has been only achieved by using the antisense technology, an approach that has strongly contributed to the understanding of its functions ^[69]. We have targeted the Cripto-Nodal interaction surface in the attempt to obtain highly specific and high affinity Nodal binders, which also inhibit the interaction with Cripto. We have privileged an approach based on the generation of monoclonal antibodies, since these reagents can be quite easily obtained by the hybridoma technique, can be produced in high amount, can be easily purified and characterized by current chromatographic techniques and, most importantly, are in most cases endowed with a sufficiently high affinity and specificity for the target antigens. The target antigen has been the region 43-69 of Nodal, described as part of the interaction surface with Cripto. The mAbs have been generated using the hybridoma technique and screened following a novel, subtractive approach, whereby only those antibodies binding the wild type peptide antigen while not binding a mutated variant on specific residues, has been used to identify highly selective molecules. The mutant peptide was the one bearing E49 and E50 mutated to alanines, so as to select mAbs interacting with high specificity with

these two residues. Among those with these features, only two of them, named 3D1 and 1F10, recognized with high affinity the full-length native protein. 3D1 was chosen for further investigations by virtue of its higher affinity toward the full length Nodal (about 1.4 nM compared to about 80 nM). The antibody has been produced on large scale (multi-mg) and purified to homogeneity. The 3D1 mAb is of the IgG1 isotype. The antibody inhibited the binding of Nodal to Cripto-1, as demonstrated by competitive SPR assays and, most importantly, blocked the Nodal-dependent activation of Smad2/3 in melanoma cancer cells. Very importantly, the antibody also blocked the Cripto-independent Nodal signalling converging on the MAPKs, as demonstrated by the concomitant effective blocking of MAPK activation. This has been demonstrated in the highly aggressive human melanoma C8161 cell line in the laboratory of Prof. Hendrix at Children's Memorial Research Center of Chicago. Given the autocrine mechanism of activation of Nodal (Smad2/3 regulate through Smad4 the expression of Nodal itself), the antibody also showed the ability to reduce Nodal expression in the supernatants of C8161 cells and indeed, 3D1 at the concentration of 40 and 50 nM reduced the expression of the protein at less than a half. In addition, it was also effective in reducing the C8161 clonogenicity and the typical vasculature-like phenotype induced by Nodal (vasculogenic mimicry), both considered as the mechanisms underlying tumor growth in melanoma cells. Remarkably, 3D1 *in vivo* also showed a potent anti-tumour activity. Indeed, it strongly reduced lung colonization induced by C8161 metastatic cells, injected in mice. Altogether the 3D1 antibody has many of the features needed for developing a new biotherapeutic able to reduce plasticity and invasiveness related to the expression of the Nodal protein in cancer cells.

The antibody has been also fully sequenced on the CDR region to delineate the main structural features and to next perform sequence optimization studies aimed at further improving the affinity. Such investigations are underway together with a study to humanize the antibody, a process required for future investigations *in vivo* on human cells and on human tissues.

Moreover, immunohistochemical analyses showed the ability of the 3D1 to affect the progression of the cell cycle by reducing Cyclin B1 and concurrently increasing p27 expression.

Given the relevant prognostic meaning of Nodal levels in human tumours and in biological fluids of affected individuals, also Nodal detection is of utmost importance for the early diagnosis of Nodal-related tumours. The 3D1 mAb, in a sandwich ELISA assay, was able to detect as low as 50 pg of rhNodal therefore the antibody could be used in this biochemical assay to detect and quantify Nodal in human biological fluids, such as urine and serum/plasma because its presence and expression are a relevant predictive prognostic marker of tumor malignancy (especially in melanomas). 3D1 was finally used also in *in vitro* assays (Western Blotting and FACS analysis) to detect endogenous Nodal in melanoma cell lines.

Collectively analytical and *in vitro* and *in vivo* functional data displayed that the 3D1 is a very promising reagent useful as diagnostic tool and, hence acting as a blocking antibody, given its ability to inhibit the Nodal functions related to its tumorigenic activity, it is also a promising novel biotherapeutic agent, as a valid alternative to chemotherapeutic and immunotherapeutic agents currently employed for the treatment of the melanoma.

In addition, the process of humanization and the generation of smaller functional fragments (Fab, ScFv), together with a step of improving the affinity for the target protein (antibody maturation) will provide a unique and invaluable reagent for use in humans (alone or in combination with other drugs) for the treatment of cutaneous melanoma and other relevant cancer diseases.

STUDY II

GENERATION AND PRODUCTION OF MONOCLONAL ANTIBODIES AGAINST POLYACETYLATED APE1/Ref1 PEPTIDES

ABSTRACT

We have generated a set of monoclonal antibodies against the region 24-39 of human APE1/Ref1 protein, which is supposed to be multiple acetylated on lysines 27, 31, 32 and 35. In order to obtain mono- or multi-acetylated-APE1 specific antibodies, we have immunized mice with a peptides library, containing 16 different peptide antigens corresponding to all combinations of acetylated lysines and, after mAbs generation, we have screened the resulting clones to select those producing acetylation-specific mAbs. The screening, performed by ELISA, using isolated mono-, di-, tri-, and tetracetylated peptides, allowed to isolate four mAbs that bound with very high affinity and specificity to the acetylated peptides, while not recognizing the non acetylated variant. All selected antibodies displayed a poor selectivity against the differently acetylated peptides, being able to only discriminate between mono-acetylated/di-acetylated/tri-acetylated and tetracetylated variants. Furthermore, all selected mAbs were able to specifically recognize the acetylated form of the human APE1 protein, as revealed by Western blot analysis, while no detection was observed with the non-acetylated form and others acetylated proteins.

II 1. INTRODUCTION

The introduction of Post-Translational Modifications (PTM) in proteins is a major mechanism for regulating their function, localization, stability, immunogenicity and other relevant properties. Among these, acetylation of the ϵ NH₂ of selected lysines, a process regulated by a fine balance between acetylases and de-acetylases, is one of the most important, playing a role, among the others, in protein-DNA binding, in secondary or higher structures modification and sub-cellular localization. Detecting acetylated lysines in specific proteins or sets of proteins is thereby a major goal for investigating the interplay between the occurrence of PTMs and cell biology. Several very robust tools for studying protein acetylation are in the hands of biochemists and cell biologists, including mass spectrometry ^[126] and batteries of highly specific monoclonal antibodies, which allow the detection of either any acetylated lysine or acetylated lysines embedded in specific protein sequences ^[127]. Detecting multiple acetylations (di-, tri- or even tetra-acetylations) within short lysine-rich protein stretches is however still a challenging task, because of the occurrence of highly similar structures with identical molecular mass differences. Only very sensitive approaches of tandem mass spectrometry can help to address/unravel this issue. Antibodies, on the other hand, are extremely specific and sensitive reagents able to recognize in a highly specific manner small as well as large macromolecules, and are also able to distinguish among very subtle molecular differences.

1.1 HUMAN APURINIC/APYRIMIDINIC ENDONUCLEASE 1

Apurinic/apyrimidinic endonuclease 1 (APE1), also known as redox effector factor-1 (Ref-1), is a multifunctional and essential protein in mammals, acting as a key regulator of cellular responses to oxidative stress (redox signalling) and contributing to the maintenance of genome stability ^[128-130].

The human APE1 is a protein of 318 amino acids with a molecular mass of approximately 35 kDa (Uniprot P27695); structural investigations revealed that the first 42 amino acids are disordered, while the remainder of the protein has a globular fold ^[131,132].

Human APE1 exerts its two most important biological activities, redox and repair, through two functionally distinct protein domains, the N-terminal and the C-terminal, that act independently each other^[133-135]. In fact, the non-structured N-terminal domain (residues 1–127), containing the nuclear localization signal (NLS) sequence, is essential for the redox activity of APE1, whereas the C-terminal domain (residues 61–318) is essential for the DNA base excision repair (BER) activity^[136].

A third APE1 function, which is regulated by Lys6/Lys7 acetylation^[137], is its transcriptional repressor activity through indirect binding to the negative Ca²⁺-response elements (nCaRE)^[138] of some promoters (i.e., PTH and APE1 promoters).

Furthermore, recent evidences highlighted a novel role for APE1 in RNA metabolism, which is modulated by nucleophosmin 1 (NPM1), thus suggesting the importance of unstructured N-terminal domain of APE1 as a flexible part of protein able to establish protein–protein interaction. The first 35 amino acids in the non-structured N-terminal domain of APE1 are required to stabilize interaction with rRNA, NPM1 and other proteins involved in ribosome biogenesis and RNA processing^[139,140] including pre-mRNA maturation/splicing and ribonucleotide catabolism. Moreover, the NPM1-APE1 interaction seems to modulate the APE1 subnuclear cellular localization^[141].

In different mammalian cell types, APE1 is mainly a nuclear protein, however, it has been reported that it is even localized into cytoplasm, mitochondria and endoplasmic reticulum^[142]. Nuclear localization of APE1, controlled by the first 20 amino acids at the N-terminal sequence^[143], is correlated with its functions in DNA repair, while cytoplasmic localization may correspond to its role in mitochondrial DNA repair or redox regulation of newly synthesized transcription factors^[144].

Interestingly, cytoplasmic expression of APE1 has been correlated with aggressiveness of different tumors^[142,144], although its role in tumorigenic processes is fully unknown.

In addition, the expression of APE1 is cell cycle dependent and the highest level of APE1 is detectable in early or middle S-phase, suggesting a particular function of APE1 in this phase of the cell cycle^[145].

1.2 REGULATION OF THE ACETYLATION STATUS

It is well established that APE1 K6/K7 may undergo acetylation during cell response to genotoxic treatment ^[146] and that the acetylation status of these K residues, controlled by the sirtuin 1 (SIRT1) deacetylase activity, may play a key role in modulating protein DNA-repair function by regulating the kinetics of its interaction with other enzymes involved in BER.

Recent studies revealed that five lysine residues K24/K25/K27/K31/K32, probably acquired during evolution, located in the region 24–35 of the unstructured human APE1 N-terminal domain, are crucial for APE1 interaction with rRNA and NPM1 and/or different protein partners and for modulation of its catalytic activity on abasic DNA through regulation of product binding. Of interest, some of these critical amino acids (K27/K31/K32 and K35) may undergo *in vivo* acetylation under basal conditions ^[147], therefore, within cells, APE1 is present with different degrees of acetylation on the above mentioned lysine residues (Ac-APE1). Since the acetylation at K27/K31/K32/K35 residues may favour a transition toward a more organized conformation, this modification may significantly modulate the interaction with several protein partners on a structural basis ^[123].

Degree of positive charges, modified by acetylation at these residues, may modulate Different functions of APE1 can be modulated by the degree of positive charges through its redirection to different substrates and/or stimulation of its DNA-repair enzymatic activity ^[141], indeed, protein–protein interactions and/or posttranslational modifications (PTMs) involving the APE1 N-terminal domain may play important roles *in vivo* in coordinating the protein's BER activity and functions on rRNA metabolism. In particular the positively charged residues located in the portion 23–33 of the enzymatic domain plays an active role in APE1 catalysis.

Interestingly, genotoxic stress promotes the acetylated APE1 form, more active than the non-acetylated one, is predominant, this is probably due to a decrease in affinity for the incised DNA product. Acetylation, in turn, may inhibit binding to RNA substrates thus, possibly, this PTM may change the equilibrium of the APE1 pool from the RNA-bound to the DNA-bound substrates ^[147].

Moreover, acetylation may also control compartmentalization of APE1 within specific subnuclear structures (such as nucleoli), where the enzyme could be

stored once bound to interacting partners as NPM1. Whether NPM1 may specifically participate in DNA repair inside of nucleoli, or even outside of the subnuclear condensed area, is currently unknown. In the first case, the genome containing rRNA gene may be a favoured substrate for APE1 *in vivo*; on the other hand, if the latter is the case, stimuli triggering NPM1 to get out of nucleoli may affect the cell response in terms of APE1 impact on genome stability. Because the protein's N-terminus is required for the stabilization of APE1 interaction with NPM1 or rRNA and for the control of the overall endonuclease activity^[147], this region-specific multitasking function can provide a “trigger” for molecular regulation with important biological significance .

In addition, the acetylation at K27/K31/K32 and K35 residues may significantly affect APE1 protein stability, since such K residues can be also polyubiquitinated by UBR3, targeting the protein for degradation by the proteasome^[148]. Indeed, since acetylation competes with ubiquitination for the same K residues, it may represent the switch for controlling protein turnover rate. In this context, the acetylation at these residues during cell response to genotoxicants may stabilize protein half-life, thus preventing its degradation. Remarkably, the acetylation status of these lysine residues is still not well understood, as indeed multiple/single specific modifications may occur depending on the cell metabolic status and on the presence/absence of different stimuli. While the occurrence of one or more acetylations can be easily monitored using non-specific pan-acetyl antibodies (Rabbit Anti-Acetyl Lysine Polyclonal Antibody Cat. # AB3879, Millipore) the exact array of acetylated/free lysines in a specific stretch of aminoacids is instead a much more difficult task and implies several steps of protein isolation, digestion by specific proteases and fine mapping of modified residues by tandem mass spectrometry.

1.3 AIM OF THE PROJECT

Given the crucial role played by APE1 acetylation on its multiple functions and the importance to understand which lysine is acetylated under specific conditions, we sought to obtain monoclonal antibodies specific for the region of APE1 spanning residues 24-39 and able to discriminate among the differently acetylated variants. The final goal was to generate an array of mAbs able to discriminate the differently acetylated forms of the 24-39 APE1/Ref1 region. The array of mAbs should contain at least one antibody specific for any given sub-structure (or group of substructures, for example the singly monoacetylated variants, or the differently di-acetylated variants and so on), so that we could use them in western blotting experiments on cell extracts to identify which lysine is acetylated and which is not under specific stimulation conditions. To try to achieve this goal, we have generated a library of peptides containing all acetylated combinations of mono-, di-, tri- and tetra-acetylated variants on lysines 27, 31, 32 and 35 (16 different peptides) of the 24-39 segment of APE1/Ref1. The pool of peptides has been used to immunize mice and to generate monoclonal antibodies by the hybridoma technique. mAbs have been then screened to select those recognising specific peptide variants while not binding to the others. The screening has been performed by ELISA using fractionated small pools of peptides, identified and characterized by mass spectrometry and subsequently by a number of different techniques.

II 2. MATERIALS AND METHODS

2.1 MATERIALS

All protected amino acids and resins for peptide synthesis were from either Novabiochem (Laufelfingen, Switzerland) or from GL Biochem (Shanghai, PRC). Fmoc-L-Lys(Ac)-OH was from Bachem (Bubendorf, Switzerland). Solvents for peptide synthesis and purification were from LabScan (Dublin, Ireland). Other reagents for peptide synthesis, Bovine Serum Albumin (BSA), Keyhole Limpet Hemocyanin (KLH), Ovalbumin (OVA) and glutaraldehyde were from Sigma-Aldrich (Milano, Italy). Preparative RP-HPLC were performed out on a Shimadzu LC-8A, equipped with a SPD-M10 AV detector and with a ONYX monolithic C18 column (100 x 10 mm ID), Phenomenex, Torrance, CA, USA). The anti-Acetyl Lysine Polyclonal Antibody (ALPA) was from Millipore (Cat. # AB3879). All media for cell culture were from Sigma-Aldrich (Milan, Italy). The RPMI 1640 medium, containing 10% Fetal Bovine Serum (FBS) and 1% Penicillin, Streptomycin and Glutamine (PSG) was used for maintaining myeloma cells. The RPMI-GM medium contained RPMI 1640 with added 1% non-essential amino acids (NEAA). For the fusion of splenocytes and myeloma cells we used an RPMI 1640 medium supplemented with 15% FBS, 2% HAT (Hypoxanthine-Aminoipterine-Thymine), 1% PSG and 10% HES (Hybridoma enhancing supplement). The medium for clone selection was RPMI 1640 supplemented with 15% FBS, 2% HAT, 1% PSG. ELISA data were fitted using the software GraphPad Prism 4, ver. 4.02 (GraphPad Software, San Diego, CA, USA).

2.2 PEPTIDE SYNTHESIS, PURIFICATION AND IDENTIFICATION

Antibodies were raised against the 24-39 region of APE1/Ref1, which recently is supposed to be acetylated. Since no direct evidences of which lysine is acetylated within the protein and to also exploit this molecular system to implement a novel mAb generation and screening procedure, we designed and prepared a mixture of 16 synthetic peptides containing all combination of sequences, whereby lys 27, 31,32 and 35 as potentially acetylated are either acetylated or non-acetylated (2^4 combinations).

The peptide mixture can be described by the following single-letter code sequence: KKSK*TAAK*K*NDK*EAAG, where K* stands for an acetylated or non-acetylated lysine. Peptides were all C-terminally amidated. Two lysines, (which are casually located in APE1/Ref1 sequence) were inserted on the N-terminus to have three additional amino groups, which strongly reduce the likelihood of glutaraldehyde conjugation on internal functional lysines.

The peptide mixture was manually prepared by Fmoc chemical synthesis by the solid phase method using a RINK amide resin having a 0.57 mmol/g substitution. The synthesis scale was 0.05 mmoles. Canonical coupling and deprotection conditions were used to incorporate amino acids into the sequence, using a 5-fold excess of protected residues (0.25 mmoles). To generate mixtures, in correspondence of K27, K31, K32, and K35, an equimolar mixture of Fmoc-L-Lys(Boc)-OH and Fmoc-L-Lys(Ac)-OH was used, preactivating the mixture as for the other residues. Synthesis progression was tightly monitored during chain assembly by removing small resin aliquots and characterizing the products by LC-MS, thus assessing identity and distribution of the expected peptides. These analytical controls were carried out after incorporation of the first Lys/Lys(Ac) incorporation (2 compounds generated), the second Lys/Lys(Ac) incorporation (4 compounds generated), the third Lys/Lys(Ac) incorporation (8 compounds generated) and the fourth Lys/Lys(Ac) incorporation (16 compounds generated). These analyses also allowed the determination of relative distribution of compounds within the mixtures, by integrating and comparing peak areas from UV traces at 214 nm of chromatographically resolved peaks. For complex mixtures where not all peaks were chromatographically resolved, the relative distribution of compounds was achieved by integrating peaks obtained by extracted ions in TIC (Total Ion Current) chromatograms. After synthesis completion, peptides were removed from the solid phase using a TFA-TIS-H₂O mixture (90:2.5:2.5, v:v:v), precipitated in cold diethyl ether and lyophilized. To remove salts deriving from the cleavage procedure, a 10 mg aliquot of the crude material was loaded on a C18 100x10 mm ID monolithic column equilibrated at 0.5% CH₃CN in H₂O, 0.1% TFA. After 10 column volume washes with the same solvent at 10 mL/min, the material was eluted by changing the solvent to 95% CH₃CN in H₂O, 0.1% TFA, collected in a single fraction and lyophilized. This material was used for conjugation to KLH.

Another aliquot of the same material was fractionated by preparative RP-HPLC using the same column. For this purpose, a 14.0 mg aliquot of the crude peptide mixture was dissolved in 2% CH₃CN in H₂O, 0.1% TFA (2.0 mL) and injected onto a column equilibrated with the same solvent at 20 mL/min. A gradient from 2% CH₃CN in H₂O, 0.1% TFA to 30% CH₃CN in H₂O, 0.1% TFA in 8 minutes was applied to separate the components, monitoring the eluate at 214 nm. 16 fractions (#1 - #16) of 10 mL were manually collected every 0.5 minutes. Isolated fractions were lyophilized and characterized by LC-MS using an LCQ XP ESI ion trap mass spectrometer (ThermoFisher, Milan, Italy) coupled to a Surveyor HPLC system, equipped with a C18 Biobasic 50x2 mm ID, operating at 0.25 mL/min. Typical gradients were from 1% CH₃CN in H₂O, 0.1% TFA to 30% CH₃CN in H₂O, 0.1% TFA. Mass spectra were acquired in the positive ion mode between m/z 200 and 2000 with the source maintained at 4.0 kV and 300 °C. Spectra were also acquired by direct infusion at 1 µL/min using a HCT Ultra ion trap mass spectrometer (Bruker Daltonics, Macerata, Italy), equipped with a nanoESI source maintained at 4.8 kV and 250 °C. Typical spectra were recorded between m/z 200 and 2800 in the positive ion mode. Four single peptides of sequence KSKTAAKKNDKEAAG, monoacetylated on either K27, K31, K32, or K35, were prepared in a similar way by solid phase synthesis, purified to homogeneity by RP-HPLC as described for library fractionation, and characterized by LC-MS. The library of c-Myc[119-161] derived acetylated peptides and the acetylated cyclized peptide (termed N_1-13) were prepared as already described.

2.3 GENERATION AND PRODUCTION OF ANTI-Ac-APE1/Ref1[24-39] mAbs

2.3.1 Antigen preparation: conjugation of antigen peptide to KLH and BSA

Conjugation reactions were performed mixing 1.0 mg peptide material with 3.0 mg carrier protein in 1.0 mL PBS containing 0.2% v/v glutaraldehyde in water. Mixtures were left under stirring for 3h, then 1.0 mL of 1.0 M glycine in water was added and reactions left at room temperature (RT) for 1h. At the end, solutions were extensively dialyzed against PBS buffer, pH 7.3 and lyophilized. The amount of peptide-protein conjugate was determined by the method of

Bradford. The desalted peptide mixture was conjugated to KLH using glutaraldehyde and used to prepare the immunogen.

A mixture of fractions #4 through #8 (thus excluding the non acetylated peptide, present only in fraction #1) was prepared by mixing identical amounts (0.2 mg) from each fraction. This mixture was subsequently conjugated to BSA as described above and named Ac-APE1/Ref1[24-39]-BSA. The isolated fractions #1, #4, #5, #6, #7, and #8 were also conjugated under the same conditions to BSA. BSA-conjugated fraction #1 was named APE1/Ref1[24-39]-BSA. Ac-APE1/Ref1[24-39]-BSA and APE1/Ref1[24-39]-BSA were used to monitor immunization progression and to perform the first step of hybridoma screening. c-Myc peptides described in the previous section, were conjugated to BSA under identical experimental conditions and used as control in several ELISA experiments. Glutaraldehyde self-conjugated BSA (BSA₂) was prepared in a similar way, omitting the peptide solution. This reagent was used as control in all ELISA tests to exclude those clones producing antibodies binding the BSA-linked glutaraldehyde or glutaraldehyde alone.

2.3.2 Immunogen preparation

The immunogen was prepared by mixing 500 µL of KLH-conjugated desalted peptide mixture at 4.0 mg/mL in PBS with 500 µL of complete TiterMax Gold Adjuvant (Sigma-Aldrich, Milano, Italy). Mixing was achieved using a 3-way valve connected with two syringes, one filled with the conjugate and the other filled with the adjuvant and allowing the aqueous solution to flow within the oily adjuvant solution.

2.3.3 Mice immunization

Two 5-week old Balb/c mice (from Jackson Lab) were immunized with 50 µL of suspension containing about 100 µg of adjuvant emulsified KLH-conjugated peptide mixtures. Two independent injections were carried out sub-cutaneously with 25 µL immunogen. Before immunization, 250 µL blood samples were taken from each mouse from the caudal vein and used as the pre-immune control (T₀ samples). Mice were again immunized with the same amount of immunogen at day 30 after the first immunization (T = 30d), at day 40 (T = 40d) and at day 60 (T = 60d), and blood samples were taken from the caudal vein (250 µL)

before every subsequent immunization and tested by ELISA assay to monitor the increase of antibody titer compared to the pre-immune serum (see the section on details for the ELISA assays). Mice showing the highest antibody titer were sacrificed and splenectomised.

2.3.4 Fusion of myeloma cells and mice splenocytes to generate hybridomas

The 2 mice showing the highest titer of specific antibodies against the peptide mixture, were sacrificed by cervical disarticulation and splenectomised, placing the spleens in a 50 mL tube containing 10 mL of RPMI-GM medium (Sigma-Aldrich, Milano, Italy) pre-warmed at 37 °C. Spleens were then moved to 100 mm plates containing 10 mL of RPMI-GM medium and grinded using a cell filter (BD-Falcon, Milano, Italy). The resulting suspensions were centrifuged at 800 rpm for 5 minutes at RT, removing the supernatants, then cells were suspended in 5 mL of RPMI-GM and counted in the presence of 0.4% Trypan Blue (Sigma-Aldrich, Milano, Italy) to exclude dead cells. To perform cell fusion, 1/5 of splenocytes in 10 mL RPMI-GM were mixed with 4/5 of SP2/0 myeloma cells in 5 mL RPMI-GM (ATCC), then 15 mL of RPMI-GM were further added. Cells were spun at 600 rpm for 5 minutes at RT. After discarding the supernatant, 1 mL of RPMI-GM containing PEG 1300-1600 (Hybri-Max, Sigma-Aldrich, Milano, Italy) and 75 µL DMSO (Sigma-Aldrich, Milano, Italy) were added. Cell pellets were gently disrupted with a pipette tip, adding at the same time 9 mL of RPMI-GM supplemented with 10% FBS. Cells were then centrifuged at 500 rpm for 7 minutes at RT, then the pellet was re-suspended in 200 mL of RPMI-HAT medium and cells seeded in twenty 96-well plates and incubated for at least 10 days at 37 °C under 5% CO₂. After about 2 weeks, supernatants were assayed by ELISA using plates coated with both Ac-APE1/Ref1[24-39]-BSA and APE1/Ref1[24-39]-BSA to detect the presence of antibodies against either the pool of acetylated peptides or the non acetylated variant, operating as described in the previous section.

The most reactive clones, were isolated, sub-cloned by limited dilution and re-tested by ELISA. By this step, 8 clones lost the productivity; the remaining clones were submitted to a stabilization process.

2.3.5 Clone stabilization and adaptation

Clones were stabilized by 3 sequential rounds of cloning performed by the method of limited dilution. At every round, cells were counted and diluted up to about 3 cells/mL; 20 mL of this solution were plated in two 96-well plates, dispensing 100 μ L/well, thus reaching about 0.3 cells/well. Cells were incubated for 2 weeks at 37 °C under 5% CO₂, then supernatants from each well were again tested for the presence of antibodies against the peptide antigen. Supernatants showing the highest antibody titer were isolated and again cloned thrice by limited dilution, always testing by ELISA the presence of specific antibodies.

To obtain secreted monoclonal antibodies in absence of serum-derived bovine antibodies, selected clones were adapted to grow in serum-free medium. To this end, the medium was first changed to OPTIMEM (Sigma-Aldrich, Milano, Italy) supplemented with 10% FBS, then FBS was progressively reduced and finally eliminated over a time period of about 4 weeks. Productivity was always monitored by ELISA assays.

2.4 ELISA ASSAYS

Titer increase of anti-peptide specific antibodies was monitored by ELISA assays performed by coating both Ac-APE1/Ref1[24-39]-BSA and APE1/Ref1[24-39]-BSA on 96-well plates (Immunoplate, NUNC Maxisorp.). Coating was performed dispensing 100 μ L of 1 μ g/mL solutions of BSA-conjugated antigens in PBS and incubating the plate over night at 4 °C in a humidified box. After 3 washings with 200 μ L/well of PBS-Tween 1% (PBS-T), all wells were filled with 200 μ L of 3% w/v BSA in PBS (30 mg/mL) and the plate incubated for 2h at 37 °C. After 3 washes with 200 μ L/well of PBS-Tween 1% (PBS-T), wells were filled with 100 μ L of solutions containing mouse sera (both pre-immune and immune samples) at various dilutions (1:100; 1:500, 1:1000; 1:5000; 1:10000; 1:100000) in PBS. Plates were incubated 1h at 37 °C, then were washed again 3 times with 200 μ L/well of PBS-T.

To detect bound antibodies, a secondary goat anti-mouse antibody conjugated to horseradish peroxidase (GAM-HRP, Biorad, Milan, Italy), diluted at 1 μ g/mL, was added to each well (100 μ L). After 1h incubation at 37 °C, the plate was washed 3 times with 200 μ L/well of PBS-T, then 100 μ L of a solution of peroxidase substrate ABTS (A319, Sigma-Aldrich, Milano, Italy) were added to

each well. The reaction was stopped with SDS 1% and the absorbance at 405 nm read using a multiwell absorbance reader (Biotek,). Antibody titers were evaluated as sufficiently high when the average absorbance values from triplicate wells incubated with immune sera diluted at 1:10000 were at least thrice those determined on wells incubated with the pre-immune serum. Clones were screened using a similar assay, but utilizing hybridoma supernatants at various dilutions instead of sera. BSA₂ was used as control in every assay to exclude those clones producing antibodies recognizing the BSA-linked glutaraldehyde.

ELISA was also used to compare relative binding of mAbs to different antigens (library fractions or single monoacetylated peptides) and to control reagents, including the Myc-derived acetylated peptide, cyclized acetylated peptide 1-44 (coated at 10 µg/mL) , BSA₂ and acetylated OVA, BSA and KLH proteins. BSA-conjugated antigens were coated at 0.02 µg/mL in PBS and after blocking, selected anti-APE antibodies were used at 0.2 µg/mL while the ALPA commercial antibody was used at 0.5 µg/mL . Detection of bound antibodies was achieved using GAM-HRP 1:2000 (0.5 µg/mL) and OPD 0.4 mg/mL in 0.1 M citric acid and 0.2 M Na₂HPO₄ buffer (pH 4.8) and adding 0.2 µl/mL of 30% H₂O₂ as substrate. The chromogenic reaction was finally stopped adding 2.5 M H₂SO₄. Absorbance at 490 nm was read using a multiwells absorbance reader (Synergy 2 Multi-Mode Microplate Reader, Biotek).

Dose-response bindings of antibodies to immobilized BSA-conjugated peptides (0.02 µg/mL) were performed using mAbs at increasing concentrations from 0.03 µg/mL to 1 µg/mL. (0.2-6.6 nM). In the same experimental conditions antigens coated at 0.2 µg/mL were tested using commercially available anti-acetylated lysine antibody (Polyclonal Antibody Cat. # AB3879, Millipore named hereafter ALPA) at 0.5 µg/mL and GAR-HRP diluted 1:500 (1 µg/mL).

Binding competition assays were performed by coating the tetrapeptide at a fixed concentration (0.02 µg/mL) and using the antibody at 0.4nM. Competitors were used at the concentration ranging between 0.15 and 118 µM.

In addition, ELISA assay was used to test the reactivity on acetylated and not OVA, BSA and KLH proteins. All proteins were coated at 1 µg/mL in PBS and all antibodies were tested at the concentration of 0.5 µg/mL. The assays were carried out as previously described.

2.5 ANTIBODY PURIFICATION

Antibodies were purified by standard procedures. After centrifugation at 12000 rpm for 20 minutes at 4°C, hybridoma cell-culture supernatants were filtered on a 0.22 µm filter and loaded onto a Protein G Sepharose column (GE, Healthcare) using PBS as loading buffer. Elution was performed using 0.1 M glycine pH 2.7. Protein G-purified mAbs were dialyzed overnight against 20 mM Tris buffer pH 7.0 at 4 °C, and then concentrated using Vivaspin™ 500 centrifugal filter (30 kDa MWCO, Sartorius) by centrifugation at 4000 rpm, at 4°C. Purity of mAbs was estimated by size exclusion chromatography (SEC) using a Superdex 200 Hr 10/30 column (GE, Healthcare) and by 12% SDS-PAGE under reducing and non reducing conditions. Concentration was determined using a BIORAD kit.

2.6 ACETYLATION OF PROTEINS

5mg of OVA, BSA and KLH and wild type pTAC-MAT/hAPE1 (kindly provide by Dr. G. Tell) proteins were dissolved in 5ml of 0.1 M Na₂CO₃ in a 15ml Falcon tube. The acetylation procedure was achieved adding slowly drop-wise with constant shaking to avoid precipitation 10µl of acetic anhydride and then 40µl of pyridine. The reactions were incubated at 30°C for 5 h and stopped adding 40µl of 1M Tris base. Finally, the proteins were extensively dialyzed against 25mM Tris pH=7.5 and 100mM NaCl o.n. 4°C. The acetylated status of proteins were assess by SDS-Page analysis.

2.7 WESTERN BLOTTING ANALYSIS

3µg of wild type and acetylated pTAC-MAT/hAPE1, BSA, OVA and KLH were loaded under reducing and denaturing conditions onto a 12% SDS-PAGE gel; after electrophoresis, proteins were transferred onto a polyvinylidene difluoride (PVDF) membrane (Schleicher & Schuell BioScience, After blocking with 5% (w/v) milk (NFDM) in Tris-buffered saline containing 0.1% (v/v) Tween-20 (TBS-T) for 1 h at room temperature under shaking, the membrane was incubated overnight at 4° C with anti-APE mAbs as primary antibodies at 2 µg/mL in 2.5% NFDM in TBS-T under shaking. The membrane was then triple-washed with TBS-T and incubated with GAM-HRP as secondary antibody diluted 1:1000 (1 µg/mL) in TBS-T for 1 h at room temperature under agitation. The target proteins were detected using the Enhanced Chemi-luminescent

Substrate method with the SuperSignal West Pico kit provided by Pierce Chemical Co. (Rockford, IL USA). The signals were acquired with the ChemiDoc™ system (Bio-Rad, Hercules, CA), using the Quantity One® software.

II 3. RESULTS

3.1 ANTIGEN PREPARATION AND CHARACTERIZATION

A mixture of 16 distinct peptides corresponding to all combinations of four acetylated/non acetylated lysines over the sequence KKSK*TAAK*K*NDK*EAAG of APE1-Ref1, was prepared by the solid phase method incorporating equimolar mixtures of Fmoc-L-Lys(Boc)-OH/Fmoc-L-Lys(Ac)-OH at the requested positions. Two additional lysines were introduced on the N-terminus to facilitate the conjugation of peptides to KLH and reduce the likelihood of conjugation on internal lysines. All generated sequences are reported in **Fig. 3.1**.

Synthesis progression was monitored by removing small resin aliquots after each incorporation of lysine mixtures and checking by LC-MS the occurrence of the expected products. Following cleavage reactions to free the corresponding peptides, resulting compounds were characterized by LC-MS obtaining the expected MW and approximate equimolar distributions of molecules (not shown).

After RP-HPLC fractionation (**Fig. 3.2**) and lyophilisation, the 16 fractions were again characterized by LC-MS. Considering the high similarity in structure and hydrophobicity, peptides bearing the same number of acetylated lysines were not separated and were recovered within the same fractions, except the di-acetylated peptides which were retrieved under two well separated fractions. In particular, the non acetylated peptide within fraction #1 (flowthrough, $MW_{\text{calcd/expm}}$: 1671.96/1672.2 amu) was recovered; in fraction #4 ($MW_{\text{calcd/expm}}$: 1716.99/1716.4 amu) all the monoacetylated peptides (four species) were recovered; in fraction #5 and #6 ($MW_{\text{calcd/expm}}$: 1758.02/1758.0 amu) all the di-acetylated peptides (6 species) were recovered; in fraction #7 ($MW_{\text{calcd/expm}}$: 1800.06/1800.1 amu) all the tri-acetylated peptides (4 species) were recovered; in fraction #8 ($MW_{\text{calcd/expm}}$: 1842.10/1841.6 amu) the single tetra-acetylated peptide were recovered (**Table 1**). The remaining fractions did not contain any material or contained unrelated side products. After lyophilisation we recovered 1.5 mg in fraction #1, 1.8 mg in fraction #4, 2.8 mg in fraction #5, 3.6 mg in fraction #6, 3.5 mg in fraction #7, and 1.7 mg in fraction #8. Single monoacetylated peptides were also prepared by chemical synthesis, obtained in

high yield and purified to homogeneity by RP-HPLC. MWs were consistent with those expected (**Table 1**).

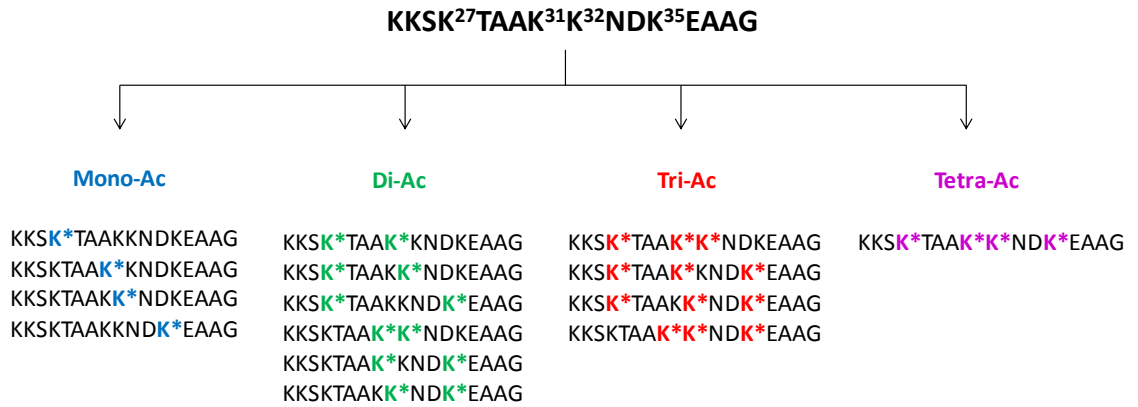


Figure 3.1: Schematic composition of the acetylated peptides library.

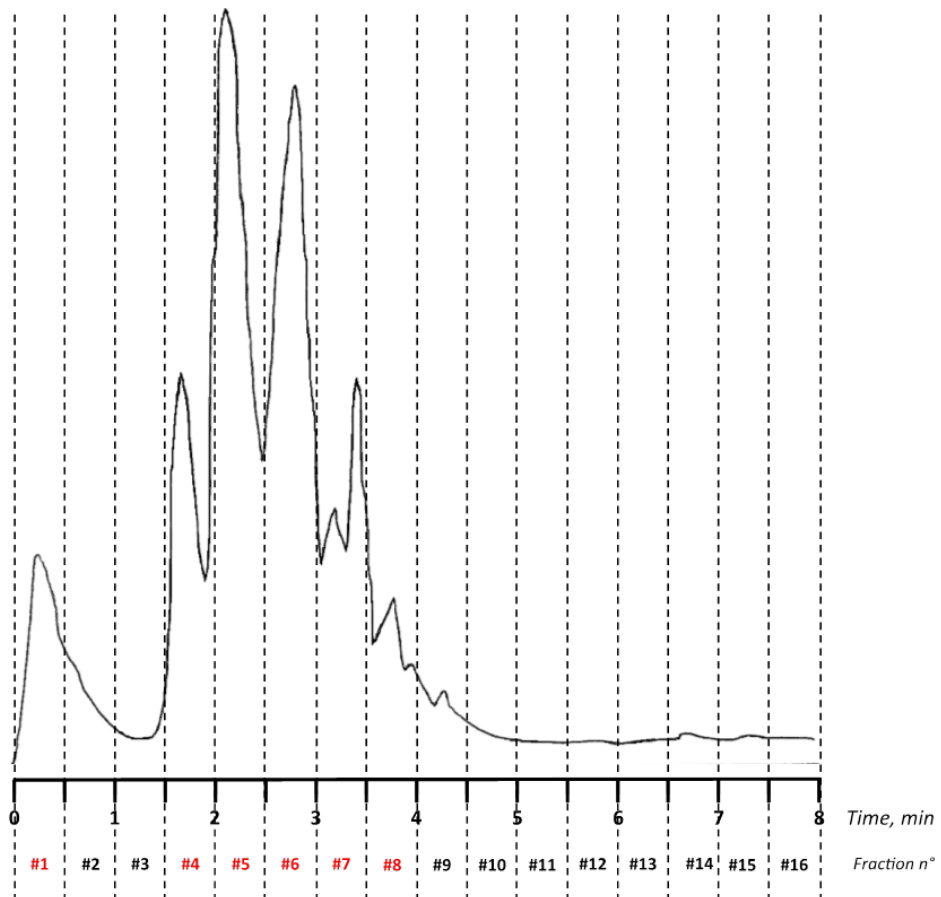


Figure 3.2: RP-HPLC fractionation of the 16 distinct peptides corresponding to all combinations of four acetylated/non acetylated lysines over the sequence KKSK***TAAK*****K*****NDK***EAAG of APE1/Ref1.

Table 1. Nomenclature, aminoacidic sequence and MW of Mono-lysine acetylated Ape1/Ref1[24-39] peptides

Peptide	Sequence	MW Theor.	MW Exp.
APE-K27	KKSK*TAAKKNDKEAAG	1673.95 uma	1672.96 uma
APE-K31	KKSKTAAK*KNDKEAAG	1673.95 uma	1672.96 uma
APE-K32	KKSKTAAKK*NDKEAAG	1673.95 uma	1672.96 uma
APE-K35	KKSKTAAKKNDK*EAAG	1673.95 uma	1672.96 uma

3.2 SCREENING OF HYBRIDOMA SUPERNATANTS ON WILD-TYPE AND ACETYLATED APE1/Ref1[24-39] PEPTIDES

Preliminary hybridoma supernatants ELISA assay was carried out coating Ac-APE1/Ref1[24-39]-BSA, APE1/Ref1[24-39]-BSA and (BSA)₂-conjugated at 1 µg/mL on 96-well plates.

By this screening we found that four clones (1D4, 1B6, 2E6 and 2G10) exhibited high selectivity toward the acetylated variant of the APE1[24-39] peptide while five other clones (3G9, 9A12, 4H9, 3G6, 2D9 and 9F11) cross-reacted with both antigens; two remaining clones (5E3 and 2A5) showed a very low signal due to aspecific binding. Only the four specific clones for the acetylated peptide were selected for expansion (see **Fig. 3.3**).

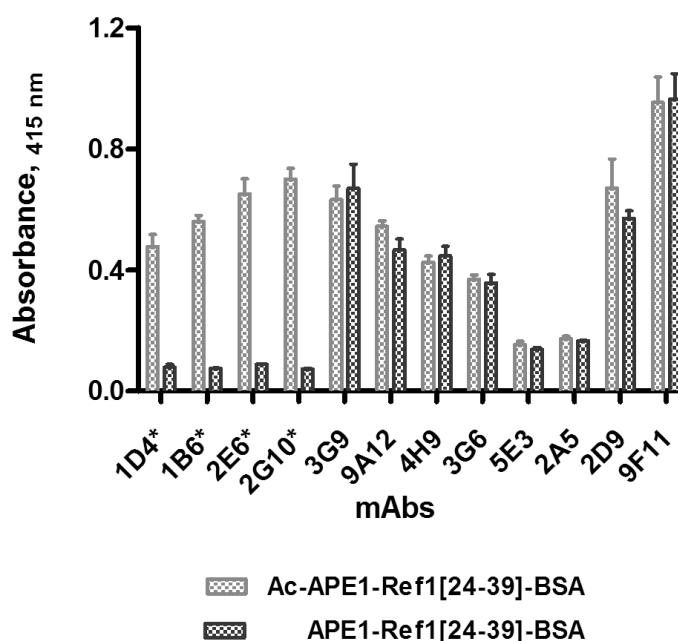


Figure 3.3: ELISA-based screening assay of hybridoma supernatants. Peptides were coated at 1 µg/mL. Hybridoma supernatants were tested at a concentration of 5µg/mL total proteins (33 nM assuming the occurrence of purified antibodies).

3.3 PURIFICATION OF ANTI-Ac-APE1/Ref1[24-39] MONOCLONAL ANTIBODIES

Clones specific for the acetylated peptides (2E6, 2G10, 1D4, 1B6) were adapted to grow in serum-free OPTIMEM medium and allowed to produce mAbs. Then the mAbs were purified from the supernatants by Protein G affinity chromatography (**Fig. 3.4A**). The elution of the mAb, indicated by the peak B, was performed after a few injections of supernatant onto the column, after washing away the unbound material (peaks A) with the loading buffer. High yield and high purity were achieved for all the four antibodies. As shown by 12% SDS-PAGE analysis (**Fig. 3.4B**), a band of 150 kDa under non reducing conditions due to the whole antibody and two bands with different mobility under reducing conditions, the upper one at 50 kDa corresponding to the heavy chains and the lower at 25 kDa corresponding to the light chains were detected. Antibody concentration was determined by the Bradford method.

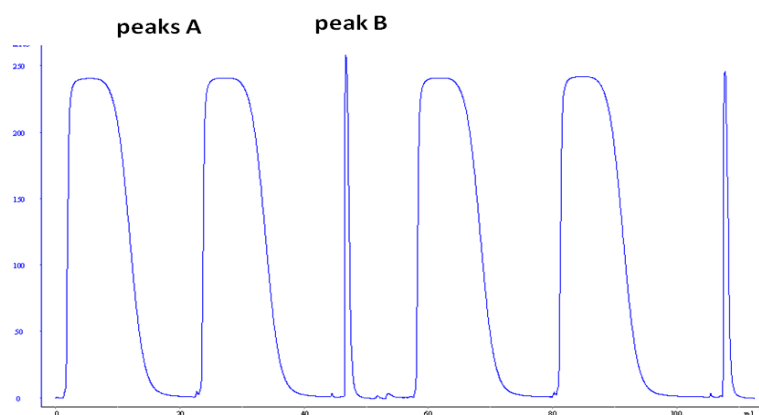


Figure 3.4A: Representative chromatogram of Protein G affinity purification of a mAb from hybridoma supernatants.

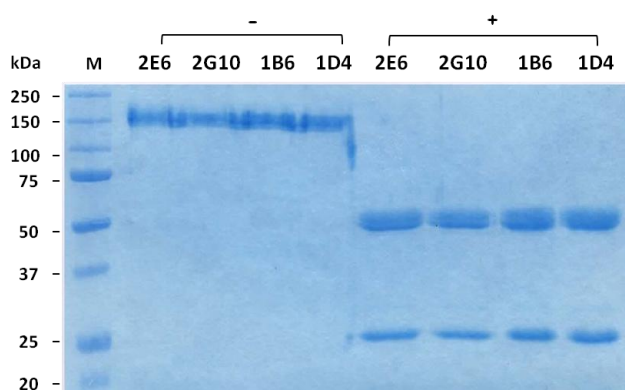


Figure 3.4B: 12% SDS-PAGE analysis under non-reducing (-) and reducing (+) conditions of purified anti-APE mAbs.

3.4 SCREENING OF SELECTED mAbs WITH LIBRARY FRACTIONS TO DETERMINE SELECTIVITY TOWARD DIFFERENTLY ACETYLATED PEPTIDES

To determine whether the selected antibodies had the ability to discriminate the different degree of acetylation of the peptides, further ELISA assays were performed with BSA-conjugated peptides from the isolated fractions coated at 0.02 $\mu\text{g/mL}$. Antibodies 2E6, 2G10, 1D4 and 1B6 were tested at 0.2 $\mu\text{g/mL}$ (**Fig. 3.5A**). In addition the same antigens were tested using as positive control the commercially available anti-acetylated lysine antibody (Polyclonal Antibody Cat. # AB3879, Millipore, named hereafter ALPA) at two concentrations corresponding to 0.5 $\mu\text{g/mL}$ and 1 $\mu\text{g/mL}$ (**Fig. 3.5B**). However, in this case, the higher concentration (0.2 $\mu\text{g/mL}$) of the coated antigen peptides and of the primary antibody, indicated the lower sensitivity of the commercial antibody compared to the anti-Ac-APE1/Ref1 peptides generated from our lab.

Data obtained from the ELISA binding assay with the different library fractions showed that, under these conditions, all antibodies bound very well peptides from all fractions with comparable signal. However, the mono-acetylated, the di-acetylated and the tri-acetylated peptides were bound with same high specificity. Interestingly, no significant binding differences were observed among the different mAbs and all of them failed to bind to the no-acetylated variant, as indicated by the absence of signal.

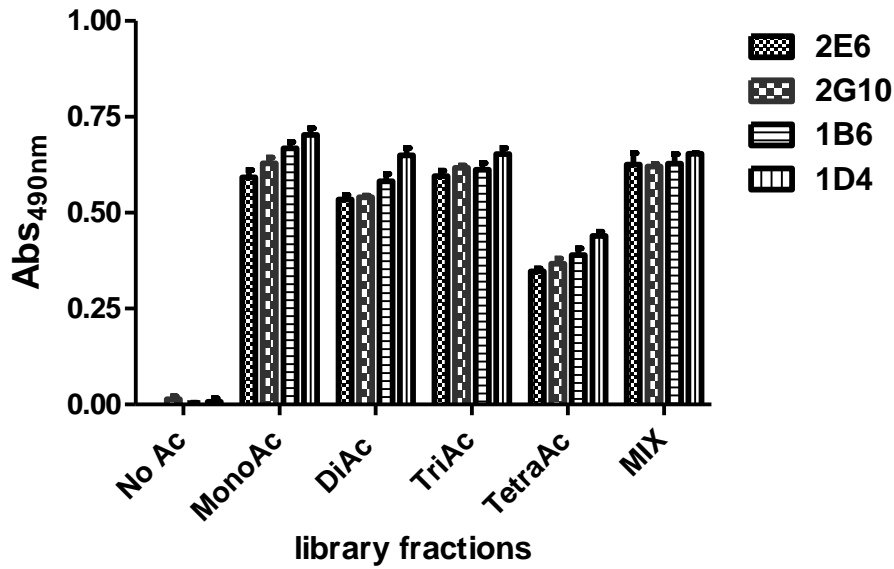


Figure 3.5A: ELISA-based screening assay of selected anti-APE antibodies. Differently BSA-conjugated acetylated Ape1/Ref1[24-39] peptides were coated at 0.02 μ g/mL. Antibodies were tested at concentration of 0.2 μ g/mL.

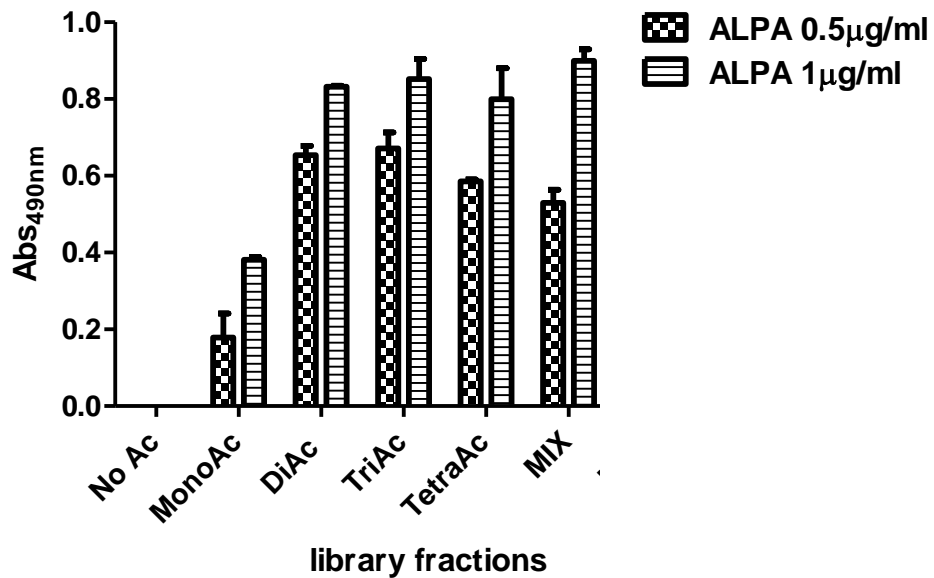


Figure 3.5B: Binding of the ALPA antibody to the APE1/Ref1[24-39] acetylated peptides coated at 0.2 μ g/mL. As expected, no binding was detected for the non-acetylated molecule, whereas ALPA binding correlated with the degree of peptide acetylation.

3.5 DOSE-RESPONSE ELISA ASSAYS

To more finely investigate the recognition properties between antibodies and the different antigens, dose-response binding assays were next performed, using the entire set of mAbs and the mono-acetylated, di-acetylated and tri-acetylated peptides.

All antibodies were used at increasing concentrations ranging from 0.2 nM to 6.7 nM and, as shown, they bound in a dose-dependent and saturable fashion to the immobilized peptides. Remarkably, no relevant differences were detected among the antibodies for the binding to the mono-acetylated and the tri-acetylated peptides (**Fig. 3.6**), whereas small, but measurable differences were recorded for the ability of the four antibodies to capture the di-acetylated peptide. An estimation of apparent dissociation constants (K_D , reported in **Table 2**) between the different antigens and the mAbs was derived. As shown, the affinity was slightly higher for the di-acetylated peptides, with K_D s ranging between 70 pM (2E6 and 1B6) and approximately 120 pM (2G10, 1D4). Furthermore, the affinities of the four mAbs for the tri-acetylated peptides were essentially identical, with K_D s between 140 and 170 pM, and were also very similar to those exhibited by 1B6, 2G10, 1D4 for the binding to the monoacetylated peptides. Of interest, the affinity between 2E6 and the monoacetylated molecules was estimated slightly lower (about 400 pM). In summary, all the mAbs displayed the highest affinity for the diacetylated peptides; a plausible explanation was that the charge localization on the lysine residues in the diacetylated form allows favourable interactions with all of the mAbs.

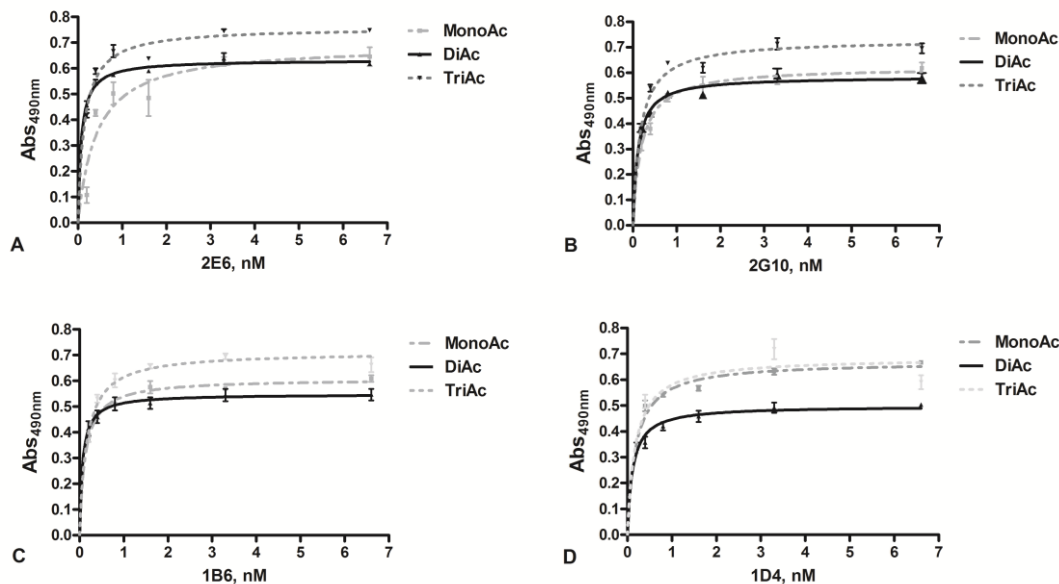


Figure 3.6A: Dose-dependent binding assay of 2E6 (A), 2G10 (B), 1B6 (C), 1D4 (D) antibodies ranging between 0.2 and 6.6 nM to the differently acetylated fractions of APE1/Ref1[24-39] BSA-conjugated peptides.

Table 2. K_D values related to the binding between each mAb and each monoacetylated APE1/Ref1[24-39] peptide. Data were fitted by Graph pad vers. 4 using a non linear regression analysis

mAb	Mono-Acetylated	Di-Acetylated	Tri-Acetylated
2E6	$0.422 \cdot 10^{-9} \text{ M} \pm 0.1815$	$0.074 \cdot 10^{-9} \text{ M} \pm 0.0096$	$0.144 \cdot 10^{-9} \text{ M} \pm 0.0301$
2G10	$0.198 \cdot 10^{-9} \text{ M} \pm 0.0303$	$0.115 \cdot 10^{-9} \text{ M} \pm 0.0203$	$0.170 \cdot 10^{-9} \text{ M} \pm 0.0341$
1B6	$0.127 \cdot 10^{-9} \text{ M} \pm 0.0126$	$0.068 \cdot 10^{-9} \text{ M} \pm 0.0067$	$0.159 \cdot 10^{-9} \text{ M} \pm 0.0231$
1D4	$0.185 \cdot 10^{-9} \text{ M} \pm 0.0326$	$0.116 \cdot 10^{-9} \text{ M} \pm 0.0244$	$0.180 \cdot 10^{-9} \text{ M} \pm 0.0891$

Subsequently, dose-response binding assays were performed between each mAb and each of the 4 mono-acetylated peptides to evaluate the ability of mAbs to discriminate among the different mono-acetylated lysines. As revealed by the estimation of apparent dissociation constants (K_D , reported in **Table 3**) between the single acetylated antigens and the mAbs, no significant differences were detected.

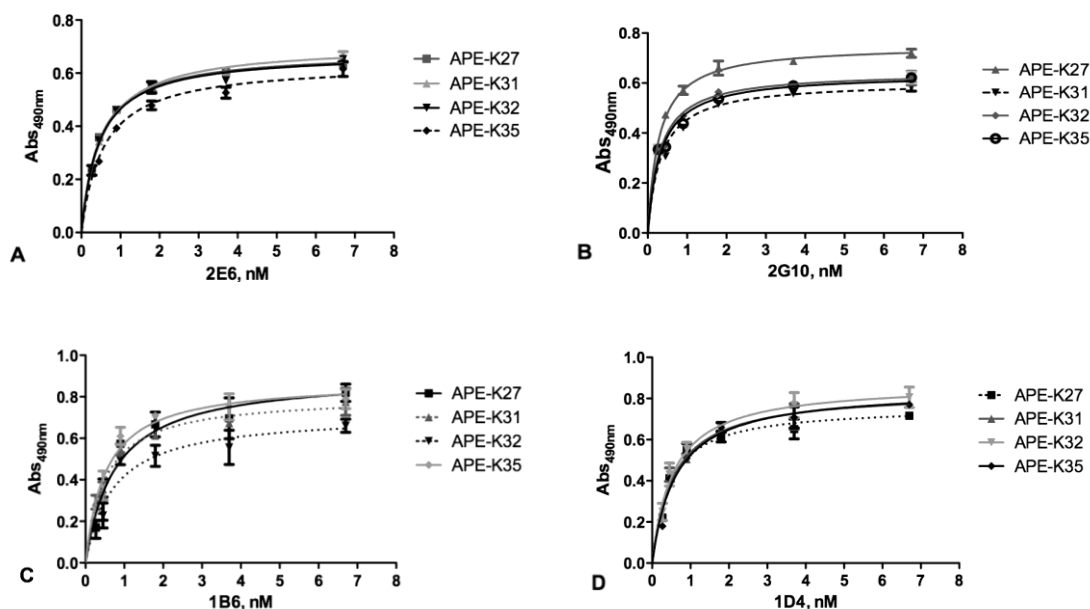


Figure 3.6B: Dose-dependent binding assay of 2E6 (A), 2G10 (B), 1B6 (C), 1D4 (D) antibodies ranging from 0.2 to 6.6 nM to the each APE1/Ref1[24-39] derived monoacetylated peptide.

Table 3. K_D values related to the binding between each mAb and each monoacetylated APE1/Ref1[24-39] peptide. Data were fitted by Graph pad vers. 4 using a non linear regression analysis

mAb	APE- K27	APE- K31	APE- K32	APE- K35
2E6	$0.283 \cdot 10^{-9} M \pm 0.038$	$0.335 \cdot 10^{-9} M \pm 0.042$	$0.303 \cdot 10^{-9} M \pm 0.049$	$0.325 \cdot 10^{-9} M \pm 0.079$
2G10	$0.448 \cdot 10^{-9} M \pm 0.016$	$0.508 \cdot 10^{-9} M \pm 0.068$	$0.456 \cdot 10^{-9} M \pm 0.046$	$0.562 \cdot 10^{-9} M \pm 0.057$
1B6	$0.445 \cdot 10^{-9} M \pm 0.020$	$0.554 \cdot 10^{-9} M \pm 0.070$	$0.545 \cdot 10^{-9} M \pm 0.022$	$0.616 \cdot 10^{-9} M \pm 0.090$
1D4	$0.760 \cdot 10^{-9} M \pm 0.093$	$0.505 \cdot 10^{-9} M \pm 0.098$	$0.714 \cdot 10^{-9} M \pm 0.064$	$0.523 \cdot 10^{-9} M \pm 0.132$

3.6 DOSE-DEPENDENT COMPETITION ASSAYS

In order to explore the difference among various monoclonal antibodies in mono-acetylated recognition, competitive ELISA assays were carried out coating mono-acetylated mixture and pre-incubating each mAb with every single mono-acetylated variant. As expected, all four monoacetylated-lysine peptides are competitive (**Fig. 3.7A**). A detailed analysis of data suggested that the peptide bearing acetylation on K35 residue is slightly more competitive for the binding only to 2G10, 1B6 and 2E6 antibodies, exhibiting a similar IC_{50} around $7 \cdot 10^{-6} M$, compared to other mono-acetylated peptides. In addition, 2G10 and 1B6 displayed a very comparable behaviour, showing the capability to similarly recognize the peptides K32, K31, K27 and K35, with an increasing affinity, respectively. By contrast, 2E6 mAb seems to bind preferentially to the peptide

containing the acetylated K35. Furthermore, no significant differences of bindings were detected between various monoacetylated peptides and 1D4. Finally, the same competitive assays were carried out using the reconstituted library achieving a similar result (**Figure 3.7B**).

These data are relevant because confirm the ability of selected mAbs to recognize the mono-acetylated variant of APE1/Ref1.

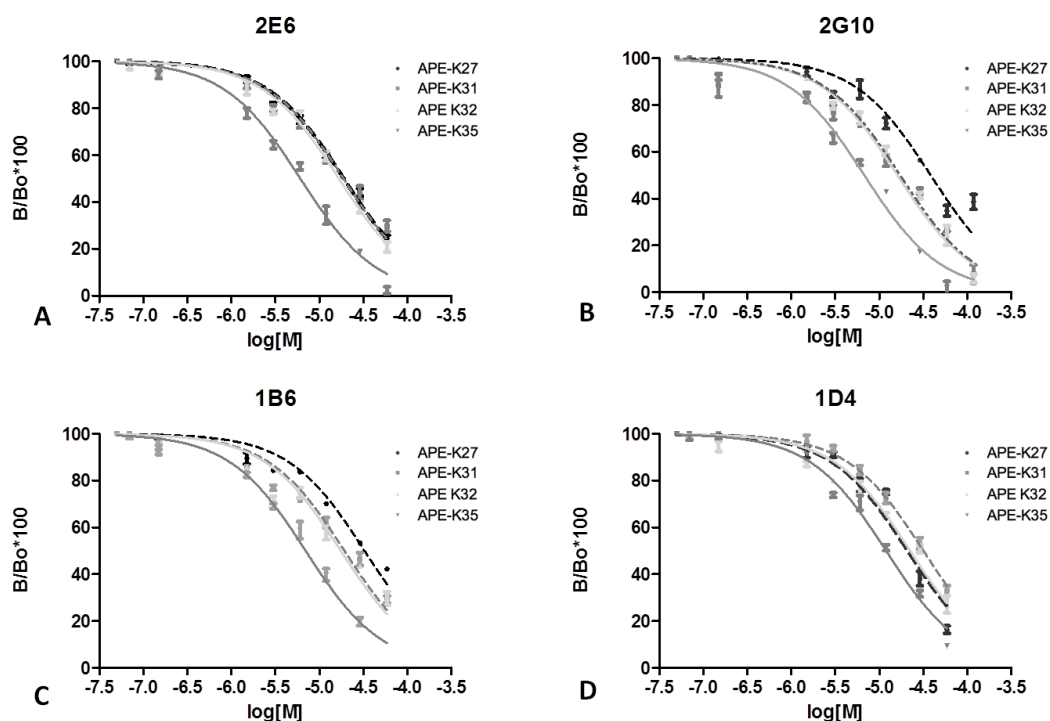


Figure 3.7A: Dose-dependent Competitive ELISA assay. Monoacetylated mixture was coated at 0.02 mg/mL. Competition solutions were set up by incubation of each antibody [2E6 (**A**), 2G10 (**B**), 1B6 (**C**), 1D4 (**D**)], at pre-saturation concentration (0.4nM), with single and free APE1/Ref1 [24-39] monoacetylated peptides at a concentration ranging between 0.15 and 118 μ M. The signal was expressed as % of relative absorbance measured at 490nm and calculated as $B/B_0 \cdot 100$.

Table 4. IC_{50} values obtained by data fitting of ELISA competitive assays

mAb	APE- K27	APE- K31	APE- K32	APE- K35
2E6	$1.89 \cdot 10^{-5} M \pm 0.026$	$1.84 \cdot 10^{-5} M \pm 0.053$	$1.67 \cdot 10^{-5} M \pm 0.029$	$0.61 \cdot 10^{-5} M \pm 0.033$
2G10	$3.87 \cdot 10^{-5} M \pm 0.056$	$1.61 \cdot 10^{-5} M \pm 0.058$	$1.73 \cdot 10^{-5} M \pm 0.031$	$6.78 \cdot 10^{-5} M \pm 0.054$
1B6	$3.27 \cdot 10^{-5} M \pm 0.043$	$1.93 \cdot 10^{-5} M \pm 0.056$	$1.75 \cdot 10^{-5} M \pm 0.059$	$7.00 \cdot 10^{-5} M \pm 0.065$
1D4	$2.11 \cdot 10^{-5} M \pm 0.056$	$3.18 \cdot 10^{-5} M \pm 0.012$	$2.25 \cdot 10^{-5} M \pm 0.048$	$1.19 \cdot 10^{-5} M \pm 0.037$

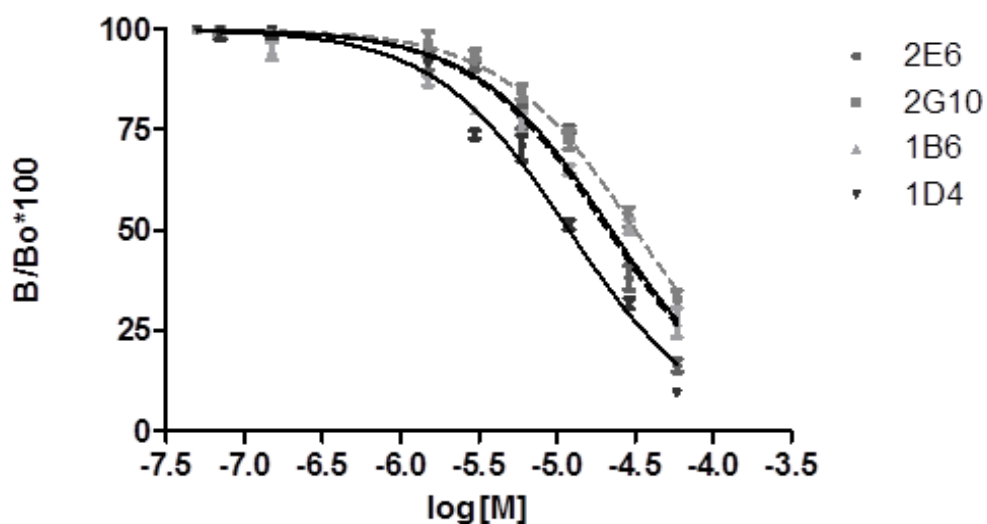


Figure 3.7B: Dose-dependent competitive ELISA assay. Each antibody (2E6, 2G10, 1B6, 1D4) at pre-saturation concentration 0.4nM was pre-incubated with reconstituted Ac-APE1/REf1[24-39] library peptides at a concentration ranging between 0.15 and 118 μ M. The solutions were added on 96-wells plate. The coating solution composed of tetracetylated mixture was fixed at 0.02mg/mL. Data were reported as % of relative absorbance, calculated as $B/B_0 \cdot 100$.

Table 5. IC₅₀ values obtained by data fitting of competitive ELISA assays between each mAb and the peptides library

2E6	2G10	1B6	1D4
$2.12 \cdot 10^{-5} \text{ M} \pm 0.055$	$3.19 \cdot 10^{-5} \text{ M} \pm 0.012$	$2.25 \cdot 10^{-5} \text{ M} \pm 0.048$	$1.2 \cdot 10^{-5} \text{ M} \pm 0.037$

3.7 SELECTIVITY ASSAYS

The specificity of anti APE1/ Ref1 antibodies was investigated evaluating their capability to bind to c-Myc[119-161] derived acetylated peptides and to an acetylated unrelated cyclic peptide (termed N_1-13) as well as to different acetylated classic carriers proteins BSA, OVA and KLH, that is the specific antigen used to generate ALPA antibody. (See **Fig.7**)

The library of c-Myc[119-161] derived acetylated peptides containing 8 distinct molecules and N_1-13 peptide (**Table 4**) were synthesized and characterized as described in the section 2.2 of Methods. The acetylation of carrier proteins, carried out as described in the Methods section, was detected by SDS-PAGE. As can be seen in **Fig. 3.8**, the acetylated proteins showed different migration because the mobility is retarded by acetylation.

Table 6. Nomenclature, aminoacidic sequence and MW of un-related acetylated peptides

Peptide	Sequence	MW Theor.	MW Exp.
c-Myc [119-161]	DDETFIKNIIQDCMWSGFSAAAK*LVSEK*LASYQAARK*DSGS	5006.147 uma	5006.05 uma
N_1-13	CLIKLKDGRKVEC	1544.842 uma	1544.05 uma

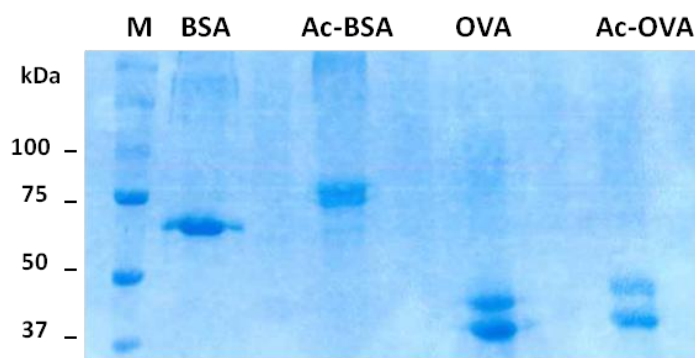


Figure 3.8: 10% SDS-PAGE analysis of non-acetylated and acetylated BSA and OVA proteins. Marker Precision Plus Protein Prestained Standards 15-150kDa. Acetylated proteins have a higher molecular weight compared to the wild-type form.

a. ELISA assays

To assess the specificity of anti-APE1-ref antibodies toward the acetylated lysine residues of the APE protein, ELISA assays were set up using both unrelated peptides at a concentration of 10 µg/mL (**Fig. 3.9A**) as well as coating all proteins at 1 µg/mL (**Fig. 3.9B**). All anti-APE mAbs were used at 1 µg/mL while the ALPA was used at 0.5 µg/mL. As shown in **Fig. 3.9**, ALPA was able

to detect both the unrelated peptides and all three acetylated proteins with a very similar signal whereas the monoclonal antibodies were inactive. As expected, no reactivity for proteins, used as negative control, was observed for all antibodies also using peptides at high concentrations.

In summary, these findings suggested that the recognition of the acetylation by our antibodies was not mediated by isolated acetyl-lysines, but it was due to acetyl-lysine residues in the context of the APE1/Ref1 sequence.

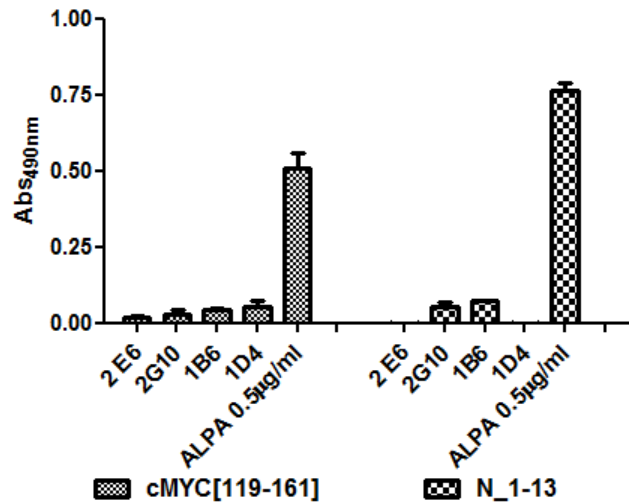


Figure 3.9A: Binding of four anti-APE1 and ALPA antibodies to cMyc-derived and N_1-13 acetylated peptides. As expected, ALPA bound to acetylated peptides while no binding was detected for anti-APE1 antibodies.

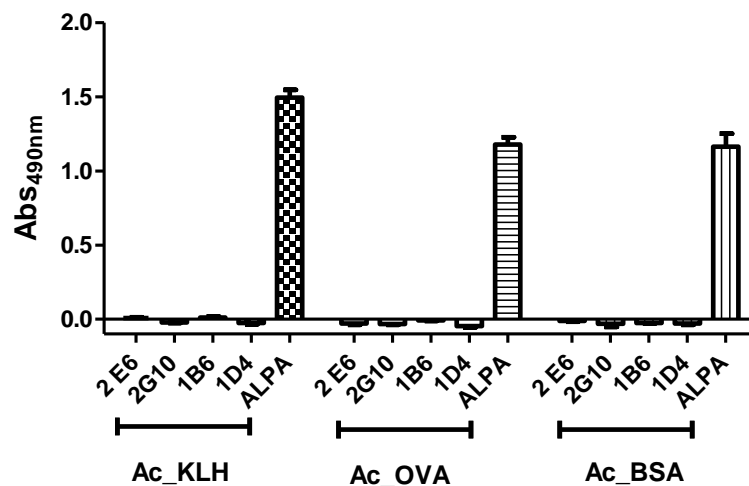


Figure 3.9B: Binding of four anti-APE1 and ALPA antibodies to acetylated proteins. As expected, no binding was detected for anti-APE1 antibodies. ALPA bound its proper antigen acetylated KLH as well as Ac_BSA and Ac_OVA.

b. Western blotting analysis

Finally the specificity of the mAbs to recognize the APE1/Ref1 proteins in acetylation status, even under reducing and denaturing conditions, was confirmed by western blotting analysis.

The wild type recombinant human APE1 [1-318 residues, Uniprot P27695-APE1_HUMAN-Ref1)] was kindly provided by Dr. G.Tell (University of Udine), expressed in *pTAC-MAT-Tag-2* Vector.

The aminoacidic sequence of protein is reported below and the lysine residues involved in their biological activity are red and underline.

60	10	20	30	40	50
MPKRGKKGAV HKTSPSGKPA	AEDGDEL RTE	PEAKKS <u>K</u> TAA	<u>KK</u> ND <u>K</u> EAAGE	GPALYEDPPD	
120	70	80	90	100	110
TLKICSWNV D LPGLSHQYWS	GLRAWIKKKG	LDWVKEEAPD	ILCLQETKCS	ENKLP AELQE	
180	130	140	150	160	170
APSDKEGYSG YVPNAGRGLV	VGLLSRQCPL	KVSYGIGDEE	HDQEGRVIVA	EFDSFVLVTA	
240	190	200	210	220	230
RLEYRQRWDE GFTPQERQGF	AFRKFLKGLA	SRKPLVLCGD	LNVAHEEIDL	RNPKGNKKNA	
300	250	260	270	280	290
GELLQAVPLA LLPALCDSKI	DSFRHLYPNT	PYAYTFWTYM	MNARSKNVGW	RLDYFLLSHS	
	310	320			
RSKALGSDHC	PITLYLAL <u>EH NHRHKH</u>				

Molecular weight: 36639.6

Figure 3.10: Aminoacidic sequence of hAPE 1-318. Molecular weight is reported. An additional linker sequence derived from the vector is reported as underline and bold.

To preliminarily investigate whether the mAbs could be used to detect the acetylated protein in cellular extracts by western blot analysis, the APE1/Ref1 recombinant protein was acetylated, as already described. The acetylation reaction was successfully achieved as confirmed by 12% SDS-PAGE analysis

Fig. 3.11A, that showed the different apparent migration of the wild-type and acetylated proteins as indicated by the band at 35 kDa corresponding to the wild type form and the slower one at approximately 45 kDa. Western blotting analyses were performed using wild-type and acetylated OVA, BSA e recombinant APE1/Ref1 proteins 2 $\mu\text{g/mL}$ and probing the membranes with the four anti-APE antibody at concentration of 2 $\mu\text{g/mL}$. The detection was carried out using Femto chemilumiscence Kit. All mAbs were able to detect only the acetylated APE1/Ref1 form, while and no detection was observed with the wild-type protein and for other proteins. A representative western blotting analysis using 2E6 mAb is reported in **Fig. 3.11B**.

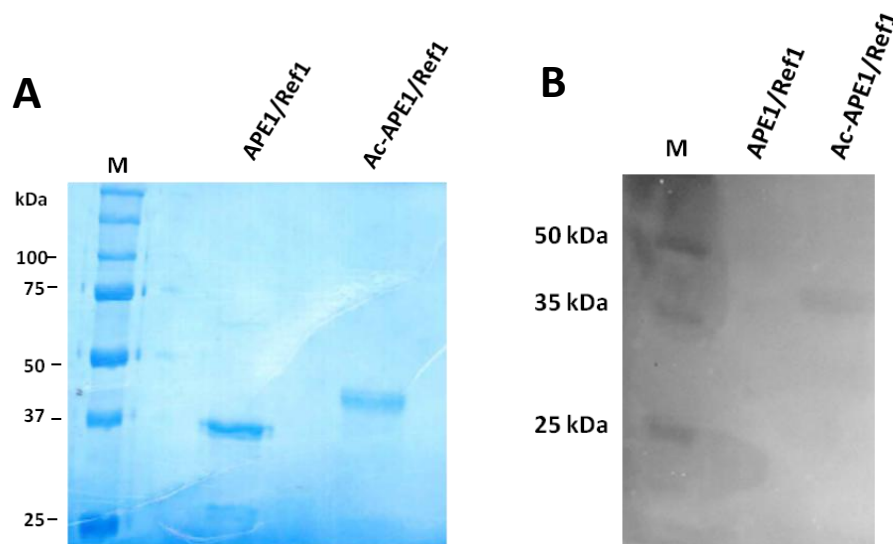


Figure 3.11: (A) 12% SDS-PAGE and (B) Western blot analysis on 15% SDS-PAGE, representative of one mAb, of wild-type and acetylated APE1/Ref1. Western blot analysis was carried out on the acetylated and the wild type form of OVA, BSA and rAPE1; as expected, anti-APE1/Ref1 mAbs were able to detect only the acetylated APE1/Ref1 protein; OVA and BSA were not detectable.

II 4. DISCUSSION

Apurinic/aprimidinic endonuclease 1 (APE1), also known as redox effector factor-1 (Ref-1), is a multifunctional and essential protein in mammals, acting as a key regulator of cellular responses to oxidative stress and contributing to the maintenance of genome stability.

Human APE1 exerts its two most important biological activities, redox and repair, through two functionally distinct protein domains, the N-terminal and the C-terminal, that act in a completely independent way, in fact, the non-structured N-terminal domain (residues 1–127) is essential for the redox activity, while the C-terminal domain (residues 61–318) is essential for the DNA base excision repair (BER) activity. APE1 is a protein that undergoes several post-translational modifications (PTMs); of interest charged K residues, located within the unstructured APE1 N-terminal domain (K24/K25/K27/K31/K32), are crucial for APE1 interaction with rRNA and NPM1 and for regulation of its catalytic activity on abasic DNA through modulation of product binding. Interestingly, some of these critical amino acids (K27/K31/K32 and K35) may undergo *in vivo* acetylation under basal conditions.

Recent results highlight the emerging role of acetylation of critical Lys residues in regulating APE1 functions. They also suggest the existence of cross-talk between different Lys residues of APE1, occurring upon genotoxic damage, which may modulate APE1 subnuclear distribution and enzymatic activity *in vivo*. Since the actual acetylation status of this protein region following different cell stimulations is currently unknown, we have explored the possibility of generating monoclonal antibodies which could specifically recognize the differently acetylated variants of the protein, so as to perform quick and very sensitive western blotting assays to monitor the protein modification under different conditions. The use of monoclonal antibodies is of particular interest in the context of the target antigen here considered, because the lysines potentially acetylated occur within a peptide segment of nine residues (K27->K35), which is the typical length of mAbs peptide antigens. This could imply that all the peptide combinations, at least the peptide sequence covering residues from Lys27 to Lys35, have the potential to be fully captured by the antibody CDR, thus recognition could be very specific with a particular antibody.

We used a pool of 16 differently acetylated peptides to immunize mice and to generate the mAbs, which were subsequently screened for their ability to interact with the different pool components. One major problem with immunizations with multiple immunogens (or mixtures) could arise with the difference in antigenicity of the different components and the consequent distribution of antibody population. However, this would not be the case, because the peptidic portion of the molecules is conserved so the overall antigenicity is largely preserved and should ensure an almost equal representation of the stimulated antibody population. This should also ensure that the resulting antibodies are at least specific for the APE1 primary sequence (as such residues are included in all the library components) and have as secondary recognition element, the variable acetylation. Following a screening approach based on the exclusion of mAbs binding the non-acetylated peptide variant, we isolated a set of monoclonal antibodies all recognizing with comparable affinity all the library components (at least when tested as sub-pools as we did in our work). Only the single tetra-acetylated peptide bound less well all the four selected mAbs. While this could be true, such an effect could instead likely be the result of a partial molecule insolubility that leads to an overestimation of the actual concentration. Importantly, all selected antibodies only bind the acetylated peptides while being completely inactive toward the non-acetylated variant. This strongly suggest that they bind with high affinity at least one acetylated lysine and a second, specific site on the peptide chain, far from acetylation sites. This is supported by the observation that all the four singly acetylated peptides tested against the antibodies had very strong binding affinities (in the sub-nM range) and is further supported by the lack of antibody recognition by both the non-acetylated and chemically acetylated proteins BSA, OVA and KLH and the strong binding observed with the acetylated recombinant APE1 protein.

However, as demonstrated, antigen recognition by our antibodies is strictly dependent on amino acid sequence surrounding the acetylated lysines.

Altogether, the data support the conclusion that monoclonal antibodies specific for the singly or multi-acetylated variants of the region 24-39 can be generated with our approach, but they are not sufficiently specific to detect the differently acetylated forms of the peptide and of the protein with enough selectivity.

Further, since the selected mAbs bind the monoacetylated variants at different positions, they also detect the poliacetylated variants. Therefore, our approach has demonstrated the feasibility of generating monoclonal antibodies (given the length of the antigen) with polyclonal features and combines the advantages of targeting multiple antigenic determinants (high avidity, low likelihood of antigen 'escape variants') with the advantages of obtaining monoclonal antibodies characterized by very high affinity. The idea reported here provided a rapid method for the generation of site-specific multi and monoacetyl-lysine antibodies which could be applicable to a protein acetylation studies in other tissues and organisms. For the first time, here we reported a new method for the high-throughput generation of monoclonal antibody suitable to generate diagnostic and/or therapeutics tools.

REFERENCES

1. Kingsley DM. The TGF-beta superfamily: new members, new receptors, and new genetic tests of function in different organisms. *Genes Dev.* 1994; 8(2):133-46.
2. Hogan BL. Bone morphogenetic proteins in development. *Curr Opin Genet Dev.* 1996; 6(4):432-8.
3. Massaguè J. How cells read TGF-beta signals. *Nat Rev Mol Cell Biol.* 2000; 1(3):169-78.
4. Attisano L, Wrana JL. Signal transduction by the TGF-beta superfamily, *Science.* 2002;296(5573):1646-7.
5. Chang H, Brown CW, Matzuk MM. Genetic analysis of the mammalian transforming growth factor-beta superfamily. *Endocr Rev* 2002;23(6):787-823.
6. Derynck R, Akhurst RJ. Differentiation plasticity regulated by TGF-beta family proteins in development and disease. *Nat Cell Biol.* 2007;9(9):1000-4.
7. Roberts AB, Flanders KC, Heine UI, Jakowlew S, Kondaiah P, Kim SJ, Sporn MB. Transforming growth factor-beta: multifunctional regulator of differentiation and development. *Philos Trans R Soc Lond B Biol Sci*1990;327(1239):145-154.
8. Shi Y & Massague J. Mechanisms of TGF-beta signaling from cell membrane to the nucleus. *Cell* 2003;113 685–700.
9. Massaguè J. TGF- β in cancer. *Cell* 2008; 134 : 215.
10. Wharton K, Derynck R. TGFbeta family signaling: novel insights in development and disease. *Development.* 2009; 136(22):3691-7.
11. Lin, S. J.; Lerch, T. F.; Cook, R. W.; Jardetzky, T. S.; Woodruff, T.K. The structural basis of TGF-beta, bone morphogenetic protein, and activin ligand binding. *Reproduction* 2006; 132, 179–190.
12. Daopin S, Piez KA, Ogawa Y, Davies DR Crystal structure of transforming growth factor-beta 2: an unusual fold for the superfamily. *Science.* 1992; 257(5068):369-73.
13. Schlunegger MP, Grütter MG. An unusual feature revealed by the crystal structure at 2.2 Å resolution of human transforming growth factor-beta 2. *Nature.* 1992; 358(6385):430-4.
14. Derynck R. TGF-beta-receptor-mediated signaling. *Trends Biochem Sci.* 1994; 19(12):548-53.
15. Moustakas A, Souchelnytskyi S and Heldin C. Smad regulation in TGF- β signal transduction. *Journal of Cell Science* 2001; 114, 4359-4369.
16. Gilboa L, Nohe A, Geissendorfer T, Sebald W, Henis YI & Knaus P. Bone morphogenetic protein receptor complexes on the surface of live cells: a new oligomerization mode for serine/threonine kinase receptors. *Molecular Biology of the Cell* 2000; 11 1023–1035.
17. Massagué J, Seoane J, Wotton D. Smad transcription factors. *Genes Dev.* 2005; 19(23):2783-810.
18. Wakefield LM, Roberts AB. TGF- β signaling: positive and negative effects on tumorigenesis. *Curr. Opin. Genet. Dev* 2002; 12(1):22–29.
19. Javelaud D, Alexaki VI, Mauviel A. Transforming growth factor- β in cutaneous melanoma. *Pigment Cell Melanoma Res* 2008; 21(2):123–132.
20. Massague J. The transforming growth factor- β family. *Ann Rev Cell Biol* 1990; 6:597-641.
21. Connolly EC, Akhurst RJ. The Complexities of TGF-beta Action During Mammary and Squamous Cell Carcinogenesis. *Curr Pharm Biotechnol.* 2011; 12(12):2138-49.
22. Connolly EC, Freimuth J, Akhurst RJ. Complexities of TGF- β targeted cancer therapy. *Int J Biol Sci.* 2012; 8(7):964-78.
23. Derynck R, Zhang YE. Smad-dependent and Smad-independent pathways in TGF-beta family signalling. *Nature.* 2003; 425(6958):577-84.
24. <http://www.cellsignal.com>.
25. Schier AF. Nodal signaling in vertebrate development. *Annu Rev Cell Dev Biol.* 2003; 19:589-621.
26. Beck S., Le Good J. A., Guzman M., Ben Haim N., Roy K., Beermann F. et al. Extraembryonic proteases regulate Nodal signalling during gastrulation. *Nat. Cell Biol.* 2002; 4: 981–985.
27. Eimon P. M. and Harland R. M. Effects of heterodimerization and proteolytic processing on Derriere and Nodal activity: implications for mesoderm induction in *Xenopus*. *Development* 2002; 129: 3089–3103.
28. Le Good J. A., Joubin K., Giraldez A. J., Ben-Haim N., Beck S., Chen Y. et al. (2005) Nodal stability determines signalling range. *Curr. Biol.* 2005; 15: 31–36.
29. Blanchet MH, Le Good JA, Mesnard D, et al. Cripto recruits Furin and PACE4 and controls Nodal trafficking during proteolytic maturation. *EMBO J* 2008; 27(19):2580–2591.
30. Scheufler, C.; Sebald, W.; Hulsmeier, M. Crystal structure of human bone morphogenetic protein-2 at 2.7 Å resolution. *J Mol Biol* 1999; 287,103–115.

31. Kirsch, T.; Sebald, W.; Dreyer, M. K. Crystal structure of the BMP-2-BRIA ectodomain complex. *Nat Struct Biol* 2000; 7,492–496.
32. Calvanese L, Marasco D, Doti N, Saporito A, D'Auria G, Paolillo L, Ruvo M, Falcigno L. Structural investigations on the Nodal-Cripto binding: a theoretical and experimental approach. *Biopolymers*. 2010; 93(11):1011-21.
33. Shi S, Ge C, Luo Y, Hou X, Haltiwanger RS, Stanley P. The threonine that carries fucose, but not fucose, is required for Cripto to facilitate Nodal signaling. *J Biol Chem*. 2007; 282(28):20133-4.
34. Crowley PB, Golovin A. Cation- π interactions in protein-protein interfaces. *Proteins*. 2005; 59(2):231-9.
35. Yeo C, Whitman M. Nodal signals to Smads through Cripto-dependent and Cripto-independent mechanisms. *Mol. Cell* 2001; 7: 949–957.
36. Watanabe K, Hamada S, Bianco C, et al. Requirement of glycosylphosphatidylinositol anchor of Cripto-1 for trans activity as a Nodal co-receptor. *J. Biol. Chem* 2007;282(49):35772–35786.
37. Bianco C, Adkins HB, Wechselberger C, Seno M, Normanno N, De Luca A, Sun Y, Khan N, Kenney N, Ebert A, Williams KP, Sanicola M, Salomon DS. Cripto-1 activates nodal- and ALK4-dependent and -independent signaling pathways in mammary epithelial Cells. *Mol Cell Biol*. 2002; 22(8):2586-97.
38. Romano V, Raimondo D, Calvanese L, D'Auria G, Tramontano A, Falcigno L. Toward a better understanding of the interaction between TGF- β family members and their ALK receptors. *J Mol Model*. 2012; 18(8):3617-25.
39. Calvanese L, Sandomenico A, Caporale A, Focà A, Focà G, D'Auria G, Falcigno L, Ruvo M. Conformational features and binding affinities to Cripto, ALK7 and ALK4 of Nodal synthetic fragments. *J Pept Sci*. 2015 Apr;21(4):283-93.
40. Schier AF, Shen MM. Nodal signalling in vertebrate development. *Nature* 2000;403(6768):385–389.
41. Kawasumi A, Nakamura T, Iwai N, Yashiro K, Saijoh Y, Belo JA, Shiratori H, Hamada H. Left-right asymmetry in the level of active Nodal protein produced in the node is translated into left-right asymmetry in the lateral plate of mouse embryos. *Dev. Biol*. 353(2): 321–30.
42. Branford WW, Yost HJ. Nodal signaling: CrypticLefty mechanism of antagonism decoded. *Current biology : CB* 2004; 14 (9): R341–3.
43. James D, Levine AJ, Besser D, Hemmati-Brivanlou A. TGF β /activin/nodal signaling is necessary for the maintenance of pluripotency in human embryonic stem cells. *Development* 2005;132(6):1273–1282.
44. Vallier L, Reynolds D, Pedersen RA. Nodal inhibits differentiation of human embryonic stem cells along the neuroectodermal default pathway. *Dev. Biol* 2004; 275(2):403–421.
45. Smith WC, McKendry R, Ribisi S Jr, Harland RM. A nodal-related gene defines a physical and functional domain within the Spemann organizer. *Cell* 1995; 82(1):37–46.
46. Tian T, Burrage K. Stochastic models for regulatory networks of the genetic toggle switch. *Proc. Natl Acad. Sci. USA* 2006; 103(22):8372–8377.
47. Massague, J. TGF-beta signal transduction. *Annu Rev Biochem* 1998, 67, 753–791.
48. Ben-Haim N, Lu C, Guzman-Ayala M, et al. The nodal precursor acting via activin receptors induces mesoderm by maintaining a source of its convertases and BMP4. *Dev. Cell* 2006;11(3):313–323.
49. Bianco C, Salomon DS. Targeting the embryonic gene Cripto-1 in cancer and beyond. *Expert Opin Ther Pat*. 2010; 20(12):1739-49
50. Reissmann, E.; Jornvall, H.; Blokzijl, A.; Andersson, O.; Chang, C.; Minchiotti, G.; Persico, M. G.; Ibanez, C. F.; Brivanlou, A.H. The orphan receptor ALK7 and the Activin receptor ALK4 mediate signaling by Nodal proteins during vertebrate development. *Genes Dev* 2001; 15, 2010–2022.
51. Di Fiore P. P. and De Camilli P. Endocytosis and signaling: an inseparable partnership. *Cell* 2001; 106:1–4.
52. Di Guglielmo G. M., Le Roy C., Goodfellow A. F. and Wrana J. L. Distinct endocytic pathways regulate TGF-beta receptor signalling and turnover. *Nat. Cell Biol*. 2003; 5: 410–421.
53. Shen MM. Nodal signaling: developmental roles and regulation. *Development* 2007;134(6):1023–1034.
54. Tian T, Meng AM. Nodal signals pattern vertebrate embryos. *Cell Mol Life Sci*.2006;63(6):672-85.
55. Chen C, Shen MM. Two modes by which Lefty proteins inhibit nodal signaling. *Curr. Biol* 2004;14 (7):618–624.

56. Harms PW, Chang C. Tomoregulin-1 (TMEFF1) inhibits nodal signaling through direct binding to the nodal coreceptor Cripto. *Genes Dev* 2003;17(21):2624–2629.
57. Piccolo S, Agius E, Leyns L, et al. The head inducer Cerberus is a multifunctional antagonist of Nodal, BMP and Wnt signals. *Nature* 1999;397(6721):707–710.
58. Strizzi L, Postovit LM, Margaryan NV, Lipavsky A, Gadiot J, Blank C, Seftor RE, Seftor EA, Hendrix MJ. Nodal as a biomarker for melanoma progression and a new therapeutic target for clinical intervention. *Expert Rev Dermatol.* 2009; 4(1):67-78.
59. Atallah E, Flaherty L. Treatment of metastatic malignant melanoma. *Curr Treat Options Oncol.* 2005; 6(3):185-93.
60. Bianco C, Strizzi L, Rehman A, et al. A Nodal- and ALK4-independent signaling pathway activated by Cripto-1 through Glypican-1 and c-src. *Cancer Res* 2003;63(6):1192–1197.
61. Lawrence MG, Margaryan NV, Loessner D, Collins A, Kerr KM, Turner M et al. Reactivation of embryonic nodal signaling is associated with tumor progression and promotes the growth of prostate cancer cells. *Prostate* 2011; 71:1198-1209.
62. Spiller CM, Bowles J, Koopman P. Nodal/Cripto signaling in fetal male germ cell development: implications for testicular germ cell tumors. *Int. J. Dev. Biol.* 2013; 57: 211–219.
63. Papageorgiou I, Nicholls PK, Wang F, Lackmann M, Makanji Y, Salamonsen LA, Robertson DM, Harrison CA. Expression of nodal signaling components in cycling human endometrium and in endometrial cancer. *Reprod Biol Endocrinol* 2009; 7:122
64. Xu G, Zhong Y, Munir S, Yang BB, Tsang BK, Peng C. Nodal induces apoptosis and inhibits proliferation in human epithelial ovarian cancer cells via activin receptor-like kinase 7. *J Clin Endocrinol Metab.* 2004; 89(11):5523-34.
65. Strizzi L, Hardy KM, Margaryan NV, Hillman DW, Seftor EA, Chen B. et al. Potential for the embryonic morphogen Nodal as a prognostic and predictive biomarker in breast cancer. *Breast Canc. Res.: BCR* 2012; 14: R75.
66. Kirsammer G, Strizzi L, Margaryan NV, Gilgur A, Hyser M, Atkinson J, Kirschmann DA, Seftor EA, Hendrix MJ. Nodal signaling promotes a tumorigenic phenotype in human breast cancer. *Semin. Cancer Biol.* 2014.
67. Lee CC, Jan HJ, Lai JH, Ma HI, Hueng DY, Lee YC, Cheng YY, Liu LW, Wei HW, Lee HM: Nodal promotes growth and invasion in human gliomas. *Oncogene* 2010; 29:3110-3123.
68. Hermann PC, Huber SL, Herrler T, Aicher A, Ellwart JW, Guba M, Bruns CJ, Heeschen C. Distinct populations of cancer stem cells determine tumor growth and metastatic activity in human pancreatic cancer. *Cell Stem Cell* 2007; 1: 313–323.
69. Lonardo E, Hermann PC, Mueller MT, Huber S, Balic A, Miranda-Lorenzo I et al. Nodal/activin signaling drives self-renewal and tumorigenicity of pancreatic cancer stem cells and provides a target for combined drug therapy. *Cell Stem Cell* 2011; 9: 433–446.
70. Gong Y, Guo Y, Hai Y, Yang H, Liu Y, Yang S, Zhang Z, Ma M, Liu L, Li Z, He Z. Nodal promotes the self-renewal of human colon cancer stem cells via an autocrine manner through Smad2/3 signaling pathway. *Biomed Res Int.* 2014; 2014:364134.
71. Chen J, Liu WB, Jia WD, Xu GL, Ma JL, Ren Y, Chen H, Sun SN, Huang M, Li JS. Embryonic morphogen nodal is associated with progression and poor prognosis of hepatocellular carcinoma. *PLoS One* 2014; 9: e85840.
72. Topczewska JM, Postovit LM, Margaryan NV, et al. Embryonic and tumorigenic pathways converge via Nodal signaling: role in melanoma aggressiveness. *Nat. Med* 2006;12(8):925–932.
73. Strizzi L, Abbott DE, Salomon DS, Hendrix MJ: Potential for cripto-1 in defining stem cell-like characteristics in human malignant melanoma. *Cell Cycle* 2008; 7:1931-1935.
74. Postovit LM, Margaryan NV, Seftor EA, et al. Human embryonic stem cell microenvironment suppresses the tumorigenic phenotype of aggressive cancer cells. *Proc. Natl Acad. Sci. USA* 2008;105 (11):4329–4334.
75. Hendrix MJ, Seftor EA, Hess AR, Seftor RE. Vasculogenic mimicry and tumour-cell plasticity: lessons from melanoma. *Nat. Rev. Cancer* 2003;3(6):411–421.
76. Hendrix MJ, Seftor EA, Meltzer PS, et al. Expression and functional significance of VE-cadherin in aggressive human melanoma cells: role in vasculogenic mimicry. *Proc. Natl Acad. Sci. USA* 2001;98 (14):8018–8023.
77. Hendrix MJ, Seftor EA, Chu YW, et al. Coexpression of vimentin and keratins by human melanoma tumor cells: correlation with invasive and metastatic potential. *J. Natl Cancer Inst* 1992;84(3):165–174.
78. Padlan EA. Anatomy of the antibody molecule. *Mol Immunol.* 1994; 31(3):169-217.
79. Milstein C, Pink JR. Structure and evolution of immunoglobulins. *Prog Biophys Mol Biol.* 1970;21:209-63.

80. Frangione B, Milstein C, Pink JR Structural studies of immunoglobulin G. *Nature*. 1969 Jan 11;221(5176):145-8.
81. <http://www.elisa-antibody.com/elisa-antibody/elisa-antibody-structure>.
82. Jefferis R, Lefranc M. Human immunoglobulin allotypes. *MAbs* 2009; 1:1-7.
83. Adams G, Weiner L. Monoclonal antibody therapy of cancer. *Nat Biotechnol*.2005;23(9):1147-57.
84. Badger CC, Anasetti C, Davis J, Bernstein ID. Treatment of malignancy with unmodified antibody. *Pathol Immunopathol Res*. 1987; 6(5-6):419-34.
85. Robert, F. et al. Phase I study of anti-epidermal growth factor receptor antibody cetuximab in combination with radiation therapy in patients with advanced head and neck cancer. *J. Clin. Oncol*. 2001; 19, 3234–3243.
86. Foon, K.A. et al. Preclinical and clinical evaluations of ABX-EGF, a fully human anti-epidermal growth factor receptor antibody. *Int. J. Radiat. Oncol. Biol. Phys.*2004; 58, 984–990.
87. McLaughlin, P. et al. Rituximab chimeric anti-CD20 monoclonal antibody therapy for relapsed indolent lymphoma: half of patients respond to a four-dose treatment program. *J. Clin. Oncol*. 1998; 16, 2825–2833.
88. Coiffier, B. et al. CHOP chemotherapy plus rituximab compared with CHOP alone in elderly patients with diffuse large-B-cell lymphoma. *N. Engl. J. Med*. 2002; 346, 235–242.
89. Leonard, J.P. & Link, B.K. Immunotherapy of non-Hodgkin's lymphoma with hLL2 (epratuzumab, an anti-CD22 monoclonal antibody) and Hu1D10 (apolizumab). *Semin. Oncol*. 2002; 29, 81–86 .
90. Witzig, T.E. et al. Randomized controlled trial of yttrium-90-labeled ibritumomab tiuxetan radioimmunotherapy versus rituximab immunotherapy for patients with relapsed or refractory low-grade, follicular, or transformed B-cell non-Hodgkin's lymphoma. *J. Clin. Oncol*. 2002;20, 2453–2463.
91. Kaminski, M.S. et al. Radioimmunotherapy with iodine (131)I tositumomab for relapsed or refractory B-cell non-Hodgkin lymphoma: updated results and longterm follow-up of the University of Michigan experience. *Blood* 96 2000; 1259–1266.
92. Lundin, J. et al. Phase II trial of subcutaneous anti-CD52 monoclonal antibody alemtuzumab (Campath-1H) as first-line treatment for patients with B-cell chronic lymphocytic leukemia (B-CLL). *Blood* 2002; 100, 768–773.
93. Sievers, E.L. et al. Selective ablation of acute myeloid leukemia using antibodytargeted chemotherapy: a phase I study of an anti-CD33 calicheamicin immunoconjugate. *Blood* 93 1999; 3678–3684.
94. Kreitman, R.J. et al. Efficacy of the anti-CD22 recombinant immunotoxin BL22 in chemotherapy-resistant hairy-cell leukemia. *N. Engl. J. Med* 2001; 345, 241–247.
95. Hodi F.S. et al. Improved survival with ipilimumab in patients with metastatic melanoma. *N Engl J Med*. 2010; 363(8):711-23.
96. Tsai KK, Zarzoso I, Daud AI. PD-1 and PD-L1 antibodies for melanoma. *Hum Vaccin Immunother*. 2014; 0(11):3111-6
97. Van den Eynde, B. J. & Scott, A. M. *Encyclopedia of Immunology* (eds Roitt, D. P. J. & Roitt, I. M.) 2424–2431 (Academic Press, London, 1998).
98. Glassman PM, Balthasar JP. Mechanistic considerations for the use of monoclonal antibodies for cancer therapy. *Cancer Biol Med*. 2014; 11(1):20-33.
99. Steplewski Z, Lubeck, M.D. & Koprowski, H. Human macrophages armed with murine immunoglobulin G2a antibodies to tumors destroy human cancer cells. *Science* 1983;221,865–867.
100. Heijnen, I.A. & van de Winkel, J.G. Human IgG Fc receptors. *Int. Rev. Immunol*.1997;16, 29–55.
101. Sulica A, Morel P, Metes D, Herberman RB. Ig-binding receptors on human NK cells as effector and regulatory surface molecules. *Int Rev Immunol*. 2001; 20(3-4):371-414.
102. Sibéril S, Dutertre CA, Boix C, Bonnin E, Ménez R, Stura E, Jorieux S, Fridman WH, Teillaud JL. Molecular aspects of human FcγR interactions with IgG: functional and therapeutic consequences. *Immunol Lett*. 2006;106(2):111-8.
103. Sunada, H., Magun, B.E., Mendelsohn, J. & MacLeod, C.L. Monoclonal antibody against epidermal growth factor receptor is internalized without stimulating receptor phosphorylation. *Proc. Natl. Acad. Sci. USA* 1986; 83, 3825–3829.
104. Li, S. et al. Structural basis for inhibition of the epidermal growth factor receptor by cetuximab. *Cancer Cell* 2005; 7, 301–311.
105. Franklin, M.C. et al. Insights into ErbB signaling from the structure of the ErbB2- pertuzumab complex. *Cancer Cell* 2004; 5, 317–328.

106. Arteaga, C.L. Overview of epidermal growth factor receptor biology and its role as a therapeutic target in human neoplasia. *Semin. Oncol.* 2002; 29, 3–9.
107. Austin, C.D. et al. Endocytosis and sorting of ErbB2 and the site of action of cancer therapeutics trastuzumab and geldanamycin. *Mol. Biol. Cell* 2004; 15, 5268–5282.
108. Scott AM, Wolchok JD, Old LJ. Antibody therapy of cancer. *Nat Rev Cancer.* 2012 Mar 22;12(4):278-87.
109. Andrew C. Chan & Paul J. Carter. Therapeutic antibodies for autoimmunity and inflammation. *Nature Reviews Immunology* 2010; 10, 301-316.
110. Wong KJ, Baidoo KE, Nayak TK, Garmestani K, Brechbiel MW, Milenic DE. In Vitro and In Vivo Pre-Clinical Analysis of a F(ab')₂ Fragment of Panitumumab for Molecular Imaging and Therapy of HER1 Positive Cancers. *EJNMMI Res.* 2011; 1(1).
111. Mage MG. Preparation of Fab fragments from IgGs of different animal species. *Methods Enzymol.* 1980;70(A):142-50.
112. Parham P. On the fragmentation of monoclonal IgG1, IgG2a, and IgG2b from BALB/c mice. *J Immunol.* 1983 ; 131(6):2895-902.
113. Ng HL, Lu A, Lin G, Qin L, Yang Z. The potential of liposomes with carbonic anhydrase IX to deliver anticancer ingredients to cancer cells in vivo. *Int J Mol Sci.* 2014 Dec 24;16(1):230-55.
114. Köhler G, Milstein C. Continuous cultures of fused cells secreting antibody of predefined specificity. *Nature.* 1975; 256(5517):495-7.
115. Tarentino AL, Plummer TH Jr. Enzymatic deglycosylation of asparagine-linked glycans: purification, properties, and specificity of oligosaccharide-cleaving enzymes from *Flavobacterium meningosepticum*. *Methods Enzymol.* 1994; 230:44-57.
116. Carrey E.A. In protein structure : a practical approach, 2nd ed., Creighton, T.E., ed., IRL Press, 1997, pp117-144.
117. Mariani, M., Camagna, M., Tarditi, L. and Seccaman, E. A new enzymatic method to obtain high-yield F(ab')₂ suitable for clinical use from mouse IgG1. *Mol. Immunol.* 1991; 28, 69-77.
118. Sepulveda. P., et al., Primary Structure of Porcine Pepsin. III. Amino Acid Sequence of a Cyanogen Bromide Fragment, CB2A, and the Complete Structure of Porcine Pepsin. *J. Biol. Chem.* 1975; 250, 5082.
119. Welch DR, Bisi JE, Miller BE et al. Characterization of a highly invasive and spontaneously metastatic human malignant melanoma cell line. *Int J Cancer* 1991; 47:227–237.
120. Saporito A. Chemical synthesis of proteins for biotechnology applications. PhD thesis 2005.
121. Wilson DS, Wu J, Peluso P, Nock S. Improved method for pepsinolysis of mouse IgG1 molecules to F(ab')₂ fragments. *J Immunol Methods.* 2002; 260(1-2):29-36.
122. Yamaguchi Y, Kim H, Kato K, Masuda K, Shimada I, Arata Y. Proteolytic fragmentation with high specificity of mouse immunoglobulin G. Mapping of proteolytic cleavage sites in the hinge region. *J Immunol Methods.* 1995; 181(2):259-67.
123. Suesskind D, Schatz A, Schnichels S, Coupland SE, Lake SL, Wissinger B, Bartz-Schmidt KU, Henke-Fahle S. GDF-15: a novel serum marker for metastases in uveal melanoma patients. *Graefes Arch Clin Exp Ophthalmol.* 2012; 250(6):887-95.
124. Franken NA, Rodermond HM, Stap J, Haveman J, van Bree C. Clonogenic assay of cells in vitro. *Nat Protoc.* 2006; 1(5):2315-9.
125. Kirschmann D, Seftor E, Hardy KM, Seftor RE, Hendrix MJ. Molecular pathways: vasculogenic mimicry in tumor cells: diagnostic and therapeutic implications. *Clin Cancer Res.* 2012 May 15; 18(10):2726-32.
126. Choudhary C, Kumar C, Gnad F, Nielsen ML, Rehman M, et al. Lysine acetylation targets protein complexes and co-regulates major cellular functions. *Science.* 2009; 325:834–840
127. Qiang, L., Xiao, H., Campos, E.I., Ho, V.C. & Li, G. Development of a PAN-specific, affinity-purified anti-acetylated lysine antibody for detection, identification, isolation, and intracellular localization of acetylated protein. *J. Immunoassay Immunochem.* 2005; 26, 13–23.
128. Fung, H. and Demple, B. (2005) A vital role for Ape1/Ref1 protein in repairing spontaneous DNA damage in human cells. *Mol. Cell,* 2005; 17, 463–470.
129. Izumi, T., Brown, D.B., Naidu, C.V., Bhakat, K.K., Macinnes, M.A., Saito, H., Chen, D.J. and Mitra, S. Two essential but distinct functions of the mammalian abasic endonuclease. *Proc. Natl Acad. Sci. USA* 2005; 102, 5739–5743.
130. Vascotto, C., Cesaratto, L., Zeef, L.A., Deganuto, M., D'Ambrosio, C. et al. Genome-wide analysis and proteomic studies reveal APE1/Ref-1 multifunctional role in mammalian cells. *Proteomics,* 2009; 9, 1058–1074.
131. Strauss PR, Holt CM. Domain mapping of human apurinic/apyrimidinic endonuclease. Structural and functional evidence for a disordered amino terminus and a tight globular carboxyl domain. *J. Biol. Chem.* 1998; 273:14435-14441.

132. Mol CD, Izumi T, Mitra S, Tainer JA. DNA-bound structures and mutants reveal abasic DNA binding by APE1 and DNA repair coordination. *Nature* 2000; 403:451-456.
133. Bapat A, Fishel ML, Kelley MR. Going ape as an approach to cancer therapeutics. *Antioxid Redox Signal*. 2009 ; 11(3):651-68.
134. Tell G, Quadrioglio F, Tiribelli C, Kelley MR The many functions of APE1/Ref-1: not only a DNA repair enzyme. *Antioxid Redox Signal*. 2009; 11(3):601-20.
135. Wilson DM 3rd, Simeonov A. Small molecule inhibitors of DNA repair nuclease activities of APE1. *Cell Mol Life Sci*. 2010; 67(21):3621-31.
136. Xanthoudakis S, Miao GG, Curran T. The redox and DNA-repair activities of Ref-1 are encoded by nonoverlapping domains. *Proc Natl Acad Sci U S A*. 1994 Jan 4;91(1):23-7.
137. Bhakat KK, Yang SH, Mitra S. Acetylation of human AP-endonuclease 1, a critical enzyme in DNA repair and transcription regulation. *Methods Enzymol*. 2003;371:292-300.
138. Kuning DT, Izumi T, Papaconstantinou J, Mitra S. Human AP-endonuclease 1 and hnRNP-L interact with a nCaRE-like repressor element in the AP-endonuclease 1 promoter. *Nucleic Acids Res*. 2002; 30:823–829.
139. Vascotto C, et al. APE1/Ref-1 interacts with NPM1 within nucleoli and plays a role in the rRNA quality control process. *Mol Cell Biol*. 2009b; 29:1834–1854.
140. Tell G, Wilson DM 3rd, Lee CH. Intrusion of a DNA repair protein in the RNome world: is this the beginning of a new era. *Mol Cell Biol*. 2010b; 30:366–371.
141. Lirussi L, Antoniali G, Vascotto C, D'Ambrosio C, Poletto M, Romanello M, et al. Nucleolar accumulation of APE1 depends on charged lysine residues that undergo acetylation upon genotoxic stress and modulate its BER activity in cells. *Mol Biol Cell*. 2012; 23(20):4079-96.
142. Tell G, Damante G, Caldwell D, Kelley MR The intracellular localization of APE1/Ref-1: more than a passive phenomenon? *Antioxid Redox Signal*. 2005; 7(3-4):367-84.
143. Jackson EB, Theriot CA, Chattopadhyay R, Mitra S, Izumi T. Analysis of nuclear transport signals in the human apurinic/apyrimidinic endonuclease (APE1/Ref1) *Nucleic Acids Res*. 2005; 33:3303–3312.
144. Kakolyris S, Kaklamanis L, Giatromanolaki A, et al. Expression and subcellular localization of human AP endonuclease 1 (HAP1/Ref-1) protein: A basis for its role in human disease. *Histopathology*. 1998;33:561–569.
145. Ono Y, Watanabe M, Inoue Y, Ohmoto T, Akiyama K, Tsutsui K, Seki S. Developmental expression of APEX nuclease, a multifunctional DNA repair enzyme, in mouse brains. *Brain Res Dev Brain Res*. 1995; 86:1–6.
146. Fantini D, Vascotto C, Deganuto M, Bivi N, Gustincich S, Marcon G, Quadrioglio F, Damante G, Bhakat KK, Mitra S, Tell G. APE1/Ref-1 regulates PTEN expression mediated by Egr-1. *Free Radic Res*. 2008; 42:20–29.
147. Fantini D, Vascotto C, Marasco D, D'Ambrosio C, Romanello M. Critical lysine residues within the overlooked N-terminal domain of human APE1 regulate its biological functions. *Nucleic Acids Res*. 2010; 38(22):8239-56.
148. Meisenberg C, Tait PS, Dianova II, Wright K, et al. Ubiquitin ligase UBR3 regulates cellular levels of the essential DNA repair protein APE1 and is required for genome stability. *Nucleic Acids Res*. 2012; 40(2):701-11.

ABBREVIATIONS

Abs : Absorbance
ABTS : 2,2-Azino-bis(3-ethylbenzothiazoline-6-sulfonic acid)
amu : atomic mass unit
APS : Ammonium persulfate
BSA : Bovine serum albumin
CDR : Complementarity determining region
CM5 : Carboxy-methylated dextran sensor chip
DIEA : N,N-Diisopropylethylamine
DMEM : Dulbecco's modified Eagle's medium
DMF : Dimethylformamide
DMSO : Dimethylsulphoxide
DTT : Dithiothreitol
ECL : Enhanced Chemiluminescence
EDC : 1-Ethyl-3-(3-dimethylaminopropyl)carbodiimide
EDTA : Ethylenediaminetetraacetic acid
ELISA : Enzyme-Linked Immunosorbent Assay
Fab : Fragment antigen-binding
FACS : Fluorescence-activated cell sorting
Fc : Fragment crystallizable
FCS : Foetal calf serum
Fmoc : Fluorenylmethyloxycarbonyl chloride
FPLC : Fast Protein Liquid Chromatography
GAM-HRP : Goat anti mouse-Horseradish peroxidase
GAR-HRP : Goat anti rabbit-Horseradish peroxidase
h : hours
HATU:1-[Bis(dimethylamino)methylene]-1H-1,2,3-triazolo[4,5-b]pyridinium-3-oxid hexafluorophosphate
HEPES : 4-(2-hydroxyethyl)-1-piperazineethanesulfonic acid
HPLC : High performance liquid chromatography
IAM : Iodoacetamide
IgG : Immunoglobulin G
kDa : kiloDalton
KLH : Keyhole Hemocyanin Limpet
LC- MS : Liquid Chromatography- Mass Spectrometry
mAb : Monoclonal antibody
MBHA : resin 4-Methylbenzhydramine Hydrochloride Salt Resin
min : minutes
MW : Molecular Weight
MWCO : Molecular Weight Cut Off
NaAc : Sodium Acetate
NFDM : Not Fat Dry Milk
NHS : N-hydroxysuccinimide ester
OD : Optical Density
o.n. overnight
OPD : o-Phenylenediamine dihydrochloride
PBS : Phosphate-Buffered Saline
PBS-T : Phosphate-Buffered Saline-Tween 20
PDA : Photodiode Array
PEG : Polyethylen glycol
PNGase F : Peptide-N-Glycosidase F
PVDF : Polyvinylidene fluoride
*r/h*Nodal : recombinant human Nodal
*r/h*Cripto-1 : recombinant human Cripto-1
RFU : Relative Fluorescence Units
RP-HPLC : Reverse phase-high performance liquid chromatography
rpm : Revolutions per minute
RPMI : Roswell Park Memorial Institute
r.t. : room temperature

RU : Resonance Unit
SDS : Sodium Dodecyl Sulphate
SDS-PAGE : Sodium Dodecyl Sulphate - PolyAcrylamide Gel Electrophoresis
SEC : Size-exclusion chromatography
SPR : Surface Plasmon Resonance
TBS-T : Tris-Buffered Saline-Tween 20
TEMED : Tetramethylethylenediamine
TFA : Trifluoroacetic Acid
TIS : Triisopropylsilane
U/ml : Unit/ml

Appendix : Original papers

During my PhD I contributed to the following publications :

1. Calvanese L, Sandomenico A, Caporale A, **Focà A**, Focà G, D'Auria G, Falcigno L, Ruvo M. *Conformational features and binding affinities to Cripto, ALK7 and ALK4 of Nodal synthetic fragments*. J Pept Sci. 2015 Apr;21(4):283-93. doi: 10.1002/psc.2733. Epub 2015 Jan 15.
2. Sandomenico A, Severino V, Chambery A, Focà A, Focà G, Farina C, Ruvo M. **A comparative structural and bioanalytical study of IVIG clinical lots**. Mol Biotechnol. 2013 Jul;54(3):983-95. doi: 10.1007/s12033-013-9655-7.



Conformational features and binding affinities to Cripto, ALK7 and ALK4 of Nodal synthetic fragments

Luisa Calvanese,^a Annamaria Sandomenico,^{a,b} Andrea Caporale,^a Annalia Focà,^{c,d} Giuseppina Focà,^{c,d} Gabriella D'Auria,^{a,b,c} Lucia Falcigno^{a,b,c,*} and Menotti Ruvo^{a,b,*}

Nodal, a member of the TGF- β superfamily, is a potent embryonic morphogen also implicated in tumor progression. As for other TGF- β s, it triggers the signaling functions through the interaction with the extracellular domains of type I and type II serine/threonine kinase receptors and with the co-receptor Cripto. Recently, we reported the molecular models of Nodal in complex with its type I receptors (ALK4 and ALK7) as well as with Cripto, as obtained by homology modeling and docking simulations. From such models, potential binding epitopes have been identified. To validate such hypotheses, a series of mutated Nodal fragments have been synthesized. These peptide analogs encompass residues 44–67 of the Nodal protein, corresponding to the pre-helix loop and the H3 helix, and reproduce the wild-type sequence or bear some modifications to evaluate the hot-spot role of modified residues in the receptor binding.

Here, we show the structural characterization in solution by CD and NMR of the Nodal peptides and the measurement of binding affinity toward Cripto by surface plasmon resonance. Data collected by both conformational analyses and binding measurements suggest a role for Y58 of Nodal in the recognition with Cripto and confirm that previously reported for E49 and E50.

Surface plasmon resonance binding assays with recombinant proteins show that Nodal interacts *in vitro* also with ALK7 and ALK4 and preliminary data, generated using the Nodal synthetic fragments, suggest that Y58 of Nodal may also be involved in the recognition with these protein partners. Copyright © 2014 European Peptide Society and John Wiley & Sons, Ltd.

Additional supporting information may be found in the online version of this article at the publisher's web site.

Keywords: SPR, Nodal; peptides; NMR; TGF-beta

Introduction

Nodal belongs to the transforming growth factor- β (TGF- β) superfamily and plays essential roles in regulating embryonic development [1] and cell fate determination [2,3]. As with other growth factors, its late re-expression in adult tissues contributes to tumor development and progression. Nodal overexpression is indeed implicated in tumorigenesis, metastasis and cancer vascularization and has been associated to various cancers [4], including ovarian [5], pancreatic [6,7], endometrial [8], breast [9–11], prostate [12,13], testicular [14], brain [15,16], colon [17], melanoma [18,19] and hepatocellular carcinoma [20]. Because the TGF- β roles in tumorigenesis frequently reflect their function in embryonic development, in the current literature, their signaling pathways are observed with a special regard as possible therapeutic targets [10,16,21–24]. The overexpression of Nodal in numerous cancers, as well as its low abundance in normal tissues, makes Nodal a potential biomarker or antitumor target. In order to achieve this goal, many efforts have been made to fully understand how Nodal works in both normal and neoplastic conditions [4].

As for other TGF- β s, Nodal triggers the signaling functions through the interaction with the extracellular domains (ECD) of type I and type II serine/threonine kinase receptors. In particular, Nodal can signal via ActRIIB type II receptor and ALK7 or ALK4 type I receptors [25,26]. Effective signaling through ALK4 requires the

* Correspondence to: Lucia Falcigno, Dipartimento di Farmacia, Università degli Studi di Napoli 'Federico II', via Mezzocannone 16, 80134, Napoli, Italy. E-mail: lucia.falcigno@unina.it

Menotti Ruvo, Istituto di Biostrutture e Bioimmagini del CNR, via Mezzocannone, 16, 80134, Napoli, Italy. E-mail: menotti.ruvo@unina.it

a CIRPeB, University of Naples Federico II, via Mezzocannone, 16, 80134 Napoli, Italy

b Istituto di Biostrutture e Bioimmagini del CNR, via Mezzocannone, 16, 80134 Napoli, Italy

c Dipartimento di Farmacia, University of Naples Federico II, via Mezzocannone, 16, 80134 Napoli, Italy

d Boker Multimedia, via P. Castellino, Napoli, 111 Italy

Abbreviations: ActRIIB, activin type II receptor B; ACN, Acetonitrile; ALK, activin receptor-like kinase; CD, Circular Dichroism; ECD, extracellular domain; EDC, 1-Ethyl-3-(3-dimethylaminopropyl)carbodiimide; DMF, Dimethylformamide; DCM, Dichloromethane; DIEA, Di-isopropylethylamine; HATU, 1-[Bis(dimethylamino)methylene]-1H-1,2,3-triazolo[4,5-b]pyridinium 3-oxid hexafluorophosphate; HOBt, N-hydroxybenzotriazole; HPLC, High Performance Liquid Chromatography; LC-MS, Liquid Chromatography Mass Spectrometry; MeOH, Methanol; HOSu, N-Hydroxysuccinimide; rh, recombinant human; SPR, Surface Plasmon Resonance; TFA, Trifluoroacetic acid; TFE, Trifluoroethanol; TFE-d₃, 2,2,2-deuterated trifluoroethanol; TGF- β , transforming growth factor- β ; TIS, Tri-isopropylsilane.

additional interaction of Nodal with the co-receptor Cripto [27]. Cripto is a membrane protein bound to the extracellular surface via glycosylphosphatidylinositol linkages [28]. It belongs to the Epidermal Growth Factor - Cripto_FRL-1_Cryptic (EGF-CFC) family and contains two cysteine-rich domains: the EGF-like domain, highly homologous to epidermal growth factor domains, and the prototypical CFC domain. Both domains are compact structural modules held together by three disulfide bridges and likely further stabilized by reciprocal interactions. Cripto is required for the formation of the multimeric complex involving Nodal and the ALK4/ActRIIB receptors. Indeed, Cripto binds ALK4 by means of its CFC domain while it interacts with Nodal via the EGF-like domain [27] (Figure 1). It is worth remembering that Nodal is absent in most normal adult tissues, but, like its cognate co-receptor Cripto, is expressed in many different tumors where they potently promote cell proliferation and growth through the phosphorylation of Smads [4]. These findings make the Nodal-Cripto signaling pathway a very attractive target for tumor therapy [24]. Indeed, many efforts are currently made to develop specific Nodal inhibitors, mostly antibodies, which can interfere with one of the several interactions established by Nodal with Cripto or with ALK7 and efficiently interrupt the downstream Smad signaling [4]. Several groups have proposed anti-Nodal antibodies that potentially target its interaction with Cripto and block tumor growth in models of metastatic melanoma cells [29]. However, developing effective and selective inhibitors remains a very challenging task in absence of a more comprehensive view of the network of interactions established by these proteins and, more importantly, in absence of a detailed understanding of the

structural features underlying mutual recognition. For these purposes, we have investigated the structural aspects underpinning the Nodal-Cripto binding and have reported the first molecular models of Nodal in complex with its receptors [30,31].

Nodal is a homodimer consisting of two subunits, each with three disulfide bonds, linked by an additional inter-chain covalent disulfide bond, highly conserved in the TGF- β superfamily [32]. The homology model of Nodal, we previously reported [30], shows the canonical, symmetric and elongated TGF- β topology (Figure 2). Each Nodal monomer is characterized by two pairs of antiparallel β -strands stretching out from the cysteine core-like fingers and by an α -helix (H3 helix). The typical curvature of these fingers creates concave and convex surfaces, namely wrist and knuckle regions, which enable the interaction of Nodal with type I and type II receptor binding epitopes, respectively. In particular, to the wrist region participate, the inner concave surface of the fingers of one monomer and the α -helix (H3 helix) and the pre-helix loop of the other monomer [33–35].

The molecular models of Nodal in complex with the ECDs of its type I receptors (ALK4 and ALK7), as well as with Cripto, were obtained by homology modeling and docking simulations. Also, potential binding epitopes were identified [30,31]. These comprise residues belonging to the Nodal wrist region. To validate such hypothesis, a series of new Nodal fragments has been now designed and synthesized. This series includes peptides from the pre-helix loop and the H3 helix of Nodal (residues 44–67) (Figure 2), and bears some mutations that will help to evaluate the role of selected hot spots in receptors binding, as discussed in the Results section.

Peptides have been synthesized, and their conformational features have been analyzed in solution by CD and NMR. To evaluate their binding affinity toward ALK4 and ALK7 receptors, as well as toward Cripto co-receptor, surface plasmon resonance (SPR) assays have been carried out. Also, a comparative binding analysis of Nodal to the ECD of recombinant human *rhCripto*, *rhALK4* and *rhALK7* has been performed to assess that the reagents used are fully active in terms of recognition and that interacting surfaces are properly exposed.

The set of data, resulting from conformational analyses and binding measurements, provide useful information that confirms the reliability of the theoretical models. On these grounds, the design of new molecules, acting as antagonists in the Nodal-receptors complex formation, can be improved with the outlook to their therapeutic and diagnostic applications.

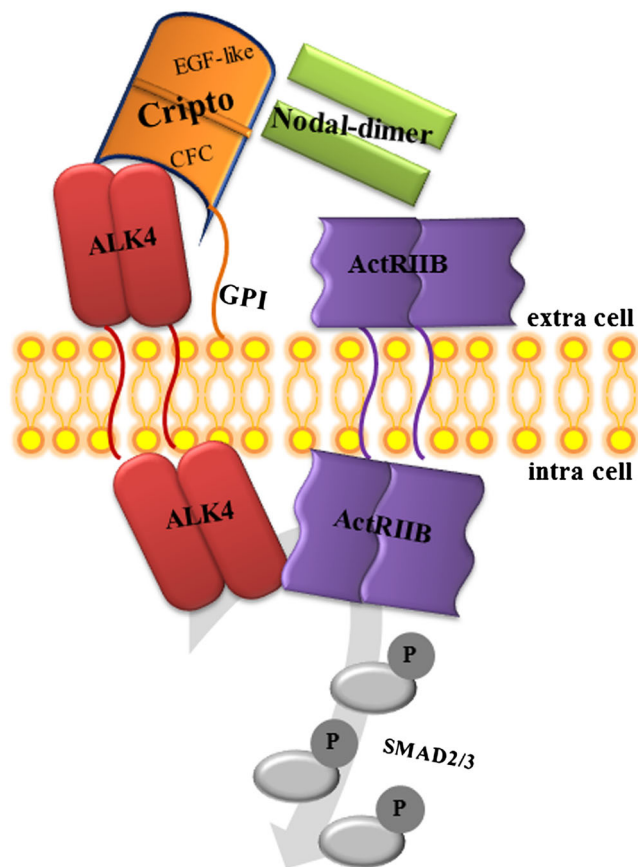


Figure 1. Schematic representation of ALK4/Cripto/Nodal/ActRIIB complex.

Materials and Methods

Reagents

Reagents for peptide synthesis were from Novabiochem (Laufelfingen, Switzerland), Inbios (Napoli, Italy) and GL Biochem (Shanghai, China). Solvents for peptide synthesis and purification, including ACN, DMF, DCM and MeOH were from Romil (Dublin, Ireland). Recombinant proteins were purchased from R&D system (MN, USA).

Peptides Synthesis and Purification

Peptides were prepared by stepwise solid-phase synthesis as C-terminally amidated molecules following standard Fmoc chemistry protocols. To increase the polypeptide's stability, the N-terminal and C-terminal ends were acetylated and amidated, respectively. A Rink-amide resin (substitution 0.53 mmol/g) and amino acid derivatives with standard protections were used in the synthesis [36]. The syntheses were performed under

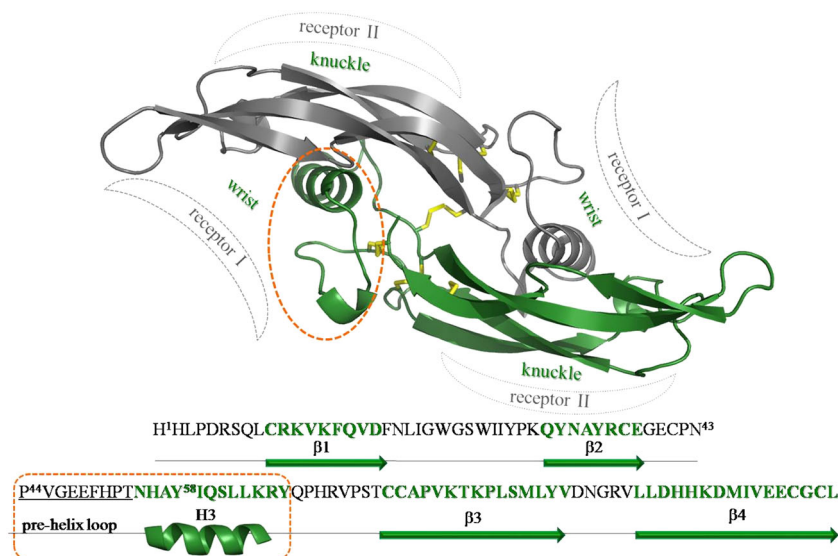


Figure 2. Ribbon representation of Nodal dimer model, with the two monomers colored in green and gray, respectively. The disulfide bridges are shown as yellow sticks. The Nodal wrist and knuckle regions, responsible for the binding to the type I and II receptors, are schematically indicated. At the bottom, both the primary and secondary structures of the Nodal monomer are reported. The Nodal fragment selected in this study is circled in orange.

canonical conditions of peptide synthesis (HATU/DIEA pre-activation, fivefold excess of Fmoc-protected amino acids). Coupling and deprotection times were kept at 30 and 20 min, respectively. Finally, N-terminal acetylation was performed on the resin using acetic anhydride at 0.5 M in DMF with 5% DIEA, 20 min at room temperature. The cleavage of peptides from the solid support was performed by treatment with a TFA/TIS/water (90:5:5, v/v/v) mixture for 3 h at room temperature, affording the crude peptides after precipitation in cold diethyl-ether. The precipitates were dissolved in water and were lyophilized. Products were purified to homogeneity by RP-HPLC using an ONYX monolithic C18 column (100×10 mm ID) applying a linear gradient of 0.05% TFA in ACN from 5% to 70% over 10 min (flow rate 20 mL/min). The purity and integrity of all peptides were estimated by LC-MS analyses using an LCQ mass spectrometer (ThermoFisher, Milano, Italy) coupled to a Surveyor system HPLC or an HCT Ultra ESI Ion Trap mass spectrometer (Bruker), coupled to a Waters Alliance HPLC system (Milford, MA, USA). LC-MS analyses were performed under conditions standardized for the detection of peptides in the positive mode. Typical gradients applied to elute the peptides were as follows: flow 0.2 mL/min; gradients from 5% solvent B (ACN, 0.05% TFA) to 70% solvent B in 10 min. Solvent A was H₂O, 0.08% TFA. Biobasic C18 50×2 mm ID columns (ThermoFisher, Milano, Italy) were used to separate peptides during LC-MS analyses.

Peptides were all prepared in amounts sufficient for the CD and NMR analyses and for the binding assays. Purities were >95% as determined by LC-MS analysis (Table 1).

Circular Dichroism Analysis

All CD analyses were performed using a JASCO J-710 spectropolarimeter (Halifax, Canada), equipped with a Peltier system for changing the temperature in a controlled way and quartz cuvettes 110-QS with 1.0 mm path length. Experiments were performed in 10 mM phosphate, pH 8.0 at a concentration of 0.5×10^{-5} M. In addition, spectra in the same buffer with added 20% of TFE were collected to increase the α -helix structure.

Spectra were collected within the wavelength range 250–190 nm at a scan rate of 50 nm/min, with a data pitch of 0.2 nm, a bandwidth of 1 nm and a response time of 4 s.

On every sample, five independent spectra were recorded, averaged and smoothed using the Spectra Manager software, version 1.53 (Easton, MD, USA). Buffer scans were recorded under the same conditions and subtracted.

NMR Analysis

NMR characterization of Nodal fragments was performed in a water/deuterated trifluoroethanol TFE-d₃/H₂O 20:80 (v/v) mixture at 298 K. Samples were prepared by dissolving weighted amounts of each peptide in water (spectroscopic purity) and adding TFE-d₃ (Sigma-Aldrich Chemicals, St. Louis, MO, USA, 99.9% D) up to a final ratio of 80/20 v/v. Final concentrations were about 3 mM.

One-dimensional and two-dimensional NMR spectra were acquired on a Varian Inova spectrometer (Agilent Technologies, Palo Alto, California, USA), operating at a proton frequency of 500 MHz,

Table 1. Sequences of Nodal fragments investigated in this study

Peptide name	Sequence	Molecular Weight theor.	Molecular Weight exp.
Nodal[44-67]	Ac-PNPVGEEFHPTNHAYIQSLLKRYQ-NH ₂	2880.2	2880.0
Nodal[44-67]EE-AA	Ac-PNPVGAAFHPTNHAYIQSLLKRYQ-NH ₂	2764.1	2764.2
Nodal[44-67]PV-AA	Ac-PNAAGEEFHPTNHAYIQSLLKRYQ-NH ₂	2826.1	2826.6
Nodal[44-67]Y-A	Ac-PNPVGEEFHPTNHAAIQSLLKRYQ-NH ₂	2788.1	2788.2

located at the 'Centro Interdipartimentale di Metodologie Chimico-Fisiche (CIMCF)' of the University Federico II of Naples. Two-dimensional (2D) experiments, such as total correlation spectroscopy (TOCSY) [37], nuclear Overhauser effect spectroscopy (NOESY) [37], and double quantum-filtered correlated spectroscopy (DQFCOSY) were recorded by the phase-sensitive States-Haberhorn method [38]. The data file generally consisted of 512 and 2048 (4096 for DQFCOSY) data points in the ω_1 and ω_2 dimensions, respectively. TOCSY experiments were acquired with a 70 ms mixing time, while NOESY experiments were acquired with 300 ms mixing time. The water resonance was suppressed by using gradients [37]. Chemical shifts were referred to internal sodium 3-(trimethylsilyl) propionate 2,2,3,3- d_4 .

Spectra were analyzed by using the CARA program [39,40]. Proton sequential assignments of the amino acid spin systems are reported as Supporting Information (Tables S1–S3). NOE intensities, evaluated by integration of cross-peaks in the 300 ms NOESY spectra, were converted into inter-proton distances by use of the CALIBA program [41]. Geminal protons were chosen as reference with a distance of 2.2 Å.

Computational Methods

Structure calculations for Nodal[44-67], Nodal[44-67]EE-AA and Nodal[44-67]Y-A started from 100 randomized conformers and used the standard CYANA-simulated annealing schedule [42] with 20 000 torsion angle dynamics steps per conformer. Three-dimensional structures were obtained by using inter-proton distances evaluated from NOEs as upper limits without the use of stereospecific assignments. All the conformers showed a fair agreement with experimental constraints showing no violations. The 40 conformers with the lowest final CYANA target function (TF) [43] values (TF average value = $0.42 \pm 0.12 \text{ \AA}^2$, $4.02E-02 \pm 3.03E-02 \text{ \AA}^2$, and $4.41E-02 \pm 4.40E-02 \text{ \AA}^2$ for Nodal[44-67], Nodal[44-67]EE-AA and Nodal[44-67]Y-A, respectively; mean global backbone RMSD = $3.51 \pm 0.97 \text{ \AA}$, $3.15 \pm 0.65 \text{ \AA}$, and $3.44 \pm 0.69 \text{ \AA}$ for Nodal[44-67], Nodal[44-67]EE-AA and Nodal[44-67]Y-A) were subjected to restrained energy minimization by use of the SANDER module of the AMBER 6.0 package [44].

The 40 minimized structures were subjected to the program CHIMERA [45] that divided them, based on structural similarity (RMSD < 0.5), into 7 clusters for Nodal[44-67], 7 clusters for Nodal[44-67]EE-AA and 6 clusters for Nodal[44-67]Y-A. The structures present in the first cluster (13 for Nodal[44-67], 17 for Nodal[44-67]EE-AA and 12 for Nodal[44-67]Y-A) were chosen as representative of the conformational space accessible to the peptide. The molecular graphics program MOLMOL [46] was employed to perform the structural statistics analysis. Statistical data are reported as Supporting Information (Tables S4 and S5).

SPR Analyses

All analyses were performed on a Biacore 3000 instrument from GE Healthcare (Little Chalfont, UK) using certified HEPES Buffered Saline (HBS) buffer (20 mM Hepes, 0.15 M NaCl, pH 7.2, P20 at 0.005%), at 25 °C.

Human ALK4 (*rh*ALK4-ECD) and ALK7 (*rh*ALK7-ECD) and Cripto (*rh*Cripto) recombinant proteins were purchased from R&D system. Proteins immobilization was carried out on the flow cells of CM5 sensor chips at 5.0 $\mu\text{g/mL}$ following the canonical EDC/HOSu (amine coupling) method, operating at 5 $\mu\text{L/min}$. In detail, human ALK7-ECD bearing as fusion protein Fc fragment human and Cripto

recombinant proteins were efficiently immobilized in NaAc pH = 4.5. For human ALK4-ECD bearing as fusion Fc fragment and the Fc fragment alone derived from an unrelated IgG1 of the same isotype, the immobilization procedure was performed in sodium acetate (NaAc) pH = 4.0. An underivatized and Fc-derivatized (IgG1) surface were prepared and used as control blank. Analyses were carried out at a flow rate of 20 $\mu\text{L/min}$, injecting a constant volume of 60 μL of peptides solutions at concentrations ranging between 0.1 and 1.0 mM. Regenerations were performed by injecting 20 μL of a solution of 10 mM glycine, pH 2.7. The proteins were immobilized at a similar level (around 3000 RU), using the wizard procedure. All binding experiments were performed at 20 $\mu\text{L/min}$ with a total contact time of 180 s (60 μL injected for every run) and the samples opportunely diluted in the HBS running buffer. For every single analysis, experimental sensorgrams were aligned, subtracted of blank signals and overlapped. The binding of synthetic peptides to ALK4, ALK7 and to Cripto was performed by injecting peptide solutions (60 μL injected for every run) at increasing concentrations, between 25 μM and 1 mM. All mathematical manipulations and fitting were performed using the BIA evaluation software, version 4.1 from GE Healthcare.

Results

Peptide Preparation

All peptides were obtained in yields ranging from about 20–30%. After purification, homogeneous products were isolated. Molecular weights were consistent with the expected values as assessed by LC-MS analyses (Table 1).

Binding of Nodal to the Immobilized Receptors

Before testing the binding of synthetic peptides to the different receptors, we first probed whether the interaction of full-length Nodal was productive under the chosen experimental conditions. To this end, we injected the recombinant protein at increasing concentrations over the three channels where the proteins were immobilized. As shown in Figure 3, Nodal binds in a dose-dependent manner to both Cripto and ALK7 and exhibiting K_D s of 5.8 nM and 1.6 nM, respectively (Table 2). These values were indicative of very strong interactions and suggested that protein surfaces required for interaction were properly and well exposed. Surprisingly, Nodal was found to bind with high affinity (1.8 nM, Table 2) also the immobilized ALK4 (Figure 3B). That result was unexpected because, according to the accepted literature, Nodal/ALK4 binding occurs *in vivo* only in the presence of the co-receptor Cripto.

Computational Analysis

Through a computational analysis of the complex containing ALK4/Cripto/Nodal (Figure 4), and ALK7/Nodal (Figure 5), obtained by homology modeling and docking simulations [30], we identified Nodal residues potentially involved in the interaction with Cripto and ALK7.

In the ternary complex containing ALK4/Cripto/Nodal (Figure 4), the EGF-like domain of Cripto was predicted to form, with G87, T88, N79, T82 and G92 residues, a polar groove in which Nodal Y58 can pocket. Furthermore, favorable electrostatic interactions are observed between E49 and E50 lying on the pre-helix loop of Nodal and the Cripto R80 residue [30].

In the ALK7/Nodal complex (Figure 5), the binding is driven by hydrophobic interactions and hydrogen bonds. Of note, major

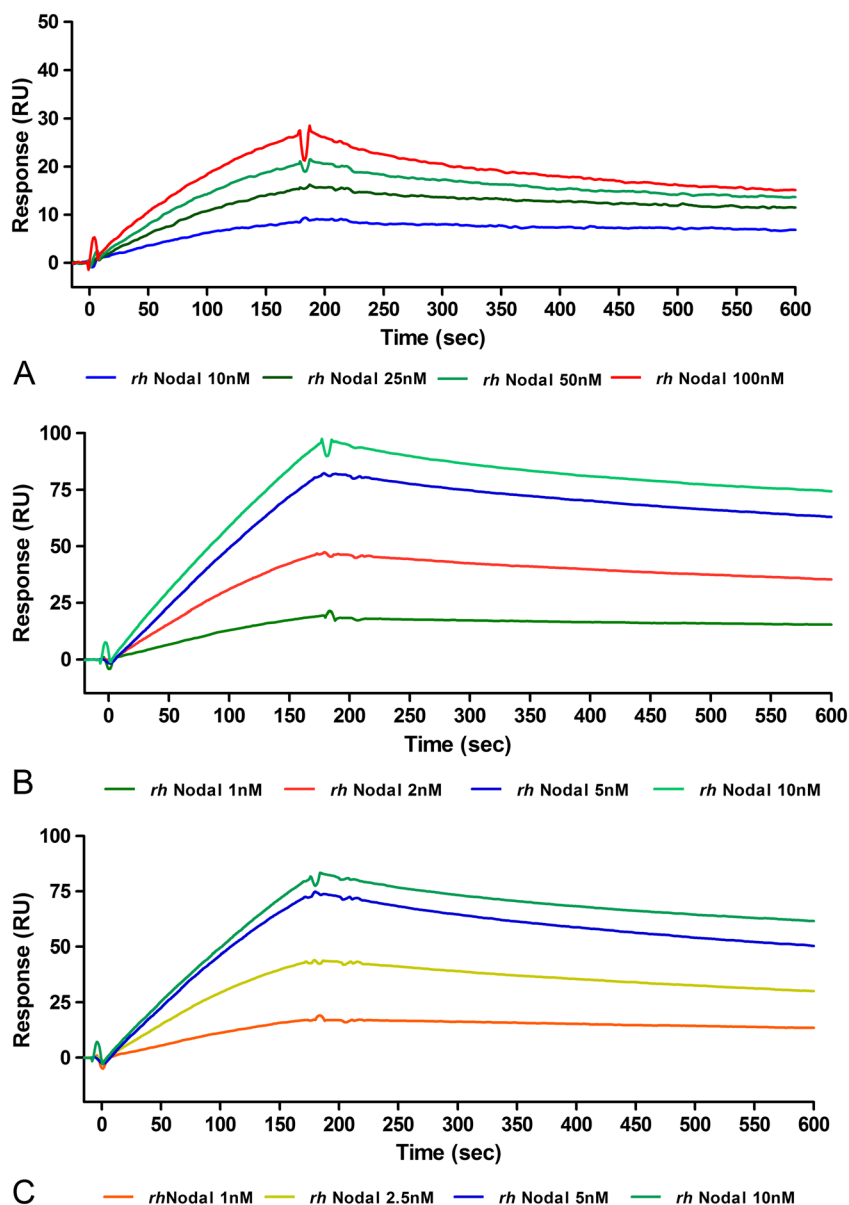


Figure 3. SPR dose-response binding sensorgrams between *rhNodal* and (A) *rhCripto*; (B) *rhALK4-ECD*; and (C) *rhALK7-ECD*, immobilized on CM5 sensor chips.

Table 2. K_D , K_a s and K_d s for the interaction of soluble Nodal with the ECD of Cripto, ALK7 and ALK4

	K_D (M)	K_a (1/Ms)	K_d (1/s)
Cripto	5.79×10^{-9}	3.20×10^5	6.11×10^{-4}
ALK7	1.58×10^{-9}	1.48×10^6	7.68×10^{-4}
ALK4	1.82×10^{-9}	1.49×10^6	5.80×10^{-4}

binding interactions are driven by a single Nodal monomer and the residues involved belong to the α -helix H3 (Y58 and L62) and pre-helix loop of Nodal (P46 and V47) and to loop 23 of ALK7 (V51 and F52) [30].

In a previous study, we demonstrated that the entire 43–69 sequence of Nodal, encompassing the α -helix H3 and pre-helix loop region, is able to bind to Cripto, while peptides reproducing the helix H3 alone do not. Moreover, the substitution of the E49

and E50 pre-helix loop residues with alanine negatively affects the binding to Cripto, confirming their involvement in the interaction [30].

On this basis, we have now designed a set of Nodal-derived peptides comprising residues 44–67, still reproducing the helix H3 and pre-helix loop region of the protein but shorter than the first published ones [30] (Table 2). Indeed, the N-terminal cysteine (C43) and the C-terminal proline (P68) and histidine (H69) have been removed as not influencing the peptide structural and binding properties.

Single or double point Ala-mutated peptides have been synthesized, purified and characterized by mass spectrometry together with the unmodified molecule. A structural characterization by NMR and circular dichroism has been then carried out in the attempt of correlating binding and structural data. Binding to Cripto, ALK4 and ALK7 receptors has been analyzed for all the peptides by SPR assays.

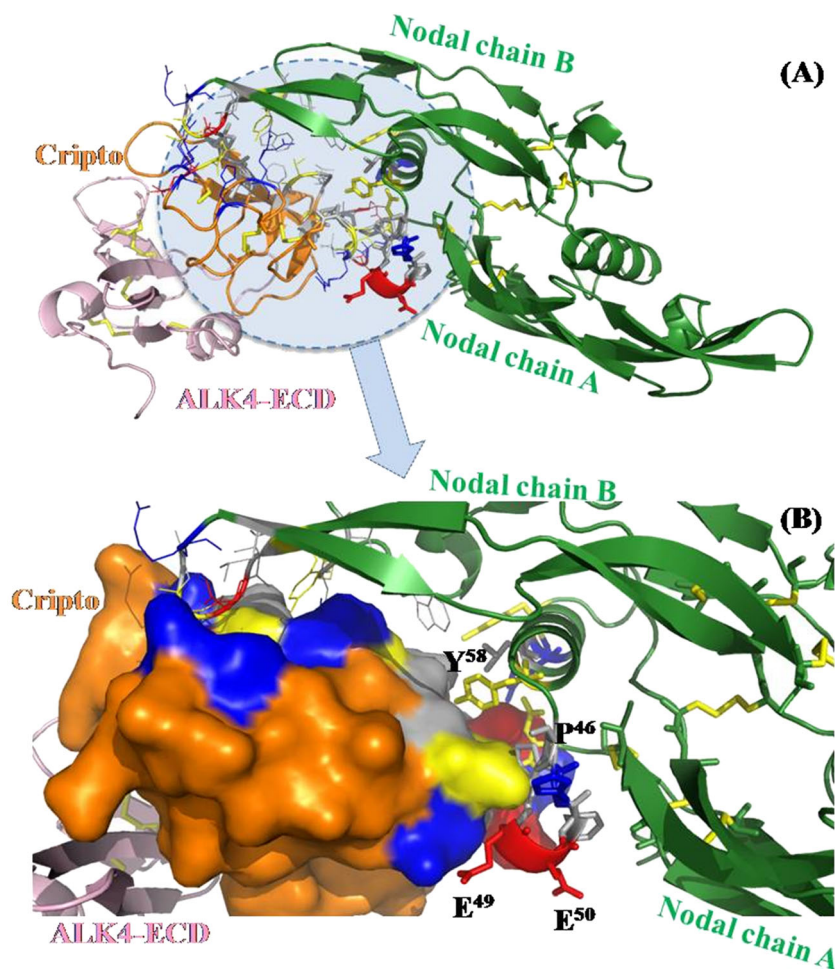


Figure 4. (A) Cartoon representation of the Nodal (green)/Cripto (orange)/ALK4-ECD (pink) complex model. (B) Cripto co-receptor is represented as Connolly surface (orange). Residues at the binding interface are colored by type.

Nodal[44-67] reproduces the 44–67 region of native human Nodal, while the first mutant, Nodal[44-67]EE-AA, bears Ala residues in place of E49 and E50; it was designed and prepared to confirm the role of the two acidic residues in the binding with Cripto [30] and a potential involvement in the interaction with ALK receptors. In the second mutant, Nodal[44-67]PV-AA, the P46 and V47 residues were replaced with alanines to verify the influence of the two hydrophobic residues of the pre-helix loop in the binding to Cripto and to ALKs. In the last mutant, Nodal[44-67]Y-A, the Y58 residue was substituted by alanine. Indeed, by analyzing the ALK7/Nodal [31] and ALK4/Cripto/Nodal molecular complexes, Y58 should be one of the residues mostly involved in the binding with the Nodal helix H3.

CD and NMR of Nodal Fragments

As shown, CD spectra (Figure 6) of peptides analyzed at 20° C in H₂O or buffer exhibited a negative band at 201 nm, typical of random coil structures. However, in presence of TFE, 20% all peptides adopted α -helical structures as suggested by the two negative bands at 207 nm and 223 nm and a positive band at 192 nm.

NMR characterization of Nodal fragments (Nodal[44-67], Nodal[44-67]EE-AA and Nodal[44-67]Y-A) was performed in a trifluoroethanol/water TFE-d₃/H₂O 20:80 (v/v) mixture at 298 K.

Proton assignment was carried out with the procedure suggested by Wuthrich [47], and the chemical shifts are reported in Tables S1–S3 of the Supporting Information.

Negative deviations of the α CH proton chemical shift of each residue from random coil values [48] are observed for all the peptides from Y58 to R65 residues, indicating the presence of helical structures in this region (see Figure S1 of the Supporting Information). Positive deviations observed in the remaining parts suggest extended conformations.

These structural diagnoses were consistent with the NOE patterns. NOE long-range effects, such as (α_i , NH_{i+3}), (α_i , β_{i+3}) and (α_i , NH_{i+4}) contacts (Figure 7), confirmed the occurrence of helical conformations in the 59–65 segment of all the three examined peptides.

A set of 153 (87 intra-residual, 48 sequential and 18 long-range), 204 (115 intra-residual, 65 sequential and 24 long-range) and 181 (129 intra-residual, 32 sequential and 20 long-range) experimental NOE constraints for Nodal[44-67], Nodal[44-67]EE-AA and Nodal[44-67]Y-A, respectively, was used as upper limits of inter-proton distances for structure calculations by CYANA program [43].

For all the peptides, the 40 CYANA structures with the lowest values of target function were subjected to restrained energy minimization by use of the AMBER 6.0 package [44] and then clustered by CHIMERA program [45]. The structures contained in the first and most-populated cluster (13 structures for Nodal[44-67], 17 for

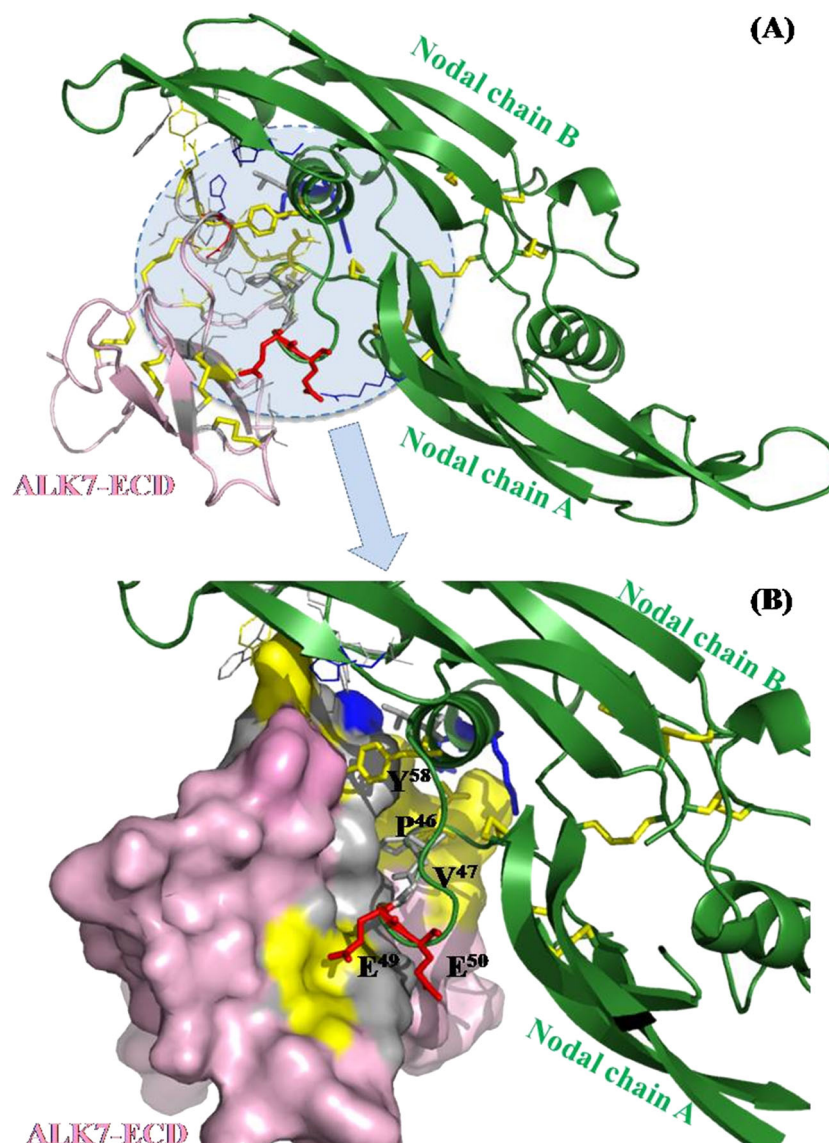


Figure 5. (A) Cartoon representation of the Nodal (green)/ALK7-ECD (pink) complex model. (B) ALK7 receptor is represented as Connolly surface (orange). Residues at the binding interface are colored by type.

Nodal[44-67]EE-AA and 12 for Nodal[44-67]Y-A) were chosen as representative of the conformational space accessible to the peptide. The statistics of the structural analysis are reported in Tables S4 and S5 of the Supporting Information.

For all the peptides, the representative clusters show structures characterized by an α -helix conformation in the 58–65 segment, where the backbone RMSD are 0.24 ± 0.12 Å, 0.26 ± 0.17 Å and 1.15 ± 0.41 Å for Nodal[44-67], Nodal[44-67]EE-AA, and Nodal[44-67]Y-A and a C-terminal flexible segment. It is worth noticing that the helical structure characterizing all three peptides reproduces the same secondary structure in the corresponding region of wild-type Nodal. In Figure 8, a superposition of the Nodal homology model (HM) [30] with the representative NMR structures of Nodal[44-67], Nodal[44-67]EE-AA and Nodal[44-67]Y-A, well represents this structural similarity. The backbone RMSD values, obtained by superimposing Nodal [44-67], Nodal[44-67]EE-AA and Nodal[44-67]Y-A NMR structures in the 58–65 segment of Nodal HM, are 0.41 Å, 0.60 Å and 0.30 Å, respectively.

The molecular model of Nodal[44-67]PV-AA was not computed, as it contains modifications that, occurring in the loop region, would not expectedly alter the helical conformation in the 58–65 tract, common to the other analogs. This hypothesis is corroborated by its CD spectrum that shows a profile similar to the others (Figure 6).

Surface Plasmon Resonance Analysis

We have studied the interaction between peptides reproducing the Nodal region 44–67 and the ECDs of ALK4, ALK7 and Cripto, evaluating the effect of specific substitutions of hot-spot residues within the pre-helix loop and helix H3 in protein recognition. SPR dose-dependent binding assays between each Nodal peptide and every single protein were carried out.

All sensorgrams obtained for the binding of Nodal peptides to immobilized Cripto, ALK4 and ALK7 recombinant proteins showed a similar kinetics profile with both fast association and dissociation rates resulting in typical 'square-pulse' sensorgrams (Figure 9 and

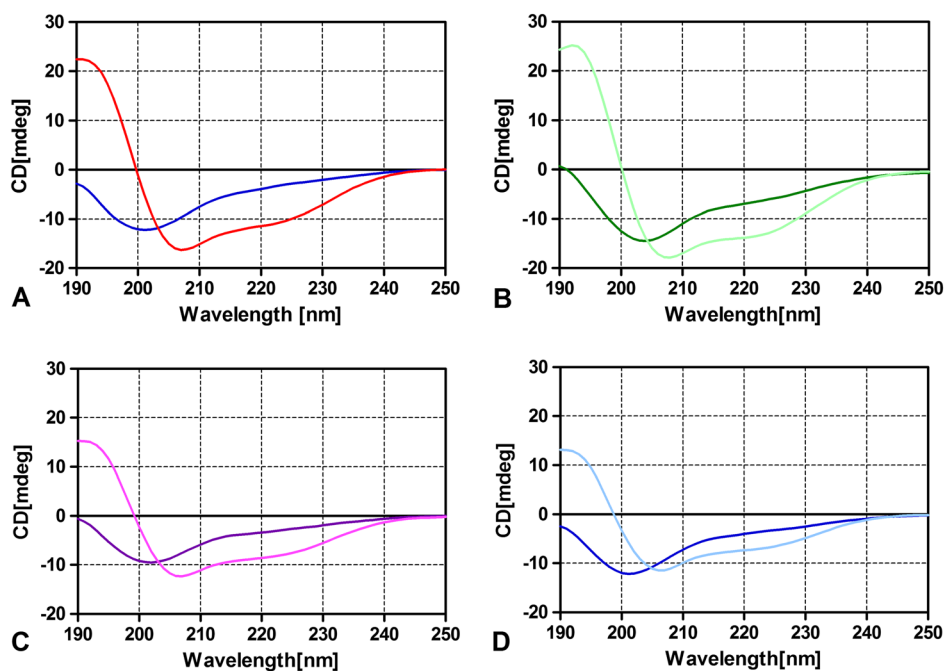


Figure 6. CD spectra of the Nodal fragments within the range 190–250 nm. (A) Nodal[44-67]: in water (blue line) and in water containing 20% TFE (v/v) (red line). (B) Nodal[44-67]EE-AA: in water (green line) and in water containing 20% TFE (v/v) (light green line). (C) Nodal[44-67]PV-AA: in water (violet line) and in water containing 20% TFE (v/v) (pink line). (D) Nodal[44-67]Y-A: in water (blue line) and in water containing 20% TFE (v/v) (cyan line).

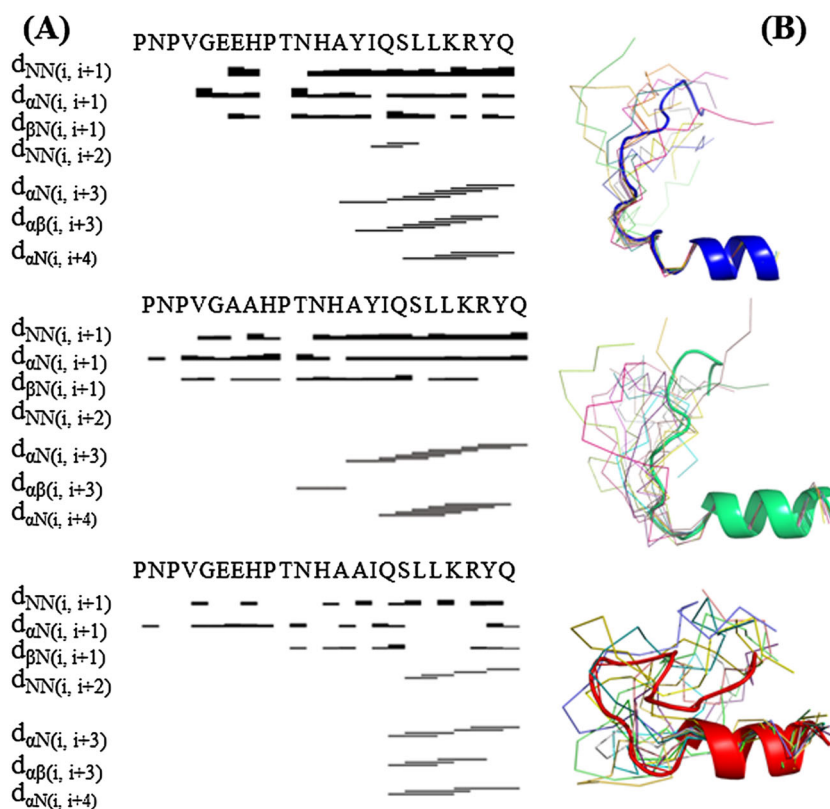


Figure 7. (A) NOE contacts graph for Nodal[44-67], Nodal[44-67]EE-AA and Nodal[44-67]Y-A. (B) Backbone superposition in the I59–Y66 segment of the structures constituting the first cluster. The representative structure of the cluster is shown with blue cartoon for Nodal[44-67], green cartoon for Nodal[44-67]EE-AA and red cartoon for Nodal[44-67]Y-A.

Figures S2 and S3 of the Supporting Information). Comparative binding data were extrapolated by curve fitting. Remarkably, although we could achieve good-fitting data for the binding of most

peptides to Cripto (except for Nodal[44-67]Y-A), all calculations performed on binding and dissociation curves to ALK4 and ALK7 did not converge to significant values (data are summarized in Table 3).

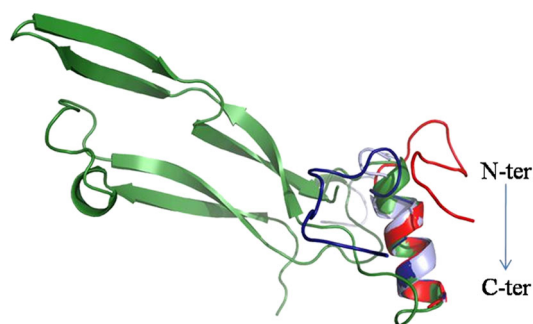


Figure 8. Structural overlap in the 58–65 segment of Nodal HM (green) [30] and the representative NMR structures of Nodal[44–67] (blue), Nodal[44–67]EE-AA (light blue) and Nodal[44–67]Y-A (red).

According to this analysis and in agreement with previous findings [30], we concluded that replacing the two glutamic acids (E49 and E50) with alanines in Nodal[44–67] reduced the affinity by about ten times ($K_D = 13.3 \mu\text{M}$) compared with that obtained with the unmodified Nodal fragment ($K_D = 1.39 \mu\text{M}$). Conversely, the affinity constant ($K_D = 3.42 \mu\text{M}$) for Cripto of Nodal[44–67]PV-AA, in which P46 and V47 were substituted with alanines, resulted very close to that of the wild-type peptide, suggesting a relatively weak contribution of these residues to the binding with Cripto and to the stability of the overall complex. Nodal[44–67]Y-A very poorly associated with immobilized Cripto (Figure 9D), and, furthermore, attempts to fit the association and dissociation curves to derive the binding parameters were all unfruitful (Table 3). The results therefore suggest that the binding of Nodal to Cripto could be mediated by tyrosine on position 58 (Y58) and is further stabilized by the upstream glutamic acid pair (E49–E50). Following the same procedure, we found that none of the peptides tested displayed sufficient binding capacity for either ALK4 and ALK7. Kinetic data, reported in Table 4, show that the Nodal peptides exhibit very similar K_{off} s (Nodal

Table 3. Affinity constant values of Nodal[44–67] and related Ala-mutated peptides to immobilized *rh*Cripto

Peptide	K_D		
	Cripto	ALK4	ALK7
Nodal[44–67]	$1.39 \times 10^{-6} \text{ M}$	nf	nf
Nodal[44–67]EE-AA	$13.3 \times 10^{-6} \text{ M}$	nf	nf
Nodal[44–67]PV-AA	$3.42 \times 10^{-6} \text{ M}$	nf	nf
Nodal[44–67]Y-A	nf	nf	nf

The K_D values were extrapolated by data fitting of dose-dependent binding curves using the BIA evaluation analysis package (version 4.1, Pharmacia Biosensor).

No fitting (nf) means that fitting of binding and association curves did not converge to any value.

[44–67]: $K_{\text{off}} = 2.86 \times 10^{-3} \text{ s}^{-1}$; Nodal[44–67]EE-AA: $K_{\text{off}} = 2.44 \times 10^{-3} \text{ s}^{-1}$; Nodal[44–67]PV-AA: $K_{\text{off}} = 2.40 \times 10^{-3} \text{ s}^{-1}$) and that the differences in affinity constants (K_D) for Cripto arise mainly from changes in the association rates (Nodal[44–67]: $2.51 \times 10^3 \text{ M}^{-1} \text{ s}^{-1}$; Nodal[44–67]PV-AA: $2.15 \times 10^3 \text{ M}^{-1} \text{ s}^{-1}$; Nodal[44–67]EE-AA: $3.23 \times 10^2 \text{ M}^{-1} \text{ s}^{-1}$). Such observations support the hypothesis that E49 and E50 positively affect the binding to Cripto by enhancing the association speed.

To try to further rationalize the data obtained and to gain a more comprehensive overview of the interaction between peptide fragments and target proteins, we also made a comparison of the RU_{max} values obtained for all molecules at a given concentration (0.1 mM). Data are reported in the Supporting Information as Figure S4 and reflect the values from sensorgrams reported in Figure 9 (A–D) and Figures S2 and S3. As shown, the most intense values are observed for the interaction between Nodal[44–67] with Cripto whereas the same molecule only very poorly binds the other receptors. Unexpectedly, peptides Nodal[44–67]EE-AA and Nodal[44–67]PV-AA were somehow captured by ALK4 and ALK7, although the

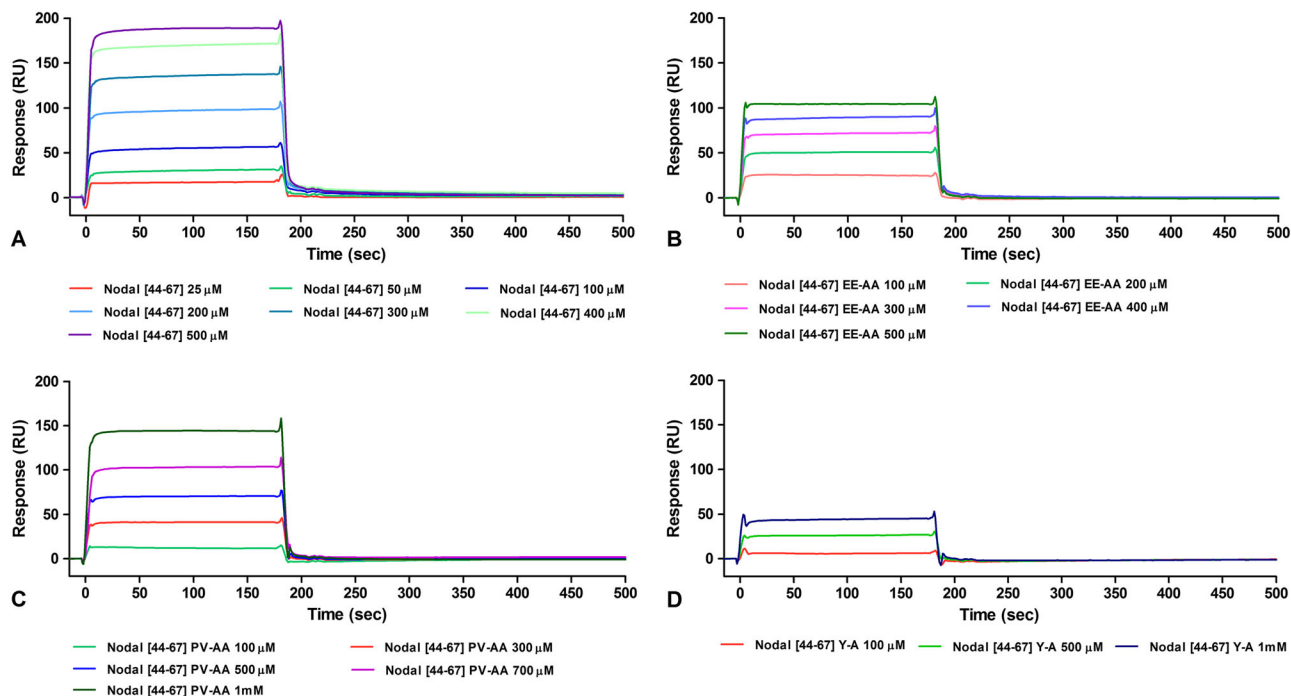


Figure 9. SPR sensorgrams obtained for the binding of Nodal peptides to immobilized *rh*Cripto. Dose–response curves were recorded at concentrations ranging between (A) 25–500 μM for Nodal[44–67]; (B) 100–500 μM for Nodal[44–67]EE-AA; (C) 100–1000 μM for Nodal[44–67]PV-AA; (D) 100–1000 μM for Nodal[44–67]Y-A.

Table 4. Kinetic constants extrapolated for the binding of Nodal [44–67] and related Ala-mutated peptides to immobilized rhCripto

Peptide	K_{on} ($M^{-1} s^{-1}$)	K_{off} (s^{-1})	K_D (M)
Nodal[44–67]	$2.51 * 10^3$	$2.86 * 10^{-3}$	$1.39 * 10^{-6}$
Nodal[44–67]EE-AA	$3.23 * 10^2$	$2.44 * 10^{-3}$	$13.3 * 10^{-6}$
Nodal[44–67]PV-AA	$2.15 * 10^3$	$2.40 * 10^{-3}$	$3.42 * 10^{-6}$
Nodal[44–67]Y-A	nf	nf	nf

The K_D values were obtained as the ratio between K_{off} s and K_{on} s.
Data were obtained using the BIA evaluation analysis package (version 4.1, Pharmacia Biosensor).
No fitting (nf) means that fitting of binding and association curves did not converge to any value.

kinetic parameters could not be determined (Tables 2 and 3). Thus, it seems that replacement of two glutamic acids (E49 and E50) or of proline 47 (P47) and valine 48 (V48) with alanine residues may favor the binding to the ALK receptors. These data could be explained by looking at the ALK7/Nodal complex binding epitope (Figure 5). Indeed, the model suggests that the Nodal E49–E50 residues are close to the ALK7 hydrophobic interface; therefore, when they are changed to alanine, the hydrophobic interactions could be enhanced. The same explanation could hold true also for ALK4, assuming that the theoretical ALK4/Nodal complex adopts the same topological structure as the ALK7/Nodal complex. Strikingly, the substitution of Y58 with alanine in Nodal[44–67]Y-A completely abolishes the binding to ALK4 and ALK7, indicating a possible role of such residue in the Nodal binding with these proteins.

Discussion

In this work, we have investigated some structural properties of the binding of Nodal with its type I receptors, ALK4 and ALK7, and with the co-receptor Cripto. An approach based on homology modeling, CD, NMR and SPR binding assays has been applied to design and study a set of synthetic peptides reproducing the pre-helix loop and the H3 α -helix region of Nodal. Nodal is reported to establish direct interactions with ALK7 and with Cripto, whereas the interaction with ALK4 was so far believed to be only mediated by Cripto. We find here for the first time that, at least *in vitro*, Nodal can directly and strongly interact with ALK4 too. However, whether this interaction occurs also *in vivo* or has a functional relevance remains to be established. We also evaluated for the first time the K_D for the Nodal/ALK7 interaction (1.58 nM). These strong interactions, together with that underlying the binding of Nodal with Cripto [30], also in the low nanomolar range, suggest that the members of the resulting molecular complex are very tightly associated, and their dissociation is a very difficult task. Using the synthetic peptides, we have further investigated the Nodal main residues involved in the binding with Cripto. Nodal binding residues have been identified using the previously published ALK4/Cripto/Nodal [30] and ALK7/Nodal [31] molecular models. On this basis, a series of Nodal fragments, which include residues 44–67 of the pre-helix loop and the H3 α -helix, have been synthesized with selected residue replacements to evaluate their putative role in receptor binding. The conformational NMR and CD analyses of Nodal peptides show their propensity to adopt α -helix structures, at least in the N-terminal tract reproducing the H3 α -helix of the parent protein. Remarkably, substitution of residues on positions 47–50 with

alanines does not seem to affect the overall propensity of the peptide C-terminal tail to adopt the helical structure. Also, changing Y58 within the helix with an alanine poorly alters the structural features of the molecule.

The ability of Nodal fragments to bind to ALK4, ALK7 receptors and Cripto, evaluated by SPR assays, has shown a preferential recognition of the wild-type Nodal 44–67 fragment for Cripto. Indeed, changing the key residues E49, E50 and Y58 to alanines interferes with and strongly impairs the recognition with this protein. Our data are also suggestive of a minor role of P47 and V48. Remarkably, the mutated synthetic peptides Nodal[44–67]EE-AA and Nodal [44–67]PV-AA, likely because of an increase of the local hydrophobicity, are also attracted to some extent by the ALK4 and the ALK7 receptors, while the substitution of Y58 abolishes the binding. All together, these data suggest that the part of the molecular surface corresponding to this region of Nodal could be shared with the other two protein partners.

In conclusion, the results reported here confirm that the binding of Nodal to the receptor complex, comprising the type I receptors ALK7 and ALK4 via the co-receptor Cripto, is influenced by glutamic acid residues (E49 and E50) and by tyrosine 58 (Y58). Such residues appear crucial to modulate Nodal specificity for one or the other receptor, thus altering also its function.

Considering the outstanding implications of Nodal in cancer, elucidation of the structural features underlying its interaction with receptors and co-receptors is fundamental in the perspective of planning strategies aimed at targeting the Nodal/Cripto-ALK receptors–Smad axis for therapeutic purposes.

Although further structural studies are required to confirm *in vivo* our observations, the identification of such *hot-spot* residues is a primary step to develop new inhibitors, especially neutralizing antibodies and small high-affinity peptides reproducing the binding interfaces on both Nodal and ALK7. The finding that Nodal can bind directly ALK4, if confirmed by other studies, could suggest the existence of a new Cripto-independent axis, which could be, independently or in combination with, targeted for developing specific antagonists that disrupt the Nodal–receptor complex(es) and block the growth and proliferation of many cancer cells.

Acknowledgements

This work was supported by funds from FIRB MERIT no. RBNE08NKH7_003 and from the PON Ricerca e Competitività 2007–2013 (PON01_01602, PON01_02342) to MR. AS is fully supported by FIRB no. RBNE08NKH7_003.

References

- Jornvall H, Reissmann E, Andersson O, Mehrkash M Ibanez CF. ALK7, a receptor for nodal, is dispensable for embryogenesis and left-right patterning in the mouse. *Mol. Cell. Biol.* 2004; **24**: 9383–9389.
- James D, Levine AJ, Besser D Hemmati-Brivanlou A. TGFbeta/activin/nodal signaling is necessary for the maintenance of pluripotency in human embryonic stem cells. *Development* 2005; **132**: 1273–1282.
- Pantic I. Cancer stem cell hypotheses: impact on modern molecular physiology and pharmacology research. *J. Biosci.* 2011; **36**: 957–961.
- Quail DF, Siegers GM, Jewer M Postovit LM. Nodal signalling in embryogenesis and tumourigenesis. *Int. J. Biochem. Cell Biol.* 2013; **45**: 885–898.
- Xu G, Zhong Y, Munir S, Yang BB, Tsang BK Peng C. Nodal induces apoptosis and inhibits proliferation in human epithelial ovarian cancer cells via activin receptor-like kinase 7. *J. Clin. Endocrinol. Metab.* 2004; **89**: 5523–5534.
- Hermann PC, Huber SL, Herrler T, Aicher A, Ellwart JW, Guba M, Bruns CJ, Heeschen C. Distinct populations of cancer stem cells determine tumor

- growth and metastatic activity in human pancreatic cancer. *Cell Stem Cell* 2007; **1**: 313–323.
- 7 Lonardo E, Hermann PC, Mueller MT, Huber S, Balic A, Miranda-Lorenzo I, Zagorac S, Alcalá S, Rodríguez-Arabaolaza I, Ramirez JC, Torres-Ruiz R, García E, Hidalgo M, Cebrian DA, Heuchel R, Lohr M, Berger F, Bartenstein P, Aicher A, Heeschen C. Nodal/activin signaling drives self-renewal and tumorigenicity of pancreatic cancer stem cells and provides a target for combined drug therapy. *Cell Stem Cell* 2011; **9**: 433–446.
 - 8 Papageorgiou I, Nicholls PK, Wang F, Lackmann M, Makanji Y, Salamonsen LA, Robertson DM, Harrison CA. Expression of nodal signalling components in cycling human endometrium and in endometrial cancer. *Reproductive Biol. Endocrinol.: RB&E* 2009; **7**: 122.
 - 9 Quail DF, Walsh LA, Zhang G, Findlay SD, Moreno J, Fung L, Ablack A, Lewis JD, Done SJ, Hess DA, Postovit LM. Embryonic protein nodal promotes breast cancer vascularization. *Cancer Res.* 2012; **72**: 3851–3863.
 - 10 Strizzi L, Hardy KM, Margaryan NV, Hillman DW, Seftor EA, Chen B, Geiger XJ, Thompson EA, Lingle WL, Andorfer CA, Perez EA, Hendrix MJ. Potential for the embryonic morphogen Nodal as a prognostic and predictive biomarker in breast cancer. *Breast Canc. Res.: BCR* 2012; **14**: R75.
 - 11 Kirsammer G, Strizzi L, Margaryan NV, Gilgur A, Hyser M, Atkinson J, Kirschmann DA, Seftor EA, Hendrix MJ. Nodal signaling promotes a tumorigenic phenotype in human breast cancer. *Semin. Cancer Biol.* 2014.
 - 12 Vo BT, Cody B, Cao Y, Khan SA. Differential role of Sloan-Kettering Institute (Ski) protein in Nodal and transforming growth factor-beta (TGF-beta)-induced Smad signaling in prostate cancer cells. *Carcinogenesis* 2012; **33**: 2054–2064.
 - 13 Lawrence MG, Margaryan NV, Loessner D, Collins A, Kerr KM, Turner M, Seftor EA, Stephens CR, Lai J, Postovit LM, Clements JA, Hendrix MJ. Reactivation of embryonic nodal signaling is associated with tumor progression and promotes the growth of prostate cancer cells. *Prostate* 2011; **71**: 1198–1209.
 - 14 Spiller CM, Bowles J, Koopman P. Nodal/Cripto signaling in fetal male germ cell development: implications for testicular germ cell tumors. *Int. J. Dev. Biol.* 2013; **57**: 211–219.
 - 15 Lee CC, Jan HJ, Lai JH, Ma H, Hueng DY, Lee YC, Cheng YY, Liu LW, Wei HW, Lee HM. Nodal promotes growth and invasion in human gliomas. *Oncogene* 2010; **29**: 3110–3123.
 - 16 Tysnes BB, Satran HA, Mork SJ, Margaryan NV, Eide GE, Petersen K, Strizzi L, Hendrix MJ. Age-dependent association between protein expression of the embryonic stem cell marker Cripto-1 and survival of glioblastoma patients. *Translational oncology* 2013; **6**: 732–741.
 - 17 Gong Y, Yu T, Chen B, He M, Li Y. Removal of cardiopulmonary resuscitation artifacts with an enhanced adaptive filtering method: an experimental trial. *BioMed Res. Int.* 2014; **2014**: 140438.
 - 18 Seftor EA, Seftor RE, Weldon DS, Kirsammer GT, Margaryan NV, Gilgur A, Hendrix MJ. Melanoma tumor cell heterogeneity: a molecular approach to study subpopulations expressing the embryonic morphogen nodal. *Semin. Oncol.* 2014; **41**: 259–266.
 - 19 Topczewska JM, Postovit LM, Margaryan NV, Sam A, Hess AR, Wheaton WW, Nickoloff BJ, Topczewski J, Hendrix MJ. Embryonic and tumorigenic pathways converge via Nodal signaling: role in melanoma aggressiveness. *Nat. Med.* 2006; **12**: 925–932.
 - 20 Chen J, Liu WB, Jia WD, Xu GL, Ma JL, Ren Y, Chen H, Sun SN, Huang M, Li JS. Embryonic morphogen nodal is associated with progression and poor prognosis of hepatocellular carcinoma. *PLoS One* 2014; **9**: e85840.
 - 21 Ganapathy V, Ge R, Grazioli A, Xie W, Banach-Petrosky W, Kang Y, Lonning S, McPherson J, Yingling JM, Biswas S, Mundy GR, Reiss M. Targeting the transforming growth factor-beta pathway inhibits human basal-like breast cancer metastasis. *Mol. Cancer* 2010; **9**: 122.
 - 22 Korpai M, Kang Y. Targeting the transforming growth factor-beta signalling pathway in metastatic cancer. *Eur. J. Cancer* 2010; **46**: 1232–1240.
 - 23 Strizzi L, Hardy KM, Kirschmann DA, Ahrlund-Richter L, Hendrix MJ. Nodal expression and detection in cancer: experience and challenges. *Cancer Res.* 2012; **72**: 1915–1920.
 - 24 Wakefield LM, Hill CS. Beyond TGFbeta: roles of other TGFbeta superfamily members in cancer. *Nat. Rev. Cancer* 2013; **13**: 328–341.
 - 25 Reissmann E, Jorvall H, Blokzijl A, Andersson O, Chang C, Minchiotti G, Persico MG, Ibanez CF, Brivanlou AH. The orphan receptor ALK7 and the activin receptor ALK4 mediate signaling by Nodal proteins during vertebrate development. *Genes Dev.* 2001; **15**: 2010–2022.
 - 26 Schier AF, Shen MM. Nodal signalling in vertebrate development. *Nature* 2000; **403**: 385–389.
 - 27 Yeo C, Whitman M. Nodal signals to Smads through Cripto-dependent and Cripto-independent mechanisms. *Mol. Cell* 2001; **7**: 949–957.
 - 28 Minchiotti G, Manco G, Parisi S, Lago CT, Rosa F, Persico MG. Structure-function analysis of the EGF-CFC family member Cripto identifies residues essential for nodal signalling. *Development* 2001; **128**: 4501–4510.
 - 29 Khalkhali-Ellis Z, Kirschmann DA, Seftor EA, Gilgur A, Bodenstine TM, Hinck AP, Hendrix MJ. Divergence(s) in nodal signaling between aggressive melanoma and embryonic stem cells. *Int. J. Canc. J. Int. du Canc.* 2014.
 - 30 Calvanese L, Marasco D, Doti N, Saporito A, D'Auria G, Paolillo L, Ruvo M, Falcigno L. Structural investigations on the Nodal-Cripto binding: a theoretical and experimental approach. *Biopolymers* 2010; **93**: 1011–1021.
 - 31 Romano V, Raimondo D, Calvanese L, D'Auria G, Tramontano A, Falcigno L. Toward a better understanding of the interaction between TGF-beta family members and their ALK receptors. *J. Mol. Model.* 2012; **18**: 3617–3625.
 - 32 Lin SJ, Lerch TF, Cook RW, Jardezyk TS, Woodruff TK. The structural basis of TGF-beta, bone morphogenetic protein, and activin ligand binding. *Reproduction* 2006; **132**: 179–190.
 - 33 Greenwald J, Vega ME, Allendorph GP, Fischer WH, Vale W, Choe S. A flexible activin explains the membrane-dependent cooperative assembly of TGF-beta family receptors. *Mol. Cell* 2004; **15**: 485–489.
 - 34 Muenster U, Korupolu R, Rastogi R, Read J, Fischer WH. Antagonism of activin by activin chimeras. *Vitam. Horm.* 2011; **85**: 105–128.
 - 35 Thompson TB, Woodruff TK, Jardezyk TS. Structures of an ActRIIB:activin A complex reveal a novel binding mode for TGF-beta ligand:receptor interactions. *Embo. J.* 2003; **22**: 1555–1566.
 - 36 Fields GB, Noble RL. Solid phase peptide synthesis utilizing 9-fluorenylmethoxycarbonyl amino acids. *Int. J. Pept. Protein Res.* 1990; **35**: 161–214.
 - 37 Bax A, Davis DG. MLEV-17-based two-dimensional homonuclear magnetization transfer spectroscopy. *J. Magn. Res.* 1985; **65**: 355–360.
 - 38 States D, Haberhorn R, Ruben D. A two-dimensional nuclear Overhauser experiment with pure absorption phase in four quadrants. *J. Magn. Res.* 1982; **48**: 286–292.
 - 39 Delaglio F, Grzesiek S, Vuister GW, Zhu G, Pfeifer J, Bax A. NMRPipe: a multidimensional spectral processing system based on UNIX pipes. *J. Biomol. NMR* 1995; **6**: 277–293.
 - 40 Johnson BA. Using NMRView to visualize and analyze the NMR spectra of macromolecules. *Methods Mol. Biol.* 2004; **278**: 313–352.
 - 41 Guntert P, Braun W, Wuthrich K. Efficient computation of three-dimensional protein structures in solution from nuclear magnetic resonance data using the program DIANA and the supporting programs CALIBA, HABAS and GLOMSA. *J. Mol. Biol.* 1991; **217**: 517–530.
 - 42 Guntert P, Mumenthaler C, Wuthrich K. Torsion angle dynamics for NMR structure calculation with the new program DYANA. *J. Mol. Biol.* 1997; **273**: 283–298.
 - 43 Guntert P. Automated NMR structure calculation with CYANA. *Methods Mol. Biol.* 2004; **278**: 353–378.
 - 44 Pearlman DA, Case DA, Caldwell JW, Ross WS, Cheatham TE III, DeBolt S, Ferguson D, Seibel G, Kollman P. AMBER, a package of computer program for applying molecular mechanics, normal mode analysis, molecular dynamics and free energy calculations to simulate the structural and energetic properties of molecules. *Comp. Phys. Commun.* 1995; **91**: 1–41.
 - 45 Pettersen EF, Goddard TD, Huang CC, Couch GS, Greenblatt DM, Meng EC, Ferrin TE. UCSF Chimera—a visualization system for exploratory research and analysis. *J. Comput. Chem.* 2004; **25**: 1605–1612.
 - 46 Koradi R, Billeter M, Wuthrich K. MOLMOL: a program for display and analysis of macromolecular structures. *J. Mol. Graph.* 1996; **14**: 51–55, 29–32.
 - 47 Wuthrich K. *NMR of Proteins and Nucleic Acids*, Wiley: New York, 1986.
 - 48 Wishart DS, Sykes BD, Richards FM. Relationship between nuclear magnetic resonance chemical shift and protein secondary structure. *J. Mol. Biol.* 1991; **222**: 311–333.

Supporting Information

Additional supporting information may be found in the online version of this article at the publisher's web site.

A Comparative Structural and Bioanalytical Study of IVIG Clinical Lots

Annamaria Sandomenico · Valeria Severino ·
Angela Chambery · Annalia Focà · Giuseppina Focà ·
Claudio Farina · Menotti Ruvo

Published online: 24 March 2013
© Springer Science+Business Media New York 2013

Abstract Intravenous immunoglobulin are important biotherapeutics used in the replacement therapy for primary and secondary immunodeficiencies, chronic inflammatory disorders and several autoimmune haematologic disorders. Currently, a number of immunoglobulin intravenous (IVIG) products have been approved by the Food and Drug Administration (FDA) and are available commercially. It is known that small differences in the manufacturing processes as well as in the formulations may affect their clinical efficacy and tolerability. Therefore, given the complexity of the multi-step process required for the isolation of IVIG from human plasma, it is necessary to ensure a rigorous quality control of final products. We show here that a set of different bioanalytical techniques can be conveniently used to comparatively characterize, at a quantitative and qualitative level, different lots of IVIG preparations and to unveil randomly occurring impurities

which can also affect the overall product stability. We have used circular dichroism, surface plasmon resonance and two-dimensional electrophoresis (2DE), and have demonstrated that this combination of bioanalytical approaches is very useful to improve the quality control of antibodies and to monitor the reliability of the IVIG manufacturing process.

Keywords IVIG · Circular dichroism · SPR · Biacore · Protein A · Thermal denaturation

Introduction

Intravenous immunoglobulin (IVIG) preparations have become the major plasma-derived product with increasingly important bio-therapeutic applications. Indeed, IVIG have been successfully employed for the treatment of several immunological and inflammatory diseases including replacement therapies for primary immunodeficiencies, such as X-linked agammaglobulinemia, hypogammaglobulinemia, some acute graft-versus-host diseases and chronic B cell lymphocytic leukaemia [1, 2]. In addition, IVIG preparations are also employed for the therapy of humoral immunodeficiencies related to several pathophysiological diseases. In this context, infusion of IVIG has been widely applied for the treatment and prevention of infectious and inflammatory diseases such as the coronary artery aneurysms in Kawasaki disease, the idiopathic thrombocytopenic purpura and the Guillain–Barré syndrome. Moreover, minor neurologic and dermatologic pathologies are also treated off-label with IVIG.

Except for the replacement therapy, the IVIG mechanism of action is not yet fully understood. However, clinical evidences suggest their involvement in the modulation

Electronic supplementary material The online version of this article (doi:10.1007/s12033-013-9655-7) contains supplementary material, which is available to authorized users.

A. Sandomenico (✉) · V. Severino · A. Focà · G. Focà · M. Ruvo
Istituto di Biostrutture e Bioimmagini, Consiglio Nazionale delle
Ricerche, via Mezzocannone, 16, 80134 Naples, Italy
e-mail: annamaria.sandomenico@gmail.com

A. Sandomenico · A. Focà · G. Focà · M. Ruvo (✉)
CIRPeB, via Mezzocannone, 16, 80134 Naples, Italy
e-mail: menotti.ruvo@unina.it

V. Severino · A. Chambery
Dipartimento di Scienze e Tecnologie Ambientali Biologiche
e Farmaceutiche, via A. Vivaldi, 43, 81100 Caserta, Italy

C. Farina
Kedrion SpA, Loc. Ai Conti, 55051 Lucca, Castelvechio
Pascoli, Italy

of multiple networks related to the expression and function of Fc receptors, the activation of the complement and cytokine pathways and the regulation of cell growth. Some effects on the activation, differentiation and effector functions of dendritic, T and B cells have been also hypothesized [3, 4].

Intravenous immunoglobulin preparations contain a pool of polyclonal IgG antibodies extracted from the plasma derived from a high number of healthy blood donors. Although manufacturing processes have been significantly improved in the last two decades to increase purity and yield of IVIG molecules, almost all the purification strategies include an initial step based on the Cohn–Oncley ethanol fractionation. Additional procedures (e.g. ion exchange chromatography, ultrafiltration, enzymatic digestion, pH and ion strength variations and organic solvent–detergent partitioning) may be applied for removing proteins and other minor contaminants, for minimizing the formation of IgG aggregates and for inactivating and removing viral contaminants such as hepatitis B virus, hepatitis C virus and human immunodeficiency virus [5].

In this framework, critical issues in the pharmaceutical production of active products, such as antibodies, are mainly related to the reproducibility and safety of the industrial-scale manufacturing processes and to the cost optimization measures. Increasingly stringent legislation at national and international level ensures the quality and safety of drugs and the materials used in their production. Therefore, given the wide use of IVIG as bio-therapeutics in a broad range of applications, there is a growing demand of powerful and reliable methodologies for the control of the IVIG production process aimed to guarantee the consistency, the quality and safety of the final drug. Although different commercial IVIG preparations are available and equivalent by a therapeutic point of view, an intrinsic variability may be present amongst different commercial products and different lots of the same products.

In this study, a set of bioanalytical methods have been used to characterize and comparatively analyse IVIG from different preparations to evaluate their application for the routine analysis of IVIG lots.

The experimental protocol for monitoring commercial IVIG preparations includes structural investigations carried out by circular dichroism (CD), protein denaturation studies, surface plasmon resonance (SPR) binding assays and two-dimensional electrophoresis (2DE).

The approach has proven to be very sensitive and reliable for the evaluation of full antibody, as well as of separate Fc and Fab, stability and integrity and for the monitoring of lot-to-lot consistency of different IVIG preparations. To demonstrate its applicability, we have analyzed in a comparative way, six different 10 % IVIG lots deriving from two distinct sets: one starting from

cryosupernatant 1 and one from fraction II–III, both purified by chromatographic methods.

Materials and Methods

Circular Dichroism Analysis

The six lots of 10 % IVIG, comprising 3 lots prepared from cryosupernatant 1 (lots A1, A2, A3) and 3 lots prepared from fraction II + III (lots B1, B2, B3) are produced by Kedrion S.p.A. 10 % solutions were used as starting material and properly diluted in the indicated buffers prior analysis. All CD analyses were performed using a JASCO J-710 spectropolarimeter, equipped with a Peltier system for changing the temperature in a controlled way and quartz cuvettes 110-QS with 1.0 mm path length. Experiments were performed in 10 mM phosphate, pH = 8.0 at a concentration of 0.20 mg/mL [6]. Spectra were collected within the wavelength range 250–190 nm at a scan rate of 20 nm/min, with a data pitch of 0.2 nm, a band width of 1 nm and a response of 4 s. In order to compare the different protein lots, far UV CD spectra were recorded at 20, 55, 60, 65, 70, 75, and 85 °C and then again at 20 °C ('after cooling' condition). The 'after cooling' spectrum was required to assess whether proteins were able to recover original structures or had undergone irreversible aggregation. Thermal denaturation experiments were performed by monitoring changes in ellipticity at 209 nm by exposure to increasing temperatures between 40 and 90 °C, at a speed of 60 °C/h (1 °C/min). The melting point was determined by the method of the first derivative.

On every sample, five independent spectra were recorded, averaged and smoothed using the Spectra Manager software, version 1.53. Buffer scans were recorded under the same conditions and subtracted. The analysis of secondary structure content was performed using the online server named *Dichroweb* [7, 10].

2D-PAGE Analysis

IVIG preparations at 100 mg/mL (10 %) were used without any further manipulation except dilution. Immobilized pH gradient (IPG) buffers, IPG strips and electrophoresis apparatus were purchased from GE Healthcare (Italy). Electrophoresis reagents, including acrylamide, *N,N,N,N*-methylenebisacrylamide, *N,N,N,N*-tetramethylethylenediamine, ammonium persulfate and sodium dodecylsulfate (SDS), were from BioRad (Milano, Italy). Chemical reagents were from Sigma-Aldrich (Milano, Italy). Gels were scanned using a Molecular Dynamics densitometer, model 375–557, from Amersham Biosciences (USA). Image analysis was performed using the

ImageJ software (Image processing and analysis in Java), available on-line on the National Institutes of Health website (Bethesda, Maryland, USA, <http://rsbweb.nih.gov/ij>). All other reagents were of analytical grade.

An extensive reduction of IgG disulphide bonds was performed on aliquots of IgG samples (50 mg/mL) by adding DTT 2.3 % in aqueous solution containing SDS 10 % (final volume: 15 μ L). Following an incubation of 5 min at 95 °C, samples were directly diluted in the rehydration solution to a final concentration of 2 mg/mL.

A total amount of 200 μ g of IgG were loaded on each gel, reduced as reported above, was analyzed by 2D-PAGE. Samples to be processed by isoelectrofocusing (IEF) were diluted with the rehydration buffer (8 M urea, 0.5 % CHAPS, 0.2 % DTT, 0.5 % IPG ampholytes and 0.002 % bromophenol blue) to a final volume of 125 μ L. The precast IPG strips (3–10 linear pH gradient, 7 cm long), used for the first dimension, were passively rehydrated and loaded with the sample at room temperature for 12 h under low-viscosity paraffin oil. IEF was then performed using an IPGphor isoelectric focusing cell, according to the following protocol: 50 V for 3 h, 100 V for 2 h, 500 V for 2 h, 1,000 V for 2 h, 3,000 V for 2 h, 4,000 V for 2 h, 5,000 V for 2 h, 6,000 V for 2 h, 8,000 V until about 25,000 V h total. Strips were then equilibrated twice for 15 min with gentle shaking in the equilibration solution (6 M urea, 50 mM Tris–Cl buffer pH 8.8, 30 % glycerol, 2 % SDS, 0.002 % bromophenol blue) containing 1 % DTT to reduce disulphide bonds, in the first equilibration step, and 2.5 % iodoacetamide to alkylate thiols, in the second. The second-dimension separation was performed in a 12 % polyacrylamide (7 \times 8 cm). The strips were fixed with 0.5 % agarose and 0.002 % bromophenol blue dissolved in SDS/Tris running buffer. The run was carried out at constant power (10 mA/gel for 15 min; 20 mA/gel until the end of the run). At the end of the electrophoresis, the protein spots were visualized by Coomassie Blue R250 staining.

After staining, 2D-gels were scanned using a Molecular Dynamics densitometer. Gel images were then processed for background subtraction and analysed for spot identification and matching using image analysis Image J software (<http://rsbweb.nih.gov/ij>). Quantification of relative band intensities to determine IgG purity was performed using the same software.

SPR Analyses

All analyses were performed on a Biacore 3,000 instrument from GE Healthcare, using certified HBS buffer (20 mM Hepes, 0.15 M NaCl, pH 7.2, P20, 0.005 %), at 25 °C.

Protein A (Sigma-Aldrich, Milano) was dissolved in deionized water at a concentration of 1.0 mg/mL. Protein immobilization was efficiently performed on the flow cells (FC) of CM5 sensor chips at 5.0 μ g/mL in sodium acetate 10 mM pH 4.5 following the canonical EDC/NHS (amine coupling) method, operating at 5 μ L/min [8]. An underivatized surface was prepared and used as control blank. Analyses were carried out at a flow rate of 20 μ L/min, injecting a constant volume of 60 μ L of IVIG solutions at the following concentration: 1.0, 2.5, 5.0, 10.0, 50.0, 100, 250, 500, 1,000, 1,500, 2,500, 3,000 nM. Dissociations were monitored for at least 600 s, performing at the end a regeneration step by injecting 20 μ L of a solution of 10 mM glycine, pH 2.7.

The immobilization of the anti-k-chain monoclonal antibody (mAb K4377, Sigma-Aldrich, Milano) was achieved in 10 mM sodium acetate pH 5, operating at a flow rate of 5 μ L/min. In this case, three flow channels were derivatized with the mAb at different immobilization levels: low density on FC2, 613 RU; medium density on FC3, 1813 RU; high density on FC4, 4718 RU. On FC1, used as reference, no protein was immobilized. Experiments were performed at 20 μ L/min with a total contact time of 180 s (60 μ L injected for every run). Dissociations were monitored for at least 600 s, regenerating at the end with a 20 mM solution of HCl with added 0.005 % v/v of surfactant P20. The concentrations of IgGs used for the binding experiments were: 10, 25, 50, 100, 500, 1,000, 1,500 and 2,000 nM. For every single analysis, experimental sensorgrams were aligned, subtracted of blank signals and overlapped. All mathematical manipulations and fitting were performed using the BiaEvaluation software, version 4.1 from GE Healthcare. Analyses were carried out using the six samples opportunely diluted in the HBS running buffer.

Fragment Crystallizable (Fc) Function

Because most of the anti-inflammatory properties of IVIG are mediated by the Fc antibody portion, evaluation of the Fc functional integrity of IgG is an indirect way to measure their therapeutic potential. This has been determined by Fc function in accordance with Eu. Ph., 2.7.9, method A [9], using haemolytic complement-fixation assay. This test is based on the haemolysis of antigen-coated fresh human red blood cells in the presence of guinea pig complement. Rubella antigen is used in the reference method. Results are reported as a ratio to an IgG standard (biological reference preparation—BRP—batch 3). For experimental details see also: British Pharmacopoeia Volume IV, Appendix XIV J. Blood and Related Products.

Results and Discussion

Comparative Evaluation of the Structural Stability Properties of Different Lots of IgG Preparations by Circular Dichroism

The thermal stability of the different IVIG lots analysed in this study, was first evaluated by CD. In Fig. 1a–f, an overlay of the far UV–CD spectra recorded for the six different samples at increasing temperatures from 20 to

85 °C and then back at 20 °C ('after cooling' condition), is reported. As shown, CD spectra of IVIG analyzed at 20 °C exhibited the canonical positive band at 202 nm, the negative band at 216–218 nm and an intensity equal to zero at 208–210 nm, typical of proteins with a high β -sheet content. Although the occurrence of several other positive and negative bands in the near UV, at around 260–300 nm is reported [6], these bands have not been considered in our analysis, because they are much less intense and poorly diagnostic. During thermal denaturation, the canonical

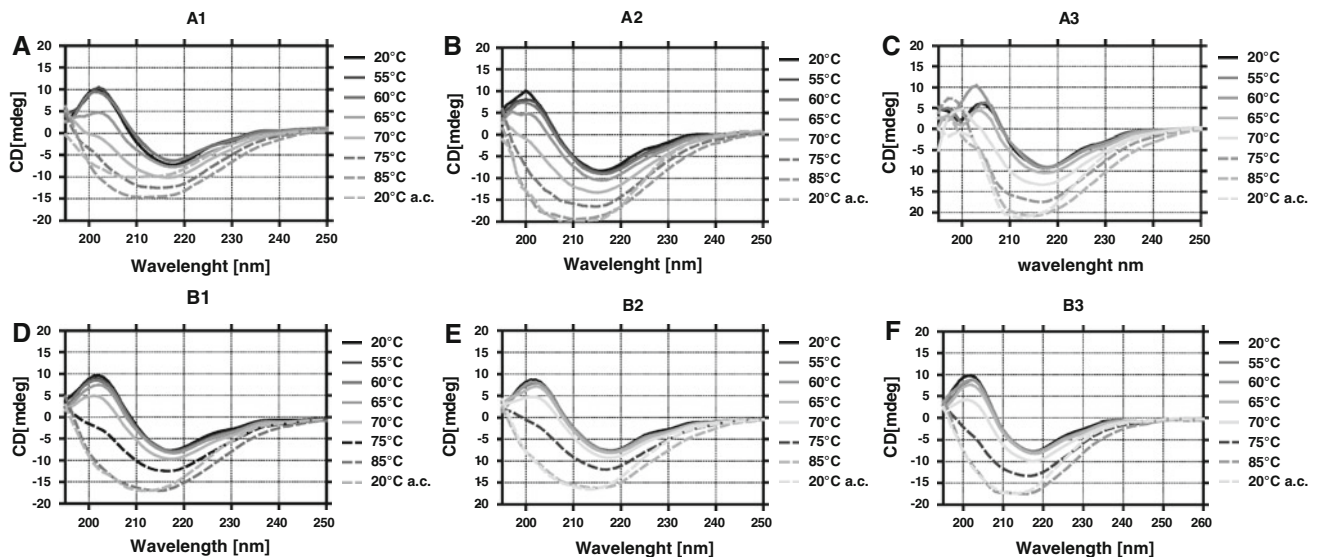


Fig. 1 a–f CD spectra of samples A1, A2, A3, B1, B2, B3 between 195 and 250 nm at the indicated temperatures

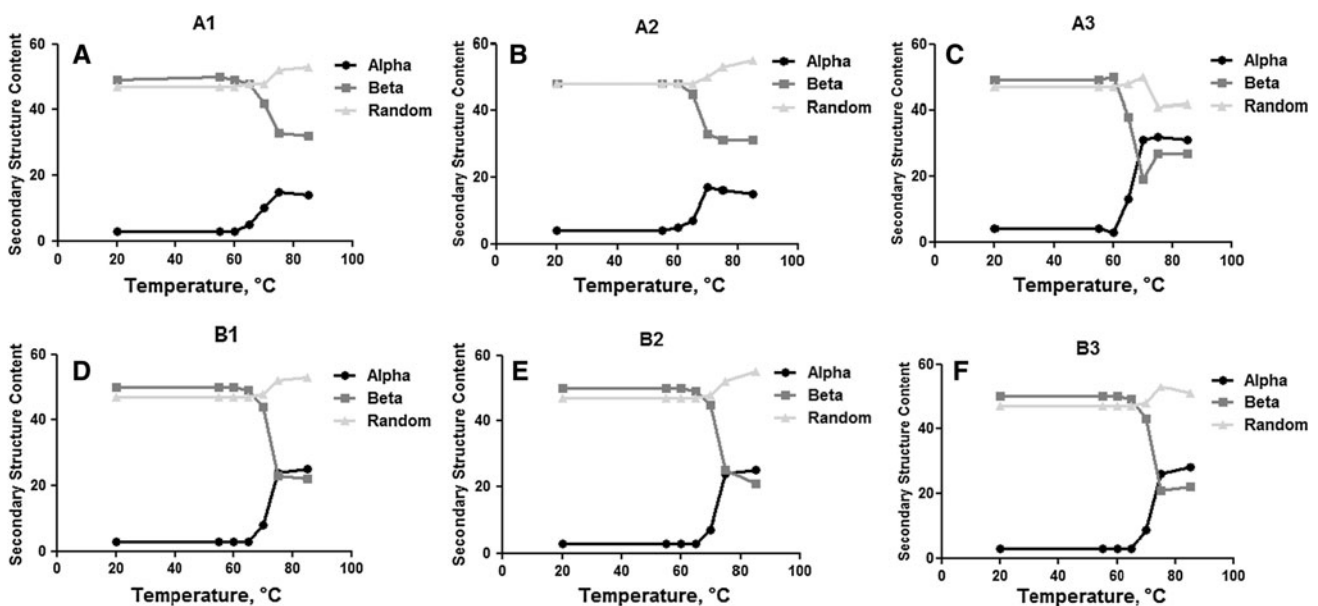


Fig. 2 a–f α -helix, β -sheet and random coil content determined for samples A1, A2, A3, B1, B2, B3 at the different temperatures using the Dichroweb server. Normalized root mean square deviation

(NRMSD), expressed as percentage, have also been determined for all analyses (not shown)

β -sheet spectrum was maintained up to 60 °C for all samples, confirming the high stability of antibodies. For temperatures below this threshold, the minimum at 216–218 nm was maintained more or less at the same intensity, between about -6 and -8 mdegrees.

Afterwards, starting from 65 °C, spectra varied considerably, suggesting severe structural changes. As shown in Fig. 1c, sample A3 exhibited a different behavior at shorter

wavelengths, with the maximum shifting from about 205 to 195 nm. Such changes are suggestive of a general reduced stability of proteins present in this preparation. By further temperature increase, a progressive denaturation was observed for all samples, witnessed by the large changes in the CD spectra. In particular, the band at 209 nm was progressively lost, leading to spectra resembling more those of proteins having a large content of α -helix (see for

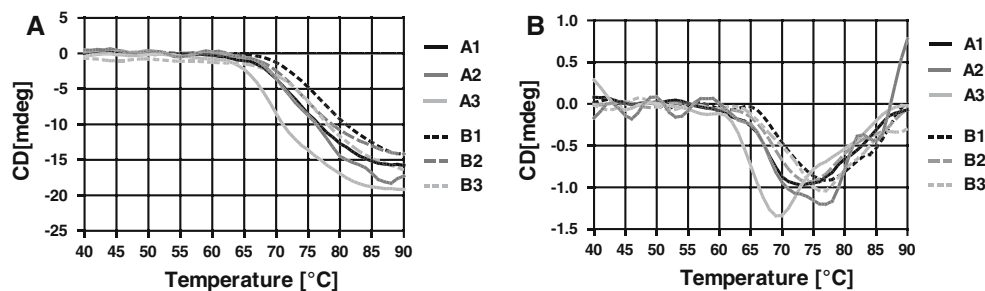


Fig. 3 **a** Curves of thermal denaturation between 40 and 95 °C for all samples analyzed in this study. **b** The corresponding first derivative for the curves are reported. Spectra were collected between 195 and 250 nm

Fig. 4 **a–f** 2D-PAGE analysis of immunoglobulin preparations on 7 cm strips (linear gradient pH 3–10). The basic isoelectric points are to the *right* and acidic to the *left*. *Red squares* three-dimensional magnifications are reported in 4g–n. **g–n** Three-dimensional profiles of 2D-maps of IgG preparations obtained using the ‘interactive 3D-surface plot’ application of ImageJ software. Magnifications of regions indicated by *red squares* in Fig. 1 are shown. *Red arrows* indicate streaks not detected in S220611, 270711 and S280911 2D-maps. (Color figure online)

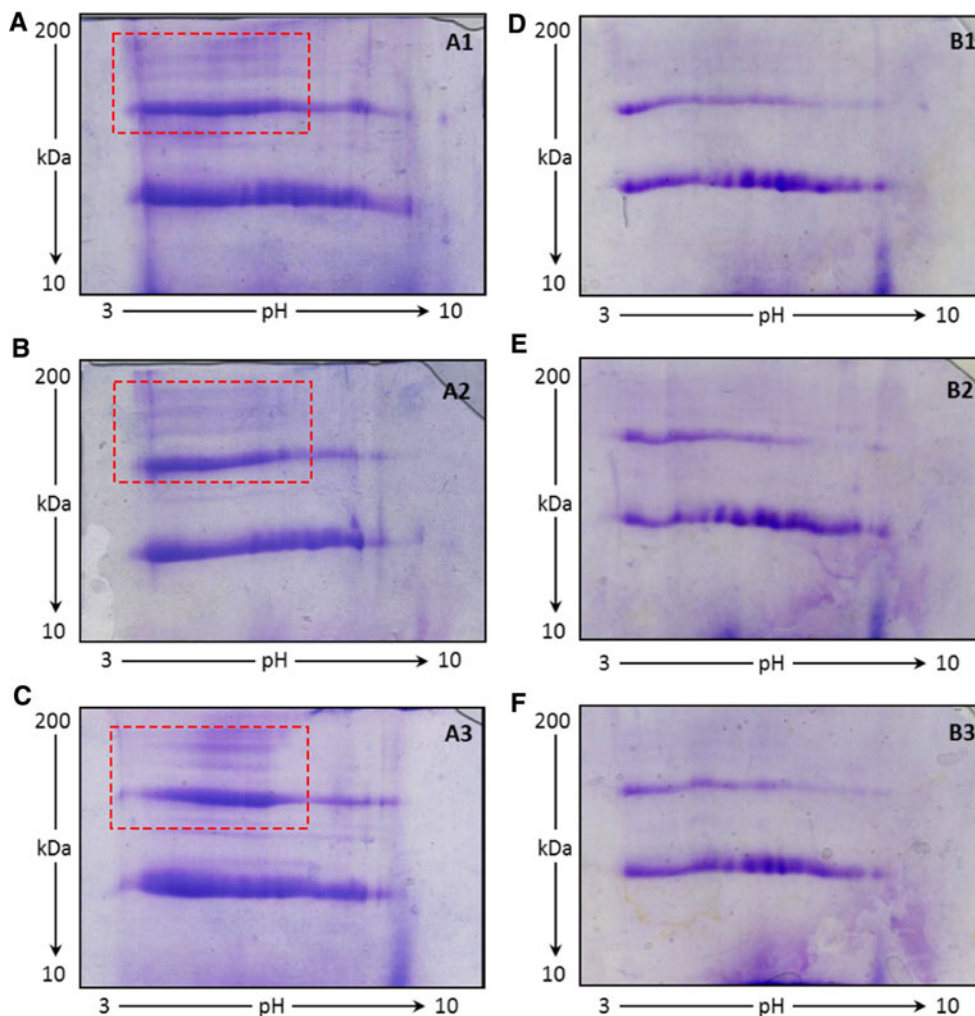
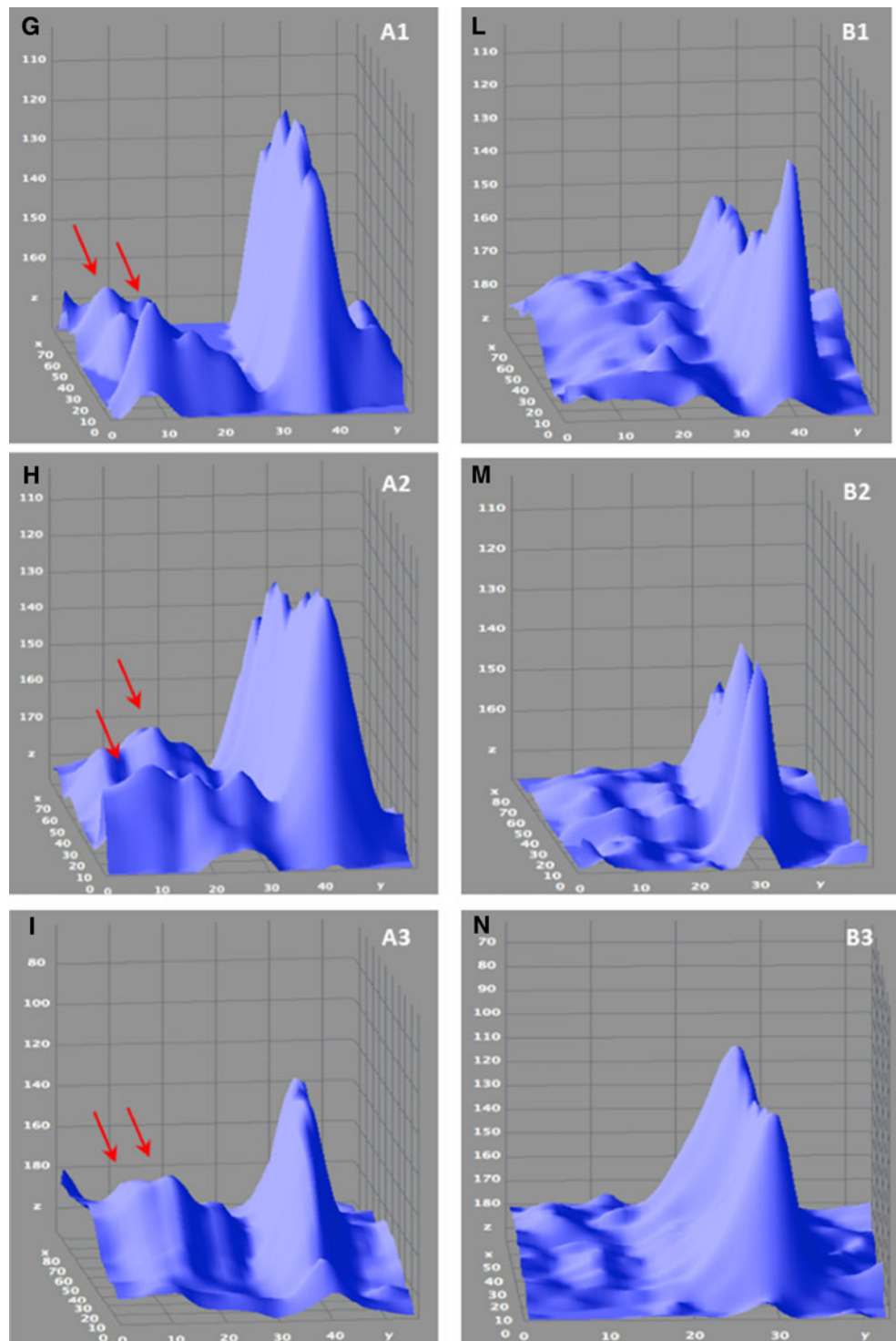


Fig. 4 continued



example spectra at 85 °C). For all samples, except A3, also a shift of the point at zero millidegrees was observed (from 208 up to about 197 nm). The shift observed by analyzing sample A3 was instead less intense, and the overall signal below 200 nm strongly changed with the temperature, certainly due to premature protein precipitation. After cooling to record again the spectra at 20 °C, original bands

were not restored and white precipitates were observed in the cuvettes for all samples. In Fig. 2a–f, the global changes in α -helix, β -sheet and random coil contents, at all temperatures, obtained using the software Dichroweb, are reported [8, 9]. According to the changes observed in spectra, a progressive and remarkable reduction of the β -sheet content was noticed, paralleled by an increase in

the α -helix character and a less intense increase of the random coil content. As shown, changes in the samples from cryosupernatant 1 were less intense; furthermore, one of these samples, A3, exhibited a decrease of the random coil character and a more marked change of the α -helix and β -sheet contents, in agreement with the spectral changes below 200 nm described before.

To further unveil possible differences in stability, melting curves were recorded following signal change at 209 nm as a function of the temperature increase. Since proteins were essentially very stable up to about 60 °C, melting curves were recorded only between 40 and 95 °C. In Fig. 3a, an overlay of melting curves for all samples is shown, and as can be seen, except that referred to as sample A3, which yet declined at 65 °C, all exhibited a sudden drop of signal starting at about 70 °C. This difference is also reflected in the graph of Fig. 3b reporting the first derivatives of all spectra, where the minimum of sample A3 is clearly shifted some 5° towards lower temperatures compared to those of other samples. Altogether, data indicate that all IVIG samples behave in a similar way in terms of resistance to thermal denaturation, with a slightly higher stability exhibited by lots deriving from cryosupernatant 1 fraction. Amongst these, sample A3, more rapidly aggregated and precipitated upon heating, thus showing unique properties, presumably deriving by the occurrence of pre-existing random aggregates.

Analysis of IVIG Preparations by 2D-PAGE

Immunoglobulins (Igs) are a heterogeneous population of proteins (polyclonal immunoglobulins), whose basic structure consists of two identical halves connected by disulphide bonds. Each half is made up of a heavy chain of ~55 kDa and a light chain of ~25 kDa, joined together by a disulphide bond near the carboxyl terminus of the light chain. The heterogeneity of Igs is not detectable using monodimensional SDS-PAGE, which only resolves the

most abundant protein bands at 55 and 25 kDa. An extensive bioanalytical characterization of all samples was thus performed by 2D-PAGE followed by densitometric analysis, in order to assess the occurrence of low-abundance impurities and a possible correlation with the different physico-chemical properties evidenced by the CD analysis. After extensive reduction, aliquots of proteins (200 μ g) were separated by 2D-PAGE using, for the first dimension, IPG strips with a linear 3–10 pH gradient. The second dimension was carried out on 12 % polyacrylamide gel, following further reduction and alkylation steps. At the end of the run, 2D-gels were stained with Coomassie Blue R250 and the resulting gels are reported in Fig. 4a–f. As expected, multiple protein spots were visualized in the regions with molecular mass of about 25 and 55 kDa, corresponding to the light and heavy chains of IgG, respectively. These profiles attested the IgG polyclonal nature with many isoforms with the same molecular weight but differing in their isoelectric point. However, though all samples appeared highly homogeneous, 2D-maps corresponding to the A group, comprising A1, A2 and A3, showed a set of streaks having MW between about 70 and 150 kDa and pIs comprised between about 4 and 7; remarkably, the most intense streaks were visible on the gel corresponding to sample A3.

A more detailed comparison of the 2D-gels of the different IgG preparations was also performed following gel images acquisition and quantitative analysis. Three-dimensional profiles of the gel image sections boxed in Fig. 4a–f are reported in Fig. 4g–n and Fig. S1a–f in the supporting material, and provide a more quantitative view of the impurities (indicated by arrows). In Table 1, the level of purity of samples studied is reported and as shown, A lots contain detectable levels of impurities (1.12, 1.15 and 1.30 %, respectively), whereas B lots appear 100 % pure. Remarkably, lot A3 has the highest content of impurities, which could account for the difference in stability observed during the CD analysis.

Table 1 Impurities detected on the six samples of IVIGs. Both absolute and percentage values are reported

Intensity	IgG samples					
	A1	A2	A3	B1	B2	B3
IgG light chain	6,174.52	9,175.93	6,372.33	3,483.64	4,229.45	3,700.35
IgG heavy chain	17,293.27	19,822.25	18,559.78	12,689.34	12,496.99	11,052.83
IgG total	23,467.79	28,998.18	24,932.11	16,172.98	16,726.44	14,753.18
Impurities	262.85	334.38	324.01	0.00	0.00	
% impurities	1.12	1.15	1.30	0.00	0.00	0.00
% IgG	98.88	98.85	98.70	100.00	100.00	100.00

Fig. 5 a–c Envelope of sensorgrams for the IgG lots A1, A2 and A3. Concentrations are reported *below* each group of curves. **d–f** Envelope of sensorgrams for the IgG lots B1, B2 and B3. Concentrations are reported *below* each group of curves

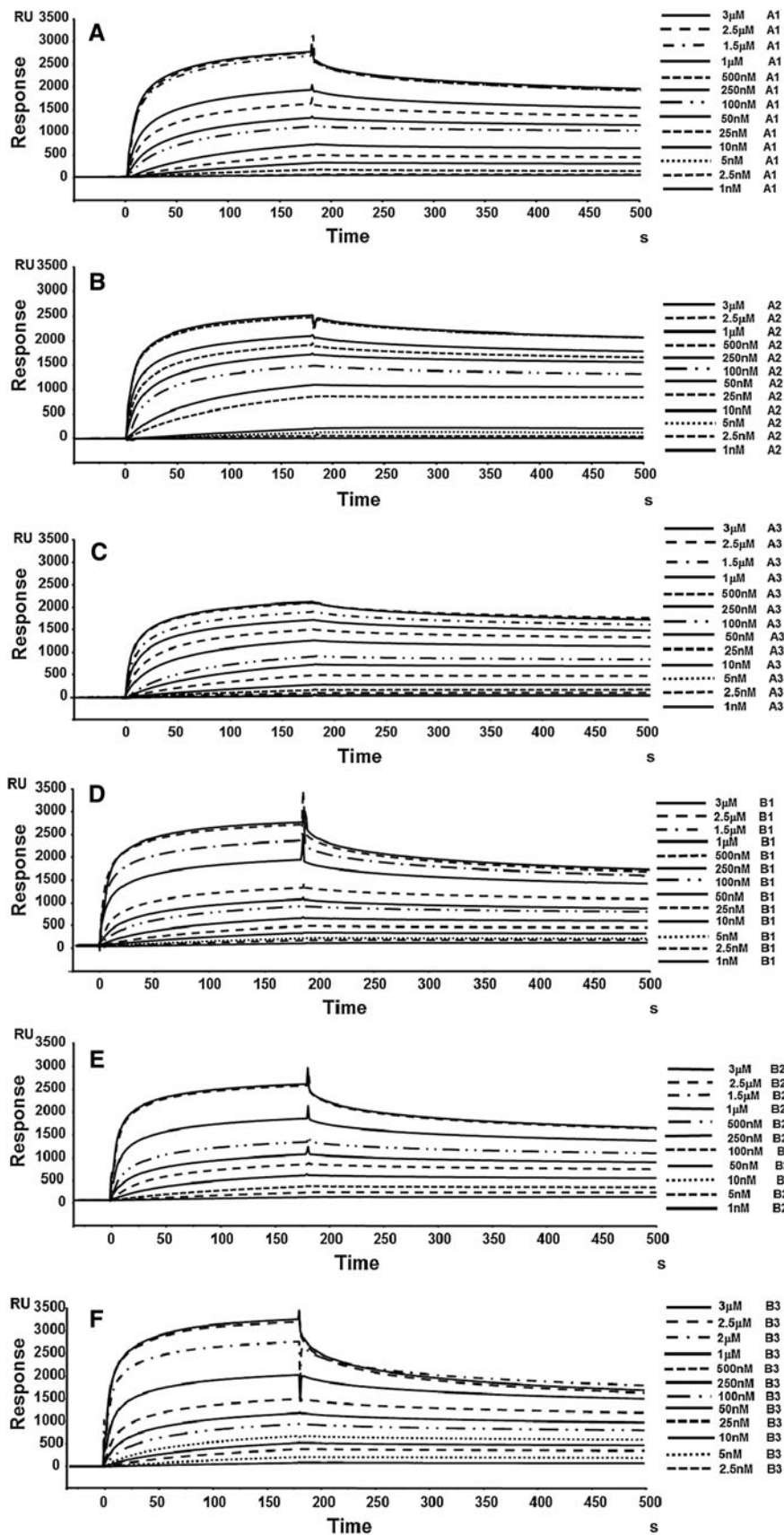


Fig. 6 a–f Correlation curves between RU_{max} values at each concentrations and concentrations itself for IgG lots A1, A2, A3 and B1, B2, B3 expressed as Log M. For each single plot the EC_{50} value calculated by this method is also reported. Correlation curves between RU_{max} values at each concentrations and concentrations itself for IgG lots A1, A2, A3 and B1, B2, B3 expressed as Log M. For each single plot the EC_{50} value calculated by this method is also reported

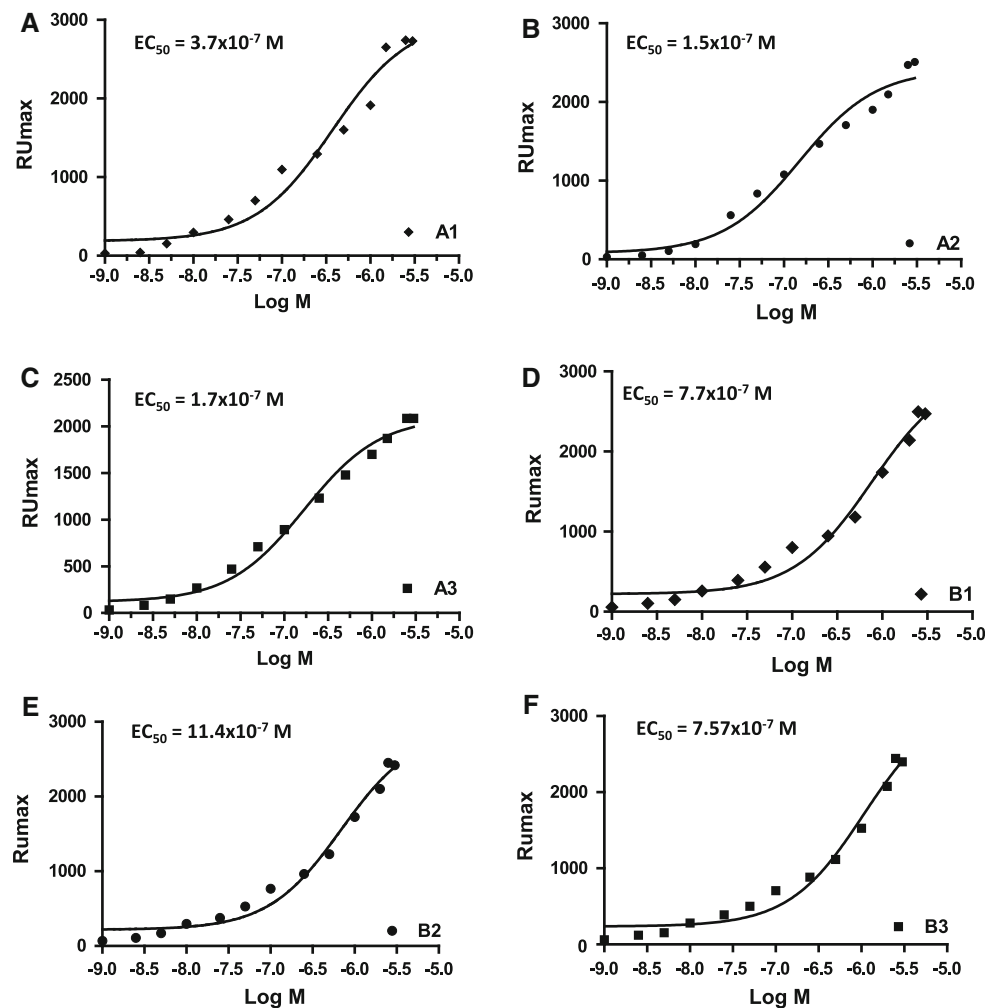


Table 2 Values of the EC_{50} values determined for all IgG lots and the relative standard errors

IgG samples	A1	A2	A3	B1	B2	B3
EC_{50} (M)	$3.7 \pm 2.0 \times 10^{-7}$	$1.5 \pm 0.8 \times 10^{-7}$	$1.7 \pm 0.7 \times 10^{-7}$	$7.7 \pm 1.0 \times 10^{-7}$	$11.4 \pm 0.7 \times 10^{-7}$	$7.5 \pm 0.7 \times 10^{-7}$

Comparative Binding Analysis of the Different Lots of IVIG to Protein A (pA) by SPR

To have a measure of the integrity of the Fc portion of IVIG, we performed binding analyses of the different IgG preparation to pA. pA is a bacterial protein largely used to purify Igs of different classes from complex matrices. It is known to bind on a region of the Fc portion that comprises residues from the $C\gamma 2$ and $C\gamma 3$, therefore comparative binding analyses can provide information on the relative integrity of this IgG region.

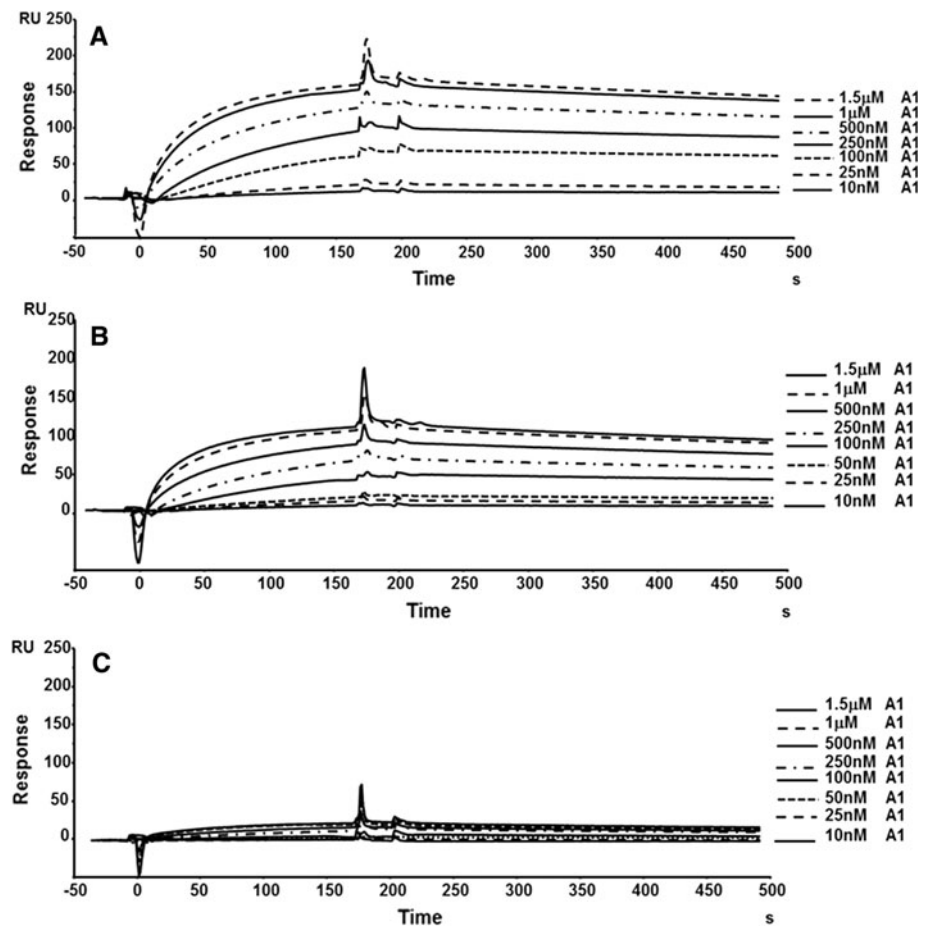
pA is a protein of 42 kDa which binds with high affinity and selectivity at least two distinct IgG molecules [11], however the exact stoichiometry is at present not known and generally is dependent on experimental conditions and

technique used. In solution the stoichiometry can be higher than 2:1 and also binding sites on the IgGs are two, therefore the mathematical models for studying this interaction can be complex [11].

Analyses were carried out by SPR, using sensor chips with immobilized pA. Optimal concentrations for these analyses were between 1 and 2,500 nM.

The envelopes of sensorgrams referred to the six IVIG lots, reported in Fig. 5a–f, show as all curves have essentially the same shape and trend, reaching the saturation for concentrations higher than 2,500 nM. Since the binding stoichiometry between pA and IgGs is not well-defined, especially for interactions occurring on solid surfaces, to derive kinetic and thermodynamic binding parameters K_{onS} , K_{offS} and K_{DS} , we tried with different mathematical

Fig. 7 a–c Sensorgrams obtained for the interaction between the immobilized Mab anti-k-chain and IgGs from the lot A1 on FC4 (high density, a), on FC3 (medium density, b) and on FC2 (low density, c)



models of interactions (including 1:1, 1:2 stoichiometries or even higher). However, all attempts to fit the curves failed or gave inaccurate results (see Fig. S2a, b in the supporting material as an example of failed fitting). Therefore, in order to compare the analyses, we built plots reporting RU_{max} values versus analyte concentration, as reported in Fig. 6a–f. Next, using an algorithm of nonlinear regression and assuming a 1:1 stoichiometry, we derived a measure of global affinities, expressed as EC_{50} which could be seen as the resultant of multiple interactions [12, 13]. EC_{50} s values determined by this method are summarized in Table 2. As expected, values are all very similar, being comprised between 1.5×10^{-7} and 3.9×10^{-7} M, however EC_{50} s for the B lots are slightly higher (about doubled), not only suggesting a higher consistency among lots within the same group, but also measurable differences among lots coming from different starting material.

A further comparison was performed by comparing RU_{max} values observed at a given concentration. Data are plotted in Fig. S3 in supporting material, whereby for each distinct lot, RU_{max} values at all concentrations are reported. It can be reasonably assumed that, the more similar are RU_{max} values, the more is expected that IgG samples are

similar each other. By analyzing data, it emerged that the set of B samples comprising lots B1, B2 and B3, appears more homogeneous with almost identical values at the same concentrations. This holds not true for samples A1, A2 and A3 which indeed showed varying RU_{max} values at the same concentration. This effect, negligible at low concentrations, is more evident for concentrations higher than 10 nM. It should be also noticed that RU_{max} values are a little bit higher for IgGs lots from set A, as compared to those obtained with IgGs from the other one. This difference could be due to the presence of small amounts of aggregates in set A, which could form (or be retained after dilution) at higher concentrations and over time. Aggregates, being bigger than monomeric IgG, provide more intense SPR signals.

Comparative Analysis of Different Lots of IVIG to Anti-k-chain mAb by SPR

The study performed with pA was paralleled by another comparative study carried out using an anti-k-chain monoclonal antibody, in order to obtain a global evaluation of the Fab integrity.

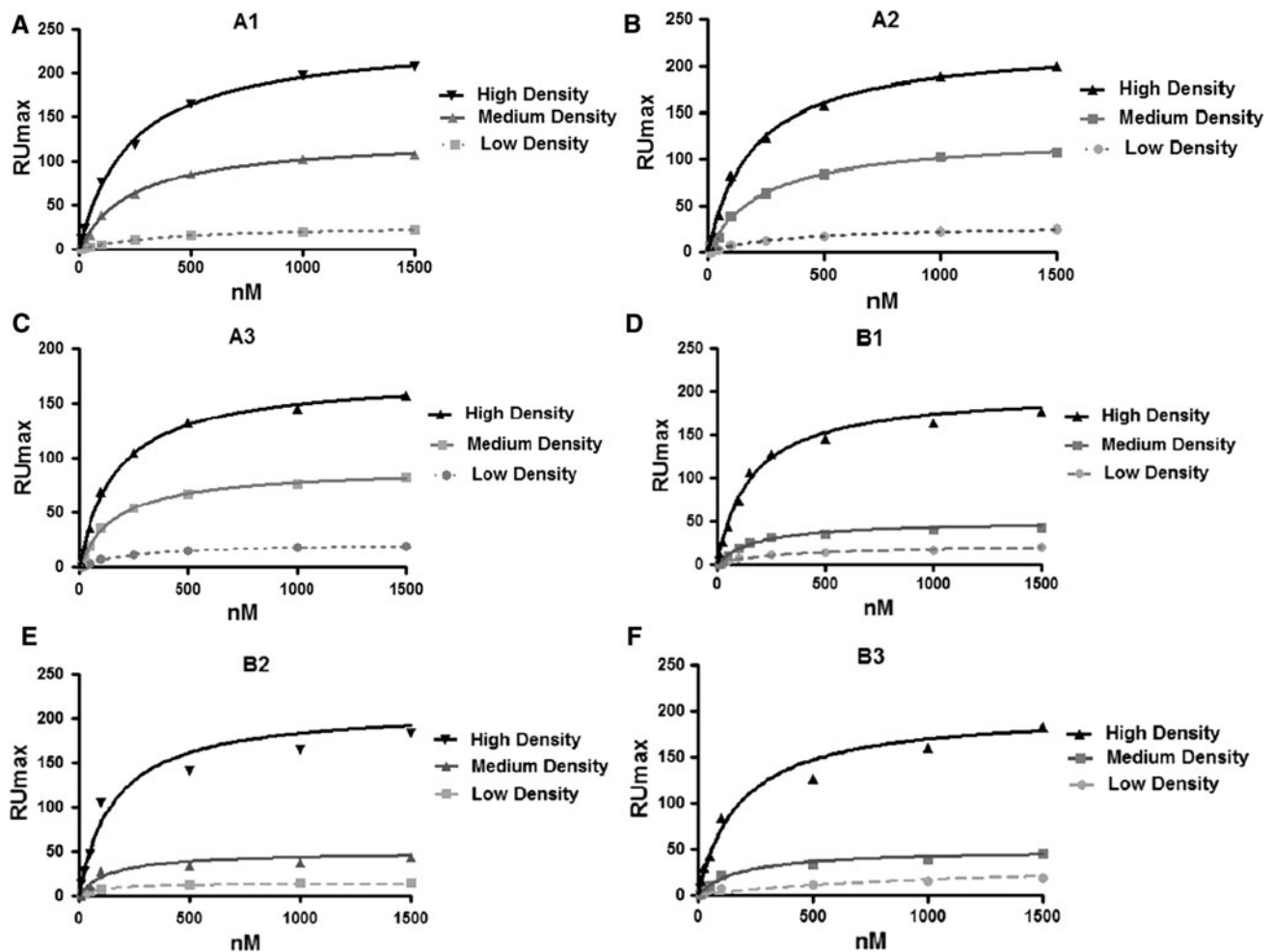


Fig. 8 a–f Plots reporting RU_{max} values versus IgGs concentration for all lots analyzed

Binding experiments were performed in parallel on three channels with different immobilization levels. In Fig. 7a–c, the envelopes of sensorgrams obtained for one of the six samples (sample A1) at three different immobilization levels, are reported. In the supporting material Fig. S4–S8, sensorgrams corresponding to the remaining five analyses are reported. In all plots, time and RU scales were kept at the same values to visualize at best differences in RUs achieved on the distinct channels by varying ligand density. As expected, lower bindings were recorded for lower ligand density and curves were all very similar. As with the pA, bindings were analyzed by determining the global K_D s plotting the RU_{max} values derived from every single injection on distinct flow channels versus the concentration of Igs. Data were then best fitted by a nonlinear regression analysis and are reported in Fig. 8a–f. K_D s determined by this method are instead reported in Table 3. As can be seen, values are very similar for the same IgG lot on channels at

different immobilization levels, thus suggesting that the analyses are very reproducible and reliable. It should be pointed out that K_D s are also very similar amongst different lots with values ranging between about 136 and 288 nM, suggesting that the population of Igs present in the different lots are highly comparable in terms of Fab homogeneity.

Fragment Crystallizable (Fc) Function

The functional integrity of the Fc fragment of all analysed lots was evaluated using a well-established method suggested by the European Pharmacopeia. Data for all six samples are presented in Table 4 and show that results are in compliance, therefore proving the full functionality of the analysed IgGs. Despite large differences in function are observed between the diverse IVIG lots, they do not correlate with the slight discrepancies emerged at the bioanalytical level.

Table 3 K_D values for the binding between IgGs and the immobilized anti-k-chain mAb K4377, as obtained by nonlinear regression analyses of curves reported in Fig. 8a–f

	Low density	Medium density	High density	Average	SD
A1					
KD (nM)	380.9	251.0	232.4	288.1	80.9
A2					
KD (nM)	347.1	254.2	203.8	264.4	73.7
A3					
KD (nM)	269.4	171.7	170.6	203.9	56.7
B1					
KD (nM)	303.2	176.3	159.5	213.0	78.5
B2					
KD (nM)	110.3	141.1	158.4	136.6	24.4
B3					
KD (nM)	1,149**	185.5	182.3	183.9	23**

SD standard deviation

** This value has not been considered for calculating the average K_D , therefore the corresponding SD is also meaningless, being derived by only two values

Table 4 Fragment crystallizable function

	Limit	From cryosupernatant 1			From Fr II + III		
		Lot A1	Lot A2	Lot A3	Lot B1	Lot B2	Lot B3
Fragment crystallizable (Fc) function (%)	>60	82	116	90	79	87	85

Limits are defined in accordance with EU pharmacopoeia: the value is stated in the leaflet accompanying the reference preparation (BRP—batch 3)

Conclusions

We have undertaken a comparative evaluation of the macroscopic physico-chemical properties of six different lots of IVIG coming from two distinct preparations. Three lots, A1–A3, came out from a chromatographic purification from a cryosupernatant fraction, whereas three other lots were obtained from fraction II–III, using the same chromatographic purification procedure. The study has been carried out using different bioanalytical techniques to gain a global view of antibody properties, to assess lot-to-lot consistency and to point out possible differences arising from the different starting material. For this purpose we have conducted on all samples: (i) a macroscopic structural analysis by CD, also evaluating IgG resistance to thermal denaturation; (ii) an evaluation of purity by 2D-gel analyses and (iii) a macroscopic evaluation of Fc and Fab

integrity by SPR, carrying out comparative binding studies to pA and to an anti-k chain monoclonal antibody.

As expected, samples displayed quite identical properties and it was difficult to unveil macroscopic dissimilarities, however subtle but measurable differences emerged amongst the different lots during the investigation, especially amongst lots coming from different starting material (lots A vs. lots B). Since the different lots have the same age and have been purified all by the same method, the presence of such impurities or degradation components demonstrates that side products occurring in these experimental IVIG lots can only arise from the diverse raw material. The reason for this has not been investigated here; we can however hypothesize that small impurities are either co-purified with the main component or generated during the purification steps or during storage. Irrespective of the way they are generated, these impurities can be detected and quantified by 2DE and, looking retrospectively at our CD data, could also be predicted to some extent by a CD analysis, which seems to be qualitatively affected by such low levels of contaminants.

Data show that IgGs purified from Fraction II–III are generally homogeneous compared to those obtained from cryosupernatant 1, but also that IgGs extracted from the same starting material have a higher lot-to-lot consistency, thus suggesting that also the very initial steps of plasma manipulation can affect final products. Furthermore, we have observed that one lot (lot A3), showed reduced resistance to thermal denaturation and, at the same time, also contained sensibly higher amounts of undetermined impurities (presumably immunoglobulin fragments), as detected by 2DE. Remarkably, lots A1 and A2, coming from the same raw material (cryosupernatant 1) also contained detectable levels of impurities (see Table 1; Fig. 4), but the resistance to thermal denaturation was comparable to that of the purer lots B1–B3. In order to further unravel differences between lots, an extensive characterization by SPR was also performed. In our experimental setting, the SPR approach would allow to dissect differences deriving from the Fab and/or the Fc antibody portions, however it proved generally less sensitive, being able to measure subtle differences only for the binding to pA and not to the anti-k-chain K4377 mAb. While confirming that samples coming from the same set of lots are more homogeneous, we also noticed that lots A are less comparable in terms of relative binding to pA in respect to B lots (see the supplementary Fig. S3).

Altogether, our results show that this set of bioanalytical techniques is useful and complementary to the analytical tests provided in the European Pharmacopoeia for a better global view of IVIG purity, stability and integrity of full antibodies, as well as of separate Fc and Fab fragments.

References

1. Kaveri, S. V., Maddur, M. S., Hegde, P., Lacroix-Desmazes, S., & Bayry, (2011). Intravenous immunoglobulins in immunodeficiencies: More than mere replacement therapy. *Journal of Clinical and Experimental Immunology*, 164(Suppl 2), 2–5.
2. Navarro, R. P., Ballou, M., Fenrick, B., & Pezalla, E. J. (2012). Considerations for the optimal use of immunoglobulin. *American Journal of Managed Care*, 18(4 Suppl), S67–S78.
3. Baerenwaldt, A., Biburger, M., & Nimmerjahn, F. (2010). Mechanisms of action of intravenous immunoglobulins. *Expert Review of Clinical Immunology*, 6(3), 425–434.
4. Bayry, J., Fournier, E. M., Maddur, M. S., Vani, J., Wootla, B., Sibénil, S., et al. (2011). Intravenous immunoglobulin induces proliferation and immunoglobulin synthesis from B cells of patients with common variable immunodeficiency: A mechanism underlying the beneficial effect of IVIg in primary immunodeficiencies. *Journal of Autoimmunity*, 36(1), 9–15.
5. Radosevich, M., & Burnouf, T. (2010). Intravenous immunoglobulin G: Trends in production methods, quality control and quality assurance. *Vox Sanguinis*, 98(1), 12–28.
6. Vermeer, A. W., & Norde, W. (2000). The thermal stability of immunoglobulin: Unfolding and aggregation of a multi-domain protein. *Biophysical Journal*, 78(1), 394–404.
7. Whitmore, L., Wallace, B. A., & DICHROWEB. (2004). An online server for protein secondary structure analyses from circular dichroism spectroscopic data. *Nucleic Acids Research*, 1(32(web server issue)), W668–W673.
8. Johnsson, B., Lofas, S., & Lindquist, G. (1991). Immobilization of proteins to a carboxymethyl-dextran-modified gold surface for biospecific interaction analysis in surface plasmon resonance sensors. *Analytical Biochemistry*, 198, 268–277.
9. In accordance with EU pharmacopoeia: the values are stated in the leaflet accompanying the reference preparation (BRP—batch 3). See also: British pharmacopoeia volume IV, appendix XIV. *Journal of Blood and Related Products*.
10. Whitmore, L., & Wallace, B. A. (2008). Protein secondary structure analyses from circular dichroism spectroscopy: Methods and reference databases. *Biopolymers*, 89(5), 392–400.
11. Cohen, S., & Sweeney, H. M. (1979). Modulation of Protein A Formation in *Staphylococcus aureus* by Genetic Determinants for Methicillin Resistance. *Journal of Bacteriology*, 140(3), 1028–1035.
12. Velge-Roussel, F., Breton, P., Lescure, F., Guillon, X., Bout, D., & Hoebeke, J. (1995). Analysis of human CD4-antibody interaction using the BIAcore system. *Journal of Immunological Methods*, 183(1), 141–148.
13. Sandomenico, A., Monti, S. M., Marasco, D., Dathan, N., Palumbo, R., Saviano, M., et al. (2009). IgE-binding properties and selectivity of peptide mimics of the Fc ν arepsilonRI binding site. *Molecular Immunology*, 46(16), 3300–3309.